

Development of a Fracture Mechanics / Threshold Behavior Model to Assess the Effects
of Competing Mechanisms Induced by Shot Peening on Cyclic Life of a
Nickel-base Superalloy, René 88DT

Dissertation
Submitted to
The College of Engineering of the
UNIVERSITY OF DAYTON


in Partial Fulfillment of the Requirements for
The Degree
Doctor of Philosophy in Materials Engineering

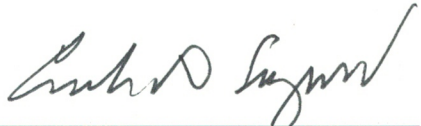
by
Marsha Klopmeier Tufft


UNIVERSITY OF DAYTON
Dayton, Ohio
April 1997


Development of a Fracture Mechanics / Threshold Behavior Model to Assess the Effects
of Competing Mechanisms Induced by Shot Peening on Cyclic Life of a
Nickel-base Superalloy, René 88DT

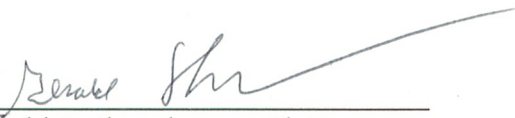
APPROVED BY:

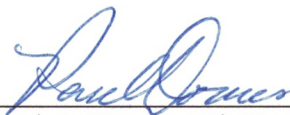

Joseph P. Gallagher, Ph.D.
Advisory Committee Chairman
Professor, Department of Materials
Engineering

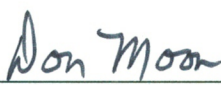

Gordon A. Sargent, Ph.D.
Committee Member
Vice President for Graduate Studies
and Research, and Dean of the
Graduate School

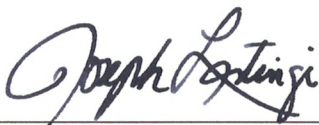

James A. Snide, Ph.D.
Committee Member
Director, Graduate Materials
Engineering


Daniel Eylon, Ph.D.
Committee Member
Professor, Department of Materials
Engineering


Gerald J. Shaughnessy, Ph.D.
Committee Member
Professor, Department of
Mathematics


Paul A. Domas, Ph.D.
Committee Member
Senior Staff Engineer
General Electric Aircraft Engines


Donald L. Moon, Ph.D.
Associate Dean
Graduate Engineering Programs & Research
School of Engineering


Joseph Lestingi, D. Eng., P.E.
Dean, School of Engineering

© Copyright by
Marsha Klopmeier Tufft
All rights reserved
1997

ABSTRACT

Development of a Fracture Mechanics / Threshold Behavior Model to Assess the Effects of Competing Mechanisms Induced by Shot Peening on Cyclic Life of a Nickel-base Superalloy, René 88DT

Marsha Klopmeier Tufft
University of Dayton, 1997

Dr. J. P. Gallagher, Advisor

This research establishes an improved lower-bound predictive method for the cyclic life of shot peened specimens made from a nickel-base superalloy, René 88DT. Based on previous work, shot peening is noted to induce the equivalent of fatigue damage, in addition to the beneficial compressive residual stresses. The ability to quantify the relative effects of various shot peening treatments on cyclic life capability provides a basis for more economic use of shot peening, and selection of shot peening parameters to meet design and life requirements, while minimizing production costs.

The predictive method developed consists of two major elements: 1) a Fracture Mechanics Model, which accounts for changes in microstructure, residual stress and topography induced by shot peening, and 2) a Threshold Behavior Map which identifies both crack nucleation and crack propagation thresholds. When both thresholds are crossed, life capability can be evaluated using the Fracture Mechanics model developed. When the crack propagation threshold is exceeded but the crack nucleation threshold is not, the FM method produces a conservative lower-bound estimate of life capability. A unique contribution is the characterization of damage induced by peening by an initial flaw size from microstructural observations of slip depth. Observations of crack formation

along slip bands in a model disk provide reinforcement for defining a flaw size from slip measurements.

Supporting research includes: 1) metallurgical and microstructural evaluation of single impact dimples and production peened coupons, 2) instrumented Single Particle Impact Tests, characterizing changes in material response due to variations in impact conditions (particle size, incidence angle, velocity), 3) duplication of 16 peening conditions used in a designed experiment, characterizing slip depth, residual stress profiles, surface roughness and velocity measurements taken during production peening conditions.

ACKNOWLEDGMENTS

I would like to thank Mr. J.W. Heyser, Mr. R.L. Ditz, Dr. P.A. Domas, and Mr. W.W. Rose of General Electric Aircraft Engines, Cincinnati, Ohio, who made it possible for me to pursue my Ph.D. with a business-related dissertation, and who provided funding for the experimental work. Without their support, this work would never have been possible.

A special thanks is due to my advisory committee members throughout the course of this effort, for the many stimulating conversations that helped to steer and shape this effort: Dr. J.P. Gallagher, my primary advisor, Dr. G.A. Sargent, Dr. J.A. Snide, Dr. D. Eylon, Dr. G.J. Shaughnessy, and Dr. P.A. Domas.

I am indebted to several colleagues from GE who helped to educate me on the details of shot peening, in particular, Mr. P.G. Bailey, Mr. D.R. Lombardo, Mr. R.W. Ellis, Mr. M.B. Happ, Dr. R.A. Thompson, and Mr. H.G. Popp. Mr. H.G. Popp also helped to focus me back onto a fracture mechanics approach. These people have been the torch-holders for shot peening at GE for many years. Their assistance is greatly appreciated. I would also like to thank the other team members from the Six Sigma Shot Peening Project, who include Dr. P.A. Domas, Mr. R.J. Meade, Mr. T.C. Kessler, Dr. A.W. Dix, Mr. M.D. Gorman, and especially our team "Black Belt," Mrs. R.E. Brands. Their dedication, enthusiasm, persistence and contributions generated many enlightening conversations. I am also indebted to our sponsors, Dr. J.C. Williams, Mr. W.W. Rose, Mrs. D.M. Comassar, and Mr. C.D. Caudill, whose reviews of this effort contributed greatly to the process of extending this work to improve ongoing design and production efforts.

I would also like to thank Dr. P.G. Roth and Dr. R.H. VanStone of GE for many helpful discussions on shot peening and fracture mechanics predictions. Special thanks are also due to Mr. W.S. Davis, Mr. T.H. Daniels, Mr. F.B. Brate, Jr., Mr. D.J. Parker, Mr. G.B. Farmer, Ms. V.A. McGee, Mr. S.L. Culp, Mr. M.L. Winiarz and Dr. R.M. Somers for their assistance in specimen preparation and analysis, including profilometry, optical microstructural and SEM analysis. I would also like to acknowledge the contributions of Mr. S. Sitzman, Dr. E. Hall and Dr. J. Sutliff of the GE Corporate Research and Development Center, who conducted EBSP and TEM analysis.

A special debt of gratitude is owed to Dr. N.S. Brar of UDRI, who introduced me to the field of impact dynamics and who made the single particle impact test effort possible, to Mr. Mark Laber, who made the tests work, and to Dr. A.T. Zehnder of Cornell University who made the transient temperature measurements possible. I would also like to thank the following people from UDRI who assisted in the single particle impact test microstructural analysis: Mr. D. Grant, Mr. D. Wolf, Mr. L.C. Sqrow. In addition, I would like to acknowledge the assistance of Mr. P. Mason and Mr. D. Hornbach of Lambda Research, who conducted the x-ray diffraction analysis, and to Dr. P. Prevey, for the many helpful discussions on x-ray diffraction analysis techniques.

I would also like to thank my parents, Mr. and Mrs. R. F. Klopmeier, who encouraged me to go into engineering in the first place. Their love and support have always provided me with the confidence to follow my dreams.

Above all, I would like to thank my husband, Stephen, for his enduring patience, support and understanding. I dedicate this work to him as a small token of my gratitude. I would also like to thank Tizer, Putney, Moggy, and Tottenham, our “furry” children (two golden retrievers and two cats) and my constant companions throughout the long nights studying and writing. They have patiently endured while I slaved away on the computer, and they lifted my spirits with games and walks.

CONTENTS

	PAGE
ILLUSTRATIONS.....	xi
TABLES.....	xiv
NOMENCLATURE.....	xv
CHAPTER 1 – INTRODUCTION.....	1
1.1 Overview – Shot Peening Impact on Life.....	1
1.2 Basic Shot Peening Terms and Process Control Parameters.....	2
1.3 Suspected Causes for the Effect of Shot Peening.....	9
1.3.1 Fatigue and Propagating Fatigue Cracks.....	9
1.3.2 Microstructural Changes.....	11
1.3.3 Residual Stresses.....	13
1.3.4 Topography / Surface Roughness Effects.....	14
1.3.5 Impact Stresses.....	14
1.3.6 Incidence Angle.....	14
1.3.7 Particle Size Effects.....	15
1.3.8 Velocity.....	15
1.3.9 Strain Rate.....	15
1.3.10 Life Behavior Observed.....	17
1.4 Objective.....	18
1.5 Overview of Approach.....	19
CHAPTER 2 – ANALYTICAL FRAMEWORK.....	21
2.1 The Fracture Mechanics Model.....	21
2.2 Model Elements Characterizing Material State due to Peening.....	25
2.2.1 Initial Crack Size from Microstructure.....	25
2.2.2 Residual Stresses.....	26
2.2.3 Kt Gradient Definition from Topography.....	27
CHAPTER 3 – MATERIALS AND EXPERIMENTAL METHODS.....	29
3.1 Material Characterization.....	29
3.1.1 Workpiece Material.....	29
3.1.2 Shot.....	30
3.2 Microstructural and Metallurgical Evaluation Methods.....	30
3.2.1 Microstructure.....	30
3.3 Single Particle Impact Tests.....	35
3.3.1 Goals of the Test Program.....	37
3.3.2 Estimating Velocity and Strain Rate for Test Conditions.....	37
3.3.3 “Designed Experiment” Approach.....	39
3.3.5 Velocity Measurements.....	44
3.3.6 Temperature Measurements Using High Speed Infrared Detectors.....	45
3.4 Production Peening of René 88DT Coupons and Velocity Measurements.....	47

CHAPTER 4 – RESULTS.....	49
4.1 Single Particle Impact Test Results.....	49
4.1.1 Hertzian Behavior Check - Measured vs. Predicted “d/D” Ratios.....	49
4.1.2 Microstructure Development.....	51
4.1.3 Slip Depth Predictions as a Function of Shot Velocity.....	53
4.1.4 Coefficient of Restitution Trends.....	54
4.1.5 Normalized Impact Stress.....	55
4.2 Evaluation of Production Peened Coupons and Velocity Measurements.....	56
4.2.1 Microstructure.....	56
4.2.2 Residual Stresses.....	59
4.2.3 Topography.....	60
4.2.4 Velocity Data.....	61
4.3 Highlights of Shot Peen DOE Analysis.....	62
4.4 Fracture Mechanics Correlations.....	64
4.5 Threshold Behavior Map.....	70
4.5.1 Driving forces behind FM model elements.....	70
4.6 Fracture Mechanics / Threshold Behavior (FM/TB) Model.....	74
4.7 Initial Crack Size Determination.....	75
4.8 Effects of Topography.....	77
CHAPTER 5 – DISCUSSION.....	78
5.1 Assumptions.....	78
5.1.1 Peening conditions were adequately duplicated.....	79
5.1.2 Slip bands are high potential crack initiation sites.....	80
5.1.3 Surface cracks will form at highest local stress concentration.....	80
5.1.4 Preferred grain orientation at crack initiation site.....	80
5.1.5 Average minimum slip layer depth characterizes the fatigue damage.....	81
5.1.6 Residual Stresses Remain in Compression Throughout Testing.....	82
5.2 Limitations.....	82
5.3 Usefulness of the Fracture Mechanics Model.....	84
CHAPTER 6 – CONCLUSIONS.....	86
CHAPTER 7 – RECOMMENDATIONS.....	88
APPENDIX A – BAILEY SHOT PEEN DOE ANALYSIS.....	90
A.1 Overview – Bailey Shot Peen Design of Experiment.....	90
A.2 Experiment Design.....	90
A.3 Results.....	91
A.4 Analysis of Variation (ANOVA).....	94
A.5 Weibull Analysis of Shot Peen DoE Results.....	96
APPENDIX B – SINGLE PARTICLE IMPACT TESTS.....	99
B.1 Contents.....	99
B.2 Experimental Difficulty.....	99
B.3 Shot Characterization.....	100
B.4 Impact Dimple Characterization.....	101
B.5 Test Results.....	102
B.5.1 Dimple Profile Data and General Results.....	102

B.5.2	Coefficient of Restitution Data.....	106
B.5.3	Precision Section Data.....	106
B.5.4	Estimation of Impact Stress Using Impact Dynamics.....	124
B.5.5	Transient Temperature Measurements.....	128
B.5.6	Derivation of Plastic Strain Estimate and Sample Dimple Profiles.....	133
APPENDIX C	– PRODUCTION PEENED COUPONS.....	143
C.1	Contents.....	143
C.2	Sample Microstructures – Production Peening DOE Conditions.....	144
C.3	Residual Stress Profiles.....	149
C.4	Plastic Strain Profiles.....	152
C.5	Saturation Curves.....	155
REFERENCES	158

ILLUSTRATIONS

	PAGE
Figure 1.1 – Fatigue Test Results for Different Shot Peening Conditions.....	2
Figure 1.2 – Basic Shot Peening Terms.....	3
Figure 1.3 – Almen Strips.....	5
Figure 1.4 – Types of Material Changes Induced by Shot Peening.....	10
Figure 1.5 – Schematic of Three Regimes of Dislocation Response.....	16
Figure 2.1 – Input Parameters for the Fracture Mechanics Model.....	22
Figure 2.2 – Crack Growth Rate Curve, da/dN vs. K , for 1000°F.....	24
Figure 2.3 – Sample “a vs. N” Curve.....	26
Figure 2.4 – Sample Residual Stress Profile and Corresponding Curve Fit.....	27
Figure 2.5 – Sample K_t Gradient.....	28
Figure 3.1 – Steps Used in the Precision Sectioning Process.....	32
Figure 3.2 – Mounting Process for Production Peened Coupons.....	33
Figure 3.3 – Scale Photos of Shot Samples.....	36
Figure 3.4 – Map of Intensity/Velocity and Intensity/Strain Rate Test Conditions.....	41
Figure 3.5 – Helium Gas Gun Used in Single Particle Impact Tests.....	42
Figure 3.6 – Shot and Sabots Used in Single Particle Impact Tests.....	43
Figure 3.7 – Closeup of Muzzle Showing Sabot Catcher Assembly and Target.....	43
Figure 3.8 – Camera’s View of Impact Site as Seen Through Overhead Mirror.....	44
Figure 3.9 – High Speed Impact Photo and Schematic of Layout.....	46
Figure 4.1 – Measured vs. Calculated “d/D” Ratio.....	50
Figure 4.2 – Microstructure Development with Increasing Velocity – CCW31 and CCW14 Shot.....	52
Figure 4.3 – Slip Depth – Predicted vs. Observed.....	53
Figure 4.4 – Coefficient of Restitution, e, vs. Normal Velocity.....	54
Figure 4.5 – Normalized Impact Stress, P^* , vs. Measured/Calculated Dimple Depth.....	55
Figure 4.6 – SEM Backscatter Electron Image Showing Crack Formation Along a Slip Band (1.5 kX).....	57
Figure 4.7 – SEM Secondary Electron Image Showing Crack Formation Along a Slip Band, Within a Grain (2.03 kX).....	57
Figure 4.8 – Competing Sites for Crack Development and Growth Due to Local Variations in Peening Condition.....	58
Figure 4.9 – K_t as a Function of Intensity, Shot Size.....	60
Figure 4.10 – Velocity as a Function of Intensity for Production Shot.....	61
Figure 4.11 – Summary of Interaction Plots for “stdev”, “a”, and “ K_t ”.....	63
Figure 4.12 – Predicted FM Life vs. Observed Life.....	68
Figure 4.13 – Fracture Mechanics vs. LCF Domain.....	68
Figure 4.14 – Predicted FM Life vs. Initial Crack Size, a.....	68

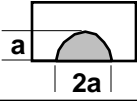
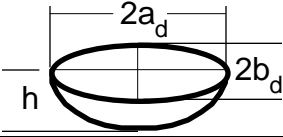
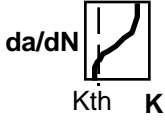
Figure 4.15 –	Compressive Stress Layer Depth as a Function of Peening Intensity.....	71
Figure 4.16 –	Threshold Behavior Map.....	73
Figure 4.17 –	Predicted Life (FM/TB model) vs. Observed Life.....	74
Figure 4.18 –	Schematic of Crack Threshold (a_{th}) and Grain Diameter (d_g) Interaction Effect on Crack Growth.....	76
Figure A.1 –	Cube Plots of Shot Peen DOE.....	92
Figure A.2 –	Plots of Significant Two-Way Interactions from DOE.....	95
Figure A.3 –	Weibull Analysis Results.....	97
Figure B.1 –	Sample Dimple Profile and Schematic of Traces Taken.....	101
Figure B.2 –	Schematic of Dimple.....	102
Figure B.3 –	Dimple Maps: Schematic of Impact Targets Showing Dimples and Precision Sections.....	109
Figure B.4 –	Dimple #3-027, CCW14, $V_0=1,350$ in/s (34 m/s), 90°	111
Figure B.5 –	Dimple #3-017, CCW14, $V_0=3,440$ in/s (87 m/s), 90°	111
Figure B.6 –	Dimple #3-079, CCW14, $V_0=3,700$ in/s (94 m/s), 45°	112
Figure B.7 –	Dimple #3-062, CCW14, $V_0=5,260$ in/s (134 m/s), 45°	112
Figure B.8 –	Dimple #3-023, CCW31, $V_0=690$ in/s (18 m/s), 90°	113
Figure B.9 –	Dimple #3-009, CCW31, $V_0=2,320$ in/s (59 m/s), 90°	113
Figure B.10 –	Dimple #3-077, CCW31, $V_0=3,490$ in/s (89 m/s), 90°	114
Figure B.11 –	Dimple #3-056, CCW31, $V_0=9,800$ in/s (249 m/s), 90°	115
Figure B.12 –	Dimple #3-010, CCW52, $V_0=2,000$ in/s (51 m/s), 90°	116
Figure B.13 –	Dimple #3-011, CCW52, $V_0=2,260$ in/s (57 m/s), 90°	117
Figure B.14 –	Dimple #3-012, CCW52, $V_0=2,670$ in/s (68 m/s), 90°	118
Figure B.15 –	Dimple #3-001, CCW52, $V_0=3,690$ in/s (94 m/s), 90°	119
Figure B.16 –	Dimple #3-020, CCW52, $V_0=8,270$ in/s (210 m/s), 90°	120
Figure B.17 –	Dimple #3-065 (right), CCW52, $V_0=8,580$ in/s (218 m/s), 45° and Dimple 3-066, CCW52, $V_0=8,980$ in/s (228 m/s), 45° (left).....	121
Figure B.18 –	Dimple #3-066 (zoom), CCW52, $V_0=8,980$ in/s (228 m/s), 45°	121
Figure B.19 –	Dimple #3-065 (zoom), CCW52, $V_0=8,580$ in/s (218 m/s), 45°	122
Figure B.20 –	Dimple #3-068, CCW52, $V_0=3,770$ in/s (96 m/s), 45°	123
Figure B.21 –	Schematic of Impact Pressure vs. Particle Velocity Diagram.....	125
Figure B.22 –	Schematic of Experimental Setup for Measuring Impact Temperature.....	129
Figure B.23 –	Test #3-037, CCW52, $V_0=7,530$ in/s (191 m/s) 45°	130
Figure B.24 –	Test #3-038, CCW52, $V_0=9,500$ in/s (241 m/s) 45°	131
Figure B.25 –	Test #3-056, CCW31, $V_0=9,800$ in/s (249 m/s) 45°	132
Figure B.26 –	Geometric Dimple Formation Process.....	133
Figure B.27 –	Schematic of a Spherical Sector.....	134
Figure B.28 –	Test #3-015, CCW14, $V_0=3,490$ in/s, 90° – Contour Plot.....	137
Figure B.29 –	Test #3-015, CCW14, $V_0=3,490$ in/s, 90° – Multiple Region Plot.....	137
Figure B.30 –	Test #3-057, CCW31, $V_0=7,580$ in/s, 45° – Multiple Region Plot.....	138
Figure B.31 –	Test #3-057, CCW31, $V_0=7,580$ in/s, 45° – Multiple Region Plot.....	138
Figure B.32 –	Test #3-015, CCW14, $V_0=3,490$ in/s, 90° – 2D Analysis Profile.....	139
Figure B.33 –	Test #3-057, CCW31, $V_0=7,580$ in/s, 45° – 2D Analysis Profile.....	139
Figure B.34 –	Test #3-057, CCW31, $V_0=7,580$ in/s, 45° – Contour Plot.....	140

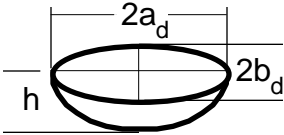
Figure B.35 –	Test #3-018, CCW31, $V_0=3,440$ in/s, 90° – 2D Analysis Profile.....	140
Figure B.36 –	Test #3-019, CCW14, $V_0=460$ in/s, 90° – Contour & 2D Profile Plot.....	141
Figure B.37 –	Test #3-018, CCW31, $V_0=3,440$ in/s, 90° – 3D view & 2D Analysis Profile.....	141
Figure B.38 –	Test #3-028, CCW14, low velocity, 90° – Contour & 2D Profile Plot.....	142
Figure B.39 –	Test #3-028, CCW14, low velocity, 90° – 3D view & 2D Analysis Profile.....	142
Figure C.1 –	Sample Microstructures.....	145
Figure C.2 –	Residual Stress Profiles.....	150
Figure C.3 –	Plastic Strain Profiles.....	153
Figure C.4 –	Saturation Curves.....	156


TABLES

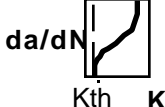
	PAGE
Table 1.1 – High Strain Rate Mechanical Response.....	17
Table 1.2 – Matrix of Shot Peening Parameters Measured or Controlled.....	20
Table 3.1 – Chemical Composition of René 88DT, Atomic Percent	29
Table 3.2 – Physical Properties of R88DT	29
Table 3.3 – Selected Physical Properties of Conditioned Cut Wire Shot.....	30
Table 3.4 – Chemical Composition of Conditioned Cut Wire Shot	30
Table 3.5 – Matrix of Metallurgical Evaluation Techniques Planned.....	31
Table 3.6 – Instruments Used to Obtain Microstructural Information.....	34
Table 3.7 – Instruments Used to Obtain Chemical Information.....	34
Table 3.8 – Instruments Used to Obtain Topographic Information.....	34
Table 3.9 – Instruments Used to Obtain Plastic Strain Information.....	34
Table 3.10 – Total Velocity and Strain Rate Estimates for DOE Shot Peen Conditions Using Thompson Relation.....	39
Table 3.11 – Controlled Single Particle Impact Test Elements.....	39
Table 3.12 – Measured Single Particle Impact Test Elements.....	40
Table 4.1 – Ranges of Velocity and Strain Rate Corresponding to Hertzian Behavior.....	50
Table 4.2 – Residual Stress Curve Fit Coefficients for Equation 2.19.....	59
Table 4.3 – Summary of Factors Evaluated by Shot Peen Design of Experiment.....	62
Table 4.4 – Summary of Results.....	65
Table 4.5 – Grouping of CCW14 DOE Conditions by Life Behavior.....	67
Table A.1 – Summary of Factors Evaluated by Shot Peen Design of Experiment.....	91
Table A.2 – Results of Shot Peen Design of Experiment (DOE) – Conditions 1-16.....	93
Table A.3 – ANOVA Summary of Shot Peen DOE Results.....	94
Table A.4 – Grouping of CCW14 DOE Conditions by Life Behavior.....	95
Table A.5 – Two Parameter Weibull Analysis Results of Shot Peen DOE data.....	97
Table A.6 – Three Parameter Weibull Analysis Results of CCW31 data.....	97
Table B.1 – General Results for CCW14 Shot Tests.....	103
Table B.2 – General Results for CCW31 Shot Tests.....	104
Table B.3 – General Results for CCW52 Shot Tests.....	105
Table B.4 – Coefficient of Restitution Data.....	107
Table B.5 – Precision Sections Data.....	108
Table B.6 – Test Conditions for Successful Transient Temperature Measurements.....	129
Table B.7 – Summary of Dimple Profile Plots Attached.....	136
Table C.1 – DOE Conditions in Standard Order.....	143
Table C.2 – Residual Stress Measurements Taken from a Low Stress Ground Coupon.....	149

Nomenclature – lowercase and uppercase English letters

Symbol	Definition	Units	Diagram or Equation
a	crack radius	inches	
a_0	initial flaw size	inches	
a_d	ellipse major axis half-length (from impact dimple)	inches	
a_f	crack size at failure	inches	$a_f = f(K_c)$
a_{th}	threshold crack size that will cause crack growth for load, temperature and residual stress conditions	inches	$a_{th} = f(K_{th})$
b	Burgers vector		
b_d	ellipse minor axis half-length (from impact dimple)	inches	
ccw14	conditioned cut wire shot, approximately 0.014" diameter		
ccw31	conditioned cut wire shot, approximately 0.031" diameter		
ccw52	conditioned cut wire shot, approximately 0.052" diameter		
d	dimple diameter (assuming spherical dimple)	inches	
d/D	ratio of dimple diameter to shot diameter (assuming spherical shapes)	--	$\frac{d}{D} = 1.28 \frac{x}{y}^{1/4} (V_n)^{1/2}$
$\frac{da}{dN}$	change in crack size per increment in cycle count, a fracture mechanics parameter usually shown as a function of K , or the stress intensity factor range	inches/cycle	
d_g	average grain diameter		
e	coefficient of restitution, the fraction of initial kinetic energy which remains after impact., a measure of elasticity of impact	--	$e = \frac{m_{out} V_{out}^2}{m_{in} V_{in}^2}$
exp	the exponential function	--	
$g(x)$	K_t gradient	--	$g(x) = (K_t - 1) \exp\left[-x / (3R_{t_m})\right] + 1$

h	dimple depth	inches	
h_{calc}	dimple depth estimated from dimple diameter and shot radius (using Thompson's relation to calculate d from shot velocity)	inches	$h_{calc} = \frac{1}{2} \left(D - \sqrt{D^2 - d^2} \right)$
\ln	natural logarithm, $\log_e(x)$	--	
\log	common logarithm, $\log_{10}(x)$	--	
m	Walker exponent	--	
m^+	Walker exponent for $R \geq 0$	--	
m^-	Walker exponent for $R < 0$	--	
m_{in}	initial mass of shot	mg	
m_{out}	mass of shot after recoil	mg	
m_s	shot mass	mg	
$m(x,a)$	weight function coefficient	--	
$pscale$	peening relaxation factor: derates residual stress profile for relaxation effects	--	
r	dimple radius	inches	
$stdev$	normalized life parameter, representing the number of standard deviations from the average life curve (LSG bar data)	--	$stdev = \frac{[\log(N_f) - \log(N_{avg})]}{[\log(N_{avg}) - \log(N_{-3})]}/3$
t	time	seconds	
t_0	Weibull threshold parameter	cycles	$F(t) = 1 - \exp \left\{ - \left((t - t_0) / \right) \right\}$
u_p	particle velocity in workpiece after impact	in/s	
\bar{v}	average dislocation velocity		
x	distance below the peened surface	inches	$r_{RS}(x) = A_1 \exp[-x/\bar{x}] \sin(B_1 x + C_1)$
\bar{x}	mean spacing between obstacles		
A_1	regression constant	--	$r_{RS}(x) = A_1 \exp[-x/\bar{x}] \sin(B_1 x + C_1)$
ASB's	adiabatic shear bands		
B_1	regression constant	--	$r_{RS}(x) = A_1 \exp[-x/\bar{x}] \sin(B_1 x + C_1)$
C	speed of sound	in/s	

C_1	regression constant	--	$_{RS}(x) = A_1 \exp[-x/] \sin(B_1 x + C_1)$
C_0	longitudinal wave velocity (in semi-infinite medium)	in/s	
C_{bar}	longitudinal wave velocity in a uni-axial body (thin rod or bar)	in/s	
C_{shot}	speed of sound in shot, assumed to be "bar" velocity (constrained geometry).	in/s	$C_{shot} \sqrt{\frac{E_{shot}}{*}_{shot}}$
C_w	speed of sound in workpiece, assumed to be "longitudinal" velocity (semi-infinite geometry).	in/s	$C_w \sqrt{\frac{E(1 -)}{*_w(1 +)(1 - 2)}}$
D	shot diameter (assuming spherical shot)	inches	
DOE	design of experiment, an experimental design strategy that permits interactions between main effects to be analyzed statistically	--	
E	Young's modulus of elasticity	psi	
F	boundary correction factor		
F(t)	Weibull function	--	$F(t) = 1 - \exp -\{(t - t_0)/\}$
G	shear modulus	psi	
H	arc height of Almen strip	mils	
HEL	Hugoniot Elastic Limit	psi	
K	stress intensity factor (fracture mechanics)	ksi \sqrt{inch}	$K = (a) (x)\sqrt{a}$
K	stress intensity factor range	ksi \sqrt{inch}	$K = K_{max} - K_{min}$
K^*	fully adjusted stress intensity, for use with da/dN curve.	ksi \sqrt{inch}	$K^* = K_0 c - c K_0^2$
K_0	Walker-shift adjusted stress intensity factor, equivalent to R-ratio=0 condition.	ksi \sqrt{inch}	$K_0 = \frac{K_p}{(1 - R)^{1-m}}$
K_c	fracture toughness	ksi \sqrt{inch}	da/dN 
K_{max}	maximum stress intensity, with residual stress contribution	ksi \sqrt{inch}	$K_{max} = K_{max} + K_{res}$
K_{max}	maximum stress intensity	ksi \sqrt{inch}	$K_{max} = (a) g(x)_{max} \sqrt{a}$
K_{min}	minimum stress intensity, with residual stress contribution	ksi \sqrt{inch}	$K_{min} = K_{min} + K_{res}$
K_{min}	minimum stress intensity	ksi \sqrt{inch}	$K_{min} = (a) g(x)_{min} \sqrt{a}$

K_p	stress intensity range adjusted for plastic zone correction	$ksi\sqrt{inch}$	$K_p = K \sqrt{1 + (K/y)^2 / (8a)}$
K_{res}	stress intensity due to residual stress contribution	$ksi\sqrt{inch}$	
K_t	stress concentration factor	--	$K_t = 1 + 4.0(R_{t_m}/S)^{1.3}$
K_{th}	threshold stress intensity, below which no crack growth will occur.	$ksi\sqrt{inch}$	
L	shot length (max. diameter from actual measurements)	inches	
LCF	low cycle fatigue	--	
LSG	low stress grind, a relatively gentle machining process	--	
LSG+P	low stress ground and polished		
N	life, cycles	cycles	
N_{-3}	minimum (-3s) life (for given stress and temperature conditions)	cycles	
N_{avg}	average life (for given stress and temperature conditions)	cycles	
N_{FM}	predicted fracture mechanics life	cycles	
N_{LCF}	predicted low cycle fatigue (LCF) life for test conditions	cycles	
N_{obs}	observed life at failure	cycles	
N_{pred}	predicted model life	cycles	
P	impact stress	psi	$P = * U_s u_p$
P^*	normalized impact stress, with K_t term		$P^* = K_t P / y$
PSB's	persistent slip bands		
Q	elliptic integral of the second kind		
R	R-ratio: ratio of minimum to maximum stress or K, depending on application.		$R = \frac{\min}{\max}$ or $R = \frac{K_{\min}}{K_{\max}}$
R_s	shot radius	inches	
R_t	average dimple height from surface roughness data	inches	
R_{t_m}	peak dimple height (+3s), from surface roughness data.	inches	$K_t = 1 + 4.0(R_{t_m}/S)^{1.3}$

S	spacing between craters, from surface roughness data.	inches	$K_t = 1 + 4.0(R_{t_m}/S)^{1.3}$
T	saturation exposure time	(relative)	
U_s	shock wave velocity in workpiece after impact, assuming longitudinal wave	in/s	$U_s = \sqrt{\frac{E(1 - \nu)}{\rho(1 + \nu)(1 - 2\nu)}}$
U_{shot}	shock wave velocity in shot	in/s	
U_w	shock wave velocity in workpiece	in/s	
V	velocity	in/s	
V_{tot}	total initial velocity	in/s	
V_0	initial velocity of projectile	in/s	
V_{in}	initial velocity of projectile	in/s	
V_n	component of velocity normal to surface	in/s	
V_{out}	velocity of shot after recoil	in/s	
W	shot width (minimum diameter from actual measurements)	inches	

Nomenclature – Greek letters

Symbol	Definition	Units	Diagram or Equation
c	experimental material coefficient for constraint-loss		
i	incidence angle	°	
r	recoil angle	°	
	Weibull shape parameter		$F(t) = 1 - \exp\left[-\left\{\frac{t - t_0}{\dots}\right\}\right]$
(a)	fracture mechanics shape factor, a function of crack size		$K = (a) (x) \sqrt{a}$
c	experimental material coefficient for constraint-loss		
	strain rate	1/s	$\dot{\epsilon} = \frac{V}{R_s}$
p	plastic strain	in/in	$\frac{d^2}{8D^2}$
	Weibull scale parameter		$F(t) = 1 - \exp\left[-\left\{\frac{t - t_0}{\dots}\right\}\right]$
	regression constant		$f_{rs}(x) = A_1 \exp[-x/\dots] \sin(B_1 x + C_1)$

	Poisson's ratio		
	density	lb_m / in^3	
*	force density	$lb_f s^2 / in^4$	* = $\frac{32.2}{12}$
D	dislocation density		
\dot{D}	rate change of dislocation density		
$shot$	density of shot	lb_m / in^3	
* $shot$	force density of shot	$lb_f s^2 / in^4$	
w	density of workpiece	lb_m / in^3	
* w	force density of workpiece	$lb_f s^2 / in^4$	
	standard deviation	--	
(x)	net stress for stress intensity equation	ksi	$K = (a) (x) \sqrt{a}$ $(x) = g(x) a(x)$
$a(x)$	stress due to applied load	ksi	$(x) = g(x) a(x)$
$applied$	applied stress	ksi	
g	shear stress	ksi	
i	applied stress - subscript used to designate tension or bending (formulations given for tension and bending loads separately)		
max	maximum applied stress	ksi	
min	minimum applied stress	ksi	
$RS(x)$	residual stress	ksi	$RS(x) = A_1 \exp[-x /] \sin(B_1 x + C_1)$
uts	ultimate tensile strength	ksi	
y	yield strength of workpiece	ksi	

CHAPTER 1

INTRODUCTION

1.1 Overview – Shot Peening Impact on Life

The beneficial effects of shot peening have long been recognized. One of the major reasons for shot peening is to induce a beneficial compressive stress layer that acts to retard the development and propagation of cracks from surface features.[1, 2] If crack formation and propagation from surface features can be suppressed, longer component operating lives can often be attained. Dörr and Wagner [3] demonstrated that shot peening was effective in retarding crack propagation of existing cracks, even when peening was applied after the development of cracks. Luetjering and Wagner [4], and others have recognized, however, that shot peening can also cause the equivalent of fatigue damage. This effect has received considerably less attention.

Based on an experimental investigation conducted by Bailey[5] to evaluate the effect of shot peening on low cycle fatigue (LCF) life of René 88DT, some peening conditions were found to result in an order of magnitude lower fatigue life than that of unpeened specimens tested at the same conditions. Life capability at other peening conditions was found to be comparable to unpeened specimens, but with significantly tighter scatter, resulting in higher minimum life capability. Figure 1.1 illustrates these effects.

A major goal of this effort is to develop an understanding of the competing mechanisms. As a result, a broad literature survey was conducted, including the fields of

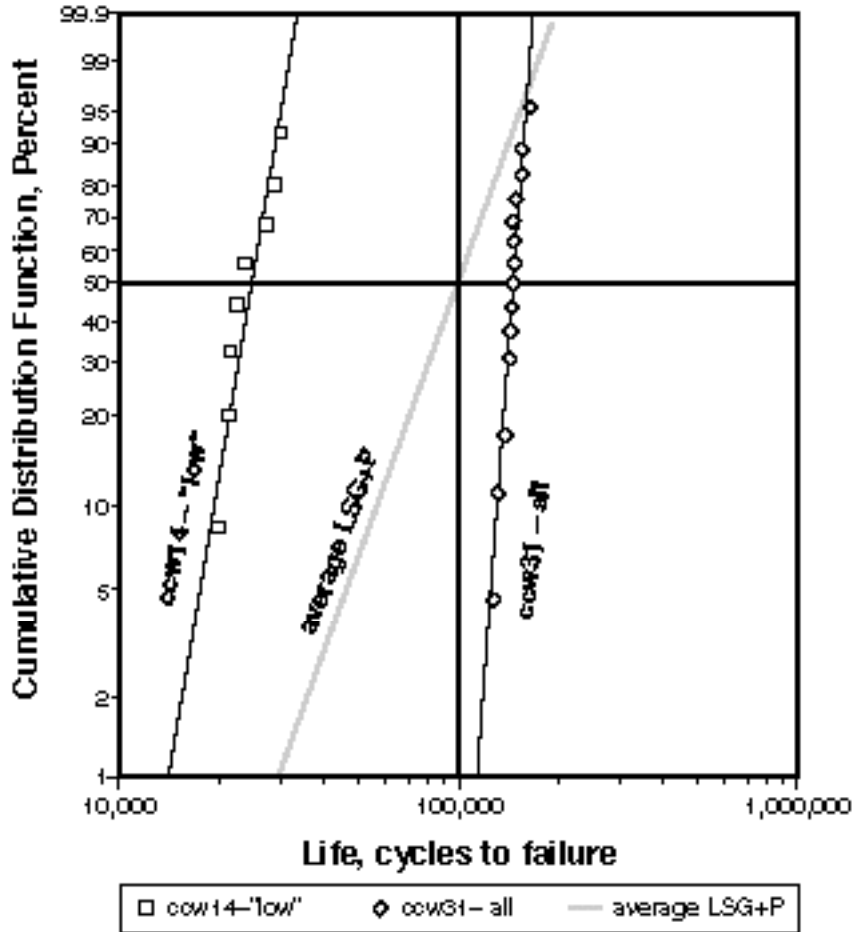


Figure 1.1 – Fatigue Test Results for Different Shot Peening Conditions

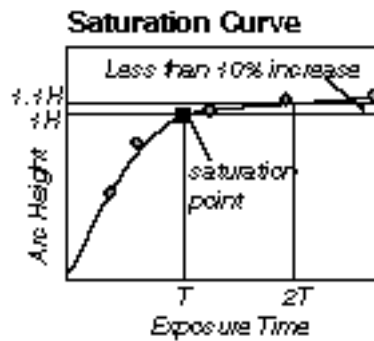
erosion and impact dynamics. These sources contribute additional tools relevant to this problem.

1.2 Basic Shot Peening Terms and Process Control Parameters

Six process parameters are used to describe a shot peening condition, as illustrated in Figure 1.2: 1) Shot (type and size), 2) Intensity, 3) Incidence Angle, 4) Saturation, 5) Coverage, and 6) Velocity. These parameters are independent of the type of shot peening machine used. Of these parameters, only shot type and incidence angle are controlled directly. The remaining parameters are measured. Peening machine

Shot sizes: ccw14 (0.014 inches), ccw31 (0.031 inches), ccw52 (0.052 inches)

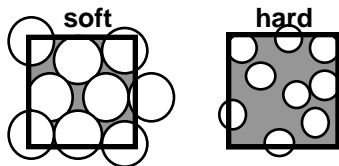
Intensity: related to **strain energy** transferred during peening. Defined by the arc height deflection of thin metal “Almen” strips, in mils, at a reference saturation condition.



Saturation: “Saturation” is used to describe the accumulation of dimples on the Almen strip surface such that plastic strain or work hardening is fairly uniform. It is often used interchangeably with the term “coverage.” *Because the arc height deflection of an Almen strip depends on the saturation or accumulation of dimples on the surface, a Saturation Curve is needed to define intensity at a reference saturation condition.* The saturation point is defined as the point on the saturation curve for which a doubling of exposure time results in less than a 10% increase in arc height. Because this is not a unique definition, variation may be observed in specimens peened by different vendors.

Incidence Angle: angle of impact from workpiece surface (). Higher incidence angles are less damaging, and result in less erosion. *(Lower velocities needed to achieve desired intensity, also less frictional heating at impact.)*

Velocity: Velocity of shot at the workpiece (V), together with shot size, shape, density and incidence angle probably controls the intensity-saturation curve behavior.



% coverage: describes % of surface covered by dimples. This is material-dependent: softer materials will cover faster *larger dimples*. The two squares at left represent different materials peened at the same intensity / saturation condition.

Figure 1.2 – Basic Shot Peening Terms [6]

parameters such as hose diameter, air pressure, shot mass flow rate, nozzle type, feed rate of nozzle along workpiece, distance of nozzle from workpiece and workpiece table speed (in revolutions per minute) are controlled and adjusted to obtain desired values of intensity, saturation and coverage. Reliable velocity measurements during the peening process have been difficult to achieve. Because of this, velocity has not been used traditionally as a process control.

Shot. A wide variety of media have been used for shot peening, including glass beads, cast steel shot, and conditioned cut wire shot, to name a few. [2] Glass or ceramic beads provide the best initial surface finish (spherical shape and smooth surface) which can lead to improved fatigue performance [7], but can fracture, leaving fairly large pieces of glass shot embedded in the surface. [8] Cast steel shot also have fairly spherical surfaces, but can also spall and fracture, resulting in debris that can become embedded in the surface layer. Cast steel shot also has a significantly wider size distribution than conditioned cut wire shot. [8]

Conditioned cut-wire shot is made from steel wire, which is cut into pieces having a length approximately equal to the wire diameter. These pieces are then “conditioned” by shooting the pieces repeatedly against a surface to knock off the rough edges. The resulting media deviate the most from perfect spheres, but they typically possess a more uniform size distribution than comparable cast steel shot, wear more uniformly, and last longer. [8] The resulting wear debris, although smaller, can become embedded in the surface. All types of shot wear and fracture to some extent. As a result, shot is sieved through two screen sizes close to the target shot size: the larger screen captures over-sized particles; the smaller screen removes wear debris and fractured particles. Wear and fracture behavior is strongly related to intensity. Low intensities prolong shot life and minimize the amount of debris that becomes embedded in the workpiece surface. Higher intensities increase the number of particles that become fractured; under some conditions fractured particles and wear debris can become embedded in the workpiece surface. This

does not necessarily cause reduced fatigue life capability. Size and shape control of shot media is important to the shot peening process, since impact of sharp, fractured particles can reduce fatigue life. [8] Because of the importance of shot shape on resulting life behavior, Gillespie [9] has been active in the development of image analysis techniques to provide controls on shot shape. Since fatigue life behavior is often controlled by the “weakest link”, the **variation** in shot **size** and **shape** may also be significant to the observed life capability.

Intensity. The shot peen intensity is not a simply defined parameter. [6] It represents a measure of strain energy transferred to thin metal “Almen” strips. The Almen strips are fabricated from SAE 1070 carbon steel. Dimensions are shown in Figure 1.3. Measurements of the arc height deflection of Almen strips are made for various exposure times and plotted on a saturation curve as shown in Figure 1.3. As more dimples accumulate on the surface, greater bending is observed and the arc height increases. The

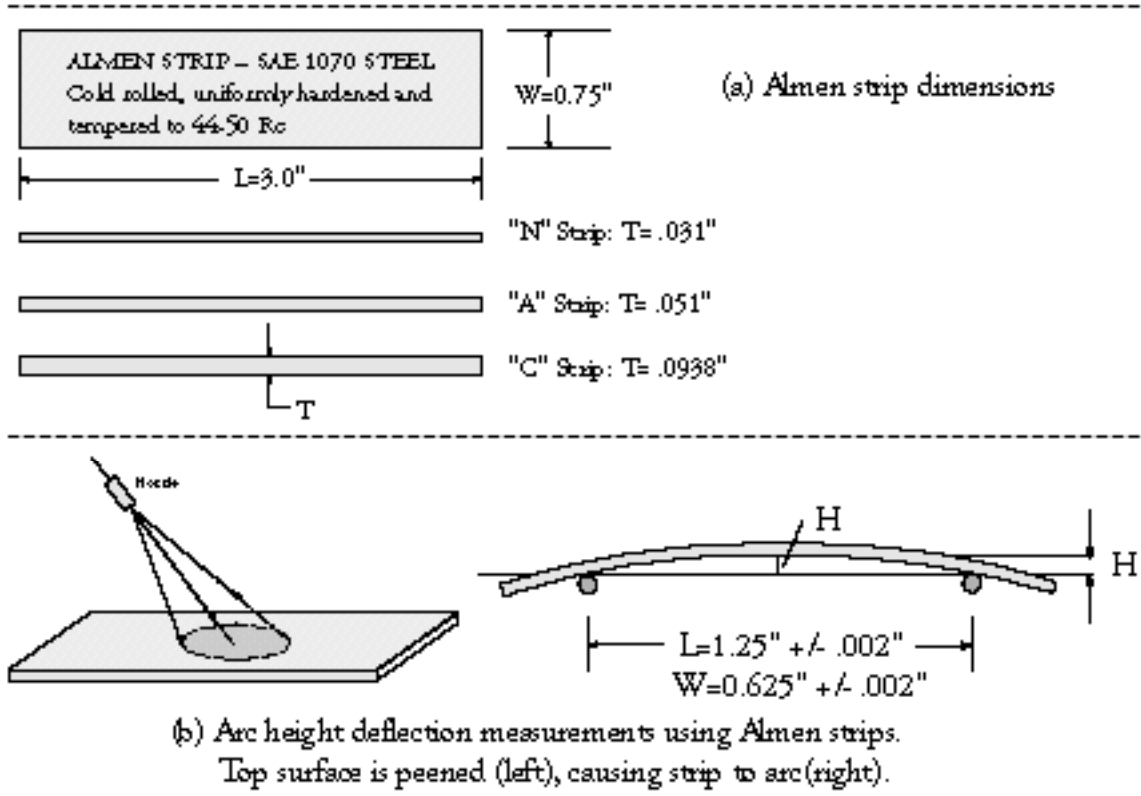


Figure 1.3 – Almen Strips

intensity is defined as that point on the saturation curve for which a doubling of the exposure time results in less than a 10% increase in arc height. [6] It appears that the intent of the definition is to ensure that the intensity reading is obtained on a point to the right of the knee of the saturation curve, where changes in exposure time provide relatively little change in arc height. However, this is not a unique definition. Intensity measurements taken using this approach can result in confounding of the effects of coverage or saturation, shot velocity and shot size. This can lead to conflicting observations.

For example, Niku-Lari [2] notes that the “multiplicity of parameters makes the precise control and repeatability of a shot-peening operation very problematical.” Niku-Lari obtained very different depths of plastic deformation layer corresponding to identical Almen deflection measurements. He concluded that very different distributions of residual stresses could be obtained for the same Almen deflection measurement. Note that a single Almen deflection measurement alone does not define the intensity. In contrast, Fuchs [10] observed a nearly linear relationship between the depth of compressive stress and Almen intensity from his experimental data. Linear regression analysis of earlier residual stress data taken from coupons of René 88DT peened with ccw14 and ccw31 shot found the depth of compressive stress layer, to be a nearly linear function of intensity (see Figure 4.15), supporting Fuchs’ observation.

Three thicknesses of Almen strips are used: N (thinnest), A, C(thickest). In the United States, the deflections are typically quoted in mils (0.001 inches) thus 6A intensity represents 0.006 inches arc height deflection of an Almen “A” strip. There is approximately a factor of three between the strips, thus 12N = 4A. Unfortunately the peening literature tends to lack rigor in reporting intensity measurements. In Europe, metric measurements are used. However, it is common to see intensities of 2A or 4A quoted in the literature without an explicit statement of scale. In addition, a general lack of awareness of the variabilities encountered in applying the intensity definition can lead to

inconsistent interpretation of intensity across the range of people and companies involved with shot peening. Almen Strip variability also contributes to uncertainty in intensity measurements, as reported by Happ and Rumpf. [11] These factors make it difficult to compare peening conditions, results and conclusions across various papers with confidence. Kirk [12] has done some work on a device that would provide interactive control of shot peening intensity which could alleviate some of these problems.

Saturation. The terms saturation and coverage are often interchanged. Both deal with the accumulation of dimples on the target surface. Strictly speaking, 100% saturation refers to a point on a saturation curve (see Figure 1.2), for which a doubling of the exposure time will result in less than a 10% increase in Almen strip arc height. Coverage describes the physical covering of the surface by dimples. Because the deflection of the Almen strip levels off with increasing exposure after ~100% coverage has been achieved, both terms characterize a similar physical event, although the saturation point does not correspond to 100% coverage.[13] Lombardo, Bailey [13] and Abyaneh [14] demonstrated that accumulation of surface coverage results in a curve having the form of the Avrami equation, which also characterizes the saturation behavior. Since saturation is defined only on Almen strips, it applies only to “coverage” of Almen strips, and is independent of the workpiece material to be peened. Because the intensity definition does not result in a unique peening condition, it is fairly common for the “100% saturation” point to be selected by a visual inspection of a peened Almen Strip surface for approximately complete dimple coverage. Additional peening conditions are then selected to complete a saturation curve. If “T” represents “100% saturation”, then typically three additional points, corresponding to 0.5T, 2T and 4T points will be run. If the arc height at the 2T condition is less than 1.1 times the arc height at the 1T condition, then the 1T point is accepted as a valid 100% saturation condition. However, more or less exposure time may be required to achieve a visual 100% coverage on the workpiece.

Incidence angle is the angle between the target surface and direction of incoming shot. Thus, 90° represents a normal impact (perpendicular to the surface) and 45° represents an oblique impact. For a desired intensity, required velocity is minimized for 90° incidence angles. Oblique incidence angles require higher shot velocities to attain a given intensity.

Velocity of the shot is one of the most important physical parameters characterizing the impact event. [2] It appears that the component of velocity normal to the workpiece surface controls the shot peening intensity. Since intensity is a measure of strain energy induced, small shot must travel at significantly higher velocities than larger shot to achieve the same intensity. Since strain rate can be estimated as the impact velocity divided by the shot radius, high velocities also mean high strain rates. For the particle sizes typically used topeen aircraft engine components, strain rates can exceed 5E+05 1/sec for small shot.

Due to the difficulty of measuring shot velocity at the workpiece, it has not been used for process control. Recently, use of laser velocity sensors developed for the field of aerodynamics have been adapted for use in shot velocity measurements in a lab environment at some locations. Electromagnetic sensors which use the magnetic properties of steel shot as they pass through an inductance coil, is the other technology that has been used. Each have different limitations. Neither is in widespread use.

Coverage is determined by a visual inspection of the shot peened surface. “100%” coverage is often used to represent approximately complete coverage of the Almen strip by peening dimples. It is also used to refer to approximately complete coverage of the workpiece (in this case, René 88DT) by peening dimples. If the workpiece material has a different hardness or yield strength than the Almen strips, then 100% coverage will not correspond to the same amount of shot peening exposure time for the two materials. Coverage is material-dependent. Softer materials will cover faster than hard materials.

“800%” coverage is achieved by peening each specimen 8 times longer than that necessary for 100% coverage.

1.3 Suspected Causes for the Effect of Shot Peening

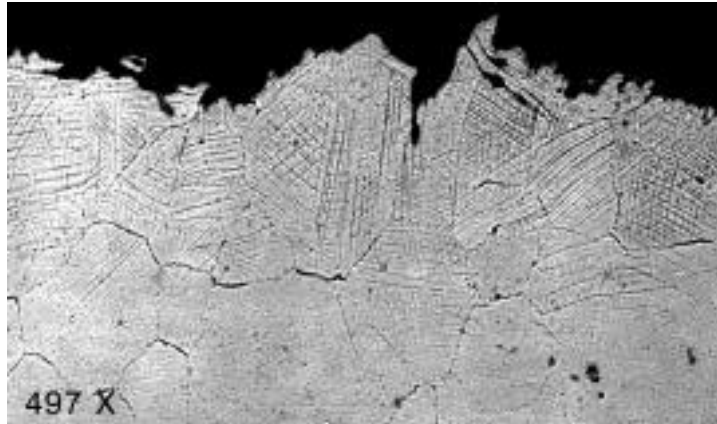
1.3.1 Fatigue and Propagating Fatigue Cracks

The fatigue process consists of four phases: 1) work hardening or work softening, 2) crack nucleation, 3) crack propagation, and 4) final failure. The three most favorable crack initiation sites are: 1) slip bands, 2) grains boundaries, 3) inclusions. [15] The shot peening process induces changes in the surface layer of the workpiece material which can be broadly grouped into three categories: 1) microstructure, 2) residual stresses, and 3) topography, as illustrated in Figure 1.4. Shot peening plastically deforms of the surface layer, although degree of saturation may depend on peening condition and coverage. Plastic deformation involves generation of dislocations; cyclic plastic deformation generates features such as persistent slip bands which are favorable crack nucleation sites. As a result, the shot peening process creates many potential crack initiation sites in the surface layer.

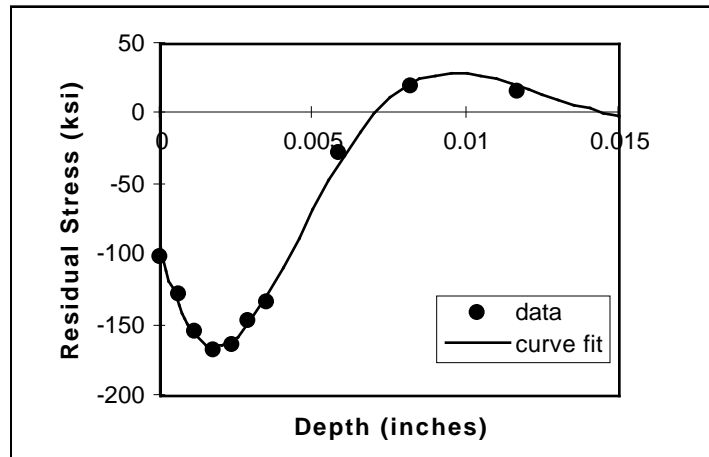
Christ and Mughrabi [16] note that the fatigue of metals is a result of repeated cyclic plastic (or micro-plastic) deformation. The mechanisms of plastic deformation during cyclic loading correlates strongly with the microstructures, thereby determining the mechanisms of failure. Pangborn, Weissmann, and Kramer [17] observed that a propagating fatigue crack was formed whenever work hardening in the surface layer reaches a critical value. They attributed the extension of fatigue life obtained when a portion of the surface layer is removed to the removal of the constraint effect due to the work hardened surface, not to removal of microcracks. “When the barrier becomes sufficiently strong, fracture occurs if the local stress field exceeds the fracture strength.” Komotori and Shimizu [18] observe that the fatigue life in the extremely low cycle fatigue

Types of Material Changes Induced by Shot Peening

1) Microstructure



2) Residual Stresses



3) Topography

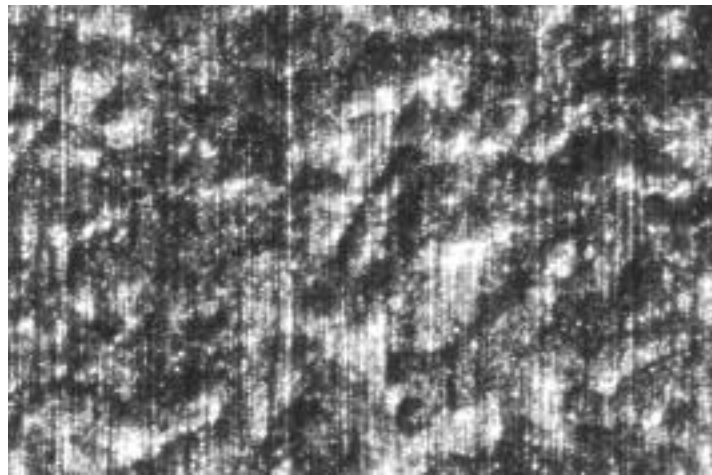


Figure 1.4 – Types of Material Changes Induced by Shot Peening

regime is primarily controlled by the mechanisms of work hardening and increase of internal micro-voids.

Burck, Sullivan and Wells [19] studied the fatigue behavior of Udimet 700, a Nickel-base superalloy, which was peened with glass beads. They employed slip band etching and cellular recrystallization to determine the extent of deformation generated by the peened layer. Consistent results were obtained, giving an average depth of about 0.002 inches for an intensity of 15N (equivalent of approximately 5A). They observed microcrack initiation at the surface along coherent annealing twin boundaries. Extrapolations conducted on linear crack length vs. number of cycles sometimes gave positive crack lengths at zero cycles, implying that the “cracks either initiated in finite lengths or that they initially grew at a rate much faster than in subsequent propagation.” Furthermore, crack initiation in peened material was similar to that for electropolished cases (except that it occurred at higher stress levels). “Once present, however, these small cracks grew at constant rates which were extremely slow compared to similar cracks in electropolished material.” However they noted that the propagation rates quickly approached those observed for the electropolished material as the cracks grew larger. This would be expected as the crack grows through the residual stress layer and is no longer influenced by it. All specimens were peened to Almen saturation condition. However, some specimens were allowed additional peening time: these showed improved fatigue strength over those peened to saturation, which they speculated was due to a more uniform stress distribution. Like Luetjering and Wagner, they also noted that excessive peening can cause the fatigue strengths of some materials to decrease.

1.3.2 Microstructural Changes

Plastic deformation, slip band development. Al-Hassani [20], Burck, Sullivan and Wells [21], Timothy and Hutchings [22], and others have characterized plastic deformation developed by repeated impacts using etching to reveal slip band formation.

Adiabatic Shear Band Development. Al Hassani [20] worked with shot peening strain rates in the range of $4E+04$ per second. He noted that heat generated at these strain rates follows adiabatic rather than isothermal conditions; i.e., heating during impact is localized, and slip bands act as adiabatic boundaries. As a result, significant strain localization is induced within single slip bands, sometimes called adiabatic shear bands. In some alloys, these bands etch white. Adiabatic shear bands also meet the criteria for “persistent slip bands”, being present even after polishing. However, adiabatic shear bands can be formed as a result of a single impact. Persistent slip bands are often formed after repeated cyclic plasticity has occurred, either due to load or strain cycling [15] or to repeated impacts.

Timothy and Hutchings [22] conducted studies using small particles ranging from 0.25 inches to 0.0313 inches (comparable to the medium ccw31 shot size) and velocities ranging from 1,970 to 13,400 in/s. Permanent indentations formed at these conditions, but optical metallography revealed that plastic deformation beneath the craters was not homogeneous at high velocities. Adiabatic shear bands were formed for impact conditions corresponding to dimple diameter / shot diameter ratios of about 0.57 to 0.65. They suggested that this occurs for some critical value of strain, and ruled out impact velocity, impact kinetic energy and strain rate as alternative criteria.

Phase changes. Ru, Wang and Li [23] observed transformation of γ' to β phase in the surface layer caused by the cyclic plastic deformation due to shot peening on René 95, resulting in a decrease of γ' from 45% to 25%, which is then increased with subsequent heating.

Sub-grain size changes. Ru, Wang and Li [23] also reported decreases in sub-grain sizes in René 95 due to shot peening which did not grow appreciably with heating to 1200°F (650°C). Original sub-grain sizes of 7.0 μin (0.179 μm) were reduced to 0.6 μin (0.015 μm).

1.3.3 Residual Stresses

A significant amount of work has been done to model, predict or measure the development of residual stresses due to specific shot peening conditions. Finite element methods have been employed by Al-Obaid [24, 25] and others. Fathallah, Inglebert and Castex [26] developed a method for predicting residual stress distributions based on the solution of elastic indentation by Hertzian contact, and extending the method to account for friction, shot velocity, incidence angle, and elastic-plastic material behavior. Chang, Schoening, and Soules [27] have developed a non-destructive eddy current inspection technique to determine residual stress profiles. More work is needed to determine the reliability and usefulness of these methods.

Other studies focused on evaluating life impact due to various residual stress states. Starker, Wohlfahrt and Macherauch [28], studying surface hardness and roughness effects, observed changes in life capability of a carbon steel which could only be explained as the direct consequence of high magnitude of compressive residual stresses induced by shot peening. They also noted that in some cases, deeper peening resulted in lower, not higher lives. They speculated that in these cases, the balancing tensile residual stresses induced subsurface may be more significant in reducing life than compressive stresses are in extending life.

Schutz [29] conducted experiments on Aluminum, Titanium and maraging steel. The aluminum alloy exhibited **complete reversal** of the residual stresses with fatigue, thus Schutz concluded that the residual stresses did not explain the fatigue benefit obtained with peening.

Wagner and Luetjering[4] observed that the cyclic stability of residual stress profiles is key to the effectiveness of shot peening on fatigue life. They also noted that fatigue life can be improved by the removal of approximately 0.8 mils (20 μm) from the surface layer for the Titanium alloys they worked with. They attributed the benefit to the

removal of surface roughness. However, Lukáš [15] credits a reduction of surface constraint with improvements in fatigue life capability.

1.3.4 Topography / Surface Roughness Effects

Li, Mei, Duo and Wang [30] reported a method for estimating a geometric stress concentration factor (K_t) due to specific surface roughness parameters, R_t (peak dimple depth) and S (dimple spacing) over some sample distance. They used a modified Goodman formula to predict fatigue life, incorporating the residual stresses as a mean stress effect and the K_t as a stress multiplier. The Goodman relation provides a method for accounting for the effect of mean stress on fatigue life [31].

1.3.5 Impact Stresses

Al-Hassani [20] used Hertzian analysis, which predicts the elastic stress distribution beneath a smooth spherical indenter, to predict impact stresses due to shot peening. Zeng, Breder and Rowcliffe [32, 33] used Hertzian analysis to predict the formation of cone cracks in brittle materials, and used this to determine a fracture toughness. Lu, Sargent and Conrad [34], also working with brittle materials, determined a critical load necessary to form Hertzian ring cracks, and found it necessary to use statistical methods to address variability observed in the critical load.

1.3.6 Incidence Angle

Erosion studies by Finnie and co-workers [35, 36] demonstrated that for ductile materials, erosion was minimized for incidence angles approaching 90° , and maximized at acute incidence angles around 10-30 degrees. For brittle materials, the maximum erosion was observed to occur at 90° . Due to the effect of velocity and small particle size on erosion, Finnie concluded that a size-effect was present, similar to those observed in metal cutting.

1.3.7 Particle Size Effects

A change in erosion behavior corresponding to particle size has been observed. Mishra and Finnie [37] concluded that the higher yield strength of shallow surface layers was responsible for the reduction in erosion observed for particle sizes below 4 mils (100 μm). Tilly [38] concluded that the critical particle size was related to impact velocity. Hutchings [39] attributed the change in behavior to be due to strain rate effects.

1.3.8 Velocity

Timothy and Hutchings [22] observed an increase in dimple diameter/shot diameter (d/D) ratios in Ti-6Al-4V as a function of velocity. Spherical projectiles made from tungsten-carbide, steel and sapphire were used. Onset of adiabatic shear banding was observed for d/D ratios between 0.57 and 0.65, regardless of projectile material. Crater volume was observed to correlate with kinetic energy.

1.3.9 Strain Rate

Ashby and Frost [40], in their work constructing deformation-mechanism maps, noted that strain rates can become very high under impact conditions, in the range of 1/s to 10^6 /s. They observed that phonon and electron drags, and relativistic effects can limit dislocation velocities at these strain rates at low temperatures, as illustrated in Figure 1.5. When material is deformed so rapidly that heat is unable to diffuse away, then slip localization known as adiabatic shear may occur.

De Rosset and Granato [41] present two different formulations of the fundamental equation of dislocation dynamics:

$$\dot{\epsilon} = \rho_D \mathbf{b} \bar{v} \quad (1.1)$$

$$\dot{\epsilon} = \dot{\rho}_D \mathbf{b} \bar{x} \quad (1.2)$$

In equation 1.1, strain rate is related to dislocation density, Burgers vector, and average dislocation velocity. In equation 1.2, strain rate is related to the rate of change of dislocation density, Burgers vector, and mean spacing between obstacles. This can be used

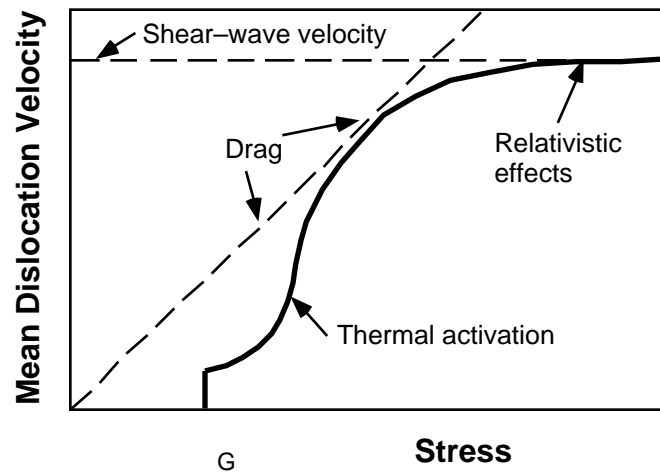


Figure 1.5 – Schematic of Three Regimes of Dislocation Response [42]

to understand saturation behavior, putting this in the context of shot peening and Figure 1.5. At the onset of shot peening, dislocation densities are very low. Initial impacts alternately increase the dislocation density, or create very fast moving dislocations, resulting in high impact stresses. As the workpiece becomes saturated, the significantly higher dislocation density results in lower mean dislocation velocities and correspondingly lower impact stresses. That is, as peening progresses, the material work hardens and subsequent impacts become more elastic in nature.

Ashby and Frost constructed a deformation map for titanium using shear strain rate and homologous temperature as the y and x axes, respectively. They mapped out regions of adiabatic shear, drag-controlled plasticity, obstacle controlled plasticity, power law creep, and diffusional flow, showing different regions of material response.

The field of impact dynamics deals with high strain rate events. Meyers [42] characterizes material response by strain rate, as shown in table 1.1.

Field and Hutchings [43] used impact dynamics to characterize surface response due to erosion by small particles. They also provide the basic impact dynamic equations used to calculate the pressure generated at impact.

Table 1.1 – High Strain Rate Mechanical Response [42]

Strain Rate	Dynamic Considerations	Common Testing Methods
$< 10^{-5} \text{ sec}^{-1}$	“CREEP” and stress relaxation	Conventional, creep testers
$10^{-5} - 5 \text{ sec}^{-1}$	“QUASI-STATIC”, equilibrium	Hydraulic, servo-hydraulic
↑↑↑	<i>Inertial forces negligible</i>	↑↑↑
↓↓↓	<i>Inertial Forces Become Important</i>	↓↓↓
$5 \cdot 10^3 \text{ sec}^{-1}$	“DYNAMIC - LOW”	High velocity hydraulic or pneumatic machines
$10^3 - 10^5 \text{ sec}^{-1}$	“DYNAMIC - HIGH”	Hopkinson bar, exploding ring
$10^5 - 10^8 \text{ sec}^{-1}$	“HIGH VELOCITY IMPACT” Shear wave and shock wave propagation involved. VERY RAPID deposition of energy at surface of the material.	Normal plate impact Inclined plate impact Explosives Pulsed laser, etc.

1.3.10 Life Behavior Observed

Empirical observations of LCF behavior. A range of fatigue behavior has been observed for shot peened specimens compared with unpeened specimens. Hammond and Meguid [44] observed improved life behavior over unpeened specimens.

Koster, Gatto, and Cammett [45] showed that many machining processes degrade the fatigue life capability, and that shot peening is often used to restore lost fatigue capability. An improvement in fatigue capability over low stress ground surfaces is not necessarily observed. Some of the most commonly encountered microscopic surface alterations are plastic deformation, laps, tears, microcracks, intergranular attack, which are the result of abusive machining practices and may be accompanied by surface residual tensile stresses.

Fracture mechanics correlations with observed life behavior. Nevarez, Nelson, Esterman and Ishii [46] were able to correlate with observed trends in fatigue test data of peened specimens by using a fracture mechanics calculation with an assumed crack size.

Their main focus was incorporation of residual stress profile effects corresponding to a variety of peening conditions.

Burck, Sullivan and Wells [19], working with Udimet 700, predicted finite initial crack sizes as a result of shot peening from extrapolations of crack growth measurements. This implies that peening pre-cracked the material.

Summary. Shot peening produces several changes in the workpiece material, including changes to microstructure, residual stresses, and topography. Some of these changes are beneficial, some are potentially detrimental. The lack of precision in the definition of shot peening intensity serves to confound many of the observed effects, making it difficult to isolate the critical factors, and contributing to conflicting reports of peening behavior. The nature of the competition between beneficial and detrimental effects makes it difficult to make broad generalizations about shot peening behavior.

1.4 Objective

As a result of observations made from the Bailey Shot Peen DOE, the following hypothesis was constructed:

- the depth of plastic deformation layer characterizes the fatigue damage induced, and provides many potential sites for crack nucleation and growth
- additional strain localization during subsequent fatigue testing would be concentrated at the most favorable site, determining the crack initiation site
- if the microstructure of the peened surface layer can be used to characterize an initial crack size, fracture mechanics can be used to predict life capability.

The objective of this research is to develop a lower-bound estimate of LCF degradation potential associated with shot peening using a fracture mechanics approach. As illustrated in Figure 1.4, material changes induced by shot peening can be grouped into three categories. The effect of topography (surface roughness) would be to produce a stress

concentration (K_t) at the surface. This can be modeled by incorporating a K_t gradient with the applied stress. Similarly, residual stresses can be incorporated directly into a fracture mechanics analysis using a weight function technique. The main challenge is the characterization of an initial crack size from microstructural observations.

1.5 Overview of Approach

It has been noted that fatigue behavior is closely linked with microstructure, and that shot particle size, incidence angle, velocity and strain rate can have significant effects on microstructure and material behavior. So, a study on shot peening influence needs to include these elements. Available test data consisted of a record of peening conditions, test conditions, life at failure, and fractography of the fracture surface. Microstructures, residual stress profiles, and surface roughness measurements did not exist for all peening conditions.

The Weibull plot (Figure 1.1) shows that all populations of peened specimens demonstrate high line slopes, resulting in low scatter characteristic of a rapid wear-out mode. This suggests that variability in the crack initiation phase has been reduced and resulting life capability of peened specimens is dominated by the crack propagation phase. If this is true, fracture mechanics should provide a useful tool for predicting life capability. Potential elements of a fracture mechanics model for shot peening include: 1) an initial crack size characterizing microstructural condition, 2) residual stress profile, and 3) stress concentration gradient characterizing surface roughness, in addition to the standard elements which include applied stress and temperature-dependent material properties.

To obtain the microstructural information needed to define an initial crack size for a fracture mechanics analysis, two parallel efforts were launched: 1) single particle impact tests using production shot to trace development of microstructure and material response as a function of shot size, velocity and incidence angle, and 2) duplication of the Shot Peen

DOE peening conditions on low-stress-ground and polished (LSG+P) coupons (flat plates) of R88DT. Table 1.2 summarizes the shot peening parameters for each effort and describes how they were measured or controlled. Detailed metallurgical and microstructural characterization was planned for each effort, to identify and understand changes in material response. Finally, velocity measurements during production peening were obtained for some conditions.

Table 1.2 – Matrix of Shot Peening Parameters Measured or Controlled

TEST		Shot Peen Process Parameters				Mechanical Behavior		
		Shot Size	Intensity	Incidence Angle	% Coverage	Velocity	Strain Rate	e, Coefficient of Restitution
1	Single Particle Impact Tests	C	-	C	-	C*	E*	M*
2	Production Shot Peening	C	C	C	C	M*	E*	-

Legend: C = controlled M = measured E = estimated * items for which incomplete data exist

It should be recognized that many of these parameters are indirectly controlled. For example, shot size is selected, but specific dimensions vary with each particle. Intensity is controlled indirectly by varying shot peening machine parameters such as air pressure, mass flow rate of shot, type of nozzle used, and nozzle feed rate. Coverage is similarly determined by these parameters. For the single particle impact tests, shot velocity is controlled indirectly by the tank pressure and sabot/barrel tolerance.

CHAPTER 2

ANALYTICAL FRAMEWORK

2.1 The Fracture Mechanics Model

A fracture mechanics approach was adapted to predict a lower-bound estimate of life degradation due to shot peening. The approach used is able to account for three major types of change to the workpiece material induced by shot peening: 1) microstructure, 2) residual stresses, 3) topography. These elements are modeled as: 1) initial crack radius, 2) residual stress profile, 3) stress concentration gradient, respectively. Figure 2.1 shows the information required for the model.

Major elements of the Fracture Mechanics Model include geometry, load, residual stress, and material properties, as illustrated in Figure 2.1. A number of adjustments are made to account for effects of plastic zone size, R-ratio, residual stresses, and constraint loss at the surface. The basic effects covered in the fracture mechanics program used for this analysis are described by the equations that follow [47]. The general form of the stress intensity factor is given in equation (2.1), where (a) is the geometric factor associated with the crack and model geometry, (x) is the remote loading, and a is the crack radius.

$$K = (a) (x) \sqrt{a} \quad (2.1)$$

For the test conditions of interest, the applied load consisted of a uniform net-section stress. Ability to model surface roughness effects was incorporated using a stress gradient, $g(x)$ multiplied by the applied load.

$$(x) = g(x) \text{ applied} \quad (2.2)$$

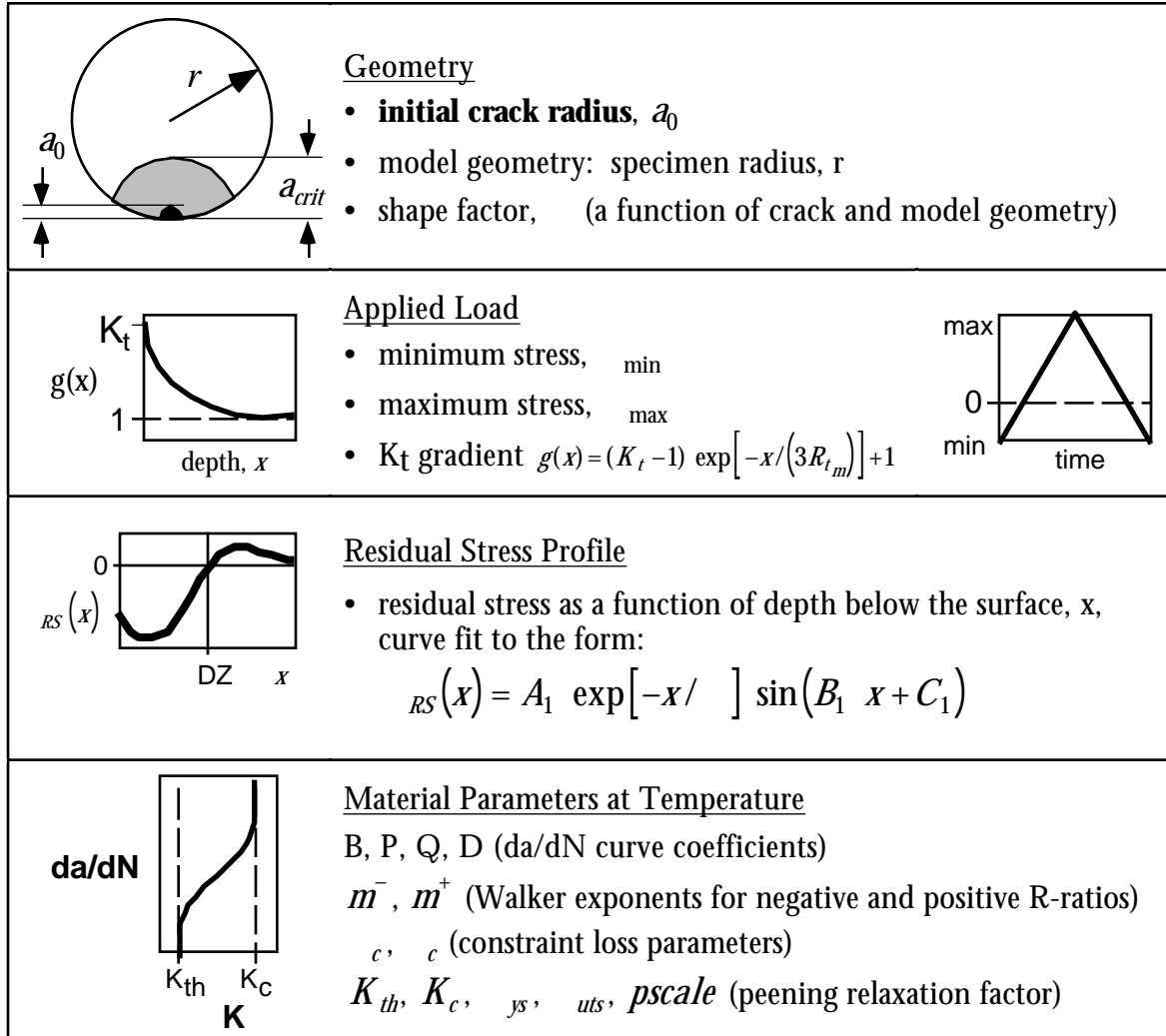


Figure 2.1 – Input Parameters for the Fracture Mechanics Model

For a round bar, a K solution developed by Newman and Raju [48] was used:

$$K = \sigma_i \sqrt{\frac{a}{Q}} F \quad (2.3)$$

Here, Q is an elliptic integral of the second kind, F is a boundary correction factor, and σ_i is the applied load (tension or bending formulations given). $\left(\frac{a}{Q}\right)$ can be written as:

$$\left(\frac{a}{Q}\right) = \frac{F}{\sqrt{Q}} \quad (2.4)$$

Several steps are needed to calculate the stress intensity that will be used with the da/dN curve to calculate life. K_{max} and K_{min} represent the contribution to the stress

intensity factor, K , due to remote loading of maximum and minimum stresses, respectively.

$$K_{\max} = g(x) \sqrt{a} \quad (2.5)$$

$$K_{\min} = g(x) \sqrt{a} \quad (2.6)$$

$$K = K_{\max} - K_{\min} \quad (2.7)$$

For non-constant stress gradients, a weight function technique is used. The general form is shown below, where $m(x, a)$ represents weight function coefficients. The formulation used is based on Yau's work [49]. Other formulations are also available [50].

$$K_{\max} = \max \int_0^a g(x) m(x, a) dx \quad (2.8)$$

$$K_{\min} = \min \int_0^a g(x) m(x, a) dx \quad (2.9)$$

Next, a plastic zone correction is made using the Irwin plastic zone correction [51].

$$K_p = K \sqrt{1 + \left(\frac{K}{\sigma_y} \right)^2 / (8 a)} \quad (2.10)$$

At this point, the contribution of the residual stresses, K_{res} , is calculated from the residual stress profile using a weight function method once again. A "pscale" factor is also incorporated to adjust for relaxation effects due to load and temperature, based on correlation with test data [52]. The general form of the weight function is given below. The exact form of the coefficients depends on the formulation used. Perhaps more important than the precise formula used is the need to calibrate calculations against test results to correctly account for stress relaxation effects due to thermal relaxation and strain or load cycling effects. A "pscale" factor is used to accomplish this here.

$$K_{res} = pscale \int_0^a g(x) m(x, a) dx \quad (2.11)$$

Local stress intensities, K_{\max} and K_{\min} , are now calculated and used to define the R ratio. The R ratio calculated is used to perform a Walker shift on K_p [53].

$$K_{\max} = K_{\max} + K_{res} \quad (2.12)$$

$$K_{\min} = K_{\min} + K_{res} \quad (2.13)$$

$$R = K_{\min} / K_{\max} \quad (2.14)$$

$$K_0 = \frac{K_p}{(1-R)^{1-m}} \quad (2.15)$$

Here, the value of the Walker exponent used depends on the R ratio: $m=m^-$ for R negative, $m=m^+$ for R positive. K_0 represents the equivalent stress intensity range corresponding to $R=0$.

Finally, an adjustment is made to account for the reduced constraint affecting surface cracks, using equation (2.16) to solve for K^* . [53]

$$K_0 = K^* \left(\frac{K^*}{K_c} \right)^c \quad (2.16)$$

The da/dN curve is a function of K^* , R, m, K_c and K_{th} . The curve used is shown below in Figure 2.2.

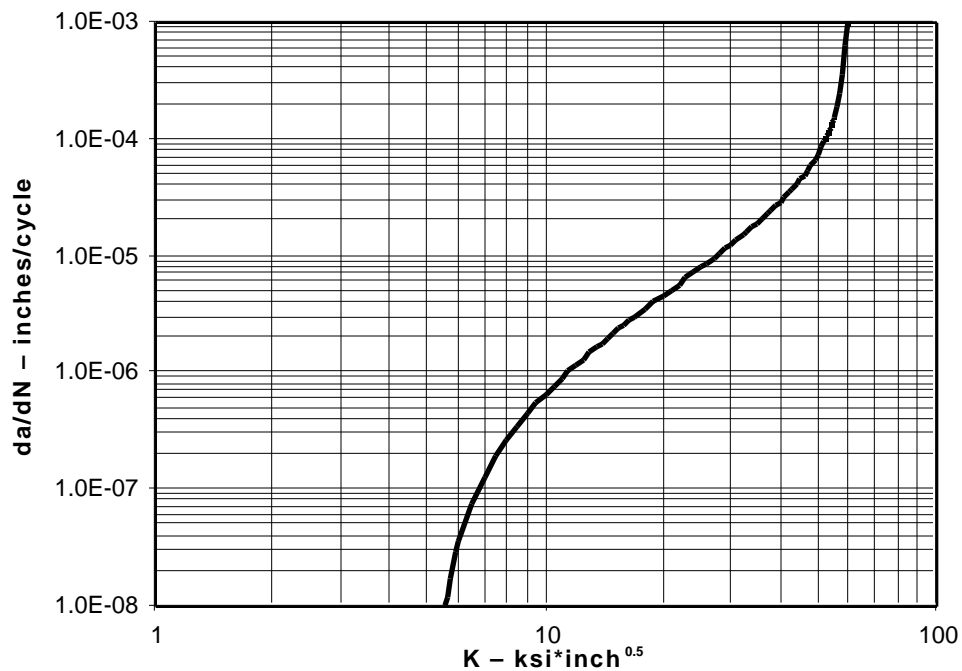


Figure 2.2 – Crack Growth Rate Curve, da/dN vs. K , for 1000°F

The da/dN curve is typically represented as either a Paris equation [54] or sigmoidal equation [55]. Equation 2.17 gives the sigmoidal formulation.

$$\frac{da}{dN} = \exp(B) \frac{K^*}{K_{th} (1-R)^{1-m}} \ln \frac{K^*}{K_{th} (1-R)^{1-m}} \ln \frac{K_c (1-R)^{1-m}}{K^*} \quad (2.17)$$

The da/dN curve is numerically integrated from an initial crack size using cycle and corresponding crack growth rate increments. The crack size is updated, failure criteria checked, and the process repeated until one of the failure criteria is satisfied.

$$a = a_0 + \frac{da}{dN} dN \quad a_f, \text{ where } a_f = f(K_c) \quad (2.18)$$

Typically the integration is performed in small steps, with intermediate results compared against failure criteria. By definition, failure occurs when $K^* \geq K_c$, where K_c is the fracture toughness of the material. A second failure criteria is often used to ensure that the net section stress does not exceed the ultimate tensile strength of the material.

2.2 Model Elements Characterizing Material State due to Peening

The steps described up to this point are basic elements of a fracture mechanics model, and not unique to the problem at hand. Incorporation of stress gradients and residual stresses are fairly standard techniques. However, the definition of the initial crack size, the residual stress profile and K_t gradient as a **function of the specific shot peening condition** is unique to this effort. The balance of this chapter focuses on defining these elements for the model.

2.2.1 Initial Crack Size from Microstructure

The fundamental challenge of this approach is how to define an initial crack size, a_0 , from microstructural information which represents the surface fatigue damage associated with shot peening. Figure 2.3 shows a schematic of a crack growth-cycles curve.

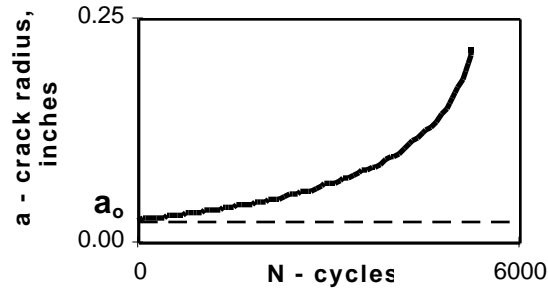


Figure 2.3 – Sample “a vs. N” Curve

Fracture surfaces from the Bailey test specimens [5] revealed oxidized (blue) semi-circular surface crack initiation sites for all “low” life results. The blue color indicates an area which was exposed to oxygen significantly longer than the rest of the fracture surface at the 1000°F test temperature. Although shot peening results in fairly uniform plastic deformation of the surface layer, surface crack initiation sites are very localized. These observations suggest that a semi-circular initial crack shape is adequate to model the failures observed. This reduces the problem to one dimension: how to define a crack radius, a . This is the focus of the experimental work, as described in chapters 3 and 4.

2.2.2 Residual Stresses

Residual stresses are readily measured using x-ray diffraction techniques. Based on prior work by VanStone [56], experience shows that good curve fits to residual stress profiles can be obtained by using a product of exponential and sine functions given as equation 2.19.

$$RS(x) = A_1 \exp\left[-x/\right] \sin(B_1 x + C_1) \quad (2.19)$$

Figure 2.4 shows an example of residual stress data plotted with the resulting curve fit generated using equation 2.19. The residual stress profile can then be incorporated into fracture mechanics analysis using principles of linear superposition via a Green’s function approach. Prior work shows that the depth of the compressive stress layer is nearly a linear function of shot peen intensity. [10]

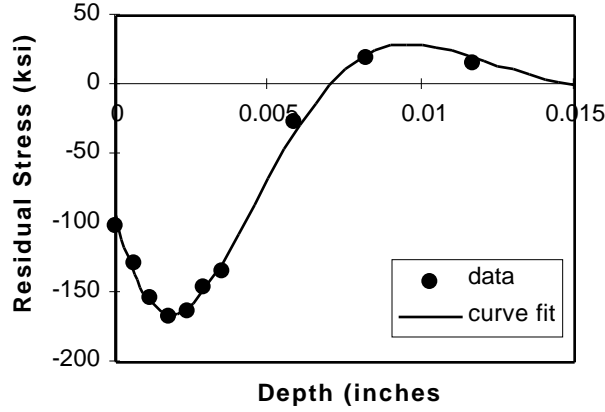


Figure 2.4 – Sample Residual Stress Profile and Corresponding Curve Fit
 Peening condition: CCW31 shot, 6A intensity, 45° incidence angle, 800% coverage.

2.2.3 K_t Gradient Definition from Topography

Work done by Li, Yao, Wang and Wang [30] established a method for estimating a surface stress concentration factor (K_t) due to multiple dimples or craters. Extensive 3D stress analysis was conducted and a formula for a K_t was extended for use with surface roughness data, as given below.

$$K_t = 1 + 4.0 \left(R_{t_m} / S \right)^{1.3} \quad (2.20)$$

R_{t_m} represents a maximum peak height, and S represents an average spacing between features. Because a maximum K_t is of interest, a maximum peak height, R_{t_m} , is used. R_{t_m} is calculated from the mean R_t and the standard deviation as shown below.

$$R_{t_m} = R_t + 3 \quad (2.21)$$

This is done for both x and y directions. A K_t is calculated for both x and y directions using the R_{t_m} and S values. The maximum K_t is used, since it is assumed that a surface crack will initiate at a location which has the highest local stress concentration.

To generate a K_t gradient, $g(x)$, as a function of depth into the material, it is necessary to fit this to a curve. An exponential curve was used, with a decay depth corresponding to 3 times the characteristic distance, R_{t_m} .

$$g(x) = (K_t - 1) \exp \left[-x / \left(3R_{t_m} \right) \right] + 1 \quad (2.22)$$

The decay depth of $3 * R_{t_m}$ was chosen because 1) the maximum peak height represents a distance characteristic of the surface roughness along the depth direction, and 2) in finite element analysis, it is commonly noted that localized effects due to application of boundary conditions decay away approximately three times a characteristic distance. Figure 2.5 shows sample K_t gradients for a K_t of 1.5 and two different decay depths.

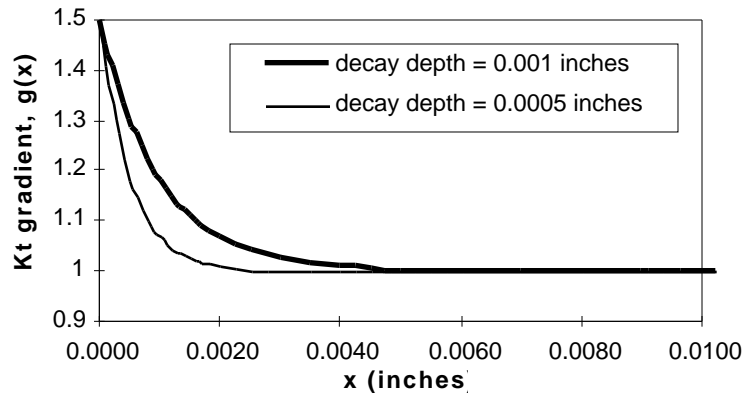


Figure 2.5 – Sample K_t Gradient

K_t of 1.5; gradients shown for two decay depths, 0.001 and 0.0005 inches.

CHAPTER 3

MATERIALS AND EXPERIMENTAL METHODS

3.1 Material Characterization

3.1.1 Workpiece Material

The material used in this investigation is René 88DT, a Nickel-based powder metal superalloy which is used in aircraft engines to meet high temperature capability requirements. René 88DT is strengthened by a gamma prime phase, which constitutes about 40% of the volume of the alloy. Both matrix and gamma prime phases have face-centered cubic structures. Chemical composition is given in Table 3.1. The crack growth rate curve for 1000°F was given in Figure 2.2 (Chapter 2). Other physical properties are summarized in Table 3.2. Average grain size is approximately ASTM 7, about 0.00126 inches diameter (32 μm).

Table 3.1 – Chemical Composition of René 88DT, Atomic Percent [57]

Ni	Cr	Co	Mb	W	Ti	Al	Cb	C	B	Zr
balance	16	13	4	4	3.7	2.1	.7	.045	.016	.045

Table 3.2 – Physical Properties of R88DT [58]

Parameter	Value	Parameter	Value
Density, lbm/in ³	0.302	Walker coefficient, m ⁺	0.167
Young's Modulus, psi	3.2 E+07	Walker coefficient, m ⁻	0.649
Poisson's ratio	0.288	Constraint-loss coefficient, c_c	1.18 E-05
Yield Strength at 75°F, ksi	168	Constraint-loss coefficient, c_c	0.94
Yield Strength at 1000°F, ksi	154	Peening relaxation factor, pscale	0.31

3.1.2 Shot

Three sizes of conditioned cut wire shot used in this investigation are summarized in Table 3.3. This type of shot is cut from steel wire, which is then conditioned to remove any sharp edges. As such, the shot diameter tends to be more uniform than for cast shot, and the shot tensile yield strength increases as wire diameter decreases. The properties of these shot types are given in SAE specification J441 [59]. Chemical composition is summarized in Table 3.4, while selected physical properties are included in Table 3.3. Although English units have been used throughout, small mass measurements are traditionally made in milligrams or grams. Due to the extremely small masses involved in weighing shot particles and mass loss due to erosion, these weights are recorded in the units of measure: milligrams (for single particle measurements) or grams.

Table 3.3 – Selected Physical Properties of Conditioned Cut Wire Shot [59]

GE Shot Size	nearest spec. size	density (lbm/in ³)	Mean wire diameter (inches)	Tensile Strength Range (ksi)	Weight of 50 random pieces (g)	Weight of 100 random pieces (g)
CCW14	CCW14	0.283	0.014	2,010 to 2,280	--	0.020 - 0.040
CCW31	CCW32	0.283	0.032	1,830 to 2,110	0.130 to 0.170	--
CCW52	CCW54	0.283	0.054	1,680 to 1,920	0.680 to 0.840	--

Table 3.4 – Chemical Composition of Conditioned Cut Wire Shot [59]

Fe	C	Mn	P	S	Si
balance	0.45 - 0.85	0.3 - 1.3	0.40 max	0.50 max	0.15 - 0.35

3.2 Microstructural and Metallurgical Evaluation Methods

Microstructural and metallurgical evaluation techniques used to describe the material state at the peened surface are summarized briefly in Table 3.5 for both the single

Table 3.5 – Matrix of Metallurgical Evaluation Techniques Planned

TEST		Metallurgical / Material Evaluation						Low Cycle Fatigue Life
		Microstructure	Chemical Composition	Topography	Erosion	Residual Stresses	Plastic Strain	
1	Single Particle Impact Tests	O,M*	M*	M*	O	-	-	-
2	Production Shot Peening	O,M	M	M	M	M	M	M
	<i>measurement methods</i>	etched, SEM	EDS, Auger	profilometry	mass meas.	x-ray	x-ray, TEM	prior LCF tests

Legend: M= measured
O= observed

* items for which incomplete data exist

Auger=Auger spectroscopy

EDS=energy dispersive spectroscopy

LCF = low cycle fatigue

SEM=scanning electron microscope

TEM=transmission electron microscope

x-ray = x-ray diffraction

particle impact test effort and duplication of production shot peening conditions on coupons. Additional information follows, including special processing and instrumentation.

3.2.1 Microstructure

Slightly different techniques were required for preparation of microstructures. Precision sections [60] were taken through 15 single particle impact dimples and etched to reveal the microstructure below the approximate center of each dimple. This involved cutting out a section of the test specimen containing the dimple, mounting the slice in Transoptic, a clear thermo-setting mount material, and polishing until the center of the dimple is reached. A schematic illustrates this in Figure 3.1.

For the production peened coupons, quarter inch slices were taken from each specimen and mounted in bakelite. A clip was mounted along with the specimen to

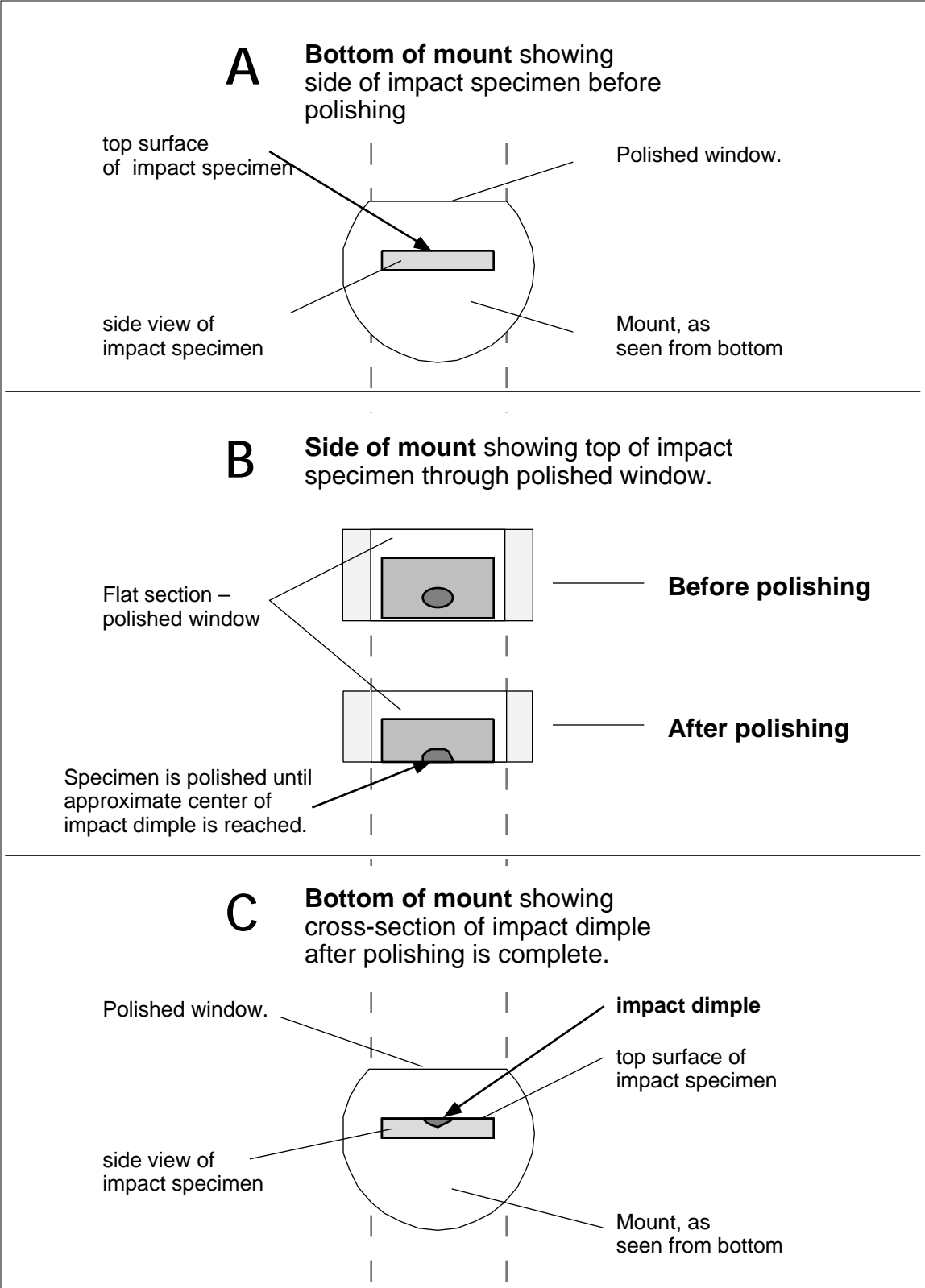


Figure 3.1 – Steps Used in the Precision Sectioning Process

identify the location of the peened surface. Figure 3.2 illustrates the mounting process. As interactions between grind direction, peening direction, material loss due to erosion and microstructure development became apparent, additional steps were taken to record direction of peening relative to specimen geometry, and to record this for future reference along with specimen number, mount number and peening conditions.

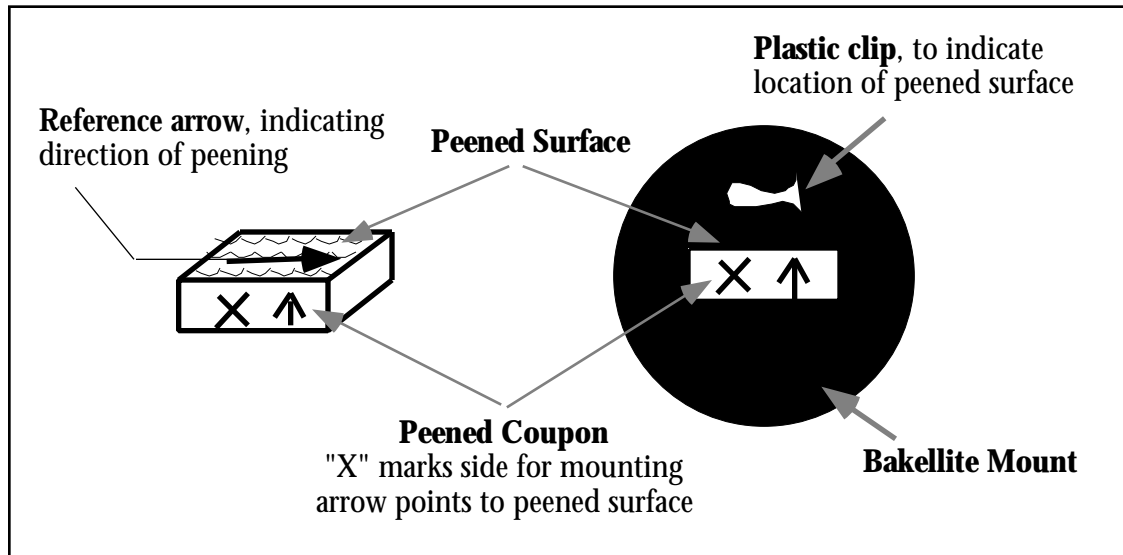


Figure 3.2 – Mounting Process for Production Peened Coupons

Specimens were polished to a .1 μm diamond finish; Linde “A” powder was used with a vibratory polisher to provide a good surface finish. After polishing, specimens were etched with a Modified Marbles or Calings etch. The active ingredient in both etches is hydrochloric acid. Subsequent work with metal clips and a different powder resulted in greater edge rounding and poor etch results. Microstructures were taken optically and with a Scanning Electron Microscope. Due to edge rounding which occurred with early epoxy mounts, the SEM provided better depth of focus of the surface layer.

An Electron Back Scatter Pattern (EBSP) technique was also used to view the surface layer due to peening. TEM analysis was also performed at 10 conditions. The results from these techniques were not directly used in the fracture mechanics model.

Tables 3.6 through 3.9 summarize the instruments used for metallurgical and microstructural evaluation of specimens from the single particle impact tests as well as production peened coupons. X-ray diffraction was conducted by Lambda Research using a sine-squared-psi technique, employing the diffraction of manganese K- radiation from the (311) planes of the FCC structure of the René 88DT. [61, 62, 63, 64]

Table 3.6 – Instruments Used to Obtain Microstructural Information

No.	Technique	Instrument Used
1	Optical microscope	Zeiss Metallograph Axiomet
2	Scanning Electron Microscope - etched microstructures	Cambridge Stereoscan 260 - typical magnifications of 500X to kX. Normal operating range up to 15 kX-50 kX maximum.
3	Scanning Electron Microscope - electropolished section	Hitachi S-800 - typical magnifications of 3 kX to 150 kX. Normal operating range up to 100 kX-300 kX maximum.
4	Scanning Electron Microscope - backscattered image of polished section	CAMSCAN CS44 with CCD backscatter detector.
5	Electron Back-Scatter Patterns (EBSP)	CAMSCAN CS44. EBSP uses Himatsu Argus 10 image capture and enhancement system.

Table 3.7 – Instruments Used to Obtain Chemical Information

No.	Technique	Instrument Used
1	Energy Dispersive Spectroscopy	HNU System 5000
2	Auger Spectroscopy	Varian 981-2702

Table 3.8 – Instruments Used to Obtain Topographic Information

No.	Technique	Instrument Used
1	Profilometer	Tencor Alpha Step 200
2	Vertical Scanning Interferometer	WYKO RST Plus

Table 3.9 – Instruments Used to Obtain Plastic Strain Information

No.	Technique	Instrument Used
1	x-ray diffraction	performed by Lambda Research
2	Transmission Electron Microscopy	Philips EM430 (300 kV microscope)

3.3 Single Particle Impact Tests

One of the major challenges has been to understand and to predict the material response due to repeated impingements of small particles over a wide range of impact conditions: particle size, velocity, incidence angle, and strain rate. Because the range of peening conditions is so wide, no single modeling technique has been able to adequately explain the entire range of material response. Due to the difficulty of conducting tests with the extremely small particle sizes involved, most experimental studies use larger balls. Typical assumptions invoked include: 1) spherical shot, 2) spherical dimples, 3) quasi-static impact, 4) homogeneous material behavior. The physical reality can differ quite drastically. For example, Figure 3.3 shows scale photos of a selection of production shot particles used in the single particle impact tests. Even a cursory glance indicates that they're not spherical in shape or particularly smooth. In fact, they deviate significantly from the perfectly smooth, spherical ball bearings used in Thompson's study [65]. Whether these deviations are significant to the material response can best be answered by data.

To avoid invoking questionable assumptions, single particle impact tests were conducted over a range of conditions relevant to production shot peening conditions of interest. Tests were conducted in an air environment at atmospheric pressure. Effects of coverage (accumulation of dimples), and interaction of multiple impacts within a short time could not be simulated in the test, although pre-peened targets could be used to evaluate change in material response with different levels of coverage. Only two tests were conducted on pre-peened targets, due to limited time, funding, and delay in getting the specimens peened.

By focusing on a single impact event, it is possible to obtain information about initial mass and velocity, as well as recoil mass, velocity, recoil angle, resulting dimple dimensions, changes in chemical composition of the surface, and microstructural changes

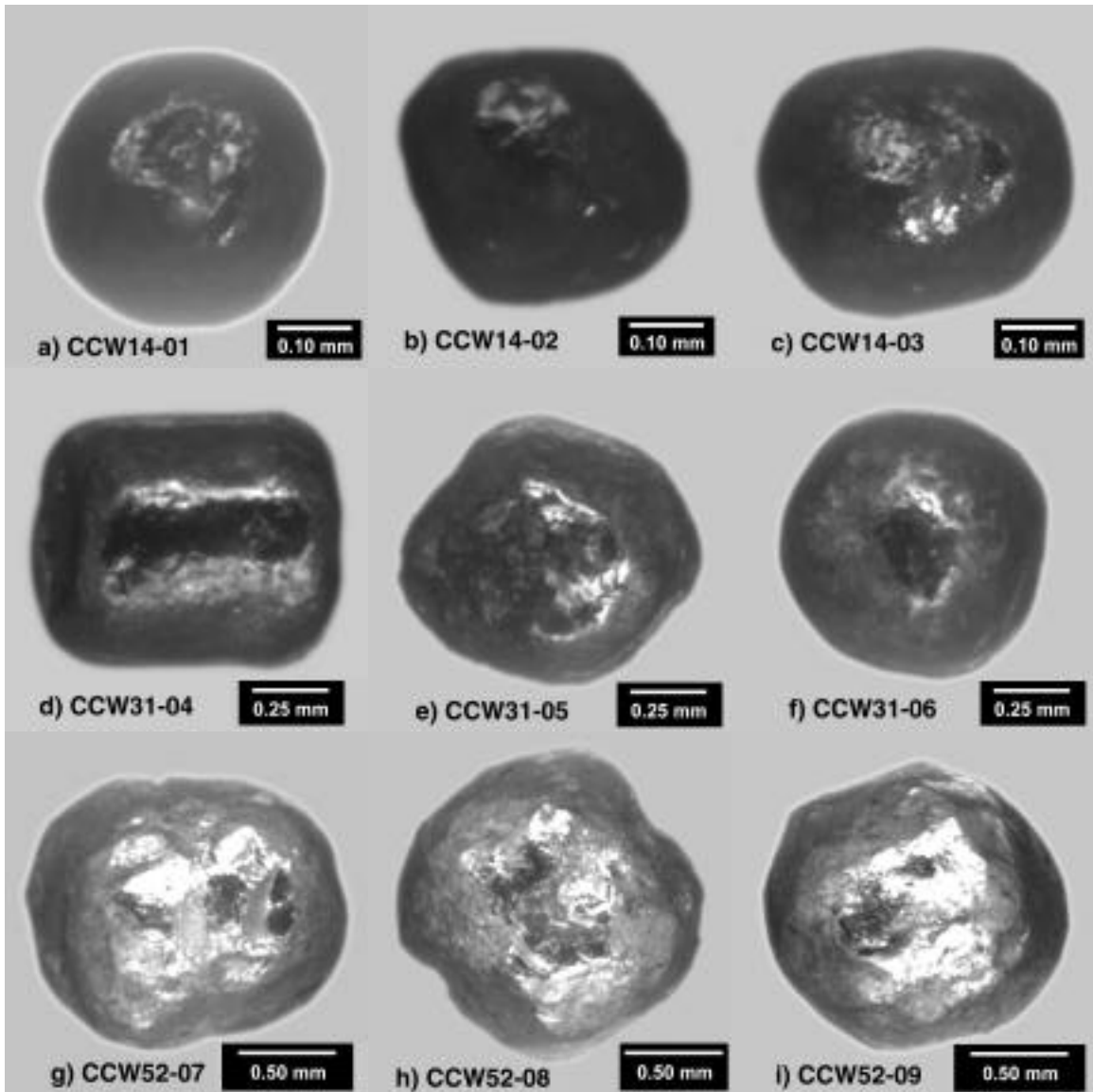


Figure 3.3 – Scale Photos of Shot Samples Used in Single Particle Impact Tests

Note that shape deviates significantly from spherical. Evidence of particle wear or spalling is evident on several samples. a-c) ccw14 shot, d-f) ccw31 shot, g-i) ccw52 shot. (0.10 mm=0.0039 inches). As conditioned, pre-impact test.

surrounding the impact site. This information can also be used to calculate the coefficient of restitution, e , which is the ratio of shot kinetic energy after impact to the kinetic energy before impact. This is a measure of the elasticity of impact, and provides some characterization of the material response.

3.3.1 Goals of the Test Program

The goal of this effort was to link specific changes in material state to impact parameters, which could then be used to understand the effects of specific shot peening conditions.

Changes in material state / response

- Microstructure development
- Dimple size (depth, diameter, shape)
- Chemical composition of surface
- Erosion (mass loss due to impact)
- Coefficient of restitution (a measure of the elasticity of the impact event)

Impact Parameters

- Shot size, shape, mass
- Shot velocity
- Incidence Angle
- Strain rate

The strategy adopted to achieve these goals was:

- 1) To produce single particle impacts which duplicate the production peening process as closely as possible under controlled conditions, using instrumentation to record as much information as possible.
- 2) Control the experimental conditions, if possible, to permit a “Designed Experiment” approach through which effects due to shot size, velocity, incidence angle and strain rate can be isolated.

To implement this strategy, shot size, incidence angle and velocity were controlled to the extent possible. Effects due to microstructural slip vector orientation relative to the impact vector could not be controlled.

3.3.2 Estimating Velocity and Strain Rate for Test Conditions

It appears that intensity is a function of shot size, mass, velocity, incidence angle and coverage, although not necessarily a unique function of these parameters. Although “intensity” or coverage effects could not be varied directly with the single particle impact

tests, it was possible to vary velocity, observe changes in material behavior with velocity, and infer a relationship with intensity.

Since velocity data was not available for production peening conditions, Thompson's relation [65] was used to estimate normal impact velocities for peening conditions of interest, as given in equation 3.1.

$$d = 1.28 \frac{\sigma_y^*}{y}^{1/4} (V_n)^{1/2} D \quad (3.1)$$

Here, d represents the dimple diameter, D the shot diameter, V_n the normal velocity of the shot. It is generally acknowledged that the dimple diameter is approximately equal to the shot peening intensity. [66] So, a peening intensity of 10A should give a dimple of approximately 0.010 inches diameter. Using this assumption, it is possible to determine the normal velocity given the shot size and intensity of interest. Note that σ_y is interpreted as the yield strength of an Almen strip, the workpiece material for the determination of intensity. $\sigma_y = 184,000$ psi is used for these calculations. *(Data from the Structural Alloys Handbook [67] was used to generate a regression relation between yield strength and Brinell hardness for 1070 steel; this was used to obtain the yield strength corresponding to the specified Almen strip hardness of RHC 44-50. Callister [68] was used to convert Rockwell C hardness values to the Brinell hardness values used for the regression.)*

$$V_n = \frac{1}{1.28} \left(\frac{d}{D} \right)^2 \left(\frac{\sigma_y}{\sigma_y^*} \right)^{1/2} \quad (3.2)$$

Because strain rate and not velocity of deformation is typically the parameter controlling material response [42], it was necessary to estimate the strain rate corresponding to the impact conditions. The strain rate for a spherical projectile can be estimated as the projectile velocity divided by one-half the projectile length [20, 42], or in this case the radius (assuming a spherical projectile), giving:

$$\dot{\epsilon} = \frac{V}{L/2} = \frac{V}{R_s} \quad (3.3)$$

Using equations 3.2 and 3.3, shot velocity and strain rate were estimated for a selection of shot, intensity and incidence angle configurations. Table 3.10 shows some approximate calculations, illustrating the range of velocities and strain rates possible for the peening conditions of interest.

Table 3.10 – Total Velocity and Strain Rate Estimates for DOE Shot Peen Conditions Using Thompson Relation

Intensity	Angle	CCW14		CCW31		CCW52	
		V_{total} in/s	$\dot{\epsilon}$	V_{total} in/s	$\dot{\epsilon}$	V_{total} in/s	$\dot{\epsilon}$
6A	45°	2513	3.6E+5	513	3.3E+4	182	7.0E+3
	90°	1777	2.5E+5	362	2.3E+4	129	5.0E+3
10A	45°	6980	1.0E+6	1424	9.2E+4	506	1.9E+4
	90°	4936	7.1E+5	1007	6.5E+4	358	1.4E+4

3.3.3 “Designed Experiment” Approach

To obtain as much information about the impact process as possible, including coefficient of restitution, mass transfer from shot to target, and adiabatic heating on impact, a number of factors needed to be measured or controlled, as shown in Tables 3.11 and 3.12.

Table 3.11 – Controlled Single Particle Impact Test Elements

Element	Before Impact	Notes / Methods
Shot type (ccw14, ccw31, ccw52)	C	Samples taken from production shot. Individual shot were weighed, measured and labeled prior to test.
Incidence Angle	C	Impact photo of recoil used to determine recoil angle.
Helium Tank Pressure	C	Pressure selected to obtain desired velocity.

Legend: C = controlled

Table 3.12 – Measured Single Particle Impact Test Elements

Element	Before Impact	After Impact	Notes / Methods
Shot mass	M	M*	Shot not always recovered after impact.
Shot dimensions (max diameter, L; min. diameter W)	M	M*	Shot not always recovered after impact.
Incidence Angle	C	M*	Impact photo of recoil used to determine recoil angle.
Shot Velocity	M*	M*	Incident velocity obtained by laser. Recoil velocity obtained from impact photo.
Transient temperature rise at impact	--	M*	High speed infrared detectors used for subset of tests to measure T at impact. When these tests were conducted, photos of recoil were not possible (flash interferes with detector).

*Legend: C= controlled; M= measured; * incomplete data exist*

The goal was to use a “design of experiment” layout so that effects of shot size, incidence angle, velocity and strain rate could be separated out. The difficulty of the test made strict adherence to a factorial design impossible. However, velocity and strain rate estimates were used to set a range of test conditions. Figure 3.4 shows maps of velocity-intensity space and strain rate-intensity space as predicted using Thompson’s relation (eq. 3.1). These maps illustrate the extreme differences in velocity and strain rate between shot sizes for a given intensity. To attain a given intensity, small shot must reach significantly higher velocities than larger shot. As a result, corresponding strain rates are significantly higher for the smaller shot.

To achieve the desired velocities and strain rates, it was necessary to use a gas gun as shown in Figure 3.5 to propel the small shot particles. An individual particle is loaded into a plastic or brass sabot, which is then stripped away from the shot before exiting the barrel.

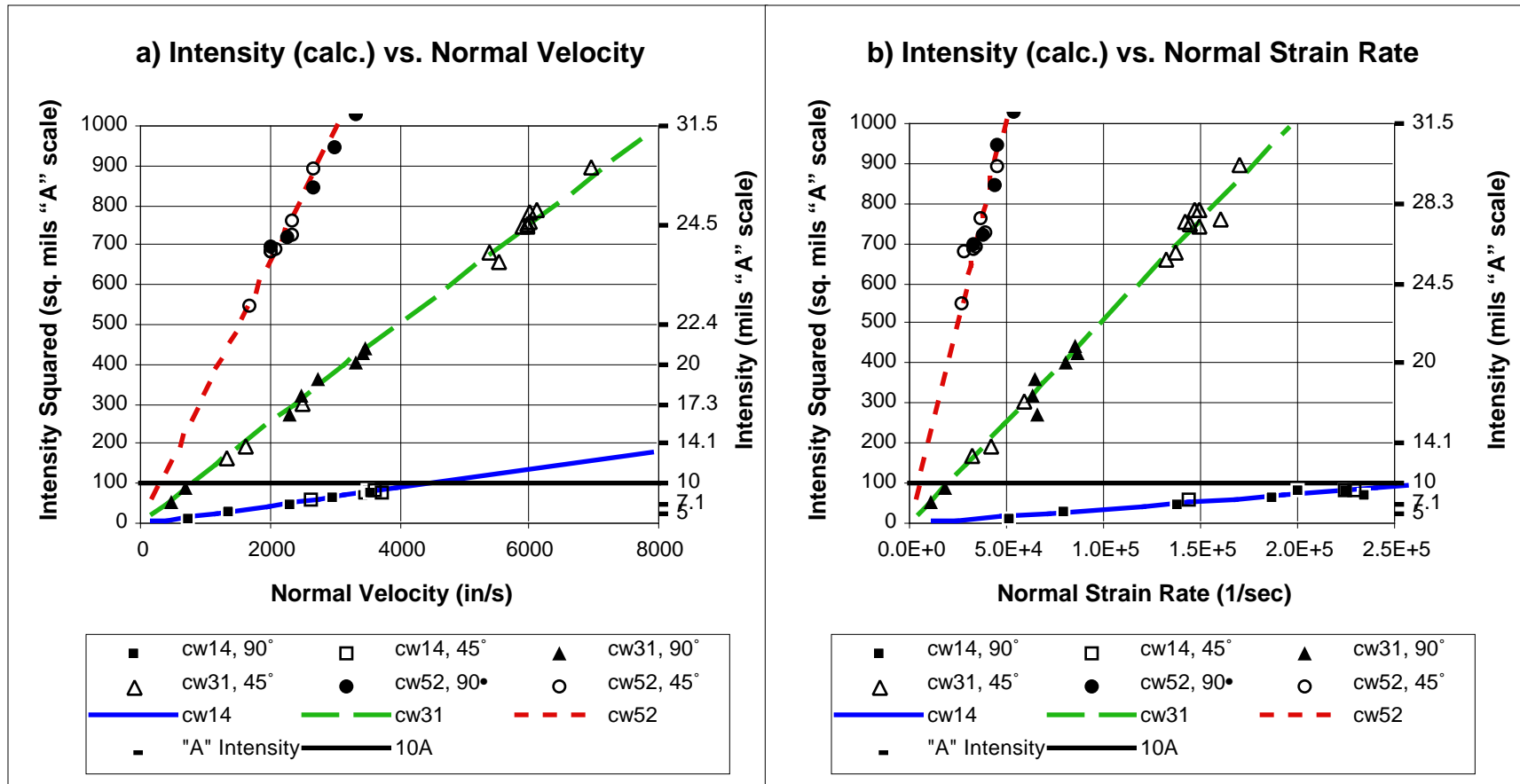


Figure 3.4 – Map of Intensity/Velocity and Intensity/Strain Rate Test Conditions

Thompson's relation used to estimate velocity as a function of intensity/dimple diameter. Intensity squared plotted to give linear relationship, as indicated on left y-axis. Corresponding intensity values shown on right side of plot.

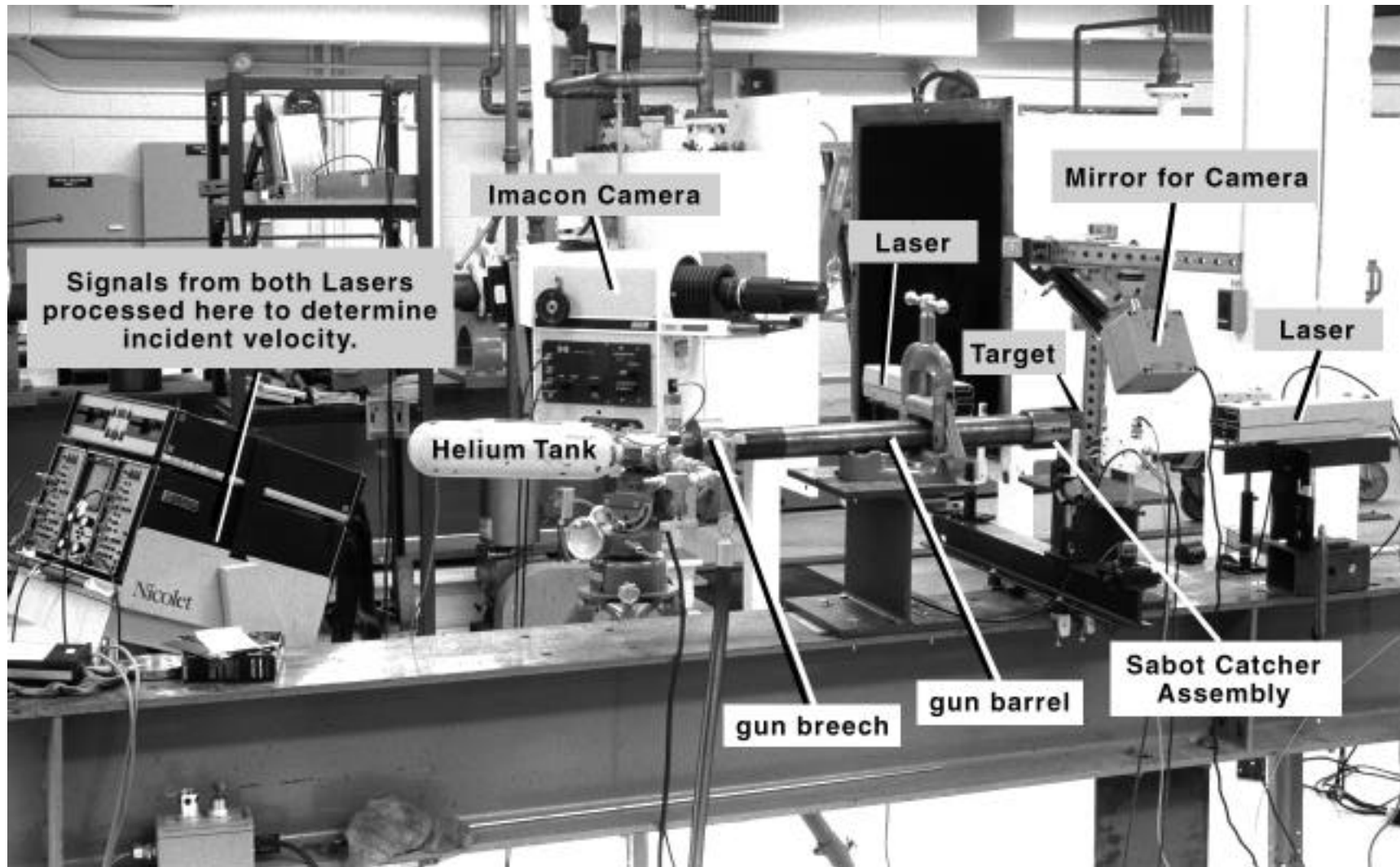


Figure 3.5 – Gas Gun used for Single Particle Impact Tests

3.3.4 Single Particle Impact Test Equipment

Tests were conducted using a Helium gas gun, as shown in Figure 3.5. Plastic or brass sabots were used to carry the shot down the barrel, as shown in Figure 3.6. Figure 3.7 provides a closeup of the muzzle, including the sabot catcher assembly, location of two laser beams, target and recoil direction.

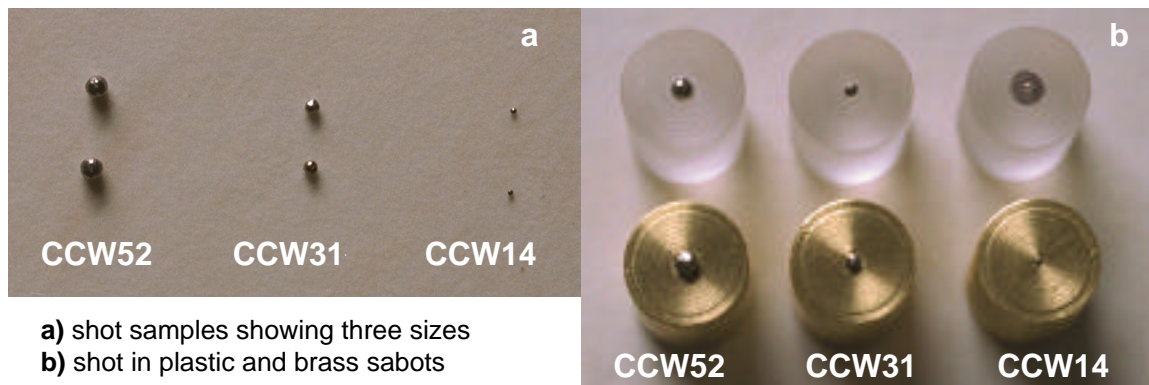
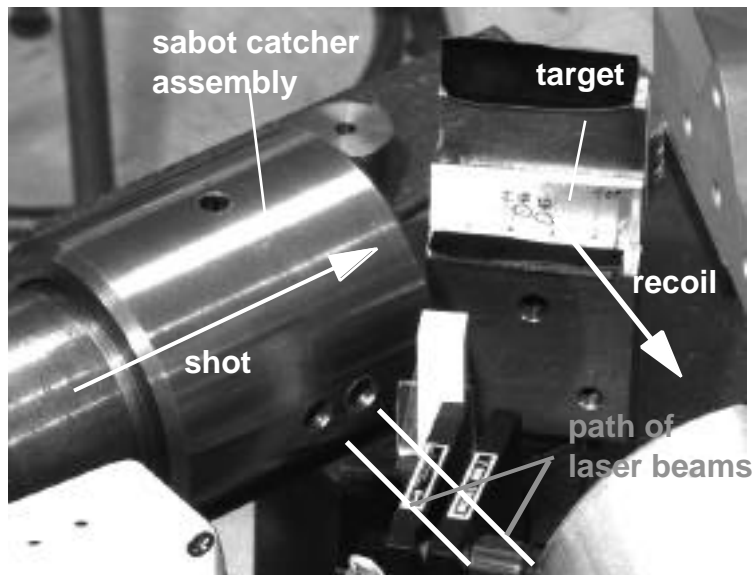


Figure 3.6 – Shot and Sabots used in Single Particle Impact Tests



When the gas is released into the gun breech, the sabot and shot are propelled down the barrel and into the sabot catcher, which strips the sabot away from the shot.

The sabot triggers the first laser beam. The shot continues down the barrel, interrupting the second laser beam on its way to the target.

Figure 3.7 – Closeup of Muzzle Showing Sabot Catcher Assembly and Target

Shot is loaded into a sabot, which is then loaded into the breech of the gun. The helium tank is attached, and pressure is selected. The gas is then released into the breech, propelling the sabot and shot along the barrel and into the sabot catcher, at which point the first laser is triggered. The sabot catcher strips the sabot away from the shot. The shot breaks the second laser beam on its way to the target. Glass sides were taped to the target holder to try catching the shot for post-impact weighing and measurement. Catching the shot was difficult, and not always successful.

3.3.5 Velocity Measurements

Two lasers were used to determine the incident velocity of the shot particle as it leaves the muzzle. Figure 3.7 shows the location of the two laser beams. The recoil velocity is obtained by high speed photos of the recoil event. A reference grid is placed in front of the target. A mirror is positioned to give the camera an overhead view of the approach to the target. Black felt is attached to the tops of the target, target holder and sabot catcher to isolate frames on the impact photo. Figure 3.8 shows the camera's view of the impact site, including the reference grid, as seen through an overhead mirror.

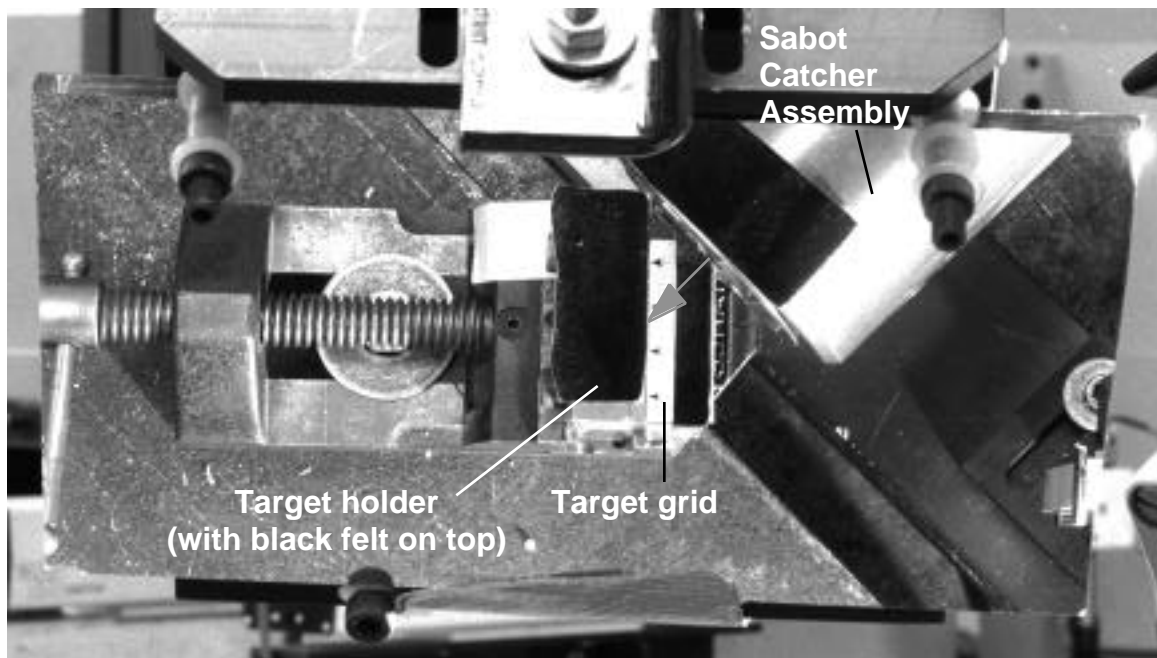


Figure 3.8 – Camera's View of Impact Site as Seen Through Overhead Mirror

The Imacon camera used is able to take up to 12 images, at 10 μ s intervals on one Polaroid photo. These images capture the shot position against a reference grid. Movement of the shot particle as it approaches or recoils from the target can be tracked by noting change of position along the reference grid placed in front of the target, as shown in Figure 3.9. Recoil velocities are estimated by counting the distance traversed between frames (using the reference grid) and dividing by the amount of time lapsed between positions.

The small size of the particles used increased the difficulty of the tests. Incident velocities had to be estimated, and a time delay calculated so that the recoil event would be captured within the 120 μ s spanned by the impact photo. Small variations in sabot/barrel fit could alter impact velocities enough so that the camera would miss the recoil event.

3.3.6 Temperature Measurements Using High Speed Infrared Detectors

A subset of tests focused on measurement of transient temperature during impact. A high speed infrared detector was used to look for temperature rise during impact. These tests were extremely difficult. An array of sixteen 0.0032 by 0.0032 inch detectors, arranged in a single line at 0.00394 inch spacing (for a total detection grid of 0.063 by 0.0032 inches) was focused onto the target at the estimated impact site. If the detectors were indeed focused on the right spot, transient temperature profiles were captured. Three successful tests were obtained. Additional information is given in Appendix B.

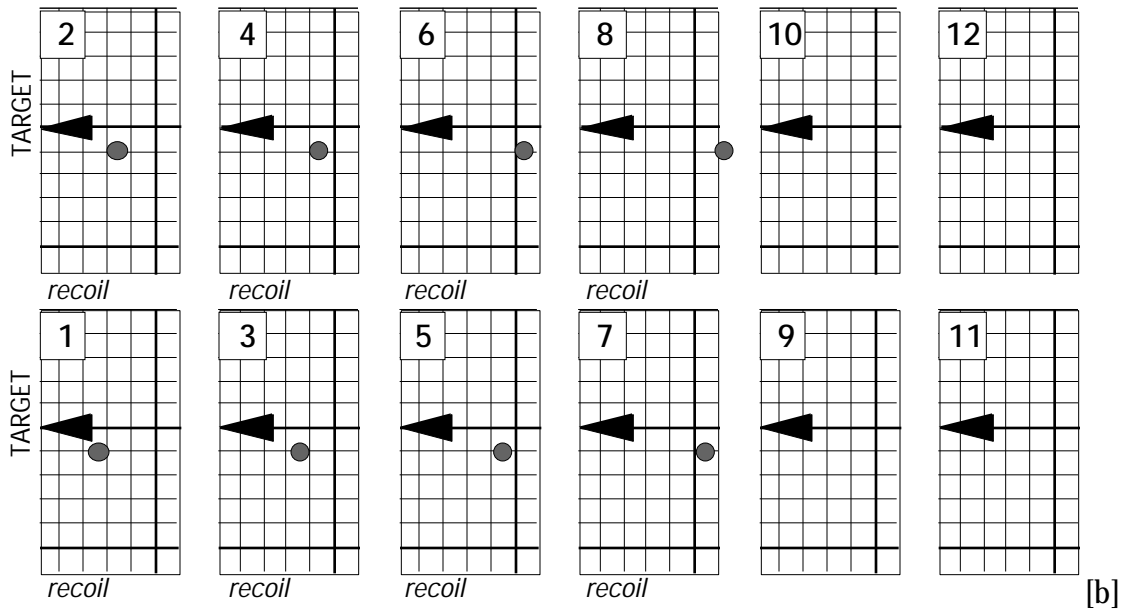
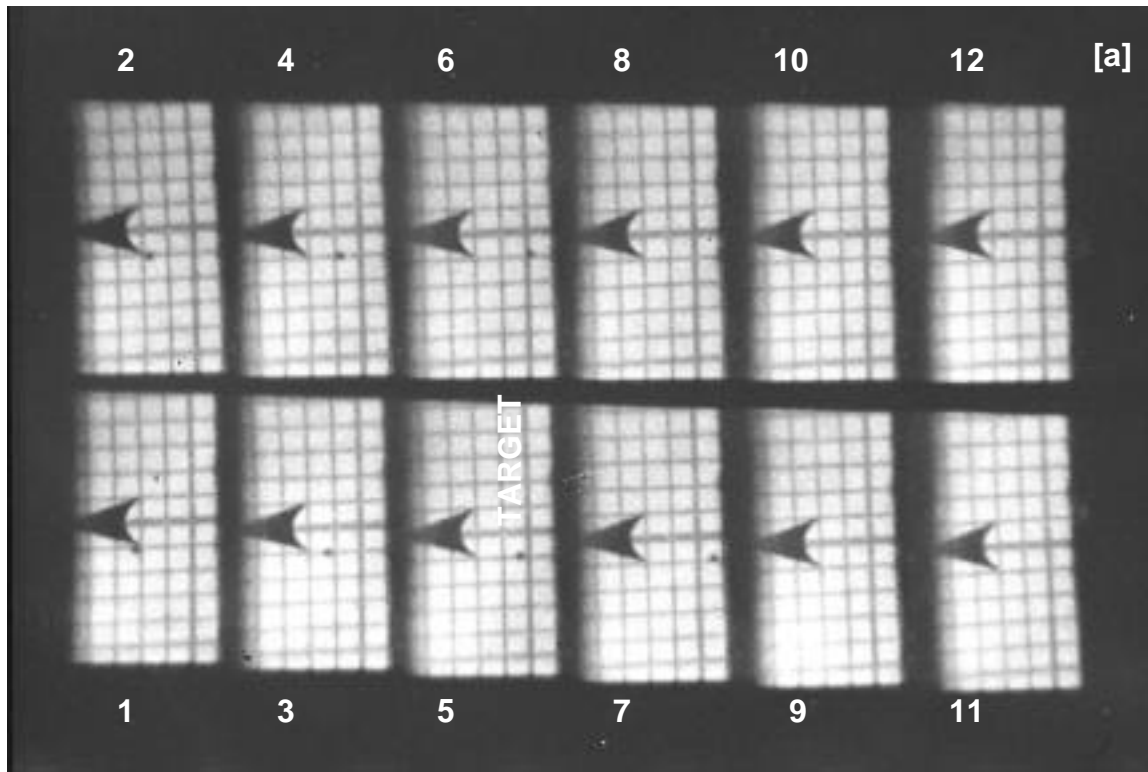


Figure 3.9 – High Speed Impact Photo and Schematic of Layout

a) Impact photo from Imacon Camera, with 12 separate frames taken $10 \mu\text{s}$ apart. Target is at left side of frame (arrow points to target); grid has 1 mm spacing. Photo shows recoil of CCW14 shot, fired at 88 m/s onto a René 88DT target. Recoil velocity is estimated from distance traveled / time. Shot moves approximately 2 mm between frames 2 and 6, a $40 \mu\text{s}$ time lapse, resulting in an estimated recoil velocity of 1,970 in/s (50 m/s). b) Schematic of Impact Photo, illustrating movement of shot along grid.

3.4 Production Peening of René 88DT Coupons and Velocity Measurements

The original LCF specimens were peened using a Progressive Technologies shot peen machine, consisting of a six-axis NC controlled single nozzle, with a pressure engine and mass flow regulation. Specific machine parameters controlling intensity and saturation include: shot size, mass flow, machine pressure, nozzle feed rate, and distance of nozzle from the workpiece. A reference set of saturation curves, listing the individual machine parameters, is usually consulted to set these parameters for a desired reference peening condition. An Almen strip is run to verify that the conditions set are representative of those used to generate the saturation curve.

Because microstructures, residual stresses and topography change with thermal exposure and stress cycling, the needed microstructural and metallurgical characterization could not be obtained from the failed test specimens. Therefore, the peening conditions used in the shot peen DOE were duplicated on new René 88DT coupons. The same shot peen machine was used, and machine conditions were set using the reference set of saturation curves. Saturation curves were requested and retained for the new peening conditions. Every attempt was made to duplicate the exact peening conditions used for the DOE. However, due to hose wear and nozzle wear, it is not possible to verify that this was accomplished. It was possible to verify that comparable changes in intensity and coverage were attained, permitting assessment of these levels of change on resulting microstructure. Sensitivity studies were conducted to quantify the effect of variability. Finally, sections were cut off from a sub-set of the test specimens to evaluate and compare the depth of the plastic strain layers of the DOE LCF specimens with the coupons peened for this investigation.

Initially, eight of the sixteen DOE conditions were selected for evaluation. Later, the remaining 12 DOE conditions were duplicated on René 88DT coupons to complete

the model validation process. Saturation curve data were obtained for each shot/intensity/incidence angle combination, due to the variability of the intensity definition. Specimens were weighed before and after peening, to identify mass loss due to erosion. Specimen dimensions recorded before peening were used to estimate surface area, so that a mass loss per unit surface area could be calculated.

An electromagnetic velocity sensor patented by Thompson was ultimately used to obtain velocity estimates for some of the peening conditions. Unfortunately, this was not available until a year after the single particle impact tests were completed. The measurements are taken at the nozzle, not at the surface of the workpiece. As a result, they do not provide reasonable characterization of shot velocities for peening conditions which required a nozzle extension to reach the intensities desired (primarily ccw14, 10A intensities), or at the low mass flow rates required for some of the higher ccw31 intensities. Therefore, it was not possible to obtain production peening velocities for all of the DOE peening conditions. However, the data collected provide a means of comparing material behavior observed from the single particle impact test results more directly with results from production-peened coupons.

CHAPTER 4

RESULTS

4.1 Single Particle Impact Test Results

The main objective of the single particle impact test effort was to gain a better understanding of what happens to the material under impact conditions similar to those used in production peening. Changes in material response were of particular interest. One of the strategies used was comparison of observed behavior against behavior predicted using Thompson's relation. Details of how dimple measurements were made and interpreted are presented in Appendix A, along with other details from this test effort.

4.1.1 Hertzian Behavior Check - Measured vs. Predicted "d/D" Ratios

Thompson's relation was used to predict a dimple/shot diameter ratio (d/D). From profilometry measurements and actual shot dimensions, a corresponding d/D was calculated. Figure 4.1 shows the measured vs. calculated values. The 1:1 line represents perfect correlation between the measured and predicted ratios. At low velocities and strain rates, the observed behavior agreed well with the predicted behavior. However, at higher velocities, a deviation from "Hertzian" behavior was noted, suggesting a change in plastic deformation mechanisms, or at least more localized plasticity.

From Figure 4.1, it can be seen that four tests correlate well with the predicted values using Thompson's relation. Table 4.1 gives the shot size, velocity, and strain rate for the test conditions bounding the observed change in behavior (the highest velocities which still correlate with Hertzian behavior, and the lowest velocities which deviate from

Hertzian behavior). For the shot sizes tested, it appears that Hertzian behavior is observed for velocities below 1,340 in/s. Deviations from Hertzian behavior were observed for velocities greater than 2,280 in/s. Strain rate, as estimated, does not appear to provide useful differentiation between conditions.

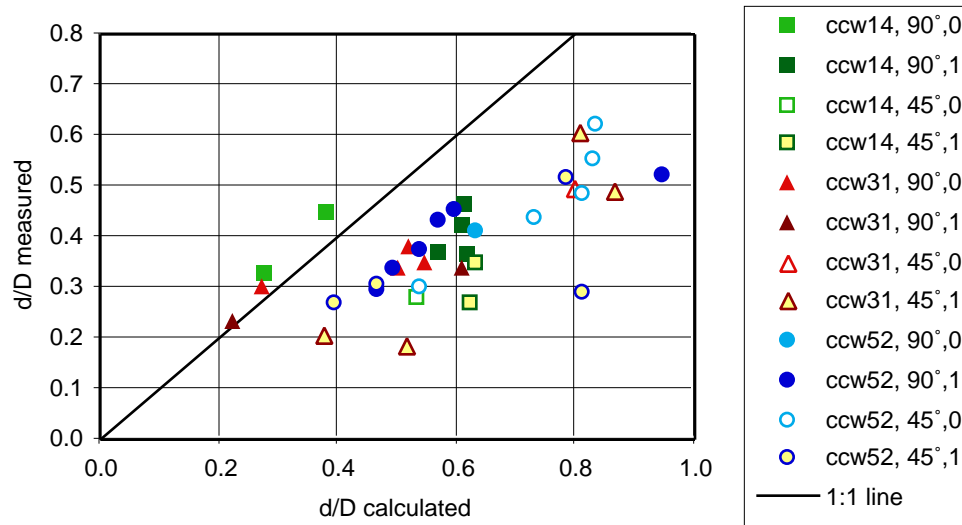


Figure 4.1 – Measured vs. Calculated “d/D” Ratio
 Data grouped by shot size, incidence angle and grind orientation (0 = grind oriented horizontally, 1= grind oriented vertically).

Table 4.1 – Ranges of Velocity and Strain Rate Corresponding to Hertzian Behavior

Shot Size	?	Velocity in/s	Velocity m/s	Strain Rate 1/s
CCW14	4	V 1,340	V 34	1.6E+5
	5	V 2,280	V 58	2.8E+5
CCW31	4	V 710	V 18	3.8E+4
	5	V 2,320	V 59	1.3E+5

4 = Hertzian behavior observed

5 = deviation from Hertzian behavior observed

It should be noted that the dimples observed were not perfectly spherical craters. Most were irregular in shape, being elongated, and often having a significant raised “lip” which was particularly pronounced for 45° incidence angles. The Thompson relation assumes only the normal component of velocity is relevant, and is unable to account for

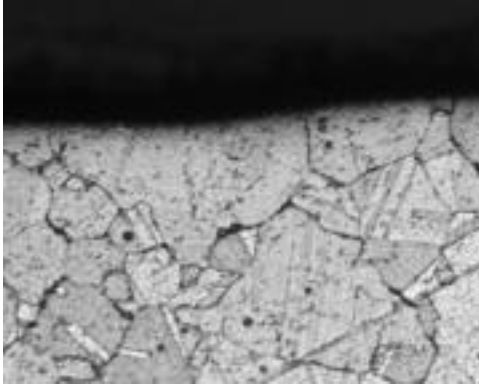
incidence angle effects. Because of cutting and sliding which can occur during impact, the minimum diameter was used for d in the d/D calculation as being more representative of the shot contact with the surface. Appendix B describes how dimple profiles were taken and processed in more detail, and includes sample dimple profiles and photos.

Iron Transfer. Selected impact dimples had EDS performed, to check for presence of iron on the surface after impact. Of the precision sections made for shot which demonstrated Hertzian behavior, no iron was detected on the surface. Iron was not detected for ccw31 at 2,320 in/s (which deviates from Hertzian behavior). Negligible to significant amounts of iron were detected for velocities of 3,400 in/s and up for all shot sizes. Transfer of iron to the surface does not appear to correlate precisely with deviation from Hertzian behavior. A somewhat more severe impact condition is needed for iron to wear from the shot and become embedded in the workpiece surface.

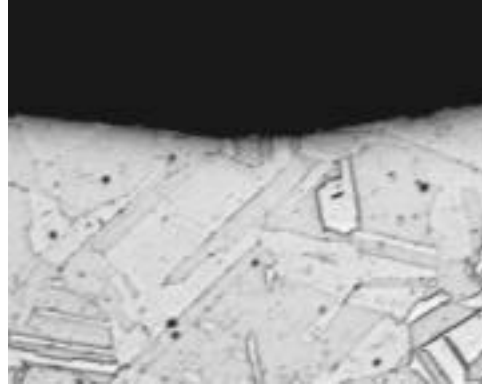
4.1.2 Microstructure Development

Precision sections were taken through selected dimples to observe microstructural changes as a function of shot size, velocity and incidence angle. Figure 4.2 shows changes among five sample microstructures with increasing velocity. Additional microstructures are included in Appendix B. Development of slip bands was the primary feature noted. Significant amounts of slip were observed at velocities greater than 2,300 inches/second, corresponding to the deviation from “Hertzian” behavior illustrated in Figure 4.1. This observation led to the hypothesis of using slip depth measurements to characterize an initial crack size for a fracture mechanics calculation. Transfer of iron from the shot to dimples was observed at higher velocities, around 3,400 in/s and higher.

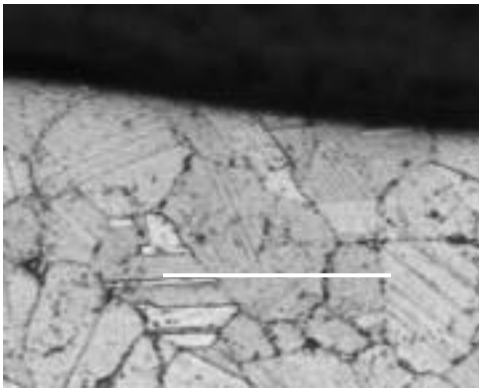
Variation in slip behavior was observed at comparable impact conditions, suggesting that favorable grain slip vector orientation relative to the shot impact vector can increase strain localization. Test 3-062 (Fig. B.7) showed less slip than 3-079 (Fig. B.6). Test 3-077 (Fig. B.10) showed greater slip (at lower velocity) than 3-056 (Fig. B.11).



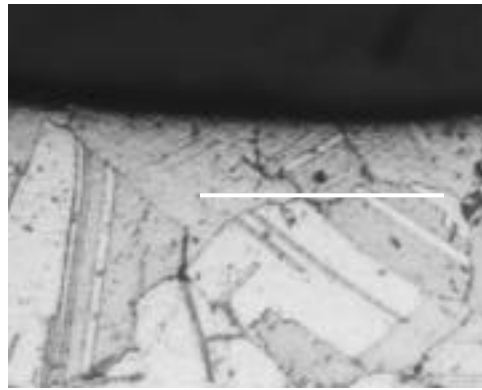
(a) CCW31 (3-023) 690 in/s, 90°
negligible slip observed



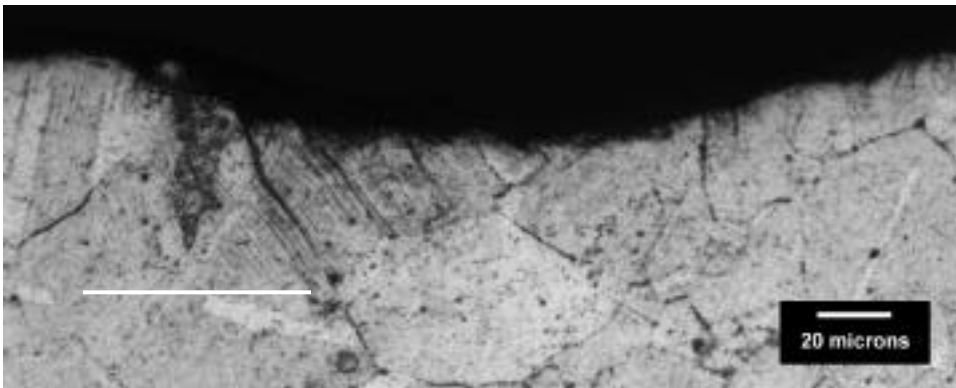
(d) CCW14 (3-027) 1,350 in/s, 90°
negligible slip observed



(b) CCW31 (3-009) 2,320 in/s, 90°



(e) CCW14 (3-017) 3,440 in/s, 90°



(c) CCW31 (3-077) 3,490 in/s, 45°

Figure 4.2 – Microstructure Development with Increasing Velocity, CCW31 and CCW14 Shot (all to same scale; 20 μm = 0.8 mils)
Test numbers given in parentheses. White lines indicate lower bound of slip observed. Note development of slip for velocities greater than 2,300 in/s. Section of dimple microstructure presented here. Complete profiles are presented in Appendix B.

4.1.3 Slip Depth Predictions as a Function of Shot Velocity

Regression analysis was performed to determine significant factors involved in predicting slip depth. Shot mass, width (minimum diameter) and total velocity were identified as the significant factors. Figure 4.3 shows the correlation obtained with and without velocity, illustrating the significance of velocity to this prediction. With a velocity term included, slip depth was predicted to within ± 0.001 inches of observed values.

Variation was observed in slip patterns and depth observed, which seemed to depend on microstructural orientation. In some cases, strong slip bands were observed parallel to the direction of impact, originating at the side of the dimple where impact first occurred. This suggests that strain localization is maximized when the slip vector of the underlying grain coincides with the impact vector of the shot. The complete set of precision section microstructures is provided in Appendix B. Arrows are included to indicate impact direction for reference.

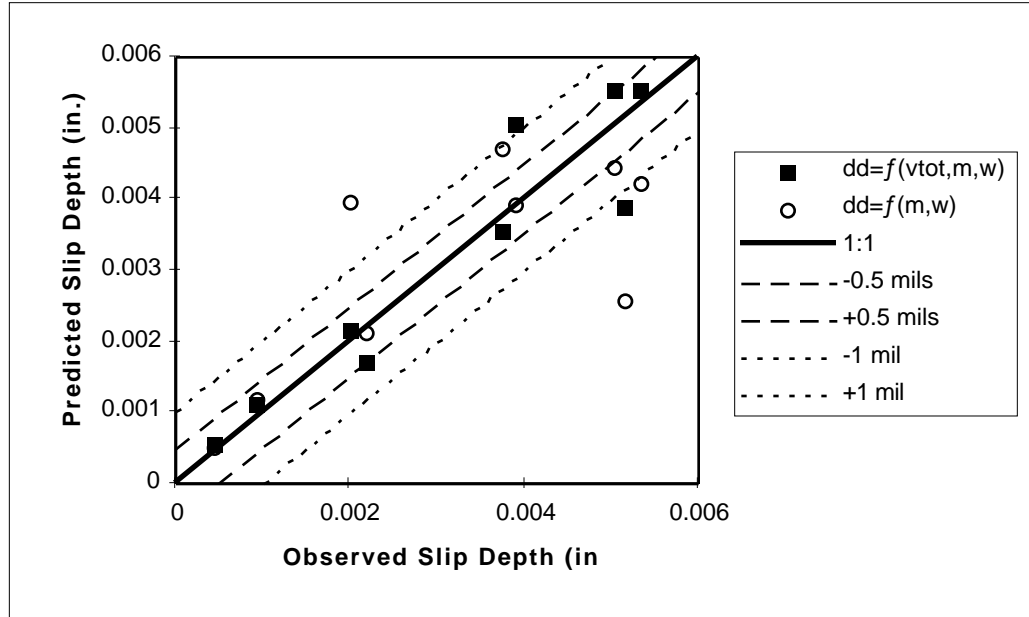


Figure 4.3 – Slip Depth – Predicted vs. Observed

Linear regression analysis was used to correlate log of slip depth as a function of the common logarithms of shot mass, m , shot width, W , and total shot velocity, V_{tot} .

4.1.4 Coefficient of Restitution Trends

Another measure of material response is “elasticity of impact,” the degree to which the impact event is perfectly elastic. The coefficient of restitution, e , provides a measure of this behavior and is defined by:

$$e = \frac{m_{out} V_{out}^2}{m_{in} V_{in}^2} \quad (4.1)$$

A coefficient of restitution of $e=1$ corresponds to a perfectly elastic impact, while $e=0$ reflects a perfectly plastic impact. Hertzian analysis typically assumes a constant coefficient of restitution close to 1. Figure 4.4 shows that the coefficient of restitution drops significantly as velocity increases (note regression line trend). Values of e ranged from 0.40 to 0.06. Coefficients of restitution were calculated only when all data were available (mass of shot before and after impact, velocity of shot before and after impact). Most of the coefficient of restitution data available are for 90° incidence angles. (Only one complete data point exists for 45° impact, but velocity ratios were compared for other test points). The observed values for 45° impacts appeared to be much higher on average, when using total velocities for the calculation. These values of e more nearly approached that for 90° impacts when using only the normal component of velocity.

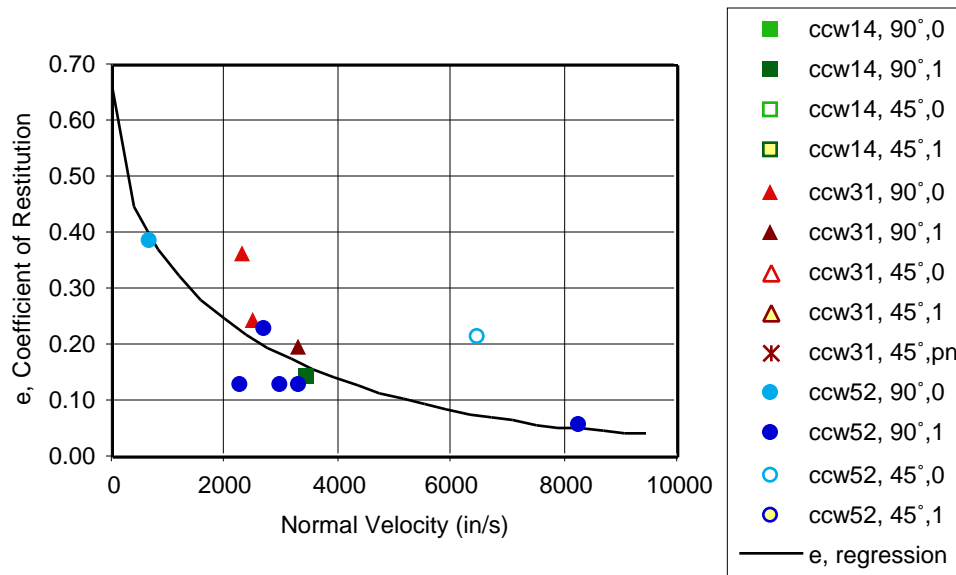


Figure 4.4 – Coefficient of Restitution, e , vs. Normal Velocity

4.1.5 Normalized Impact Stress

The data analyzed suggest that Hertzian analysis is appropriate for low velocities, while impact dynamics analysis is appropriate at higher velocities. A normalized impact stress was calculated and compared with a normalized dimple depth (measured / predicted). Details are presented in Appendix B. The final equation obtained is:

$$P^* = K_t \frac{P}{y} = \frac{K_t \rho_w U_w V_0 \frac{\rho_{shot} U_{shot}}{\rho_{shot} U_{shot} + \rho_w U_w}}{y} \quad (4.2)$$

The impact stress, P, is estimated from the workpiece density, particle velocity in the workpiece after impact, and the shock wave velocity. Because this expression is used for flat plate impacts, an adjustment was made to account for shape of the particle by including the K_t of the resulting impact dimple. This is an estimate. Figure 4.5 shows that deviations from observed/predicted dimple depth correspond to increasing P^* values.

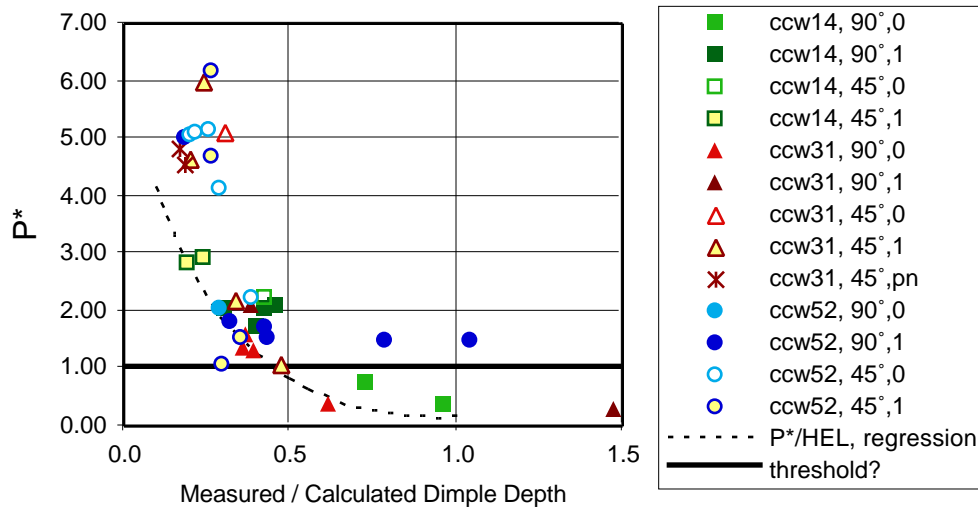


Figure 4.5 – Normalized Impact Stress, P^* , vs. Measured/Calculated Dimple Depth

Equation 4.2 is significant in that it permits a prediction of non-elastic behavior as a function of basic material properties and shot velocity. Initial shot velocity, V_0 or V_{tot} , appears in the numerator. Yield strength appears in the denominator. This predicts that

higher velocities would be needed to produce a reference amount of plastic deformation in higher yield strength materials, compared with lower yield strength materials. Since yield strength typically increases with decreasing grain size, a grain size effect can also be inferred from this relation.

4.2 Evaluation of Production Peened Coupons and Velocity Measurements

Coupons of René 88DT were peened to the same conditions used in the DOE. Coupons were weighed before and after peening. Observation of significant mass loss (erosion) corresponded to low life behavior. Higher K_t 's were also observed. Presence of iron in the surface layer (transferred from shot) also corresponded to the most severe life loss conditions. However, these factors did not permit a direct correlation with life behavior. Emphasis was placed on defining elements for the fracture mechanics model.

4.2.1 Microstructure

Slip depth was identified as the critical feature corresponding to an initial crack size. Microstructural evaluation conducted on a model disk that had been tested to failure (unrelated to this program) revealed crack formation along slip bands. Figure 4.6 shows a crack which had opened and was visible (with the naked eye) from the surface. A slice was taken and mounted for microstructural observation. Figure 4.7 shows a crack in the process of forming along a slip band, which was found on the same mount. Note that the slip bands favored for crack formation are favorably oriented for shear.

Figure 4.8 illustrates the rationale used for the slip depth measurement criteria. Conditioned cut wire shot impart a fairly uniform slip layer in the workpiece. Crack formation is known to occur in regions of high stress localization, i.e. high K_t region. So, a competition is likely to develop among the deepest dimples on the surface. The dimple having the most favorably oriented slip system (aligned with the shot impact vector and favorably oriented for shear), is likely to win. Regions with lower K_t 's are likely to lose the

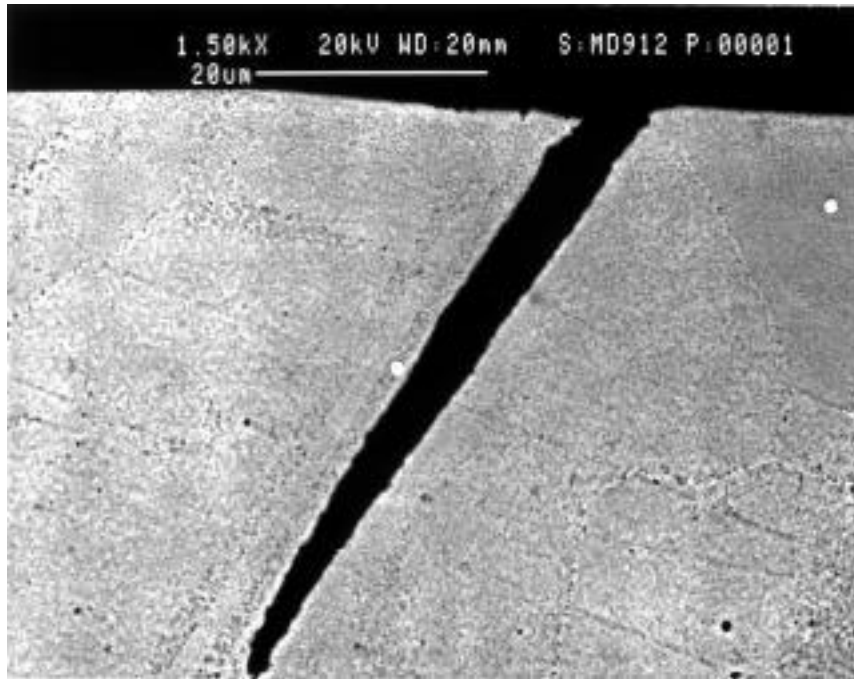


Figure 4.6 SEM backscatter electron image showing crack formation along a slip band (1.5 kX).

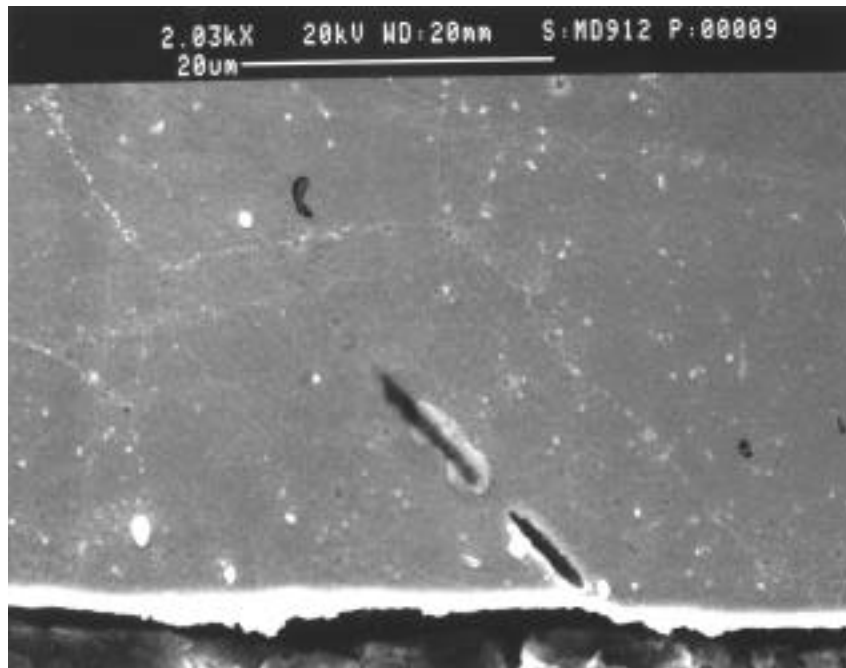
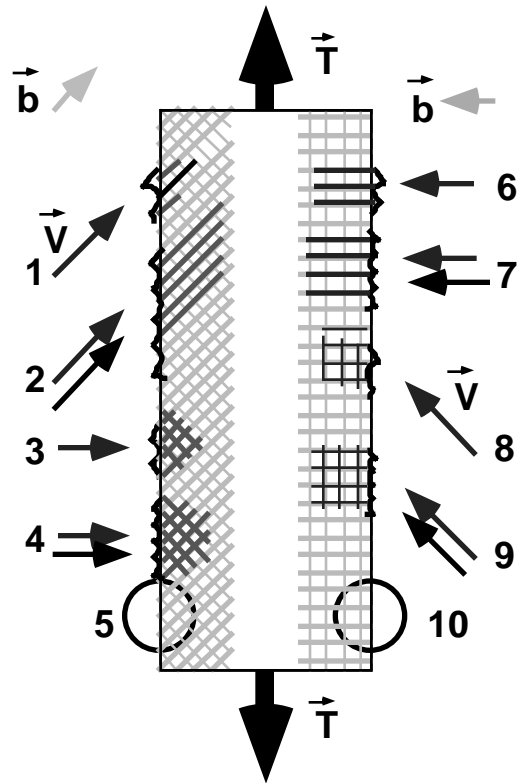


Figure 4.7 SEM secondary electron image showing crack formation along a slip band, within a grain (2.03 kX).



Case	$\vec{b} ? \vec{T}$	$\vec{V} ? \vec{b}$	Kt	Coverage (slip depth)	Favorability for crack
1	$\vec{b} / 45^\circ \vec{T}$	$\vec{V} \parallel \vec{b}$	very high	low	very high **
2			medium-low	high	moderate
3		$\vec{V} \not\parallel \vec{b}$	medium	low	moderate
4			very low	high	low
5			no impact	0	0
6	$\vec{b} \perp \vec{T}$	$\vec{V} \parallel \vec{b}$	high	low	moderate
7			very low	high	very low
8		$\vec{V} \not\parallel \vec{b}$	medium	low	moderate
9			low	high	low
10			no impact	0	0

Legend:



\vec{b} = slip vector	 underlying slip orientation	** - most favorable condition for crack formation and growth
\vec{T} = tensile axis	 Peening- induced slip bands	45° at a 45° angle to
\vec{V} = impact vector		\perp perpendicular to
		\parallel parallel to
		$\not\parallel$ not parallel to

Figure 4.8 – Competing Sites for Crack Development and Growth Due to Local Variations in Peening Condition

competition, even if there is no slip depth, or greater slip depth beneath the surface. From the surface roughness data, it was found that the K_t generally decreases with increasing coverage. However, slip depth was observed to increase with increasing coverage. Thus, it appears that a relative minimum slip depth will correspond to the crack initiation site for René 88DT targets peened with conditioned cut wire shot. This may also create a “plastic hinge” effect, resulting in a relatively weaker low slip region sandwiched between more highly work-hardened regions, creating a “weak link” for additional strain localization. Additional information is presented in Section 4.7 and Table 4.4.

4.2.2 Residual Stresses

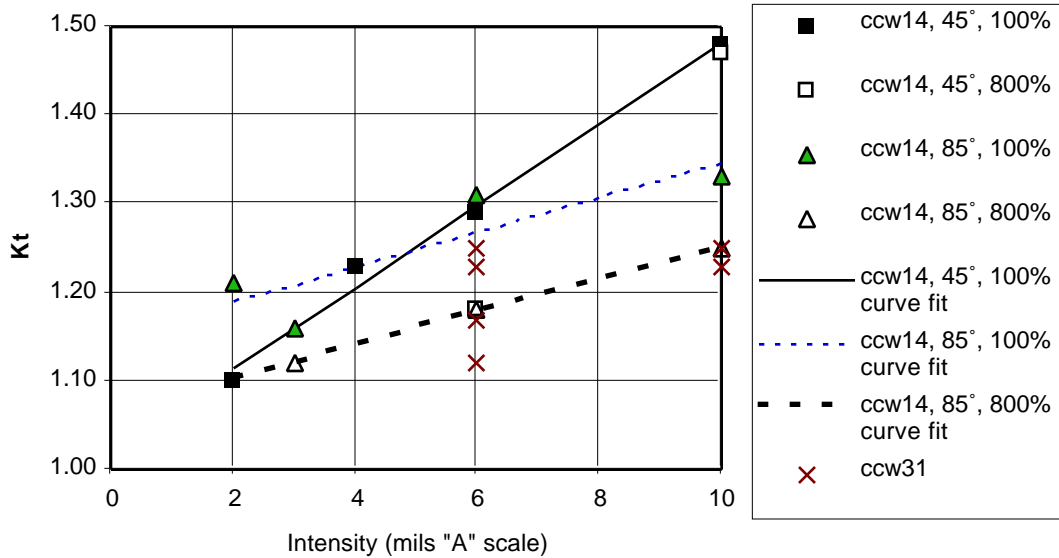
Residual stresses were obtained from Lambda Research x-ray diffraction measurements. Curve fits using equation 2.19 were conducted to generate smooth curves for the fracture mechanics model. Plots of the data and corresponding curve fits can be found in Appendix C. Table 4.2 provides a summary of the curve fit coefficients for the DOE conditions in standard order.

Table 4.2 – Residual Stress Curve Fit Coefficients for Equation 2.19

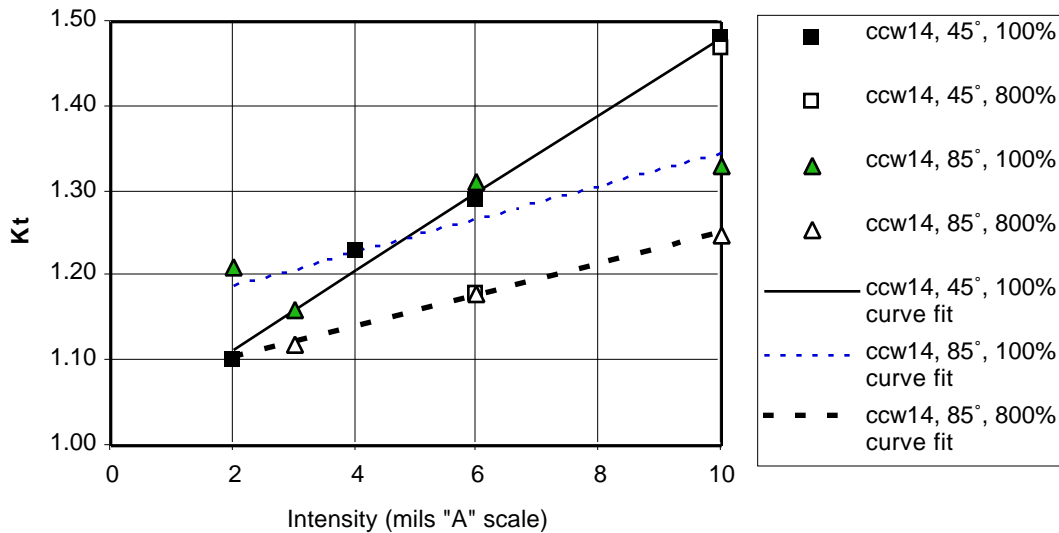
	Shot	Intensity	Angle	Coverage	Curve Fit Coefficients			
					A	B	C	
1	ccw14	6A	45°	100%	263.70	242.63	464.67	-2.68
2				800%	319.04	298.78	525.31	-2.82
3			85°	100%	330.05	305.97	557.04	-2.77
4				800%	357.67	310.67	432.77	-2.72
5	ccw14	10A	45°	100%	217.45	219.25	371.74	-2.82
6				800%	182.85	390.32	269.81	-3.02
7			85°	100%	190.18	289.51	332.52	-2.77
8				800%	257.07	405.51	320.37	-2.90
9	ccw31	6A	45°	100%	120.45	152.94	297.28	-2.19
10				800%	219.86	280.55	400.96	-2.80
11			85°	100%	293.78	311.82	371.41	-2.72
12				800%	236.15	340.52	346.03	-2.77
13	ccw31	10A	45°	100%	217.45	219.25	371.74	-2.82
14				800%	259.02	407.84	335.36	-2.97
15			85°	100%	148.57	205.14	296.20	-2.52
16				800%	188.39	299.24	306.63	-2.80

4.2.3 Topography

Surface roughness data was used to generate a K_t gradient for each condition, using equations 2.20 and 2.22. Figure 4.9 shows how K_t varied as a function of peening condition. From Figure 4.9 (a), it can be seen that ccw31 shot results in a lower K_t at the same intensity. From Figure 4.9 (b), the effects of higher coverage and higher incidence angles on reducing K_t can be observed more easily.



a) ccw14 and ccw31 data



b) ccw14 data only

Figure 4.9 – K_t as a Function of Intensity, Shot Size

4.2.4 Velocity Data

Velocity measurements for a subset of production peening conditions were obtained after the fracture mechanics model had been developed and correlated. Figure 4.14 illustrates the difference in velocity behavior as a function of intensity between shot sizes. This is consistent with behavior identified at the Sixth International Conference on Shot Peening during a general discussion among participants. In particular, Le Guernic [69] observed a linear relationship between intensity and shot velocity, while Thompson obtained a parabolic relationship in his previous work [65] with large shot - 1 mm diameter ball bearings – at low velocities. At shot sizes and velocities corresponding to Hertzian behavior, a parabolic relationship between velocity and intensity is observed. At shot sizes and velocities corresponding to impact dynamics behavior, a linear relationship between intensity and velocity is observed. This provides another indicator of a change in plastic deformation behavior between “good” and “low” life conditions.

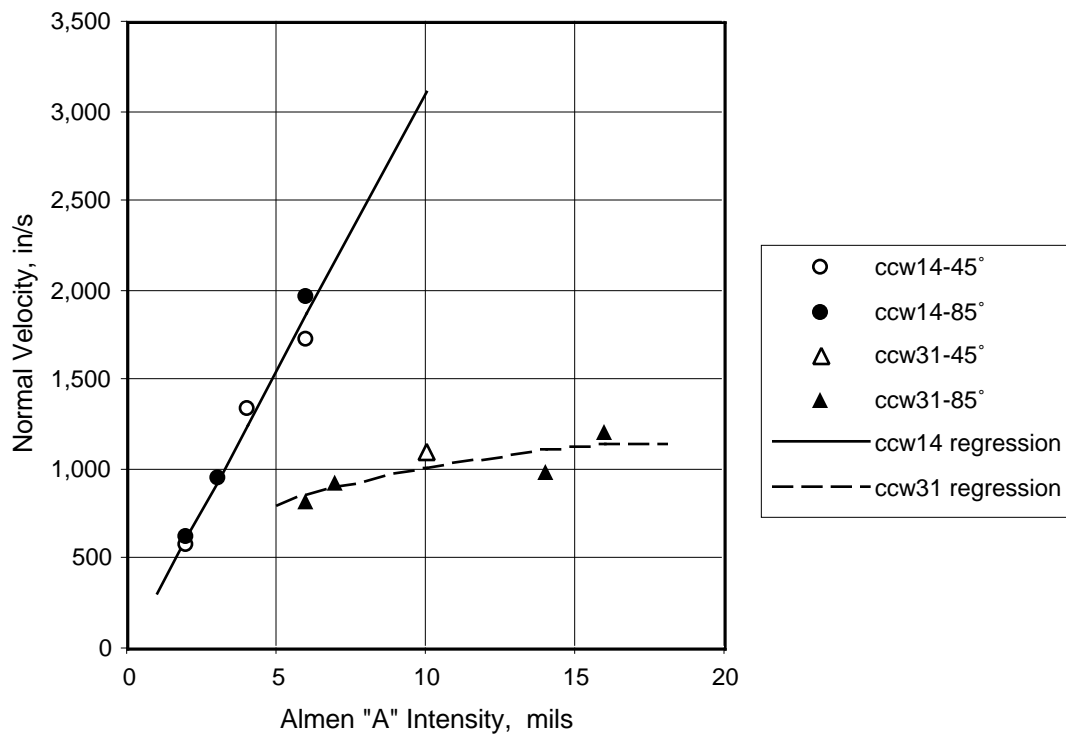


Figure 4.10 – Velocity as a Function of Intensity for Production Shot

4.3 Highlights of Shot Peen DOE Analysis

A total of four factors were evaluated at two levels each as shown in Table 4.3, for a total of 16 different peening conditions. Tests at each condition were replicated, for a total of 32 tests. Standard smooth round bar specimens, 0.4 inches in diameter were used. The tests were run at 1000°F, at a stress level chosen to yield an average life of 100,000 cycles for low-stress ground and polished (LSG+P) specimens.

Table 4.3 – Summary of Factors Evaluated by Shot Peen Design of Experiment

	Factor	Low Level	High Level
1	Shot	CCW14	CCW31
2	Intensity	6A	10A
3	Incidence Angle	45°	85°
4	% Coverage	100%	800%

A detailed summary of analysis of variance conducted on the DOE results can be found in Appendix A, along with details of the Weibull analysis performed. This analysis identified shot size, intensity, coverage and incidence angle as having significant impact on life behavior. It also identified significant interactions between shot size and the other three main effects (intensity, coverage and incidence angle). These interactions are illustrated in the interaction plots of Figure 4.11, a-c. A normalized life parameter, “stdev,” is used to represent a test life result in terms of the number of standard deviations from average low cycle fatigue capability for that condition (see section 4.4). Interaction plots follow for initial crack size, as obtained from microstructural data, and K_t , as obtained from surface roughness data. Each point on the plot represents an average of four conditions. For example, the ccw14-6A point represents the average life behavior from 1) ccw14/6A/45/100%, 2) ccw14/6A/45/800%, 3) ccw14/6A/85/100%, 4) ccw14/6A/85/800%. This acts to highlight significant trends, and filter out noise.

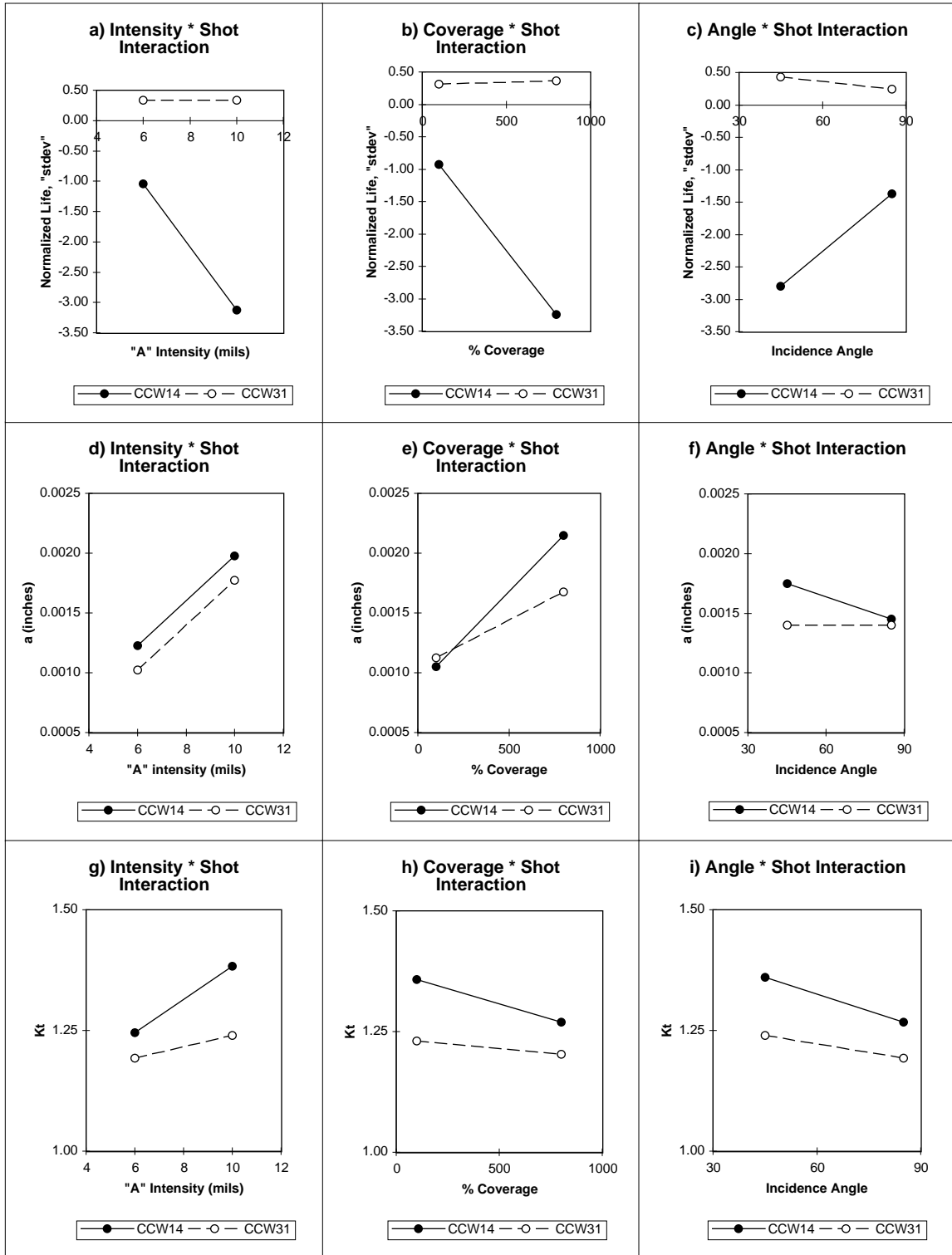


Figure 4.11 – Summary of Interaction Plots for "stdev", "a", and "K_t"

Shot interactions with intensity, % coverage and incidence angle for normalized life (stdev), initial flaw radius (a), and stress concentration factor (K_t). Shot sizes: ccw14 = 0.014 inches diameter; ccw31 = 0.031 inches diameter, approximately.

4.4 Fracture Mechanics Correlations

Table 4.4 provides a summary of selected results for life correlations with the sixteen DOE conditions in standard order. Also included are four test results at a light peening condition (12N or approximately 4A intensity for ccw14 shot), and 3 unpeened test results, to provide a benchmark for the test conditions and material source. The light peening data provides a comparison of ccw14 peened behavior at velocities comparable to those used for ccw31. Table 4.4 includes information about shot peening conditions, life behavior, stress concentration factor and initial crack size measured from microstructural data. Life information is provided in a number of ways to facilitate comparisons with low cycle fatigue behavior as well as fracture mechanics-dominated behavior, including the parameters “stdev”, “ N_{FM}/N_{obs} ”, and “ N_{LCF}/N_{obs} ”, where N_{obs} is the observed life, N_{FM} is the fracture mechanics prediction, N_{avg} or N_{LCF} is the average low cycle fatigue life, and N_{-3} is the minimum “-3” low cycle fatigue life for LSG+P tests.

The normalized life parameter, “stdev,” is used to represent a test life result in terms of the number of standard deviations from average low cycle fatigue capability for that condition, and is defined as:

$$stdev = \frac{\left[\log(N_{obs}) - \log(N_{avg}) \right]}{\left[\log(N_{avg}) - \log(N_{-3}) \right] / 3} \quad (4.3)$$

Here, N_{obs} represents the observed life at failure. N_{avg} represents the average LCF life for the stress and temperature condition for LSG+P data, and N_{-3} represents the minimum life. As a result, $|stdev| > 3$ indicates test results which are very uncharacteristic of the average population of LSG+P test results. Approximately 68% of data points should be within $|stdev| < 1$, while 95% should be within $|stdev| < 2$, and 99.7% should fall within $|stdev| < 3$.

Table 4.4 – Summary of Results

cond. #	Shot	Intensity	Incidence Angle	Coverage	Average stdev	K_i	a (inches)	Initiation Site	ACTUAL LIFE, N_{obs}	Predicted Life, N_{pred}	FM prediction, N_{FM}	LCF prediction, N_{LCF}	$\frac{N_{pred}}{N_{obs}}$	$\frac{N_{FM}}{N_{obs}}$	$\frac{N_{LCF}}{N_{obs}}$	stdev
1	ccw14	6A	45	100%	0.06	1.29	0.0009	I	156,558	102,855	1,000,000	102,855	0.66	K<Kth	0.66	0.10
				800%	-3.62	1.18	0.0021	S	23,598	19,810	19,810	92,607	0.73	K<Kth	0.73	0.03
2	ccw14	6A	45	100%	0.06	1.29	0.0009	I	156,558	102,855	1,000,000	102,855	0.66	K<Kth	0.66	0.10
				800%	-3.62	1.18	0.0021	S	23,598	19,810	19,810	92,607	0.73	K<Kth	0.73	0.03
3	ccw14	6A	85	100%	0.55	1.31	0.0005	I	163,647	95,248	1,000,000	95,248	0.58	K<Kth	0.58	0.55
				800%	-1.16	1.18	0.0014	S	29,523	21,877	21,877	97,072	0.74	K<Kth	0.74	-3.42
4	ccw14	6A	85	100%	0.55	1.31	0.0005	I	163,647	95,248	1,000,000	95,248	0.58	K<Kth	0.58	0.55
				800%	-1.16	1.18	0.0014	S	29,523	21,877	21,877	97,072	0.74	K<Kth	0.74	-3.42
5	ccw14	10A	45	100%	-3.44	1.48	0.0014	I	134,393	88,607	88,607	92,607	0.66	0.66	0.69	0.16
				800%	-4.19	1.47	0.0026	S	39,504	45,486	45,486	85,167	1.15	1.15	2.16	-2.47
6	ccw14	10A	45	100%	-3.44	1.48	0.0014	I	134,393	88,607	88,607	92,607	0.66	0.66	0.69	0.16
				800%	-4.19	1.47	0.0026	S	39,504	45,486	45,486	85,167	1.15	1.15	2.16	-2.47
7	ccw14	10A	85	100%	-0.89	1.33	0.0014	I	138,633	83,426	83,426	90,048	0.60	0.60	0.65	0.29
				800%	-4.00	1.25	0.0025	S	49,529	72,501	72,501	90,048	1.46	1.46	1.82	-2.07
8	ccw14	10A	85	100%	-0.89	1.33	0.0014	I	138,633	83,426	83,426	90,048	0.60	0.60	0.65	0.29
				800%	-4.00	1.25	0.0025	S	21,621	22,784	22,784	97,800	1.05	1.05	4.52	-4.17
9	ccw31	6A	45	100%	0.32	1.25	0.0012	I	137,555	89,573	95,976	89,573	0.65	0.70	0.65	0.29
				800%	0.61	1.23	0.0013	S	141,969	89,371	71,039	89,371	0.63	0.50	0.63	0.36
10	ccw31	6A	45	100%	0.32	1.25	0.0012	I	137,555	89,573	95,976	89,573	0.65	0.70	0.65	0.29
				800%	0.61	1.23	0.0013	S	141,969	89,371	71,039	89,371	0.63	0.50	0.63	0.36
11	ccw31	6A	85	100%	0.14	1.17	0.0005	I	143,627	101,921	1,000,000	101,921	0.71	K<Kth	0.71	-0.05
				800%	0.28	1.12	0.0011	S	139,635	89,371	1,000,000	89,371	0.64	K<Kth	0.64	0.32
12	ccw31	6A	85	100%	0.14	1.17	0.0005	I	143,627	101,921	1,000,000	101,921	0.71	K<Kth	0.71	-0.05
				800%	0.28	1.12	0.0011	S	139,635	89,371	1,000,000	89,371	0.64	K<Kth	0.64	0.32
13	ccw31	10A	45	100%	0.44	1.25	0.0010	I	142,725	86,978	900,000	86,978	0.61	stall	0.61	0.43
				800%	0.36	1.23	0.0021	S	151,554	92,607	900,000	92,607	0.61	stall	0.61	0.44
14	ccw31	10A	45	100%	0.44	1.25	0.0010	I	142,725	86,978	900,000	86,978	0.61	stall	0.61	0.43
				800%	0.36	1.23	0.0021	S	151,554	92,607	900,000	92,607	0.61	stall	0.61	0.44
15	ccw31	10A	85	100%	0.36	1.25	0.0018	I	143,340	90,048	25,334	90,048	0.63	0.17	0.63	0.37
				800%	0.20	1.23	0.0022	S	161,649	99,248	28,226	99,248	0.61	0.18	0.61	0.35
16	ccw31	10A	85	100%	0.36	1.25	0.0018	I	143,340	90,048	25,334	90,048	0.63	0.17	0.63	0.37
				800%	0.20	1.23	0.0022	S	161,649	99,248	28,226	99,248	0.61	0.18	0.61	0.35
17	CW14	12N	45	100%		1.2		I	214,209	99,577		99,577	0.46		0.46	1.39
				400%				S	243,843	98,535		98,535	0.40		0.40	1.63
18	CW14	12N	45	100%		1.15		I	193,937	93,810		93,810	0.48		0.48	1.28
				800%				S	188,658	93,810		93,810	0.50		0.50	1.23
19	UNPN	0	0A	0	0%			S	69,436	96,782		96,782	1.39		1.39	-0.59
	UNPN	0	0A	0	0%			S	48,048	98,890		98,890	2.06		2.06	-1.30
	UNPN	0	0A	0	0%			S	82,656	86,978		86,978	1.05		1.05	-0.09

I = Internal Initiations

S = Surface Initiations

Table 4.4 – Summary of Results, continued

cond. #	Shot	Intensity	Incidence Angle	Coverage	min a for correlation	max a for correlation	min	max	a, min measured	a, max measured	Velocity in/s	stdev of Velocity, in/s	Vn, in/s	Velocity, m/s	Vn, m/s	P	P/ y	P*
1	ccw14	6A	45	100%	0	0.0013	0.0009	0.0004	0.0009	0.0019	2444.8	205.9	1729	62.1	43.9	2.0E+5	1.3	1.7
2	ccw14	6A	45	800%	0.0015	0.0042	0.0006	0.0021	0.0021	0.0025	2444.8	205.9	1729	62.1	43.9	2.0E+5	1.3	1.5
3	ccw14	6A	85	100%	0	0.0015	0.0005	0.0010	0.0005	0.0013	1979.1	197.6	1972	50.3	50.1	1.6E+5	1.0	1.4
4	ccw14	6A	85	800%	0	0.0014	0.0014	0.0000	0.0014	0.0021	1979.1	197.6	1972	50.3	50.1	1.6E+5	1.0	1.2
5	ccw14	10A	45	100%	0.0012	0.0030	0.0002	0.0016	0.0014	0.0023								
6	ccw14	10A	45	800%	0.0016	0.0042	0.0010	0.0016	0.0026	0.0033								
7	ccw14	10A	85	100%	0	0.0019	0.0014	0.0005	0.0014	0.0022								
8	ccw14	10A	85	800%	0.0019	0.0042	0.0006	0.0017	0.0025	0.0033								
9	ccw31	6A	45	100%	0	0.0012	0.0012	0.0000	0.0012	0.0019								
10	ccw31	6A	45	800%	0	0.0013	0.0013	0.0000	0.0013	0.0020								
11	ccw31	6A	85	100%	0	0.0015	0.0005	0.0010	0.0005	0.0011	821.6	481.5	818	20.9	20.8	6.7E+4	0.4	0.5
12	ccw31	6A	85	800%	0	0.0016	0.0011	0.0005	0.0011	0.0017	821.6	481.5	818	20.9	20.8	6.7E+4	0.4	0.5
13	ccw31	10A	45	100%	0	0.0011	0.0010	0.0001	0.0010	0.0021	1548.4	3.2	1095	39.3	27.8	1.3E+5	0.8	1.0
14	ccw31	10A	45	800%	0	0.0014	0.0021	-0.0007	0.0021	0.0035	1548.4	3.2	1095	39.3	27.8	1.3E+5	0.8	1.0
15	ccw31	10A	85	100%	0	0.0013	0.0018	-0.0005	0.0018	0.0035								
16	ccw31	10A	85	800%	0	0.0013	0.0022	-0.0009	0.0022	0.0033								
17	CW14	12N	45	400%							1885.3	143.0	1333	47.9	33.9	1.5E+5	1.0	1.2
18	CW14	12N	45	800%							1885.3	143.0	1333	47.9	33.9	1.5E+5	1.0	1.1
19	UNPN	0	0A	0														

I = Internal Initiations

S = Surface Initiations

A second normalized LCF life parameter, N_{LCF} / N_{obs} , provides a different parameter to benchmark life behavior. Values falling within $0.5 \leq N_{LCF} / N_{obs} \leq 2$ would indicate behavior which is fairly characteristic of the normal LCF behavior. Typically scatter in LCF data is fairly large, and would not necessarily fall within a 2X factor of predicted life capability, which is one reason minimum life curves are typically used to define LCF life capability.

Similarly, a normalized fracture mechanics (FM) life parameter, N_{FM} / N_{obs} , provides a parameter to benchmark fracture mechanics life behavior. Values falling within $0.5 \leq N_{FM} / N_{obs} \leq 2$ would indicate behavior which is fairly characteristic of the normal FM behavior. Typically scatter in FM data is much tighter than in LCF data, and correlation within a factor of 2X is considered good correlation.

Figures 4.12 - 4.14 provide different reference frames for characterizing the observed life behavior, compared with the predicted behavior using fracture mechanics and low cycle fatigue benchmarks. Test results were grouped into four categories according to life behavior for plotting and comparison purposes, as indicated in Table 4.5. A consistent set of symbols was used for all plots.

Table 4.5 – Grouping of CCW14 DOE Conditions by Life Behavior

Group	“stdev” Range	Peening Condition
A - CCW14 “Low” life results	-4.23 < stdev < -3.0	2) ccw14/6A/45°/800% 5) ccw14/10A/45°/100% 6) ccw14/10A/45°/800% 8) ccw14/10A/85°/800%
B - CCW14 “Transition” cases	-3 < stdev < -2 surface 0.16 < stdev < 0.29 internal	4) ccw14/6A/85°/800% 7) ccw14/10A/85°/100%
C - CCW14 “Good” life results	0.03 < stdev < 0.55	1) ccw14/6A/45°/100% 3) ccw14/6A/85°/100%
CCW31	0.14 < stdev < 0.61	all ccw31 peening conditions

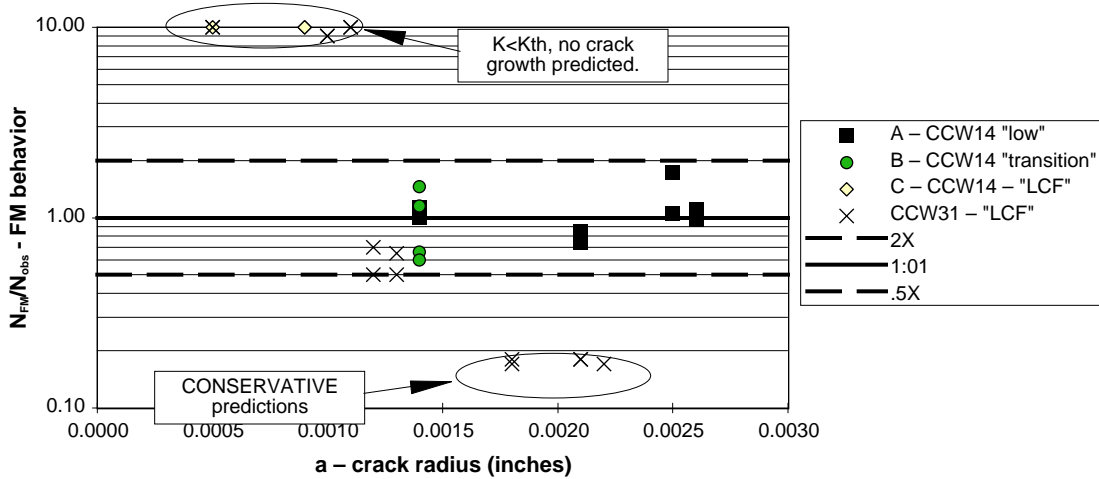
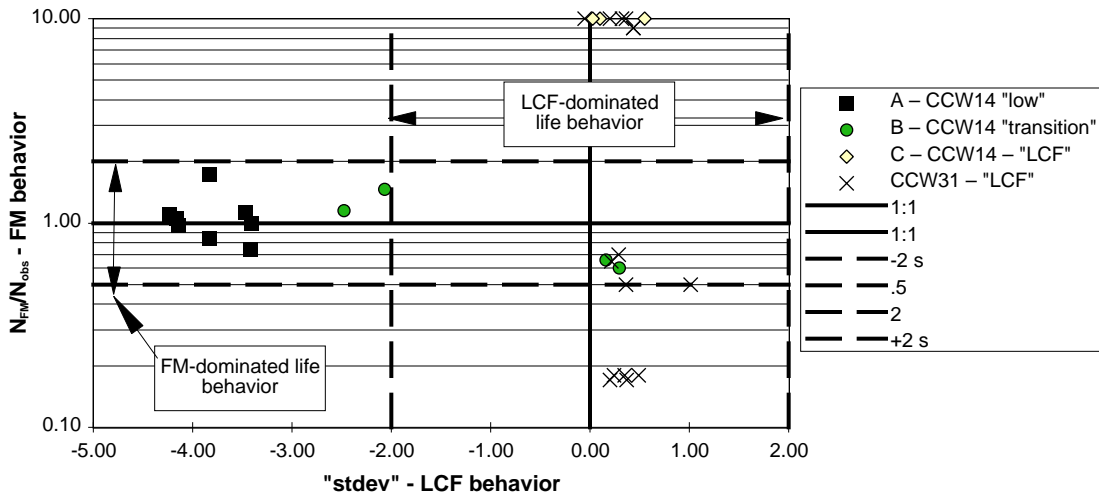
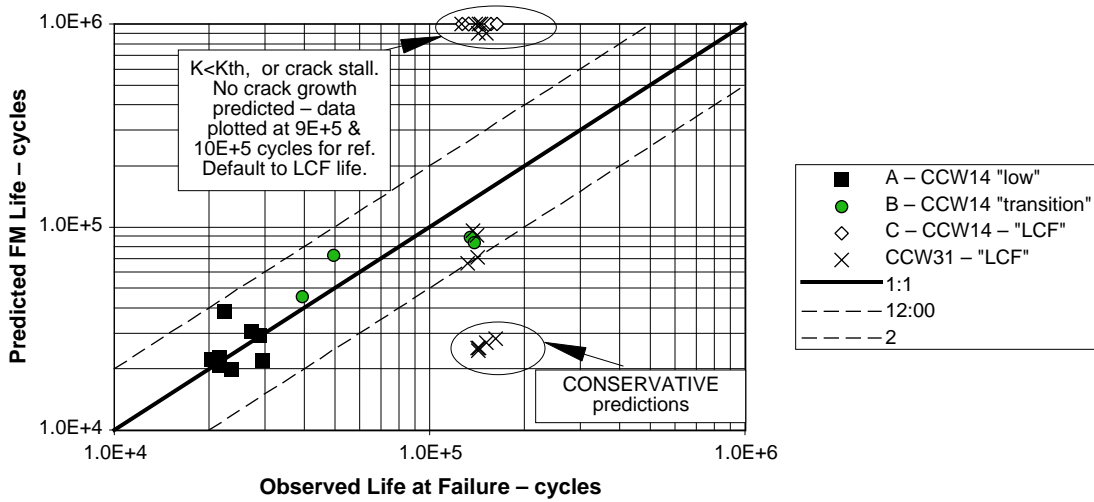


Figure 4.12 shows predicted FM life versus observed life, with 2X scatterbands for reference. There are two populations which do not fit within the 2X scatterbands and are not well predicted by the FM calculations: 1) the top cluster, for which crack arrest or no crack growth was predicted by the model, and 2) the lower cluster, which is a conservative prediction. The top cluster included ccw14 group “C” - good life conditions and ccw31 data. All had internal initiation sites, and life capability characteristic of average LCF data. In this case, the initial crack size was below that required for crack growth, and an LCF life estimate would be used to characterize the life capability of these specimens. The lower cluster consisted of ccw31 data with internal initiation sites.

Figure 4.13 shows the data ranked and mapped in terms of “LCF” behavior and “FM” behavior regimes. Scatterbands of ± 2 are provided on the “stdev” or LCF axis, and should characterize 95% of data points representative of this population, while 2X scatterbands are provided on the “ N_{FM} / N_{obs} ” or FM axis. Points which do not fall within the FM scatterbands do fall within the LCF scatterbands. Note that all ccw31 specimens had life behavior that was characteristic of LCF, but some also fell within the FM regime as well - that is, the two regimes overlapped.

Figure 4.14 shows normalized FM life (N_{FM} / N_{obs}) plotted against initial crack size. Here it can be seen that conditions for which no crack growth was predicted corresponded to small initial crack sizes.

Specimens having low life behavior correlated with FM behavior in all cases. This means that the microstructural feature measured has crack-like behavior from essentially the first load cycle. That is, shot peen-induced plasticity, similar to cyclic plasticity, causes fatigue damage and is capable of generating crack-like features for further strain localization and crack growth. It also appears that there are some cases for which shot peening has not accomplished sufficient strain localization to complete the crack nucleation event. Note that onset of FM behavior is dependent on operating loads and

temperatures, so the threshold crack size for which crack growth is predicted will vary with operating conditions.

The method established so far is able to provide lower-bound life estimates for the range of conditions evaluated. This provides a conservative life estimate, which is useful. To improve robustness of design and production processes, it would also be helpful to gain understanding of the factors responsible for the conservatism of the ccw31 peening behavior. A threshold behavior map was developed to address this.

4.5 Threshold Behavior Map

An initial assessment of peening conditions indicated that intensity, incidence angle and coverage alone could not explain the difference in observed life behavior between ccw14 and ccw31 shot. From the literature, it appeared that shot velocity and strain rate at impact were likely candidates for the difference in observed material data. This was the motivation for the single particle impact tests. In order to improve the understanding of driving forces, the single particle impact test data and production peening velocity data were analyzed, and the driving forces behind the FM model elements were identified.

4.5.1 Driving forces behind FM model elements

Microstructural slip depth. From Figure 4.11, it can be seen that the microstructural slip depth defined appears to be largely driven by intensity and coverage, with limited contributions due to shot size and incidence angle. The depth of slip does not characterize the degree of strain localization. However, attempts at using plastic strain estimates from x-ray diffraction or TEM selected area diffraction pattern arc lengths did not provide a useful degree of differentiation between peening conditions. Slip depth appears to be a necessary but not sufficient criteria for crack development.

Residual stresses. The residual stress profile is largely characterized by the yield strength of the material and the shot peening intensity. The depth of the compressive stress layer is nearly a linear function of intensity. Figure 4.15 illustrates this. Note that a small compressive stress layer is present in LSG+P (unpeened) specimens.

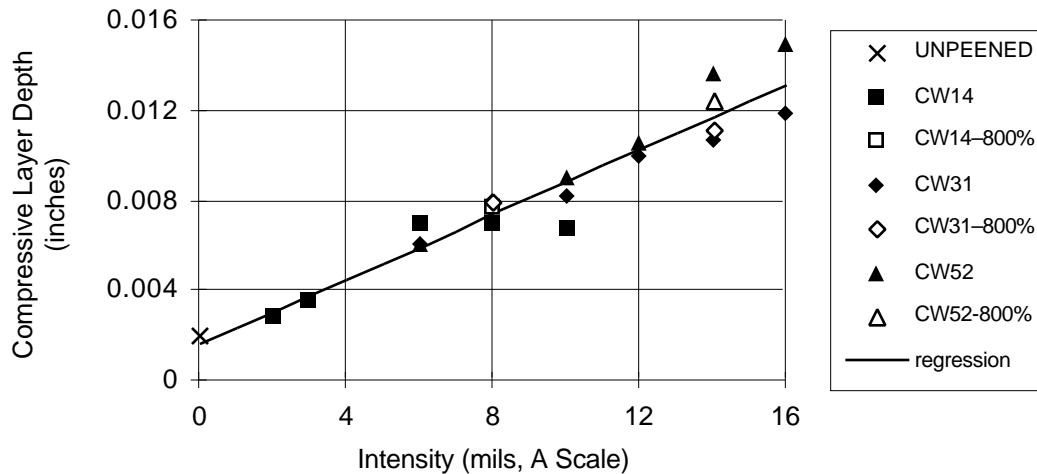


Figure 4.15 – Compressive Stress Layer Depth as a Function of Peening Intensity

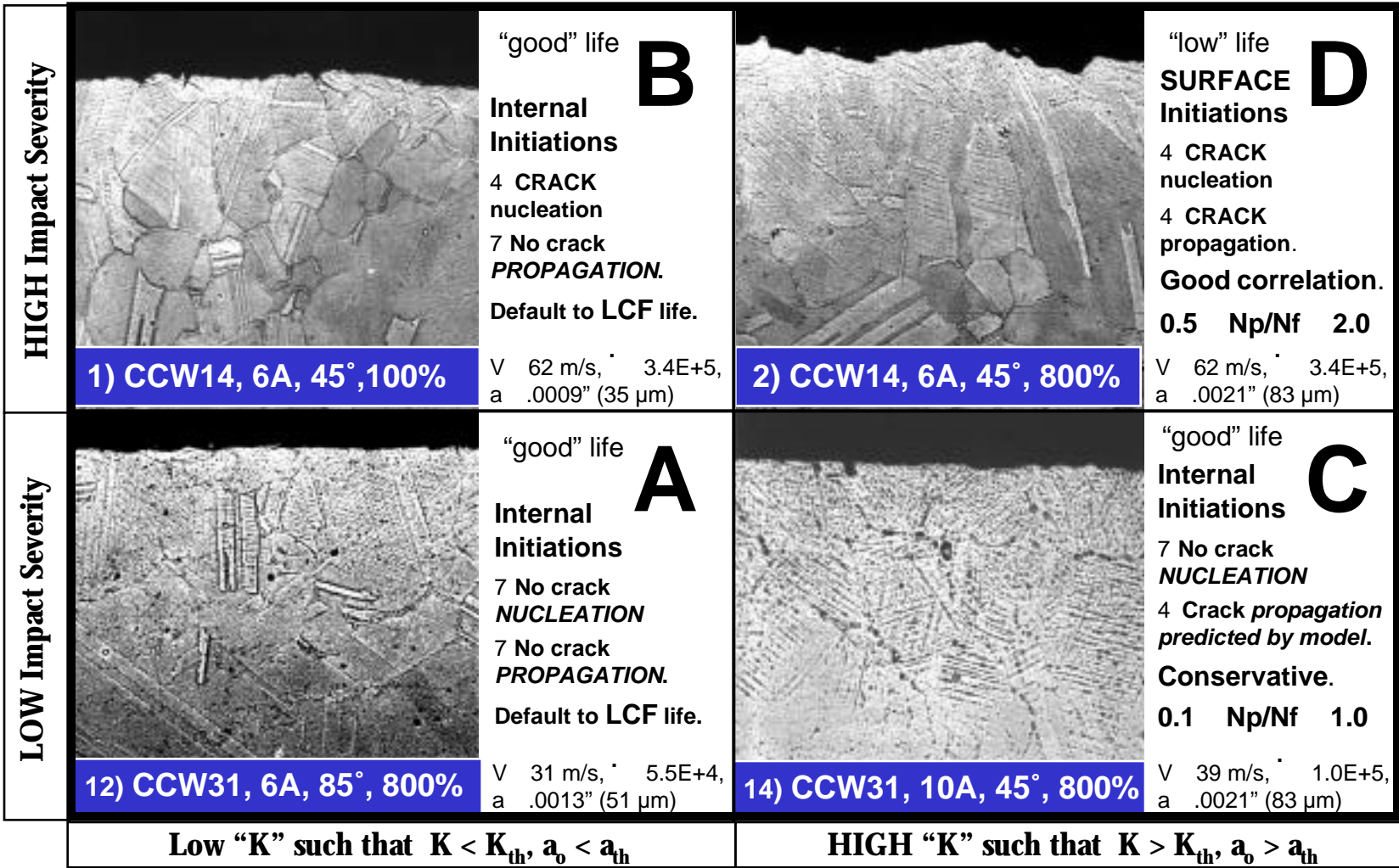
Surface Roughness. From Figure 4.11, it can be seen stress concentration factor due to surface roughness does show dependence on shot size. Of the three FM model elements used to characterize peening condition (initial crack size, residual stress profile, K_t gradient), this is the one which provides greatest differentiation between shot sizes. However, the effect of the stress concentration factor did not have a major impact on life at the stress levels evaluated. So, although surface roughness does not appear to provide the correlation sought, it might be the only quantifiable factor which is defined from the workpiece material alone (as opposed to shot peen process parameters) which could serve to identify “gentle” and “severe” impact conditions.

Velocity. From the single particle impact test data, deviation from Hertzian behavior was observed to occur at velocities of 2,280 in/s and higher. Hertzian behavior was observed for velocities of 1,340 in/s and lower. Precision sections through selected dimples showed increasing amounts of slip band development with increasing velocities

above this threshold velocity. Velocity appears to drive plastic deformation response. A review of production peening velocities obtained (in Table 4.4, second page) indicates that transitional life behavior was observed for velocities around 2000 in/s, and “low” life behavior was observed for velocities of 2,400 in/s when coupled with sufficient slip depth to exceed the threshold stress intensity value. Velocities corresponding to “low” life behavior appear to correspond to velocities at which deviation from Hertzian behavior is observed. This suggests that velocity could be used as an indicator of strain localization needed to induce adequate “cyclic” plasticity, adiabatic shear band or persistent slip band formation for crack-like behavior.

Figure 4.16 shows a “threshold behavior map” illustrating sample microstructures corresponding to “good” and “low” life conditions. The microstructures are sorted according to life behavior, slip depth and shot velocity. The horizontal axis divides the population into those with slip depths resulting in stress intensity factors below the threshold value at the stress condition used. Microstructures A and B had good life behavior and low slip depths. However slip depth alone does not appear to be a sufficient criterion for crack-like behavior. A strain-rate or velocity parameter appears to be involved, perhaps through the normalized impact stress given in equation 4.2. The vertical axis divides the samples into “high impact severity” conditions and “low impact severity” conditions. Microstructures B and D fall into the severe impact category. Microstructure B results in “good” life capability because the initial crack size a is less than the threshold value required for propagation. Microstructure D has “low” life capability, with severe impact condition and initial crack size greater than threshold value. Microstructure C had “good” life capability. Fracture mechanics calculations predict “low” life capability. It appears that additional strain localization is needed to complete macro crack development for case C. Use of a fracture mechanics model provides a conservative estimate of life capability for case C.

Crack NUCLEATION Threshold



Crack PROPAGATION Threshold

Figure 4.16 – Threshold Behavior Map

4.6 Fracture Mechanics / Threshold Behavior (FM/TB) Model

If a velocity threshold criteria is used to determine when to apply the fracture mechanics model, some conservatism can be removed. Referring to Figure 4.16, an LCF life estimate would be used for cases A and B, since fracture mechanics predicts no crack growth. For case C, a velocity threshold could be used to determine that an LCF life estimate should also be used here. Fracture mechanics predictions would be used only for case D conditions. Figure 4.17 shows the correlation obtained when incorporating LCF predictions for cases A-C.

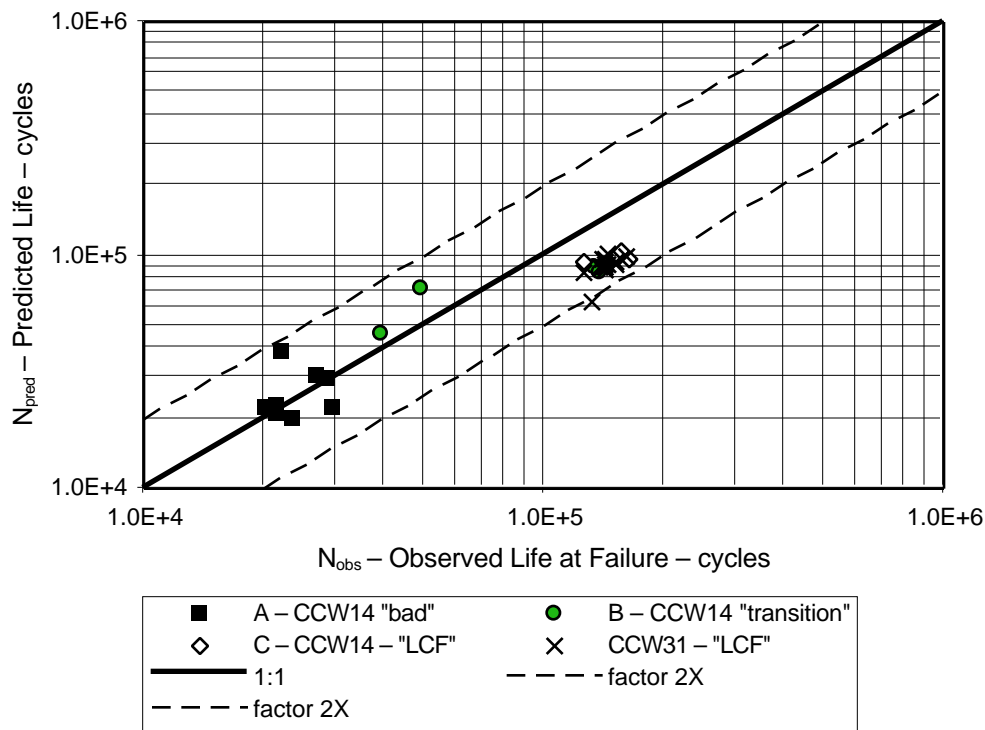


Figure 4.17 – Predicted Life (FM/TB model) vs. Observed Life

4.7 Initial Crack Size Determination

The fundamental contribution made by this effort is the definition of an initial crack size which allows the damage state to be characterized from microstructural data.

Two rationales were developed for determining an initial crack size from microstructures of peened specimens and evaluated using fracture mechanics correlations with the DOE shot peen life results: 1) a minimum slip depth, and 2) a maximum uninterrupted slip band depth. An average of three measurements were taken for both parameters, to account for variability of peening conditions and interaction of microstructural slip orientation relative to impact direction. Figure 4.8 illustrates the rationale used to identify the most favorable sites for crack development and growth.

Support for average minimum slip depth measurement. Experience shows that surface cracks initiation favors the most highly locally stressed location. For uniaxial round bar specimens loaded in tension, this would correspond to the maximum K_t site. Roughness and microstructural data show that slip depth increases with coverage, but K_t decreases. This suggests that the highest K_t location will correspond to a relative minimum slip depth. Orientation of underlying grain structure relative to both the impact vector and tensile axis will also affect the selection. As a result, an average was taken from three measurements of minimum slip depth. It should be noted that zero slip depth observations cannot be counted, since this likely corresponds to missed coverage (no dimple). This site would have a K_t of 1, and would not favor crack development. The average minimum slip depth method permitted correlation with test results.

Maximum uninterrupted slip band depth. The theory behind this hypothesis reflects the fact that grain boundaries form barriers to dislocation movement and crack formation. Microstructural results from tested model disks show cracks initiating along slip bands within a single grain. However, this method does not account for the difference in properties between the strong plastically deformed surface layer and the more ductile

substrate. Predictions made using this approach were **non-conservative** for case D – “low” life conditions. However, it raises the issue of grain size. Fracture mechanics calculations predict a minimum crack size of approximately 0.0011 inches (28 μm) is needed for crack growth to occur at the stress and temperature conditions evaluated. This is less than the average grain size of 0.00126 inches (32 μm). This suggests that an additional criteria for crack growth is that the threshold crack size be smaller than the grain size. Once a “macro” crack (i.e., crack radius $a > a_{\text{th}}$) has been developed, grain boundaries are not as effective in disrupting crack growth. Figure 4.18 provides a schematic. Miller [70] and Hertzberg [31] both discuss crack growth behavior regimes in terms of crack size relative to grain diameter and threshold crack size. In these cases, a_{th} is typically much greater than d_g . For the stress levels encountered here, these dimensions sometimes overlap.

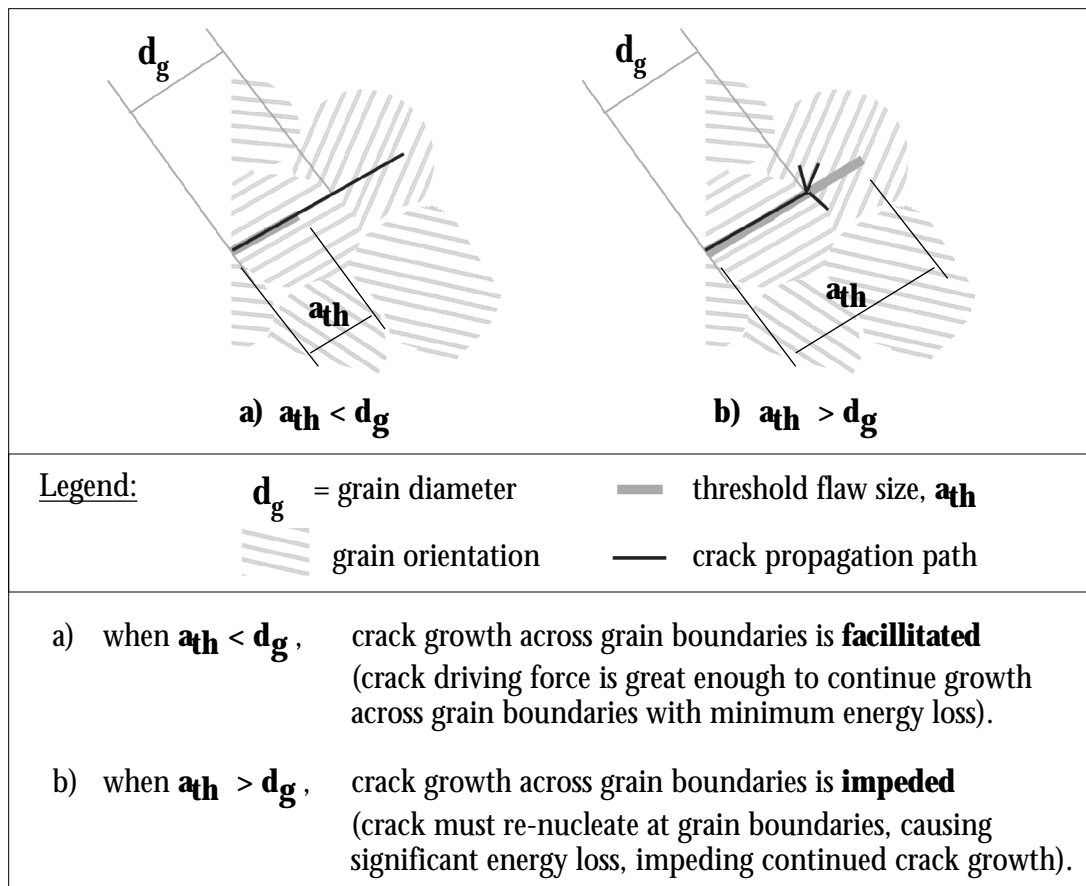


Figure 4.18 – Schematic of Crack Threshold (a_{th}) and Grain Diameter (d_g) Interaction Effect on Crack Growth

4.8 Effects of Topography

A K_t gradient was calculated from surface roughness data to account for the effects of surface roughness. The data obtained provided valuable insight which helped identify the significant slip depth characteristics. However, at the stress levels evaluated, incorporation of the K_t gradient did not significantly improve the correlation. This may be fortunate, since wide variations in surface roughness measurements can be obtained depending on system used, and complex surface features are difficult to measure [71]. Three potential explanations for the limited effect of K_t gradient observed are:

- 1) the depth of the gradient is very shallow, typically shallower than the crack depth defined, so the effect is extremely localized.
- 2) the yield strength has already been exceeded in tension from the applied load, inducing plasticity and additional strain localization; as a result, additional stresses applied above the yield strength would either be redistributed via plastic deformation, or undergo relaxation due to micro-cracking and void formation [72]:

“Stress Relaxation. As microscopic damage grows, stress-free surface is generated in the material, thus diminishing the amount of stress caused by overall deformation. This stress relaxation occurs by two basically different processes. First, under tension the existing cracks or voids open to accommodate some of the imposed volumetric strain. The volumetric strain of the matrix material can therefore relax elastically, and the associated mean-tensile stress also relaxes. Second, as discussed by Carroll and Holt (1972), the decrease of load-bearing area introduces a correlation factor

$$\bar{\sigma} = \sigma^s (1 - \phi) \quad (7)$$

where $\bar{\sigma}^s$ is the stress tensor in the matrix material, $\bar{\sigma}$ is the continuum-stress tensor (the average stress obtained by dividing the force on the void-containing material by area) and ϕ is the relative void volume (shown by Carroll and Holt to be equal to the area fraction of randomly distributed and oriented voids.)

In our modeling work for microcracks and cracks under tension [Seaman et al. (1976)], we have found that the first stress-relaxation effect is dominant until the last stages of coalescence. However, for adiabatic shear bands, in which no continuum tensions are present, the second mechanism (7) is dominant.” [72]

- 3) The slip layer is already being modeled as a crack, which is a conservative approach. The effect of surface roughness is likely to be more significant at stress levels in the elastic range, where the presence of a K_t could induce local plasticity.

CHAPTER 5

DISCUSSION

5.1 Assumptions

Although effort was made to avoid a need for simplifying assumptions, there are model limitations which need to be addressed and put into perspective. The main assumptions invoked for the analysis conducted are:

- 1) Peening conditions used for the production peened coupons of this study are representative of those used in the initial Shot Peen Designed Experiment.
- 2) Slip bands are high potential crack initiation sites in René 88DT.
- 3) Surface cracks will initiate at the highest local stress concentration.
- 4) Of several comparable stress concentrations (peening dimples), the one favored for crack initiation will be the one for which the impact vector was most closely aligned with the slip vector of the underlying grain, and for which the slip planes are favorably oriented for shear to occur during specimen loading.
- 5) An average minimum slip layer depth best characterizes the fatigue damage resulting from shot peening, not the depth of uninterrupted slip bands (i.e. constrained to one grain).
- 6) Residual stresses remain in compression, even though relaxation occurs.

Each of these assumptions will be addressed in turn.

5.1.1 Peening conditions were adequately duplicated

Duplication of peening conditions. Microstructural analysis was not performed on coupons peened at the same time as the original DOE LCF specimens. There is a chance that the peening conditions reproduced differ from those on the test specimens. However, coupons were peened on the same machine, using reference conditions established by a reference saturation curve. Although hose wear and nozzle wear require small adjustments to be made to machine process parameters to achieve the desired intensity and saturation conditions, the Almen strip measurement provides an independent measure of the peening intensity. Although the intensity definition is not unique, and interpretation can vary from vendor to vendor, peening was conducted at the same source, and a consistent interpretation of the intensity definition was used for both sets of specimens. This characterizes both the intensity and saturation condition, thus coverage was also consistently interpreted within the metrics available. Although shot wear over time, changing size and shape, two screens are used to filter out broken or worn shot, and to ensure that oversize shot are excluded. Shot control was consistently used. To summarize, the following peening process parameters were consistently controlled for both coupons and specimens: 1) shot peen intensity, 2) shot media size and shape, 3) incidence angle, 4) coverage.

Effect of peening conditions on model parameters. It has been established that the compressive stress layer depth is controlled primarily by shot peen intensity; intensity was controlled. Correlations show that K_t is controlled by shot size, intensity, incidence angle and coverage. These factors were controlled. Observations of the average minimum slip depth indicate that this is largely driven by intensity and coverage; these factors were controlled. All critical peening process parameters linked to fracture mechanics model elements were consistently controlled.

Velocity was not controlled or measured for both coupons and specimens, but velocity appears to be linked to crack nucleation effects, and is not associated with the

fracture mechanics model elements. However, the data obtained do not provide a conclusive mechanism or criteria for complete characterization of crack nucleation. The aspect of a crack nucleation threshold is introduced to provide a framework for interpreting and applying fracture mechanics model results. This research does not provide a new lifing methodology for shot peened components: it provides a new tool which can be used to interpret and predict potential life capability due to a given set of peening conditions.

5.1.2 Slip bands are high potential crack initiation sites

Observations of small cracks which formed during testing of a shot peened model disk verified that cracks formed along a slip band, within a single grain. The cracks observed were not the critical crack.

5.1.3 Surface cracks will form at highest local stress concentration

It is known that failures often initiate at the most highly locally stressed tensile regions of a component. For a specimen uniformly loaded in tension, such as an LCF round bar specimen, the location of highest local stress will coincide with the highest local stress concentration feature.

5.1.4 Preferred grain orientation at crack initiation site

Observations of small cracks which formed during testing of a shot peened model disk verified that cracks formed along a slip band oriented at an acute angle to the surface and to the hoop stress direction (main tensile stress direction). Grain orientations at acute angles, such as 45° , maximize the shear stress concentration in the slip direction. Plastic deformation will be maximized on shear bands favorably oriented for shear, leading to the crack nucleation event. Once a crack of sufficient size is fully nucleated, additional crack growth is normally dominated by tensile loading (mode I growth).

5.1.5 Average minimum slip layer depth characterizes the fatigue damage

Failure will occur at the weakest link. The weakest link will be the one with the highest loading and lowest strength. On a single specimen, variation in local coverage will occur from spot to spot due to the somewhat random nature of the peening process. For a given intensity, the surface roughness data showed that the K_t decreased with increasing coverage. That is, additional coverage resulted in flattening of dimple peaks, reducing the local K_t . Observations of slip depth show that slip depth increases with increasing coverage. Cracks will initiate at the highest local K_t ; the highest local K_t will occur in a region of a relative minimum slip - thus a minimum slip depth will be characteristic of the weakest link. For comparable dimples, the one located at a grain favorably oriented for slip will be the preferred site for additional strain localization, thus a sampling of minimum slip locations is appropriate due to the variability of microstructural orientation. Therefore, an average of several minimum slip depth measurements provides the best estimate of the initial crack size used to characterize the fatigue damage.

The critical feature for René 88DT is not the maximum depth of continuous slip bands. Correlations using this approach were non-conservative. Instead, an average minimum slip depth appears to provide better characterization of the damage layer induced by conditioned cut wire shot. Work by Domas [73] indicates that significant loss of fracture ductility occurs in the peened layer. Thus, shot peening creates significant changes in the surface layer, significantly increasing the yield strength and lowering the true fracture strain. Mechanical properties of the surface layer are no longer characteristic of the substrate material. This appears to facilitate crack growth through the peened layer.

Grain size appears to be very relevant to the fatigue behavior of shot peened specimens. Materials such as René 88DT having relatively large grains show greater sensitivity to peening conditions than smaller grained materials. For the test conditions used, crack sizes of 0.0011 inches and lower resulted in initial stress intensities below the threshold value: thus no crack growth is predicted. Crack sizes of 0.0012 and larger

resulted in finite life predictions. The average grain size of René 88DT is approximately 0.00126 inches (32 μm), which is large enough to accommodate a fully nucleated growing crack. Once such a “macro” crack ($a > a_{th}$) is formed, it is fairly easy to continue crack growth across grain boundaries [31]. Of course, specific grain sizes vary. Surface grains as large as 0.0033 inches deep (84 μm) were observed. Thus it is possible for all of the observed slip depths measured to have occurred within a single grain, although large grains typically provided regions of maximum slip depth.

From the microstructural data observed, it appears more likely that the plastic deformation layer itself is a significant feature, having different behavior from the matrix material. The plastic deformation layer has a higher yield strength from the matrix, making it less ductile relative to the matrix. It also has a high number of potential crack initiation sites, facilitating crack nucleation and growth. A region of relative minimum slip depth with a high K_t adjacent to regions of relative maximum slip depth could act as a plastic hinge [74], further concentrating additional plastic deformation and contributing to the crack initiation and propagation event.

5.1.6 Residual Stresses Remain in Compression Throughout Testing

Residual stress measurements were made on specimens peened and tested at comparable conditions as part of an independent electro-polish study (looking at effects of material removal on life). Even though yielding occurred on the first cycle, in all cases, residual compression was retained at the surface.

5.2 Limitations

In addition to the assumptions used, there are limitations to this analysis which must be recognized. It is important that these results not be extrapolated and applied to conditions outside those covered by the data presented. Under some conditions, it is possible to place residual tensile stress on the surface, accelerating crack growth.

The main limitations of this research follow:

- 1) Material used, René 88DT is a face-centered-cubic Nickel-base superalloy which exhibits observable slip at the surface due to shot peening at magnifications of 500X.
- 2) Slip is observable in etched specimens which have not been thermally exposed or cycled. Thus, absence of observable slip in a specimen which has been heated after shot peening is not an indication that significant slip was not induced at these conditions.
- 3) Strain-controlled tests were conducted at comparatively high stress levels, exceeding the yield strength of the material, under uni-axial loading and at an initial strain R-ratio = 0. Thus, the specimens yielded in tension, and were forced into compression on the surface upon unloading. Elastic cycling after the initial cycle followed. The stabilized stresses have a negative R ratio (minimum stresses were compressive, maximum stresses tensile). Residual compression from the shot peening was retained on the surface, even at the end of the test.
- 4) Simple geometries were studied: flat coupons or smooth LCF round bar specimens.
- 5) Tests conducted at 1000°F (crack formation, threshold stress intensity factor and crack growth behavior characteristic of this temperature regime).
- 6) Conditioned cut wire shot used. This media is fairly uniform in size and shape, which deviates significantly from a smooth spherical ball; it also tends to wear uniformly rather than fracture. Resulting microstructures showed fairly consistent slip fields. Resulting life behavior at a given peening condition was very repeatable, except at “transition” conditions, when slip depth approached threshold crack size.

The method developed relies on observation of slip at magnifications of 500X. Alloys which do not exhibit observable slip, e.g., due to crystal structure or high volume gamma prime strengtheners would not be good candidates for direct application of this technique. An alternate method of characterizing the critical feature of the plastic deformation zone would be needed.

Simple geometries were studied - no corners or bolt holes. Intensity is defined on a flat surface, where shot impact can be distributed over an approximately circular area, distributing the impact force and reducing the impact stress. Impact on corners would result in reduced seating: the impact force would be concentrated along a line, increasing the impact stress. In reality, few corners approach perfectly sharp edges. Most have some degree of rounding due to manufacturing process. However, the sharpness of the edge could have a significant interaction with shot peening conditions and greatly affect life behavior.

Cast steel shot were not included in this study, because life data in the form of a designed experiment did not exist. Some data exist for s110H shot, which is comparable in size to ccw14 shot. Comparisons were made for life behavior, slip depth, velocity and surface roughness at the limited number of common peening conditions (6A, 45°, 100% coverage and 10A, 45°, 100% coverage). S110H is nominally screened to the same size as ccw14. However, it is significantly different than ccw14 shot: s110H cast shot has a smoother, more spherical shape than ccw14, however there is greater variability in shot size than for conditioned cut wire shot. Differences were observed in shot velocity vs. intensity relationship, variability of observed microstructures and surface roughness. Follow-on work is being conducted to extend use of the model to cast steel shot, but there are real differences in shape and size distribution which appear to affect life behavior. This highlights the potential role of additional factors, shape and size variability, on life behavior. Better surface finish correlates with improved life behavior [7].

5.3 Usefulness of the Fracture Mechanics Model

All assumptions and limitations aside, the model developed has many useful features.

- Method developed is useful for predicting life capability due to shot peening with conditioned cut wire shot for simple LCF specimens. It offers the potential to account for geometry effects through direct observation of microstructural slip depth.
- The model developed is general, and able to account for changes in material / workpiece including microstructure, residual stresses and topography. It is possible that this could be extended to the analysis of other cold work-inducing processes such as metal removal by drilling, milling, and turning, to name a few.
- The model provides the potential to link shot peening process capability directly to life capability as it provides a physical interpretation for the effects of factors observed from analysis of the shot peen DOE. Because of this, it could be used as a design tool to assist in optimizing peening conditions for specific component geometry, operating loads, and life objectives, in support of Design For Six Sigma (DFSS) goals.
- The model provides a direct method for estimating the impact of rework (removal of some amount of surface layer) on resulting life capability, by permitting direct interpretations for the effects of removing surface roughness and reducing the plastic deformation zone size. Effects of material removal on residual stresses would require verification, but could easily be incorporated into the analysis.
- By providing a physical model for the individual effects of shot peening, the information learned from future test programs can be maximized and focused on “blind spots” - areas where data do not exist. It should minimize the amount of test data required: validation is easier than characterization.

CHAPTER 6

CONCLUSIONS

A Fracture Mechanics / Threshold Behavior model was developed to explain and predict the LCF life behavior observed from shot peening conditions studied in a designed experiment on a Nickel base alloy, René 88DT tested at 1000°F, peened with conditioned cut wire shot. Good correlation was obtained. The following conclusions were made as a result of this investigation:

- The shot peening process causes cyclic plastic deformation to occur in the surface layer. Cyclic plastic deformation is the precursor of fatigue damage.
- The depth of the plastic deformation layer is related to a primary damage feature. Microstructural measurements of slip layer depth can be used to characterize an initial crack size. Specifically, averaging three measurements of different minimum slip depth observations was found to characterize an initial crack size for conditioned cut wire shot.
- Residual stresses act to counterbalance the effect of fatigue damage induced.
- Surface roughness contributes to the damage process by locally increasing stresses acting on the surface. For the stress ranges and initial crack sizes observed, accounting for these effects improved the correlation. However, correlation within a factor of two was still possible without accounting for these effects. The contribution of surface roughness is likely to be greater at lower stresses (in the elastic range), where the presence of a K_t could induce local plasticity.

- Use of the fracture mechanics model developed provides a conservative lower-bound estimate of the life capability of shot peened specimens over the range of test and peening conditions evaluated.
- A level of severity threshold must be exceeded to complete the crack nucleation event. No readily measurable microstructural feature was identified that could be used to quantify the completion of the crack nucleation event. The operating loads applied may also contribute to this event. At this point, shot velocity or normalized impact stress appear to offer the best characterization of this threshold.
- For conditions in which the crack propagation threshold is not exceeded, no crack growth is predicted and the standard method for calculating LCF life should be used.

The method developed does not explain all aspects of shot peening on life behavior. However, the method provides a new tool for analyzing shot peening impact on life behavior, particularly at the high end potentially damaging peening conditions.

CHAPTER 7

RECOMMENDATIONS

A Fracture Mechanics / Threshold Behavior model was developed for a Nickel-base superalloy, René 88DT from microstructural data and LCF test data at a strain R-ratio of 0, uni-axial tensile loading into the plastic regime, for a simple geometry. The model developed was successful in predicting the impact of shot peening on life capability for the conditions evaluated. “Data gaps” exist, particularly for R-ratios other than 0, complex geometries and other alloys. However, the model developed appears to identify physical phenomenon which are directly linked to life capability. As such, the model provides a useful tool that can be used to increase the understanding of shot peening impact on life behavior. As a fracture mechanics-based model, it offers quantitative capability for design decisions:

- Effect of rework by surface layer removals can be analyzed directly.
- Effects of stress and temperature can be accounted for directly in fracture mechanics calculations (assuming appropriate materials data are available and incorporated).
- Effects of material changes induced by shot peening can be represented by model elements.

Because of this capability, the method developed can be used to support Design For Six Sigma objectives, linking shot peening process capability directly to life capability.

Additional test data are required for validation to apply the model beyond the range of test conditions for which it was developed. This includes complex geometries,

materials other than René 88DT, fatigue ratios (R) other than 0, multi-axial loading, other types of shot.

Based on the information learned during this effort, the following recommendations are made for future shot peening-related studies:

- Request and retain saturation curve data for all peening conditions, including all relevant machine settings such as pressure, nozzle type, shot mass flow rate, nozzle feed rate.
- As a minimum, obtain microstructures, residual stress profiles and surface roughness measurements for all peening conditions used in a test program. This could be done by having spare specimens or flat coupons peened to the same conditions at the same time. These should be saved for future reference, additional microstructural / metallurgical evaluation, and validation of peening conditions achieved. A sample of production shot should be bagged, labeled and stored as well, to characterize shape and size distribution of media.
- Conduct additional testing to evaluate effects of different R-ratios on resulting life capability.
- Conduct additional testing to evaluate effects of different specimen geometries, including corner radius or the ratio of shot radius to corner radius on initial effective crack size and resulting life capability.
- Develop a database to store and retain relevant test data, so that maximum leverage of available data can be achieved.
- Obtain velocity data to serve as a potential process control for the shot peening process whenever possible.
- Develop a consistent interpretation of shot peen intensity, incorporating a curve fit technique and minimum of a four point saturation curve.

APPENDIX A

BAILEY SHOT PEEN DOE ANALYSIS

A.1 Overview – Bailey Shot Peen Design of Experiment

Several years ago, a shot peen DoE was conducted by Bailey [5] to evaluate the effect of shot peening on low cycle fatigue (LCF) life of René 88DT. Life capability at some of the peening conditions evaluated was found to be an order of magnitude lower than that of unpeened specimens tested at the same conditions, supporting the idea that shot peening can “damage” a surface. Life capability at other peening conditions was found to be comparable or slightly superior to unpeened specimens, but with significantly tighter scatter, resulting in higher minimum life capability.

The significance of this study is that it clearly demonstrated shot peening’s potential to *reduce* life capability. Various attempts at modeling or predicting the life behavior were not entirely successful. “Damage maps” were developed to “plot” regions of low life behavior, which were then used to establish safe process windows. This appendix documents the analysis that was conducted using data from the Bailey DOE.

A.2 Experiment Design

A total of four factors were evaluated at two levels each as shown in Table A.1, for a total of 16 different peening conditions. Each condition was tested twice, for a total of 32 tests. Standard smooth round bar specimens, 0.4 inches in diameter were used. The

tests were run at 1000°F, at a stress level chosen to yield an average life of 100,000 cycles for low-stress ground specimens.

Table A.1 – Summary of Factors Evaluated by Shot Peen Design of Experiment

	Factor	Low Level	High Level
1	Shot	CCW14	CCW31
2	Intensity	6A	10A
3	Incidence Angle	45°	85°
4	% Coverage	100%	800%

A.3 Results

Figure A.1 shows cube plots of the ccw14 and ccw31 peening conditions. Table A.2 gives the results in standard order, along with initiation site, life in cycles, and normalized life parameter, “stdev,” which is defined as:

$$stdev = \frac{\left[\log(N_{obs}) - \log(N_{avg}) \right]}{\left[\log(N_{avg}) - \log(N_{-3}) \right] / 3} \quad (A.1)$$

Here, N_{obs} represents the observed life at failure. N_{avg} represents the average life for the stress and temperature condition for low stress grind and polish (LSG+P) data, and N_{-3} represents the minimum life. As a result, $|stdev| > 3$ indicates test results which are very uncharacteristic of the average population of LSG+P test results. Approximately 68% of data points should be within $|stdev| < 1$, while 95% should be within $|stdev| < 2$, and 99.7% should fall within $|stdev| < 3$.

In addition to the 16 conditions evaluated by the Shot Peen DOE, results from two light peening coverage) are included in Table A.2 as conditions 17-18, along with unpeened specimen results (to serve as a benchmark) as condition 19. The light peening conditions are also included in the Weibull analysis of the following section, and in

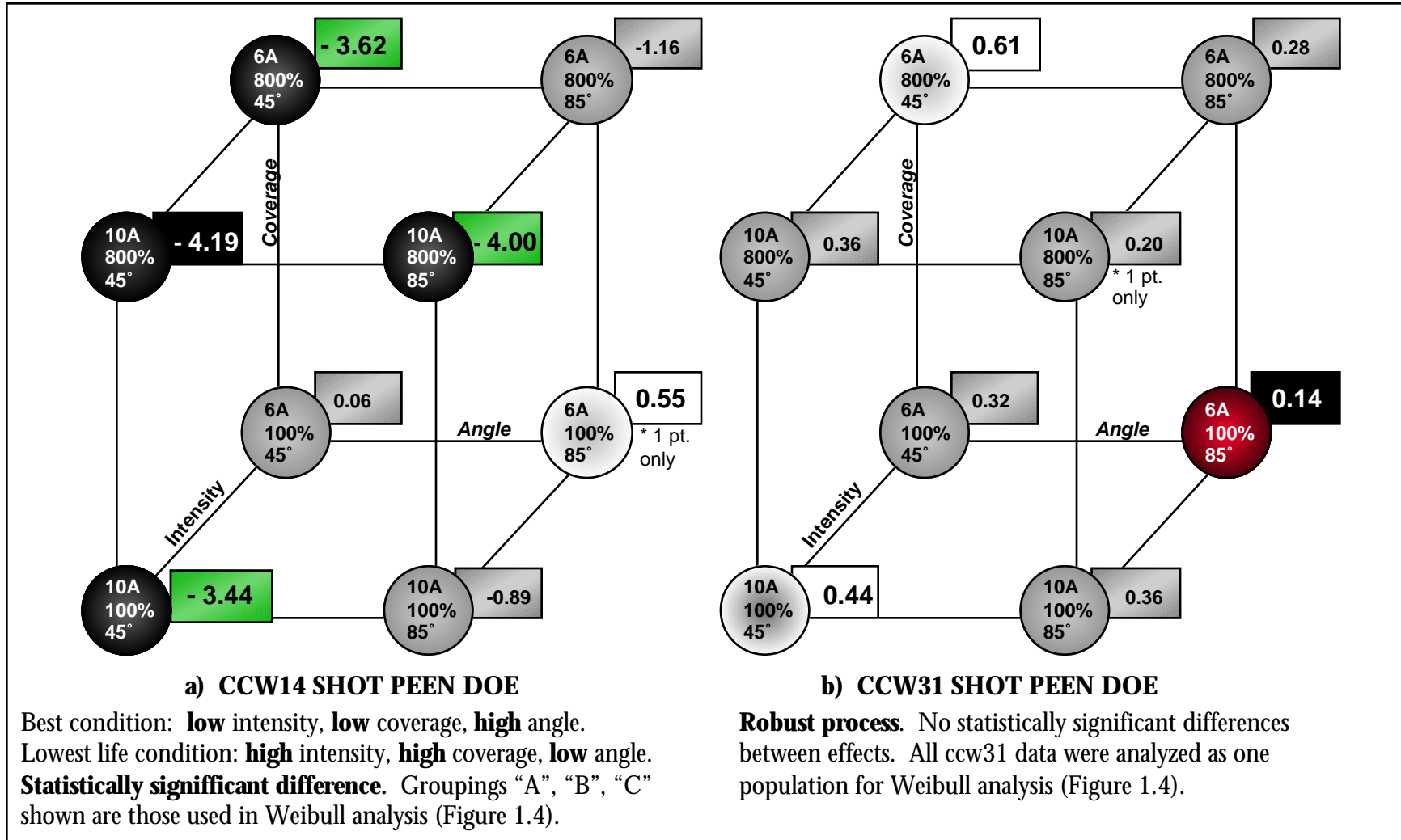


Figure A.1 – Cube Plots of Shot Peen DOE

Average life values given in **standard deviations** of **average LCF life** (calculated on log scale).

Table A.2 – Results of Shot Peen Design of Experiment (DOE) – (conditions 1-16)

Additional light peening results (conditions 17-18), and unpeened baseline (condition 19) included for reference.

DOE condition	Shot	Intensity	Incidence Angle	Coverage	Average <i>stdev</i>	First Replicate			Second Replicate		
						Initiation Site	Life, Nf	<i>stdev</i>	Initiation Site	Life, Nf	<i>stdev</i>
1	ccw14	6A	45	100%	0.06	I	126,779	0.03	I	156,558	0.10
2	ccw14	6A	45	800%	-3.62	S	23,598	-3.83	S	29,523	-3.42
3	ccw14	6A	85	100%	0.55	I	163,647	0.55	invalid test		
4	ccw14	6A	85	800%	-1.16	I	134,393	0.16	S	39,504	-2.47
5	ccw14	10A	45	100%	-3.44	S	28,909	-3.47	S	27,203	-3.41
6	ccw14	10A	45	800%	-4.19	S	20,253	-4.23	S	21,467	-4.15
7	ccw14	10A	85	100%	-0.89	I	138,633	0.29	S	49,529	-2.07
8	ccw14	10A	85	800%	-4.00	S	21,621	-4.17	S	22,311	-3.83
9	ccw31	6A	45	100%	0.32	I	137,555	0.29	I	141,969	0.36
10	ccw31	6A	45	800%	0.61	I	141,026	0.21	I	132,206	1.02
11	ccw31	6A	85	100%	0.14	I	143,627	-0.05	I	139,635	0.32
12	ccw31	6A	85	800%	0.28	I	126,348	0.20	I	145,630	0.36
13	ccw31	10A	45	100%	0.44	I	142,725	0.43	I	151,554	0.44
14	ccw31	10A	45	800%	0.36	I	141,723	0.24	I	150,913	0.49
15	ccw31	10A	85	100%	0.36	I	161,649	0.35	I	143,340	0.37
16	ccw31	10A	85	800%	0.20	I	143,004	0.20	invalid test		
17	ccw14	12N	45	400%	1.39	I	214,209	1.39	I	243,843	1.63
18	ccw14	12N	45	800%	1.28	I	193,937	1.28	I	188,658	1.23
19	unpeened				-0.59	S	69,436	-0.59	S	48,048	-1.30

Initiation site: “I” indicates **internal** initiation; “S” indicates **surface** initiation. Tests conducted at 1000°F, A-ratio=1, stress selected to give approximate life of 100,000 cycles. Actual stresses varied by as much as 6% from target value. For the target stress level, N_{avg} = 96,800 cycles and $N-3s$ = 17,700 cycles. However, “stdev” calculations use values of N_{avg} and $N-3s$ for the actual stress level. $|stdev| > 3$ indicates test results which are very uncharacteristic of the average population of LSG test results.

velocity comparisons provided later. Each condition was replicated, due to the large scatter inherent in low cycle fatigue data.

Note that surface crack initiations are highlighted in Table A.2 with bold type, while internal initiations have shaded cells. In all cases, internal initiation sites provide an indication of a “good” life result, one that is well characterized by average LCF specimen data, having a $|\text{stdev}| < 2$ or 3 . However, these lives were not significantly above average. Of the ten peened conditions with a surface crack initiation, eight had lives with $\text{stdev} < -3$. Of the two conditions with $-3 < \text{stdev} < -2$, the other replicate had internal initiations with a “good” life result, perhaps indicating a borderline condition.

A.4 Analysis of Variation (ANOVA).

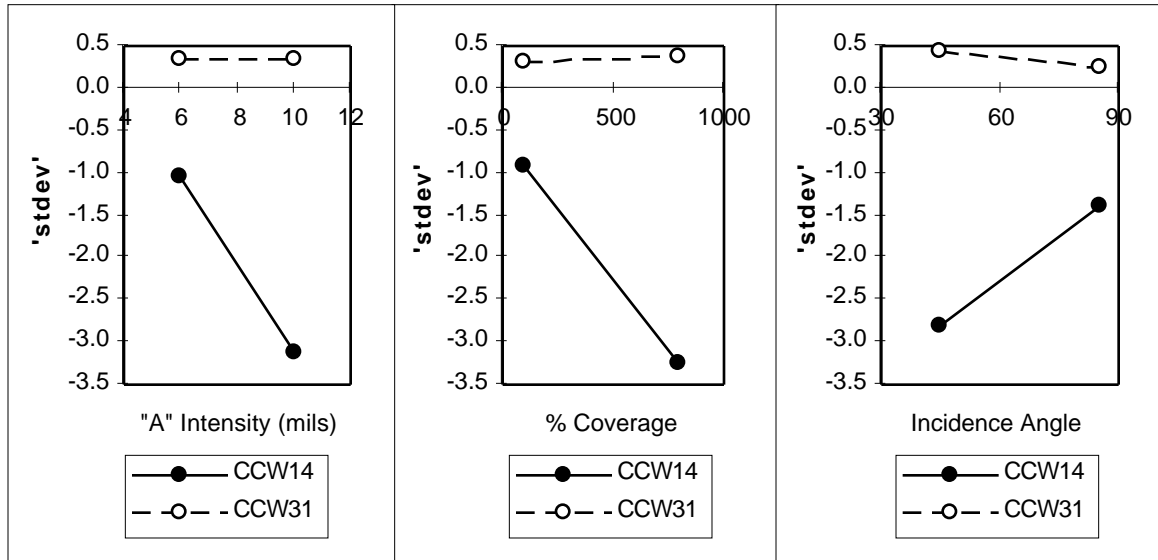
The DOE data provide evidence of significant interactions between peening parameters. A total of nine effects, including all four main effects, 3/6 two-way interactions, 1/4 three-way interactions and the single four-way interaction were found to be significant at the 95% confidence level. These factors are listed in Table A.3, along with the corresponding probability. Probability values below 0.05 indicate factors having a significant effect on life capability. See Box, Hunter & Hunter [75] for ANOVA analysis.

Table A.3 – ANOVA Summary of Shot Peen DOE Results

Main Effects & Interactions which are significant at the 95% confidence level. Normalized lives analyzed. Arcsine transformation used to reduce scatter in residuals: $\text{arcsine}(\text{stdev}/6)$.

#	Factor	Pr > F
1	shot	0.0001
2	shot*coverage	0.0003
3	coverage	0.0005
4	shot*intensity	0.0015
5	intensity	0.0018
6	shot*incidence angle	0.0038
7	incidence angle	0.0161
8	shot*intensity*angle*coverage	0.0446
9	intensity*angle*coverage	0.0498

When multiple factor interactions become significant, this indicates that one or more of the factors does not produce the same trend in life behavior over all levels of the other factors. This is illustrated in the two-way interaction plots in Figure A.2 (a)-(c).



a) Intensity*Shot Interaction b) Coverage*Shot Interaction c) Angle*Shot Interaction

Figure A.2 – Plots of Significant Two-Way Interactions from DOE

From Figure A.2, it is quickly seen that the ccw31 shot produced uniformly good life results over the range of peening conditions evaluated by the study. A range of life behaviors was observed for the smaller ccw14 shot, and the eight ccw14 DOE conditions were grouped into three categories for further analysis, as summarized in Table A.4.

Table A.4 – Grouping of CCW14 DOE Conditions by Life Behavior

Group	“stdev” Range	Peening Condition
A “Low” life results	-4.23 < stdev < -3.0	2) ccw14/6A/45°/800% 5) ccw14/10A/45°/100% 6) ccw14/10A/45°/800% 8) ccw14/10A/85°/800%
B “Transition” cases	-3 < stdev < -2 surface 0.16 < stdev < 0.29 internal	4) ccw14/6A/85°/800% 7) ccw14/10A/85°/100%
C “Good” life results	0.03 < stdev < 0.55	1) ccw14/6A/45°/100% 3) ccw14/6A/85°/100%

A.5 Weibull Analysis of Shot Peen DoE Results.

A Weibull analysis was also conducted, as illustrated in Figure A.3. For this analysis, all the ccw31 data points were analyzed together as one group. The ccw14 data points were grouped into three groups, as characterized by their life behavior and identified in Table A.4 and Figure A.1. In addition, the results from four light peening conditions, ccw14/12N/45° and 400-800% coverage were included as a separate population for comparison. A reference curve showing the behavior of comparable low stress grind specimen data is also presented in Figure A.3.

The cumulative distribution function for the Weibull distribution [76] is given as:

$$F(t) = 1 - e^{-((t-t_0)/\theta)^m} \quad (\text{A.2})$$

where t is the life, t_0 is a threshold parameter which applies only to a three-parameter Weibull, m is the shape parameter and θ is the scale parameter.

Table A.5 gives a summary of the two parameter Weibull analysis results for all populations analyzed. The slope factor from the Weibull analysis can be used to indicate the type of failure mode (slope <1 = infant mortality, slope=1 random, slope=2-3 LCF, slope>5 rapid wear out). The 50% line gives the average life (also the scale factor). The average lives for the peened ccw31 specimens are not significantly different from low stress ground specimens, but the slopes are much steeper (indicating rapid wear out mode), thereby resulting in lower variation (and higher -3 lives). This suggests that shot peening reduces the crack initiation time (by accumulating plastic strain, which is equivalent to fatigue damage); however it also increases the crack propagation life due to the beneficial residual stress layer imparted. This is another way of describing the effects of competing mechanisms of beneficial residual stresses vs. detrimental plastic strain. Population "A" – ccw14, good lives – has a curve comparable to the ccw31 population.

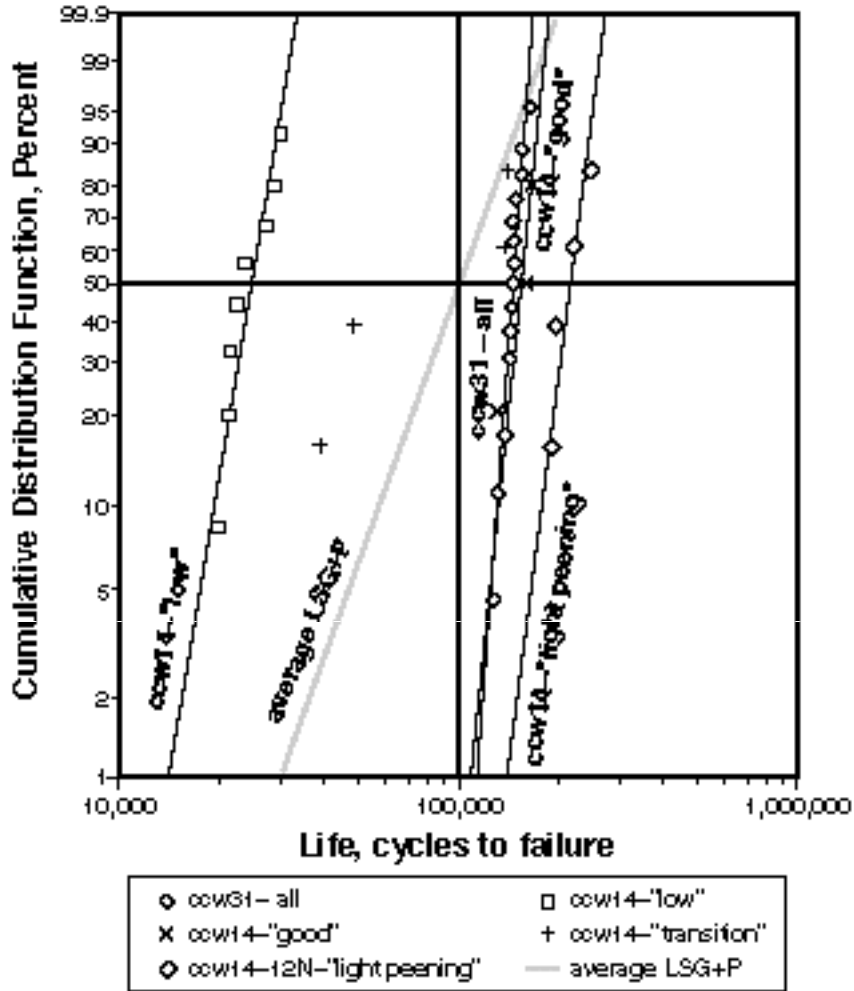


Figure A.3 – Weibull Analysis Results
(1000 °F, stress level chosen to give approx. 100,000 cycle nominal life.)

Table A.5 – Two Parameter Weibull Analysis Results of Shot Peen DOE data

symbol	shot	group	SCALE (average life)	SHAPE (failure mode)	Interpretation of SHAPE factor	SCALE std. error	SHAPE std. error
xx	CCW14	A – good	155,845	12.80	rapid wear out	7,352	6.51
++	CCW14	B – transition	102,808	2.13	LCF (mixed modes)	25,489	0.89
□□	CCW14	C – low	25,891	7.71	rapid wear out	1,259	2.12
◆◆	CCW31	D – all	146,672	17.48	rapid wear out	2,302	3.15
◇◇	CCW14	E – light peening	220,353	10.01	rapid wear out	11,696	3.79

Table A.6 – Three Parameter Weibull Analysis Results of CCW31 data

symbol	shot	Threshold	SCALE	SHAPE	Interpretation	R ²
◆◆	CCW31	-333,308	479,694	71.45	Significant damage accumulated (due to shot peening) prior to test.	1.0

The ccw14 population “C” - “low” lives - show a similarly steep slope, but the curve is shifted to the left by nearly one order of magnitude. Thus, more damage is accumulated leaving less crack nucleation life remaining. The fit obtained for the population “B” - the transition in mechanisms group – is relatively poor and reflects the high amount of variability in lives for these specimens.

The ccw14 population “A” - good lives - is virtually indistinguishable from the ccw31 curve. The ccw14 - 12N light peened curve is further to the right, suggesting that light peening does even less “detrimental plastic strain damage” resulting in higher average lives in the absence of any surface inclusions. There is other data which suggests that "light peening" does not provide the same level of protection when a surface inclusion is present. More work is needed to understand the limits of light peening in the presence of inclusions.

The results of a three-parameter Weibull analysis performed on the ccw31 data is summarized in Table A.6 and shows a negative t_0 (threshold) value. If this analysis is valid, it indicates that a significant amount of the total life capability (about 70%) is consumed by peening; however because of the beneficial effects of the residual stresses, the total life capability is increased by ~480% over low stress ground and polished (LSG+P) specimens. The net effect is an average life which is slightly higher than that of average LSG+P specimens (146,000 vs. 100,000). The three-parameter Weibull analysis is a non-linear analysis and requires a minimum of about 14 data points to yield significant results. It appears to be sensitive to initial values used to start the parameter estimates, so it is possible to find either positive or negative solutions with varying goodness-of-fit characteristics. The analysis conducted resulted in a perfect R^2 regression correlation coefficient of 1. The interpretation of the negative t_0 parameter is consistent with the idea of cold work processes generating the equivalent of fatigue damage.

APPENDIX B

SINGLE PARTICLE IMPACT TESTS

B.1 Contents

A subset of the results are presented in Chapter 4. This section is provided to complement that material, and to document how the data were processed and interpreted in more detail. Because of the difficulty of the tests and funding limitations, incomplete data exist for most tests. To simplify documentation, test results are split up into tables covering subsets of the results analyzed. Results from this effort were presented at the Sixth International Conference on Shot Peening. [77]

B.2 Experimental Difficulty

B.3 Shot Characterization

B.4 Impact Dimple Characterization

B.5 Test Results

B.5.1 Dimple Profile Data and General Results

B.5.2 Coefficient of Restitution Data

B.5.3 Precision Section Data

B.5.4 Estimation of Impact Stress Using Impact Dynamics

B.5.5 Transient Temperature Measurements

B.5.6 Derivation of Plastic Strain Estimate and Sample Dimple Profiles

B.2 Experimental Difficulty

The objective of the single particle impact tests was to understand changes in material behavior and response as a function of shot size, velocity and incidence angle.

Ideally, shot would be weighed and measured before and after impact, however catching shot after impact was difficult. Incident velocity measurements were obtained by having the particle trigger two lasers on the way to the target. However, the particle sizes were so small that even slight deviations in path could allow them to miss the second laser beam. Results were improved by moving the second laser closer to the first. High speed impact photos were used to determine velocity after impact. A delay time had to be estimated to trigger the camera after the second laser was triggered. Variations in velocity could result in the impact photo missing the recoil event.

Identifying the impact site was also challenging at times. The low stress ground surfaces of the specimens had machining grooves, nicks and dents in them. Low speed impacts caused gentle dimples, some of which relaxed out over a period of time. Higher speed impacts resulted in a bright impact dimple where the oxide film had been cut away. Small amounts of metal debris was observed on the catcher cloth, indicating that some amount of workpiece and/or shot was removed during impact. Due to the difficulty of the tests, it was not possible to obtain “complete” data for all test conditions, and it was difficult to obtain specific velocity conditions, thus the intended structure of a designed experiment was not possible. However, the data obtained have been extremely valuable in shedding light on the shot peening process.

B.3 Shot Characterization

It should be noted that neither the shot nor the impact dimples were perfectly spherical in nature. Scale photos of shot samples used were presented in Figure 3.2. Shot were weighed to the nearest 0.1 grams, photographed and measured using image processing software. The three dimensional nature of the shot and two-dimensional nature of the photo resulted in an incomplete representation of the shot dimensions. A minimum length, W , and maximum length, L , were recorded for each particle. The maximum

length, L , was used for strain rate estimates, while the minimum length, W , was used for intensity calculations, assuming that shot would fly in the most aerodynamic (streamlined) orientation.

B.4 Impact Dimple Characterization

Similarly, the resulting impact dimples were not symmetrical. Four profile traces were taken through the center of each dimple as illustrated in Figure B.1 (b). A sample trace is shown in Figure B.1 (a). Since the impact process could result in plowing/cutting of material from the surface as well as local heating and pushing of material to form lips around the crater, three measurements were taken for each profile: 1) "well" diameter, characterizing the projection of the deepest dimple section with the surface, 2) "shelf" diameter characterizing the largest diameter intersecting the surface, and 3) "lip" diameter characterizing the largest diameter intersecting the surface, and 3) "lip" diameter, characterizing the diameter including any "pushed-up" region, until the profile is again flush with the reference surface.

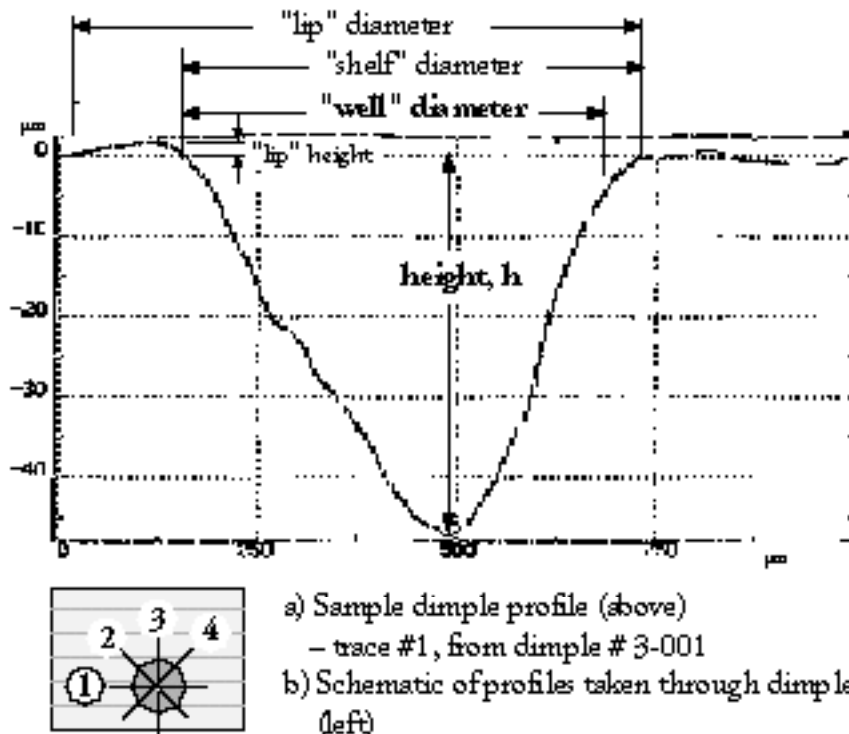


Figure B.1 – Sample Dimple Profile and Schematic of Traces Taken

From the four profile measurements taken for each dimple, the minimum and maximum “well” diameters, along with the maximum dimple depth were determined. The dimple was modeled as a hyperbolic ellipsoid, with a major axis diameter of $2a_d$ corresponding to the maximum well diameter, a minor axis diameter of $2b_d$, corresponding to the minimum well diameter, and a maximum depth of h . This is illustrated in figure B.2.

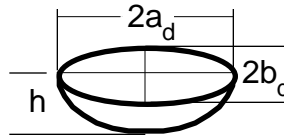


Figure B.2 – Schematic of Dimple

For correlation purposes with the Thompson relation, the minor axis diameter of $2b_d$ was used as a dimple diameter, as being most characteristic of the dimple dimension controlled by shot impact. For 45° impacts in particular, additional sliding and cutting occurred along the impact path, so the minimum diameter was most characteristic of the impression due to the shot size alone. Thompson’s relation is not able to account for effects due to incidence angles other than 90° .

A collection of other dimple profiles obtained using the WYKO vertical scanning interferometer are presented in section B.5.6.

B.5 Test Results

B.5.1 Dimple Profile Data and General Results

For most tests, incident velocity, initial shot dimensions, and dimple profile data were obtained. Recoil velocity was more difficult, but generally available except when infrared detectors were being used to evaluate temperature rise due to impact. Tables B.1, B.2 and B.3 summarize this general test result data for ccw14, ccw31 and ccw52 shot, respectively.

Table B.1 – General Results for CCW14 Shot Tests

Test	Angle	Temp Instr?	Shot #	Target #	Grind	Incident		Recoil				Initial shot dimensions			Dimple dimensions			Total Strain Rate	Normal Strain Rate	d/D	d/D	Normal Intensity calc.	Kt	P*K	P*	h/2b	h/W		
						V, in	Vn, in	Vr	Vr,n	Vr,t	Recoil Angle	L	W	m	a	b	h											in/s	in/s
3-079	45		CCW14-14	R88-08	0	3699	2616	2323	1012	2102	26	0.0182	0.0149	0.4	0.004	0.002	0.0005	4.1E+5	2.9E+5	0.53	0.28	9.2	1.24	375,966	2.24	0.12	0.03		
3-063	45	IR	CCW14-13	R88-16	1	5102	3608	0	0	0		0.0161	0.0150	0.2	0.003	0.002	0.0003	6.4E+5	4.5E+5	0.62	0.27	10.9	1.14	476,445	2.84	0.08	0.02		
3-062	45	IR	CCW14-10	R88-16	1	5263	3722	0	0	0		0.0162	0.0144	0.1	0.003	0.003	0.0004	6.5E+5	4.6E+5	0.63	0.35	10.6	1.15	492,010	2.93	0.08	0.03		
3-024	90		CCW14-05	R88-09	0	722	722	0	0	0		0.0141	0.0135	0.1	0.003	0.002	0.0003	1.0E+5	1.0E+5	0.28	0.32	3.7	1.10	64,922	0.39	0.06	0.02		
3-027	90		CCW14-06	R88-09	0	1350	1350	0	0	0		0.0171	0.0147	0.1	0.006	0.003	0.0004	1.6E+5	1.6E+5	0.38	0.45	5.5	1.11	122,079	0.73	0.06	0.03		
3-029	90		CCW14-09	R88-10	1	2976	2976	0	0	0		0.0159	0.0147	0.1	0.003	0.003	0.0005	3.7E+5	3.7E+5	0.57	0.37	8.2	1.19	289,304	1.72	0.10	0.04		
3-017	90		CCW14-04	R88-04	1	3444	3444	1837	1837	0		0.0147	0.0142	0.2	0.004	0.003	0.0007	4.7E+5	4.7E+5	0.61	0.42	8.5	1.24	347,513	2.07	0.11	0.05		
3-015	90		CCW14-03	R88-04	1	3493	3493	1575	1575	0		0.0175	0.0151	0.2	0.005	0.004	0.0007	4.0E+5	4.0E+5	0.61	0.46	9.1	1.19	340,193	2.02	0.10	0.05		
3-016	90		CCW14-01	R88-04	1	3543	3543	1638	1638	0		0.0158	0.0148	0.3	0.004	0.003	0.0005	4.5E+5	4.5E+5	0.62	0.36	9.0	1.18	340,317	2.03	0.09	0.03		
3-028	90		CCW14-07	R88-10	1							0.0166	0.0145	0.2	0.004	0.002	0.0003				0.26		1.15		0.08	0.02			

Grind direction: 0=horizontal orientation (shot hitting parallel to grind), 1=vertical orientation (shot hitting across grind for 45° impacts)

IR indicates infrared detectors used for temperature measurements.

Table B.2 – General Results for CCW31 Shot Tests

Test	Angle	Temp Instr?	Shot #	Target #	Grind	Incident		Recoil				Initial shot dimensions			Dimple dimensions			Total Strain Rate	Normal Strain Rate	d/D	d/D	Normal Intensity calc.	Kt	P*K _t	P*	h/2b	h/W	
						V, in	Vn, in	Vr	Vr,n	Vr,t	Recoil Angle	L	W	m	a	b	h											
						in/s	in/s	in/s	in/s	in/s	°	in.	in.	mg	in.	in.	in.											
3-078	45		CCW31-28	R88-08	0	8324	5886	6535	3689	5394	34	0.0410	0.0351	3.3	0.012	0.009	0.0021	4.1E+5	2.9E+5	0.80	0.50	32.6	1.26	855,581	5.09	0.12	0.06	
3-050	45	IR	CCW31-17	R88-08	0							0.0410	0.0348	3.1								0.0						
3-075	45		CCW31-25	R88-16	1	1850	1308					0.0412	0.0354	3.3	0.005	0.004	0.0006	9.0E+4	6.3E+4	0.38	0.20	15.5	1.16	175,466	1.04	0.08	0.02	
3-077	45		CCW31-27	R88-16	1	3494	2471	2362	571	2283	14	0.0426	0.0346	3.4	0.007	0.003	0.0008	1.6E+5	1.2E+5	0.52	0.19	20.8	1.28	365,382	2.17	0.13	0.02	
3-057	45	IR	CCW31-20	R88-16	1	7576	5357					0.0391	0.0351	3.2				3.9E+5	2.7E+5	0.76		31.1						
3-058	45	IR*	CCW31-21	R88-16	1	7813	5524					0.0418	0.0340	3.5				3.7E+5	2.6E+5	0.77		30.6						
3-055	45	IR	CCW31-18	R88-06	1	8475	5992					0.0402	0.0356	3.5	0.016	0.011	0.0015	4.2E+5	3.0E+5	0.81	0.61	33.4	1.12	775,163	4.61	0.07	0.04	
3-060	45	IR*	CCW31-23	R88-19	100%	8621	6096					0.0418	0.0354	3.6	0.015	0.013	0.0014	4.1E+5	2.9E+5	0.81	0.73	33.4	1.09	763,917	4.55	0.05	0.04	
3-056	45	IR***	CCW31-19	R88-06	1	9804	6932					0.0410	0.0354	3.3	0.012	0.009	0.0021	4.8E+5	3.4E+5	0.87	0.49	35.6	1.26	1,005,211	5.98	0.12	0.06	
3-059	45	IR*	CCW31-22	R88-16	1	11905	8418					0.0402	0.0348	3.3				5.9E+5	4.2E+5	0.95		38.7						
3-076	45		CCW31-26	R88-16	1			1535	945	1220	38	0.0394	0.0340	2.8	0.021	0.004	0.0004						1.07			0.05	0.01	
3-061	45	IR	CCW31-24	R88-20	800%	8475	5992					0.0375	0.0351	3.2	0.014	0.007	0.0012	4.5E+5	3.2E+5	0.81	0.38	32.9	1.17	809,371	4.82	0.09	0.03	
3-023	90		CCW31-13	R88-09	0	690	690	343	343	0		0.0364	0.0348	3.3	0.007	0.005	0.0004	3.8E+4	3.8E+4	0.27	0.30	9.3	1.06	59,690	0.36	0.04	0.01	
3-009	90		CCW31-09	R88-05	0	2318	2318	1394	1394	0		0.0387	0.0338	3.1	0.007	0.006	0.0009				0.50	0.34	16.5	1.15	216,700	1.29	0.08	0.03
3-008	90		CCW31-02	R88-05	0	2480	2480	1312	1312	0		0.0394	0.0353	3.1	0.009	0.007	0.0009	1.3E+5	1.3E+5	0.52	0.38	17.9	1.12	227,696	1.36	0.07	0.03	
3-007	90		CCW31-01	R88-05	0	2756	2756					0.0426	0.0356	3.6	0.008	0.006	0.0011	1.3E+5	1.3E+5	0.55	0.35	19.0	1.17	262,176	1.56	0.09	0.03	
3-025	90		CCW31-14	R88-09	0			1531	1531	0		0.0412	0.0343	3.1	0.008	0.006	0.0014					0.37	1.23			0.11	0.04	
3-026	90		CCW31-15	R88-09	0			1732	1732	0		0.0407	0.0351	3.2	0.011	0.008	0.0009	0.0E+0	0.0E+0		0.44		1.10			0.06	0.03	
3-019	90		CCW31-10	R88-10	1	458	458					0.0407	0.0341	3.3	0.004	0.004	0.0006	2.2E+4	2.2E+4	0.22	0.23	7.4	1.15	43,105	0.26	0.08	0.02	
3-018	90		CCW31-gen	R88-10	1	3444	3444	1427	1427	0		0.0404	0.0349	3.3	0.008	0.006	0.0014	1.7E+5	1.7E+5	0.61	0.34	20.8	1.25	351,582	2.09	0.12		
3-005	90		CCW31-06	R88-02	var	3307	3307	1575	1575	0		0.0353	0.0333	2.8				1.9E+5	1.9E+5	0.60		19.5						
3-002	90		CCW31-03	R88-02	var							0.0402	0.0346	3.5														
3-003	90		CCW31-04	R88-02	var							0.0438	0.0339	3.6														
3-004	90		CCW31-05	R88-02	var							0.0384	0.0355	3.2														
3-006	90		CCW31-08	R88-02	var							0.0409	0.0350	3.2														

Grind direction: 0=horizontal orientation (shot hitting parallel to grind), 1=vertical orientation (shot hitting across grind for 45° impacts)

IR indicates infrared detectors used for temperature measurements.

Table B.3 – General Results for CCW52 Shot Tests

Test	Angle	Temp Instr?	Shot #	Target #	Grind	Incident		Recoil				Initial shot dimensions			Dimple dimensions			Total Strain Rate	Normal Strain Rate	d/D	d/D	Normal Intensity calc. (mils)	Kt	P*K, psi	P*	h/2b	h/W
						V, in	Vn, in	Vr	Vr,n	Vr,t	Recoil Angle	L	W	m	a	b	h										
						in/s	in/s	in/s	in/s	in/s	°	in.	in.	mg	in.	in.	in.										
3-068	45		CCW52-27	R88-09	0	3773	2668					0.0588	0.0569	12.4	0.014	0.009	0.0017	1.3E+5	9.1E+4	0.54	0.30	35.5	1.21	371,204	2.21	0.10	0.03
3-049	45	IR	CCW52-18	R88-08	0	6937	4905					0.0654	0.0567	13.7				2.1E+5	1.5E+5	0.73		48.0					
3-064	45		CCW52-23	R88-09	0	6988	4941					0.0623	0.0603	13.5	0.016	0.013	0.0027	2.2E+5	1.6E+5	0.73	0.43	51.2	1.21	691,065	4.11	0.10	0.05
3-051	45	IR	CCW52-19	R88-08	0	7164	5066					0.0604	0.0568	12.4				2.4E+5	1.7E+5	0.74		48.9					
3-052	45	IR	CCW52-20	R88-08	0	7246	5124					0.0575	0.0556	10.6				2.5E+5	1.8E+5	0.74		48.1					
3-045	45	IR	CCW52-14	R88-08	0	8245	5830					0.0673	0.0561	13.4				2.5E+5	1.7E+5	0.79		51.8					
3-047	45	IR	CCW52-16	R88-08	0	8245	5830					0.0641	0.0572	12.9				2.6E+5	1.8E+5	0.79		52.8					
3-046	45	IR	CCW52-15	R88-08	0	8404	5942					0.0646	0.0564	13.3				2.6E+5	1.8E+5	0.80		52.6					
3-048	45	IR	CCW52-17	R88-08	0	8569	6059					0.0636	0.0564	12.6				2.7E+5	1.9E+5	0.81		53.1					
3-065	45		CCW52-24	R88-09	0	8576	6064	5512	2402	4961	26	0.0630	0.0560	13.1	0.017	0.014	0.0030	2.7E+5	1.9E+5	0.81	0.48	52.7	1.23	861,019	5.13	0.11	0.05
3-066	45		CCW52-25	R88-09	0	8984	6353					0.0639	0.0571	13.5	0.020	0.016	0.0026	2.8E+5	2.0E+5	0.83	0.55	55.0	1.15	845,797	5.03	0.08	0.05
3-067	45		CCW52-26	R88-09	0	9129	6455	5630	2992	4764	32	0.0598	0.0585	13.4	0.020	0.018	0.0028	3.1E+5	2.2E+5	0.84	0.62	56.8	1.15	854,217	5.08	0.08	0.05
3-074	45		CCW52-gen	R88-16	1	2021	1429	1378	756	941	39	0.0621	0.0564	12.863	0.009	0.008	0.0007	6.5E+4	4.6E+4	0.39	0.27	25.8	1.07	176,620	1.05	0.04	
3-072	45		CCW52-gen	R88-07	1	2388	1689	1693	945	1425	34	0.0621	0.0564	12.863				7.7E+4	5.4E+4	0.43		28.0					
3-073	45		CCW52-31	R88-16	1	2844	2011					0.0615	0.0575	12.6	0.009	0.009	0.0012	9.3E+4	6.5E+4	0.47	0.31	31.2	1.12	259,560	1.55	0.07	0.02
3-071	45		CCW52-30	R88-07	1	2948	2084					0.0604	0.0567	12.1				9.8E+4	6.9E+4	0.47		31.3					
3-069	45		CCW52-28	R88-07	1	3329	2354					0.0597	0.0547	12.2				1.1E+5	7.9E+4	0.50		32.1					
3-070	45		CCW52-29	R88-07	1	3329	2354					0.0645	0.0560	13.4				1.0E+5	7.3E+4	0.50		32.8					
3-043	45	IR*	CCW52-02	R88-07	1	7407	5237					0.0658	0.0554	13.3				2.3E+5	1.6E+5	0.75		48.5					
3-037	45	IR*	CCW52-gen	R88-07	1	7534	5328					0.0621	0.0564	12.863				2.4E+5	1.7E+5	0.76		49.8					
3-039	45	IR	CCW52-gen	R88-07	1	7534	5328					0.0621	0.0564	12.863				2.4E+5	1.7E+5	0.76		49.8					
3-053	45	R* movin	CCW52-21	R88-06	1	8065	5702					0.0628	0.0572	13.2	0.017	0.015	0.0029	2.6E+5	1.8E+5	0.79	0.51	52.2	1.20	787,406	4.69	0.10	0.05
3-041	45	IR ??	CCW52-10	R88-07	1	8404	5942					0.0580	0.0554	11.6				2.9E+5	2.0E+5	0.80		51.6					
3-042	45	IR	CCW31-16	R88-07	1	8404	5942					0.0420	0.0351	3.5				4.0E+5	2.8E+5	0.80		32.7					
3-044	45	IR*	CCW52-13	R88-07	1	8404	5942					0.0609	0.0553	13.2				2.8E+5	2.0E+5	0.80		51.6					
3-040	45	IR ?	CCW52-gen	R88-07	1	8569	6059					0.0621	0.0564	12.863				2.8E+5	2.0E+5	0.81		53.1					
3-054	45	IR	CCW52-22	R88-06	1	8621	6096					0.0633	0.0564	13	0.009	0.008	0.0031	2.7E+5	1.9E+5	0.81	0.29	53.2	1.47	1,037,250	6.17	0.19	0.06
3-038	45	**IR**	CCW52-gen	R88-07	1	9500	6718					0.0621	0.0564	12.863				3.1E+5	2.2E+5	0.85		55.9					
3-022	90		CCW52-09	R88-09	0	648	648	402	402	0		0.0627	0.0561	13				2.1E+4	2.1E+4	0.26		14.5					
3-001	90		CCW52-03	R88-01	0	3689	3689	1312	0	0		0.0637	0.0573	13	0.013	0.012	0.0019	1.2E+5	1.2E+5	0.63	0.41	35.4	1.15	345,446	2.06	0.08	0.03
3-010	90		CCW52-04	R88-03	1	2000	2000					0.0608	0.0580	13.1	0.014	0.009	0.0035	6.6E+4	6.6E+4	0.47	0.29	26.4	1.51	246,024	1.46	0.20	0.06
3-011	90		CCW52-05	R88-03	1	2255	2255	787	787	0		0.0604	0.0556	12.8	0.010	0.009	0.0028			0.49	0.33	26.9	1.35	248,011	1.48	0.15	0.05
3-012	90		CCW52-06	R88-03	1	2667	2667	1247	1247	0		0.0610	0.0554	12.7	0.013	0.010	0.0019	8.7E+4	8.7E+4	0.54	0.37	29.1	1.18	255,905	1.52	0.09	0.03
3-013	90		CCW52-07	R88-03	1	2988	2988	1066	1066	0		0.0665	0.0554	13.7	0.014	0.012	0.0021	9.0E+4	9.0E+4	0.57	0.43	30.8	1.17	285,474	1.70	0.09	0.04
3-014	90		CCW52-08	R88-03	1	3307	3307	1181	1181	0		0.0615	0.0549	13.5	0.015	0.012	0.0018	1.1E+5	1.1E+5	0.60	0.45	32.1	1.13	304,841	1.81	0.07	0.03
3-020	90		CCW52-01	R88-06	1	8267	8267	1969	1969	0		0.0611	0.0568	12.8	0.017	0.015	0.0035	2.7E+5	2.7E+5	0.95	0.52	52.5	1.25	841,183	5.01	0.12	0.06
3-021	90		CCW52-gen	steel		647	647					0.0621	0.0564	12.9				2.1E+4	2.1E+4	0.26		14.6					

Grind direction: 0=horizontal orientation (shot hitting parallel to grind), 1=vertical orientation (shot hitting across grind for 45° impacts)
 IR indicates infrared detectors used for temperature measurements.

B.5.2 Coefficient of Restitution Data

For a few tests, shot were caught after impact, weighed and measured. For these tests, the coefficient of restitution could be calculated, as given in equation B.1.

$$e = \frac{m_{out} V_{out}^2}{m_{in} V_{in}^2} \quad (B.1)$$

The data used for these calculations are presented in Table B.4.

B.5.3 Precision Section Data

For a subset of test dimples, precision sections were taken through the approximate dimple center. After mounting and polishing to the dimple, the specimens were etched to reveal the microstructure. Progressive development of slip bands was the microstructural feature observed that corresponded to increases in velocity and strain rate. Since “low” life test conditions also correlated with shot velocities greater than a threshold of approximately 2,000 in/s, it is inferred that development of slip also corresponds to an increase in the “damage” condition. Thus, plastic deformation appears to be related to the “damage” state.

These data are presented in Table B.5, sorted by shot size, incidence angle and velocity. Figure B.3 presents “dimple maps” showing schematics of test targets with impact dimple locations and approximate orientation of precision sections taken. Grind orientation is also represented on these maps. Microstructures for all precision sections taken follow in Figures B.4-B.20.

Table B.4 – Coefficient of Restitution Data

Test	Angle	Shot #	Target #	Grind Dir.	Incident		Recoil				Initial dimensions			Final dimensions			Change			Coef. of Restitution		Total Strain Rate	Normal Strain Rate	d/D	d/D	Normal Intensity calc.	Kt
					V _i , in	V _n , in	V _r	V _{r,n}	V _{r,t}	Recoil Angle	L	W	m	L	W	m	L	W	m	e _{,total}	e _{,normal}						
					in/s	in/s	in/s	in/s	in/s	°	in.	in.	mg	in.	in.	mg	in.	in.	mg								
3-020	90	CCW52-01	R88-06	1	8,267	8,267	1,969	1,969	0		0.0611	0.0568	12.8	0.0625	0.0575	12.7	-0.0014	-0.0007	0.1	0.06	0.06	2.7E+5	2.7E+5	0.95	0.52	52.5	1.25
3-013	90	CCW52-07	R88-03	1	2,988	2,988	1,066	1,066	0		0.0665	0.0554	13.7	0.0691	0.0548	13.8	-0.0026	0.0006	-0.1	0.13	0.13	9.0E+4	9.0E+4	0.57	0.43	30.8	1.17
3-011	90	CCW52-05	R88-03	1	2,255	2,255	787	787	0		0.0604	0.0556	12.8	0.0625	0.0575	13.5	-0.0021	-0.0019	-0.7	0.13	0.13	7.5E+4	7.5E+4	0.49	0.33	26.9	1.35
3-014	90	CCW52-08	R88-03	1	3,307	3,307	1,181	1,181	0		0.0615	0.0549	13.5	0.0652	0.0556	13.7	-0.0037	-0.0007	-0.2	0.13	0.13	1.1E+5	1.1E+5	0.60	0.45	32.1	1.13
3-017	90	CCW14-04	R88-04	1	3,444	3,444	1,837	1,837	0		0.0147	0.0142	0.2	0.0157	0.0150	0.1	-0.0010	-0.0007	0.1	0.14	0.14	4.7E+5	4.7E+5	0.61	0.42	8.5	1.24
3-005	90	CCW31-06	R88-02	var	3,307	3,307	1,575	1,575	0		0.0353	0.0333	2.8	0.0366	0.0341	2.4	-0.0013	-0.0008	0.4	0.19	0.19	1.9E+5	1.9E+5	0.60		19.5	
3-067	45	CCW52-26	R88-09	0	9,129	6,455	5,630	2,992	4,764	32	0.0598	0.0585	13.4	0.0636	0.0575	13.3	-0.0038	0.0010	0.1	0.38	0.21	3.1E+5	2.2E+5	0.84	0.62	47.8	1.15
3-012	90	CCW52-06	R88-03	1	2,667	2,667	1,247	1,247	0		0.0610	0.0554	12.7	0.0650	0.0573	13.3	-0.0040	-0.0019	-0.6	0.23	0.23	8.7E+4	8.7E+4	0.54	0.37	29.1	1.18
3-008	90	CCW31-02	R88-05	0	2,480	2,480	1,312	1,312	0		0.0394	0.0353	3.1	0.0395	0.0349	2.7	-0.0001	0.0004	0.4	0.24	0.24	1.3E+5	1.3E+5	0.52	0.38	17.9	1.12
3-009	90	CCW31-09	R88-05	0	2,318	2,318	1,394	1,394	0		0.0387	0.0338	3.1	0.0429	0.0350	3.1	-0.0043	-0.0012	0	0.36	0.36	1.2E+5	1.2E+5	0.50	0.34	16.5	1.15
3-022	90	CCW52-09	R88-09	0	648	648	402	402	0		0.0627	0.0561	13	0.0650	0.0578	13	-0.0023	-0.0017	0	0.39	0.39	2.1E+4	2.1E+4	0.26		14.5	

Grind direction: 0=horizontal orientation (shot hitting parallel to grind), 1=vertical orientation (shot hitting across grind for 45° impacts)

Shaded cells indicate precision section obtained for this condition.
 V_i,in = total incident velocity V_n,in= normal incident velocity/V_r=total recoil velocity

3-020 Bold test numbers indicate precision sections taken on these dimples
 V_{r,n}=normal component of recoil velocity V_{r,t}=tangential component of recoil velocity

Table B.5 – Precision Sections Data – sorted by shot type (ccw14, ccw31, ccw52), incidence angle (90, 45) & velocity

Test	Angle	Temp Instr?	Shot #	Target #	Grind	Incident Velocity				Recoil Velocity				EDS	e,total	e,normal	Total Strain Rate	Normal Strain Rate	d/D calc.	d/D meas.	Normal Intensity calc. (mils)	Kt	
						English		Metric		English			Metric										
						V, in	Vn, in	V, in	Vn, in	Vr	Vr,n	Vr,t	Recoil Angle										Vr
in/s	in/s	m/s	m/s	in/s	in/s	in/s	°	m/s	m/s														
3-027	90		CCW14-06	R88-09	0	1,350	1,350	34	34							1.6E+5	1.6E+5	0.38	0.45	5.5	1.11		
3-017	90		CCW14-04	R88-04	1	3,444	3,444	87	87	1,837	1,837	0	47	47	negl. Fe	0.14	0.14	4.7E+5	4.7E+5	0.61	0.42	8.5	1.24
3-079	45		CCW14-14	R88-08	0	3,699	2,616	94	66	2,323	1,012	2,102	26	59	26	0.015		4.1E+5	2.9E+5	0.53	0.28	7.8	1.24
3-062	45	IR	CCW14-10	R88-16	1	5,263	3,722	134	95							6.5E+5	4.6E+5	0.63	0.35	9.0	1.15		
3-023	90		CCW31-13	R88-09	0	690	690	18	18	343	343	0	9	9	no Fe		3.8E+4	3.8E+4	0.27	0.30	9.3	1.06	
3-009	90		CCW31-09	R88-05	0	2,318	2,318	59	59	1,394	1,394	0	35	35	no Fe	0.36	0.36			0.50	0.34	16.5	1.15
3-077	45		CCW31-27	R88-16	1	3,494	2,471	89	63	2,362	571	2,283	14	60	15	0.036		1.6E+5	1.2E+5	0.52	0.19	17.5	1.28
3-056	45	IR***	CCW31-19	R88-06	1	9,804	6,932	249	176							4.8E+5	3.4E+5	0.87	0.49	29.9	1.26		
3-010	90		CCW52-04	R88-03	1	2,000	2,000	51	51							6.6E+4	6.6E+4	0.47	0.29	26.4	1.51		
3-011	90		CCW52-05	R88-03	1	2,255	2,255	57	57	787	787	0	20	20	0.033	0.13	0.13			0.49	0.33	26.9	1.35
3-012	90		CCW52-06	R88-03	1	2,667	2,667	68	68	1,247	1,247	0	32	32		0.23	0.23	8.7E+4	8.7E+4	0.54	0.37	29.1	1.18
3-001	90		CCW52-03	R88-01	0	3,689	3,689	94	94	1,312	1,312	0	33		negl. Fe		1.2E+5	1.2E+5	0.63	0.41	35.4	1.15	
3-020	90		CCW52-01	R88-06	1	8,267	8,267	210	210	1,969	1,969	0	50	50	0.030	0.06	0.06	2.7E+5	2.7E+5	0.95	0.52	52.5	1.25
3-068	45		CCW52-27	R88-09	0	3,773	2,668	96	68							1.3E+5	9.1E+4	0.54	0.30	29.9	1.21		
3-066	45		CCW52-25	R88-09	0	8,984	6,353	228	161							2.8E+5	2.0E+5	0.83	0.55	46.3	1.15		
3-065	45		CCW52-24	R88-09	0	8,576	6,064	218	154	5,512	2,402	4,961	26	140	61			2.7E+5	1.9E+5	0.81	0.48	44.3	1.23

Grind direction: 0=horizontal orientation (shot hitting parallel to grind), 1=vertical orientation (shot hitting across grind for 45° impacts)

EDS = ratio of Fe peak height to Ni peak height, indicating presence of iron on dimple surface, transferred from shot at impact

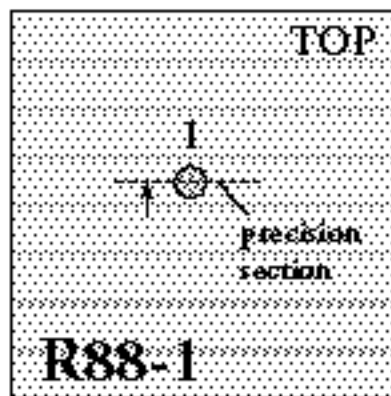
V,in = total incident velocity

Vn,in= normal incident velocity

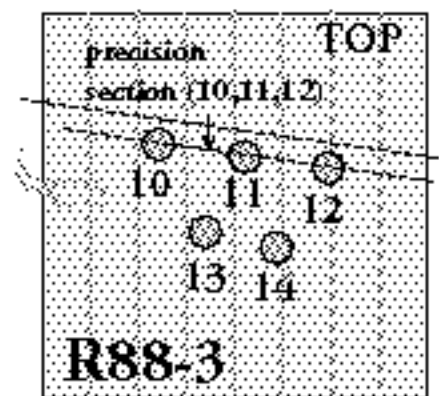
Vr=total recoil velocity

Vr,n=normal component of recoil velocity

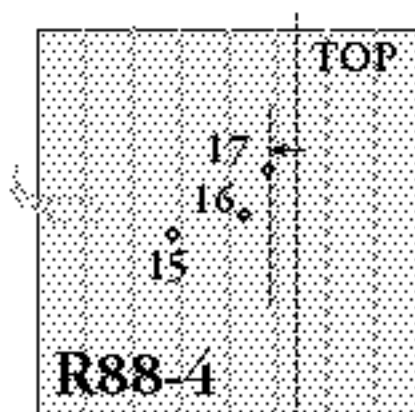
Vr,t=tangential component of recoil velocity



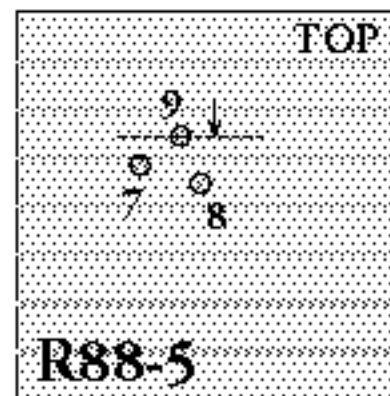
a) Target R88-1



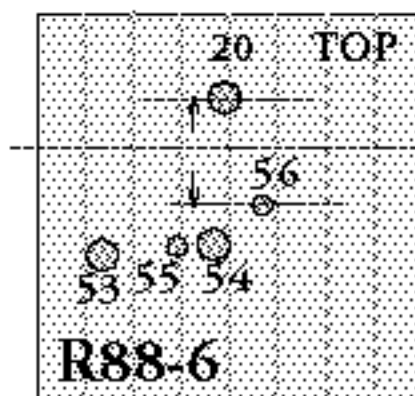
b) Target R88-3



c) Target R88-4



d) Target R88-5



e) Target R88-6

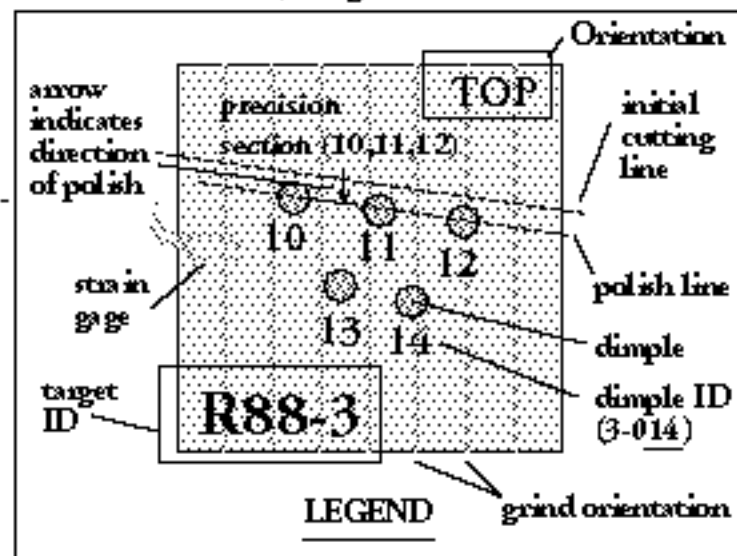
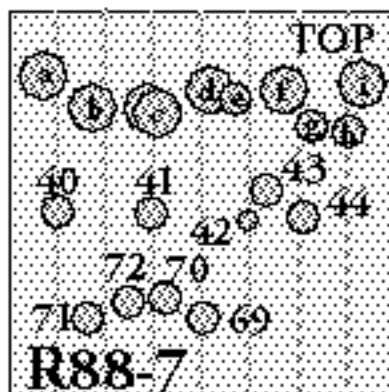
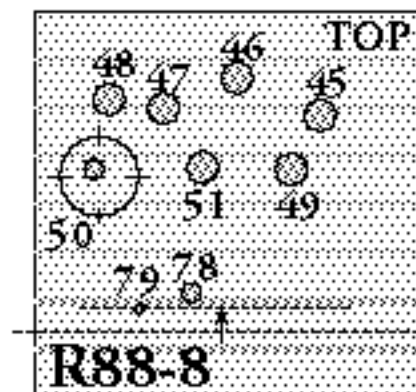


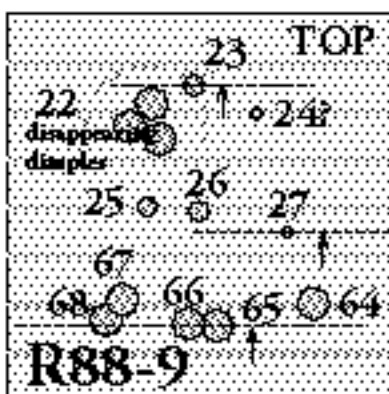
Figure B.3 – Dimple Maps:
Schematic of Impact Targets Showing Dimples and Precision Sections



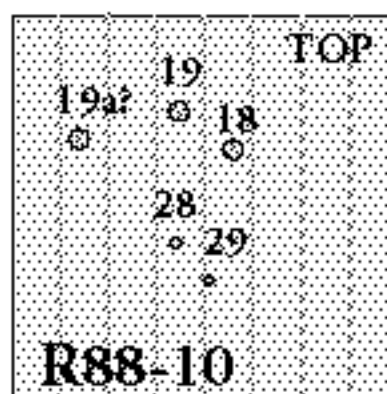
f) Target R88-7



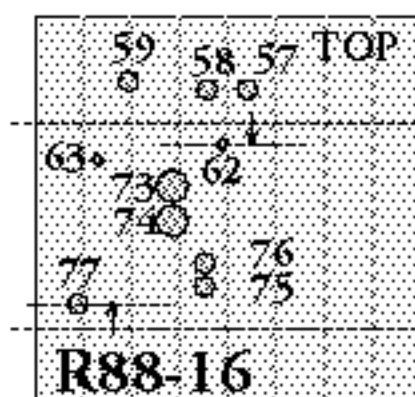
g) Target R88-8



h) Target R88-9



i) Target R88-10



j) Target R88-16

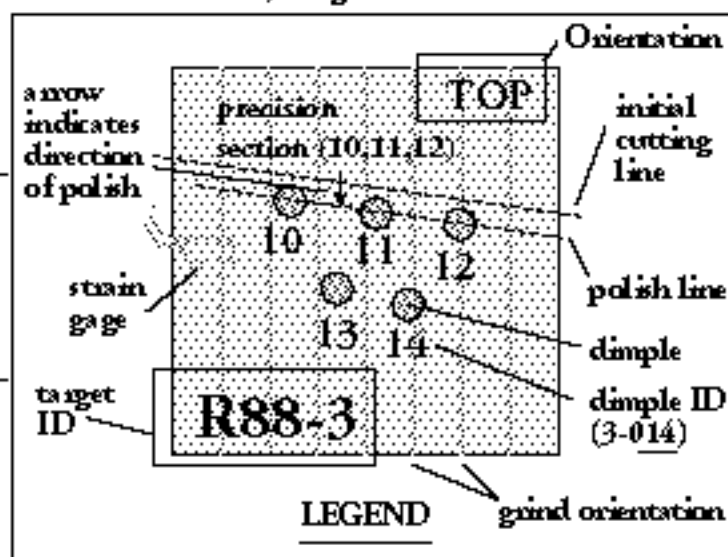


Figure B.3 – Dimple Maps, continued
Schematic of Impact Targets Showing Dimples and Precision Sections

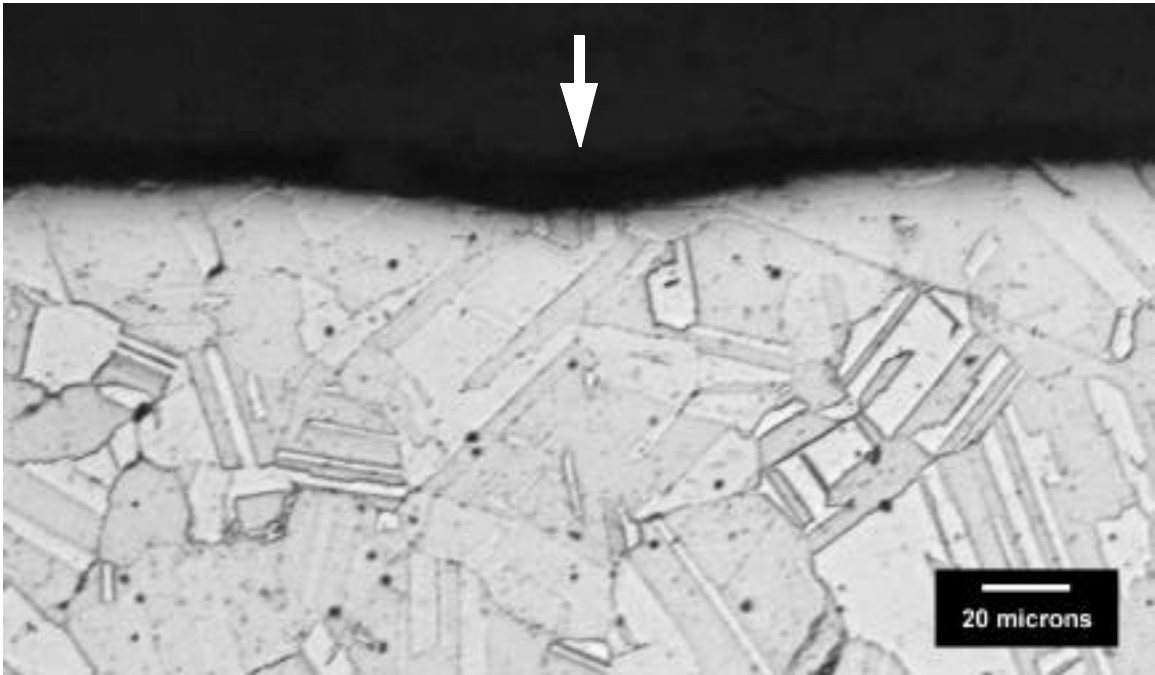


Figure B.4 Dimple #3-027, CCW14 , $V_0 = 1,350$ in/s (34 m/s), 90°

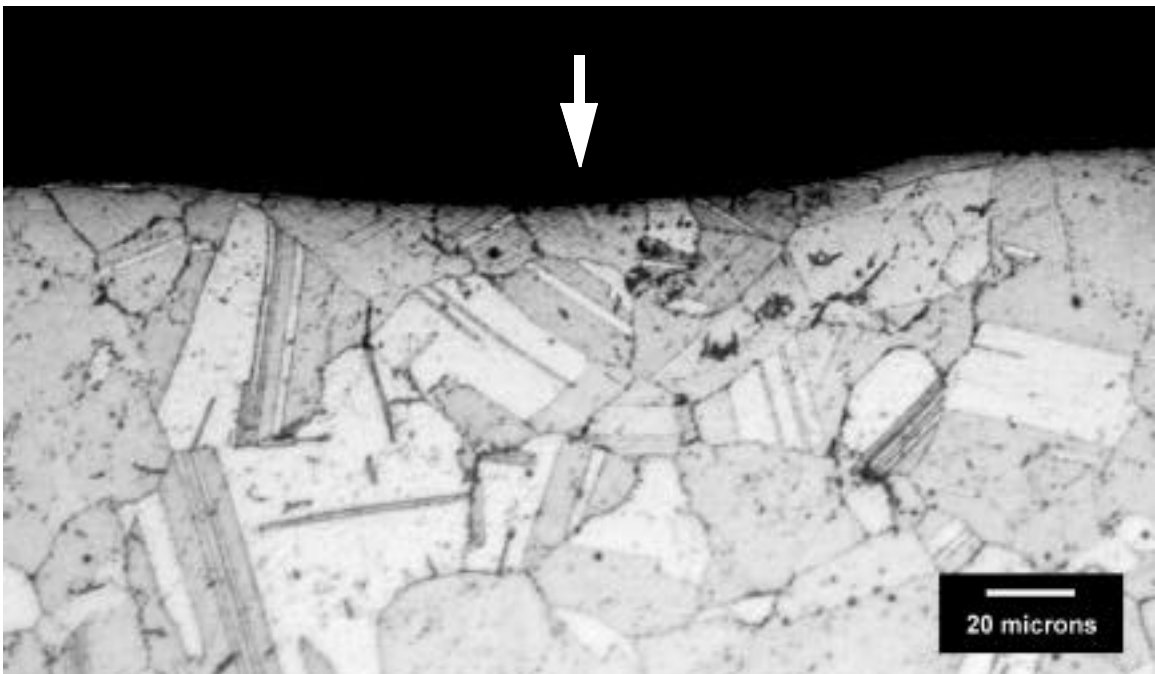


Figure B.5 Dimple #3-017, CCW14 , $V_0 = 3,440$ in/s (87 m/s), 90°

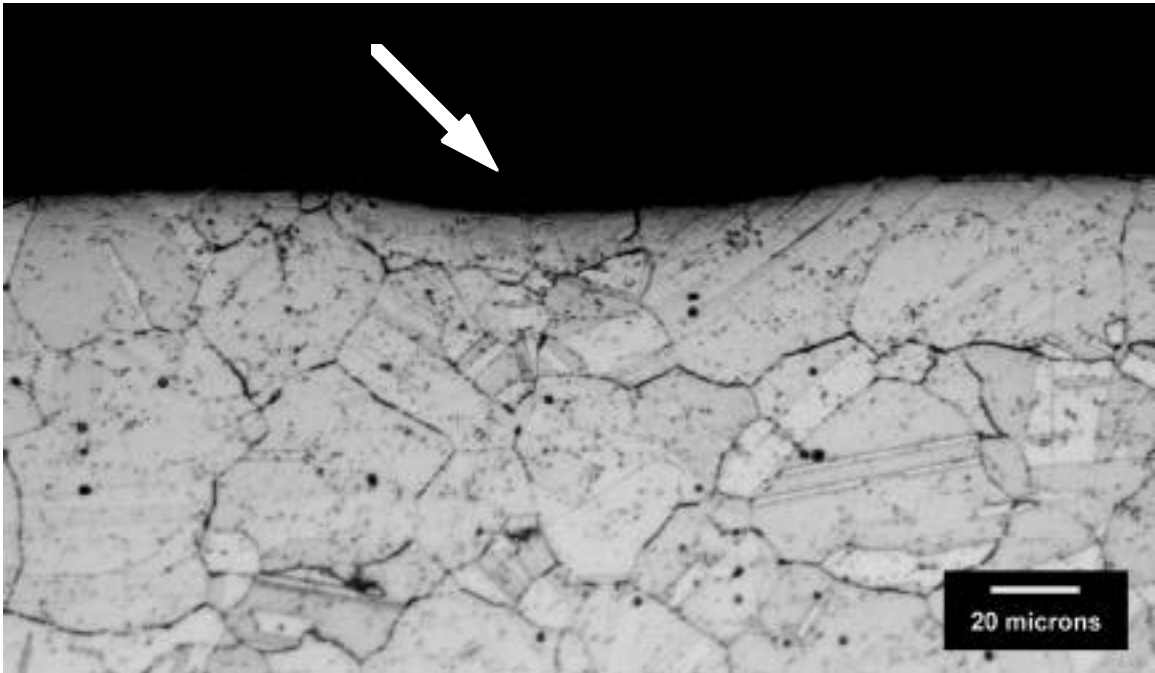


Figure B.6 Dimple #3-079, CCW14 , $V_0 = 3,700$ in/s (94 m/s), 45°
Normal velocity, $V_n = 2,616$ in/s (66 m/s)

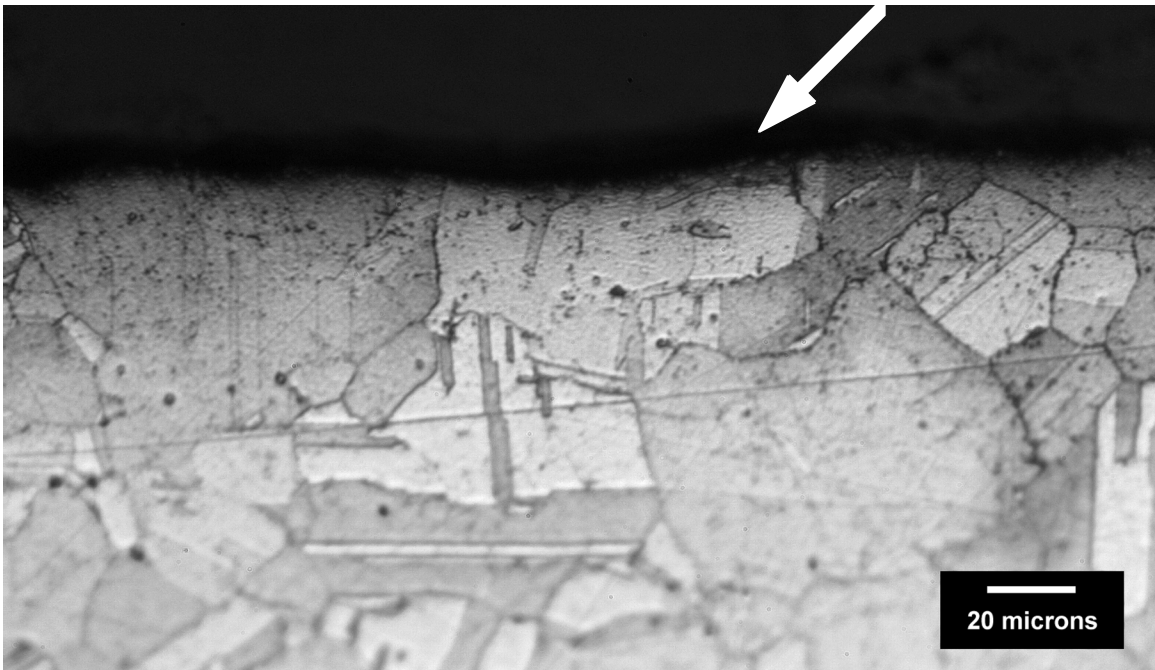


Figure B.7 Dimple #3-062, CCW14 , $V_0 = 5,260$ in/s (134 m/s), 45°
Normal velocity, $V_n = 3,720$ in/s (95 m/s)

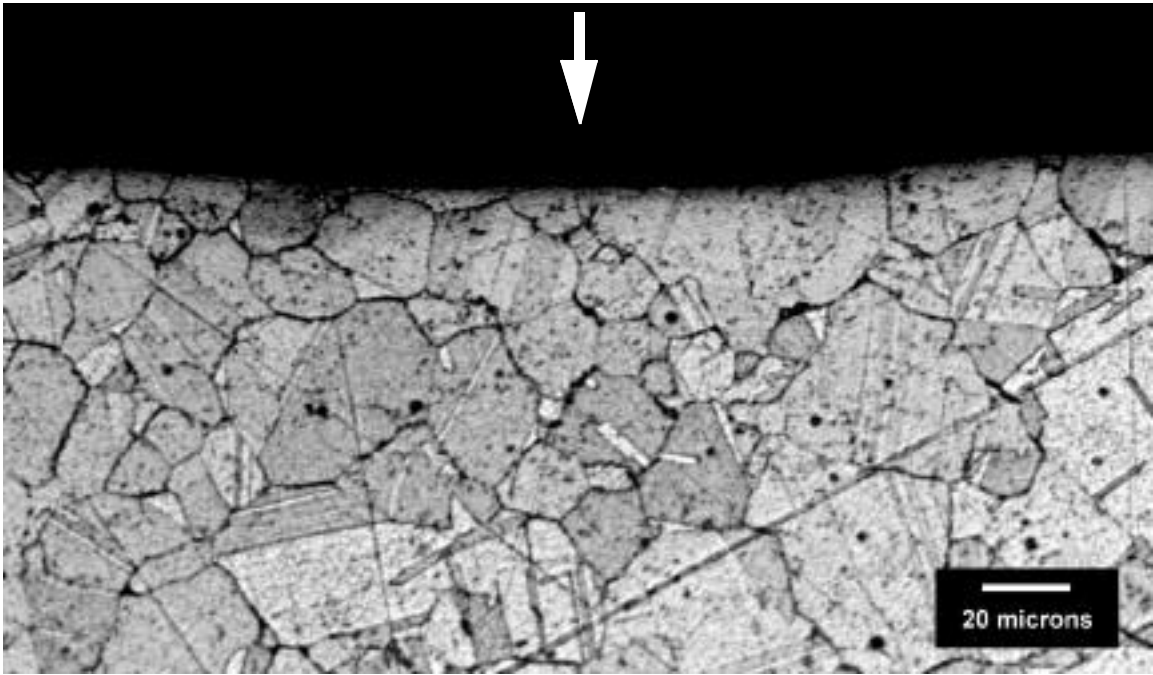


Figure B.8 Dimple #3-023, CCW31, $V_0 = 690$ in/s (18 m/s), 90°

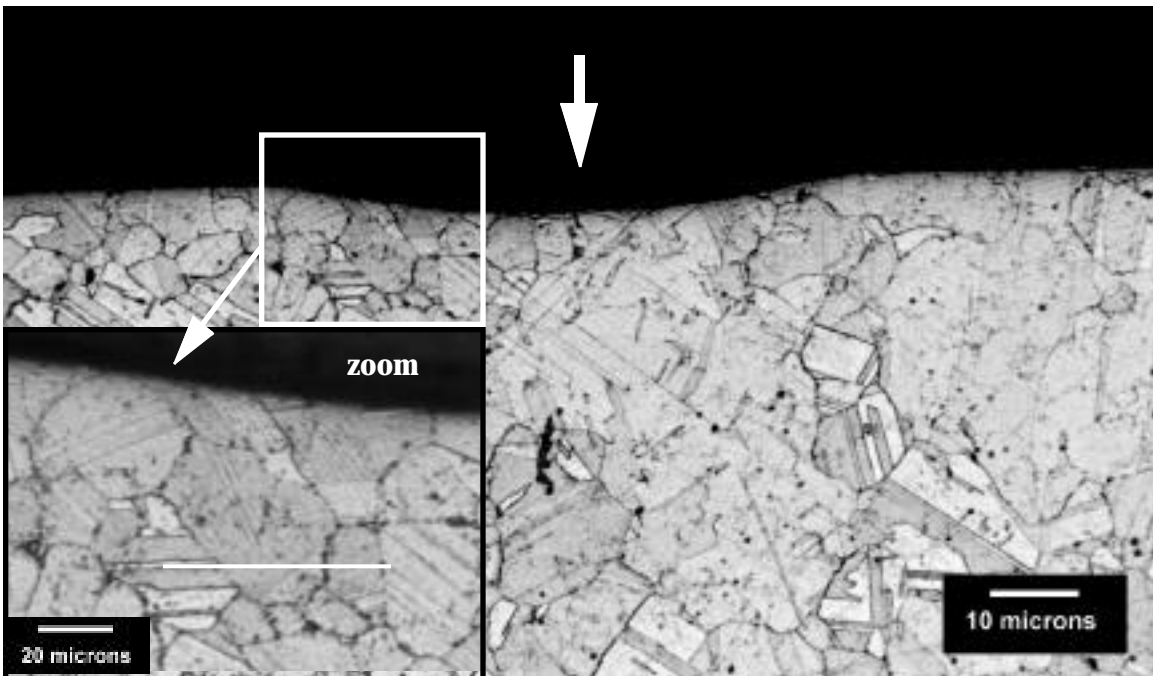


Figure B.9 Dimple #3-009, CCW31, $V_0 = 2,320$ in/s (59 m/s), 90°

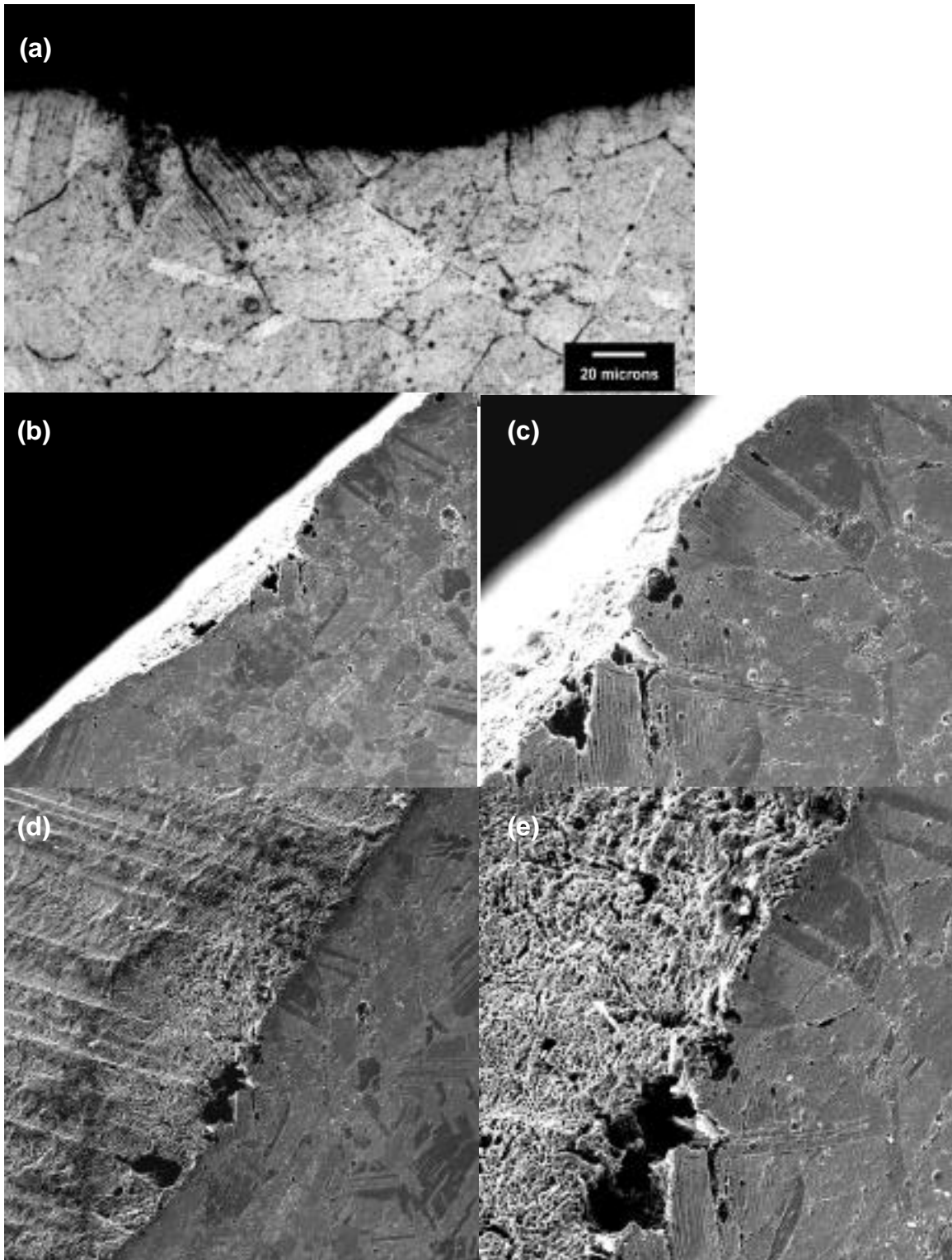


Figure B.10 Dimple #3-077, CCW31, $V_0 = 3,490$ in/s (89 m/s), 45°
Normal velocity, $V_n = 2,470$ in/s (63 m/s)
(a) optical micrograph (reduced size); (b)-(e) SEM images showing dimple and microstructure beneath dimple; (f) - next page - optical micrograph

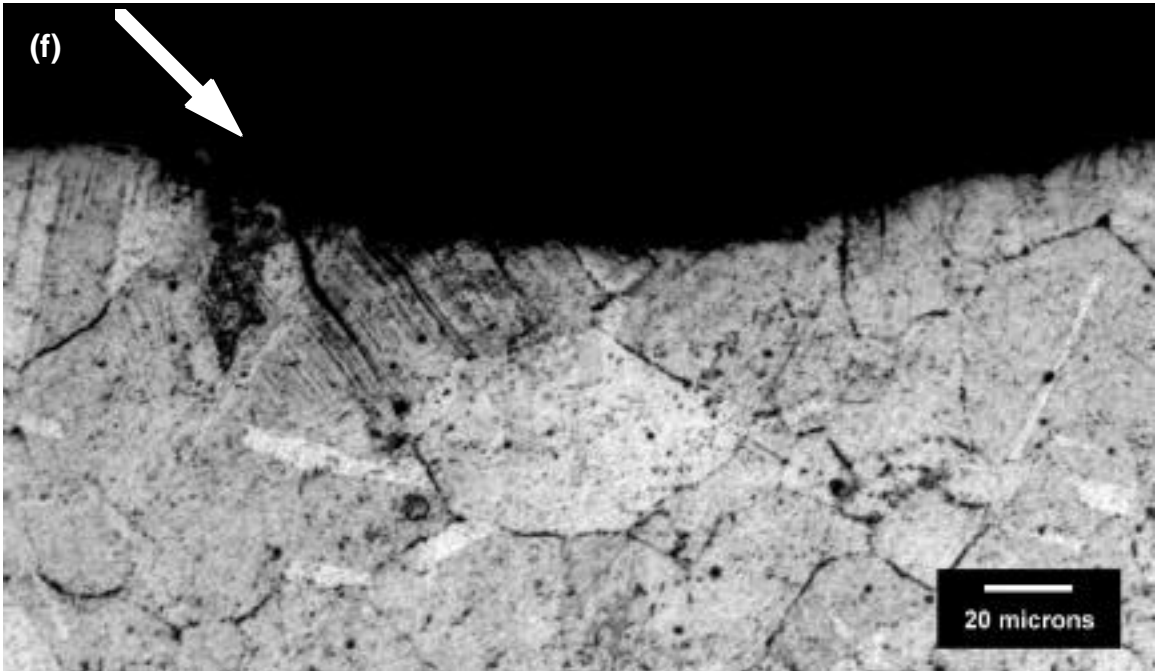


Figure B.10 (f), continued Optical Micrograph (standard size)
Dimple #3-077, CCW31, $V_0 = 3,490$ in/s (89 m/s), 45°
Normal velocity, $V_n = 2,470$ in/s (63 m/s)

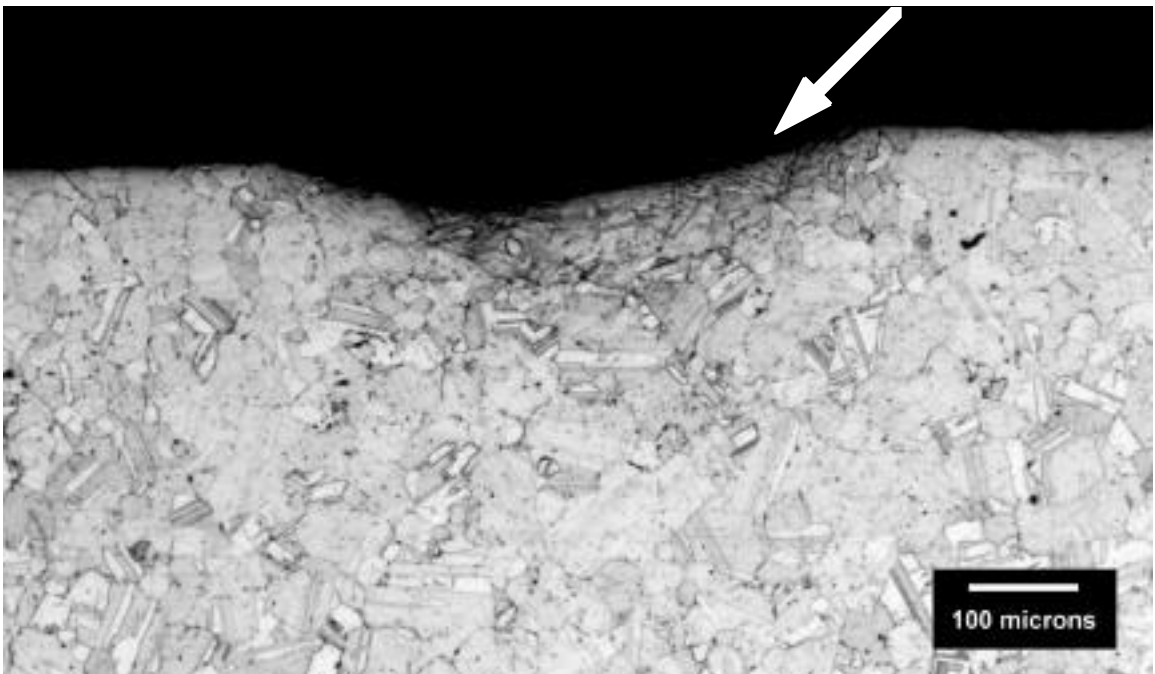


Figure B.11 Dimple #3-056, CCW31, $V_0 = 9,800$ in/s (249 m/s), 45°
Normal velocity, $V_n = 6,930$ in/s (176 m/s)

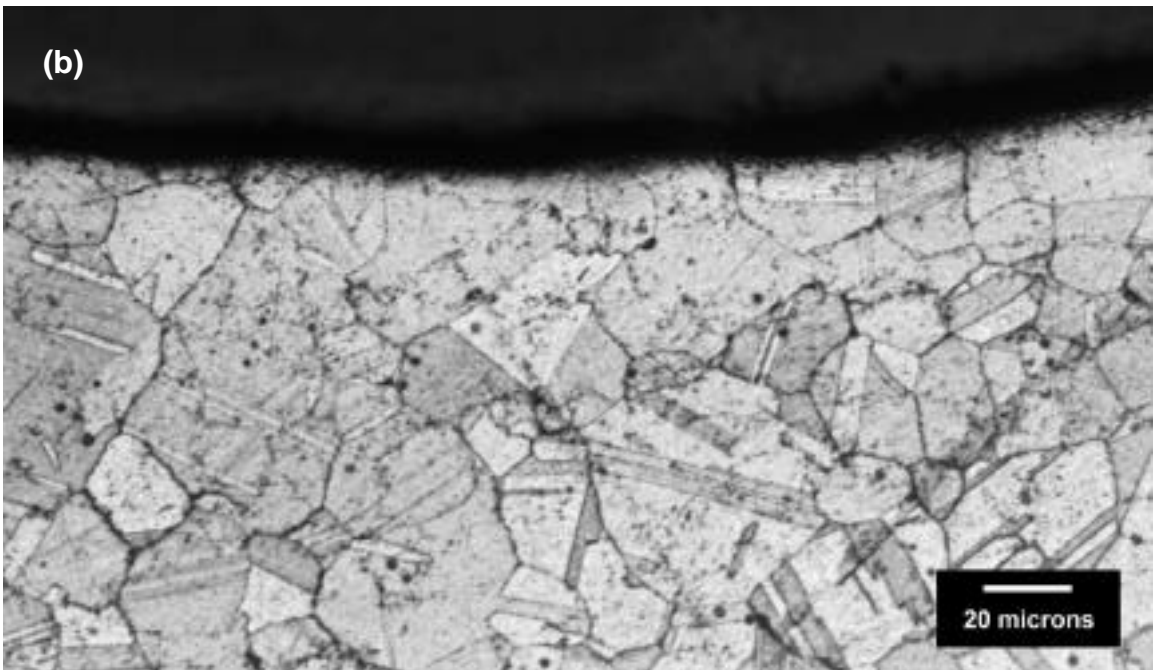
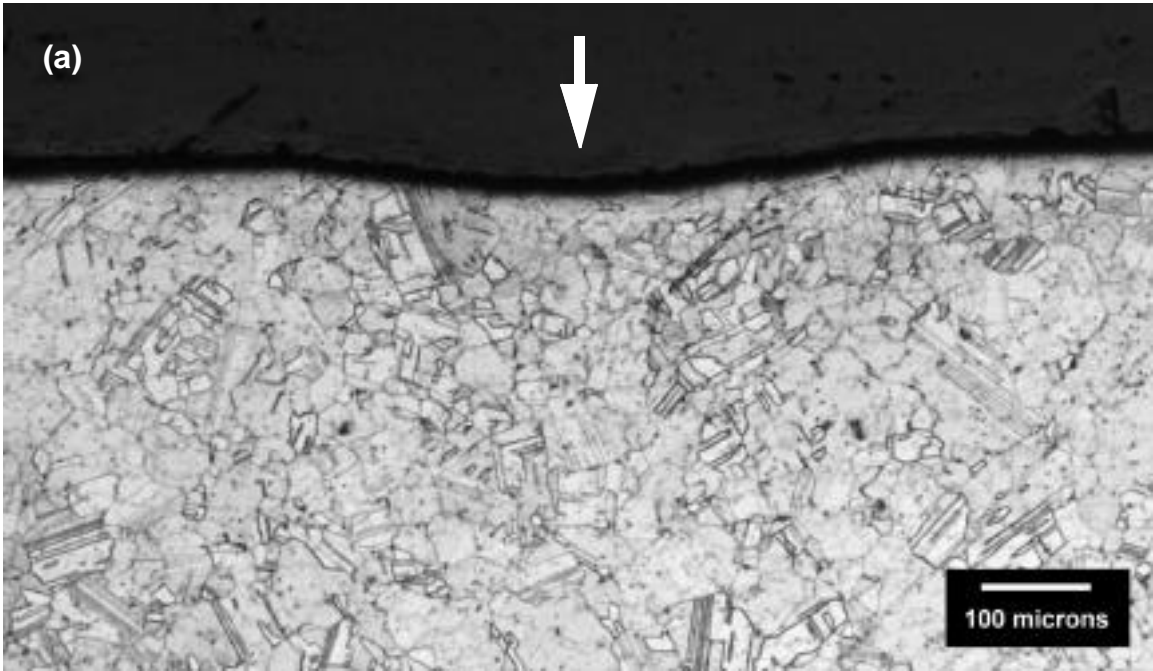


Figure B.12 Dimple #3-010, CCW52, $V_0 = 2,000$ in/s (51 m/s), 90°
(a) $100\ \mu\text{m} = 3.9$ mils; (b) $20\ \mu\text{m} = 0.8$ mils

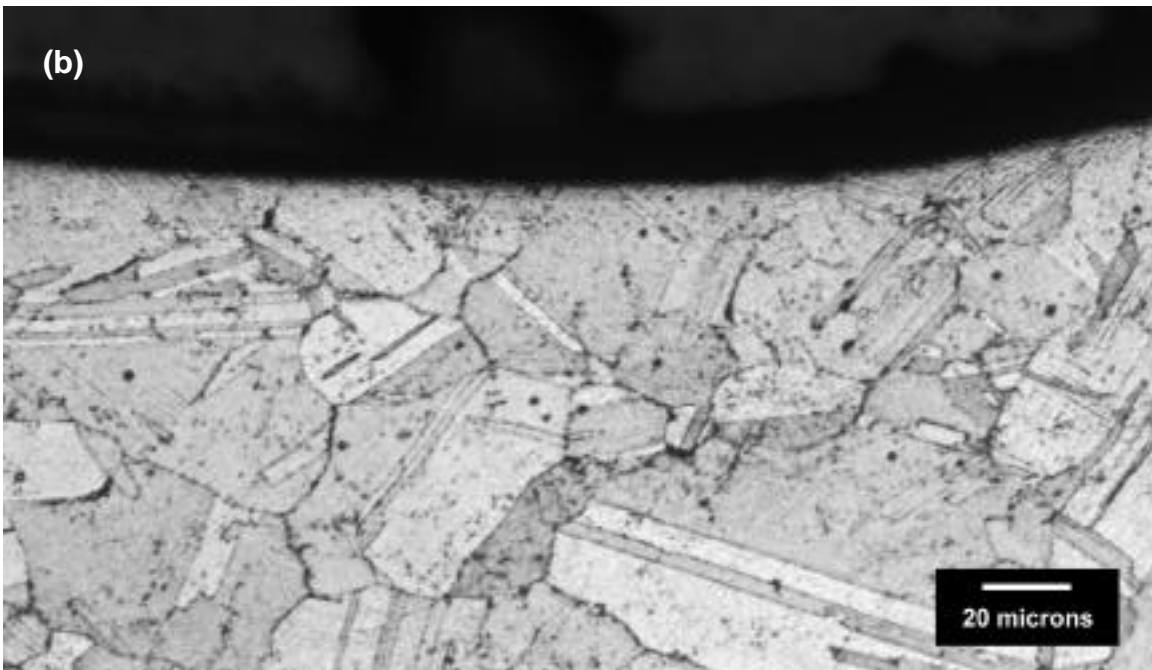
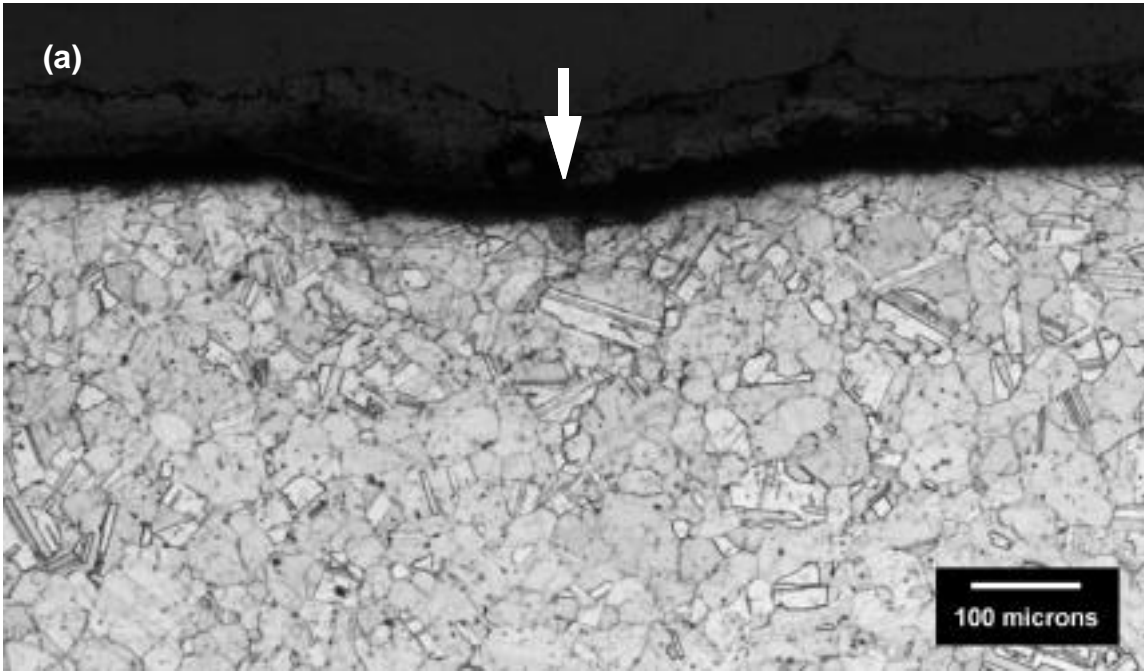


Figure B.13 Dimple #3-011, CCW52, $V_0 = 2,260$ in/s (57 m/s), 90°
(a) $100\ \mu\text{m} = 3.9$ mils; (b) $20\ \mu\text{m} = 0.8$ mils

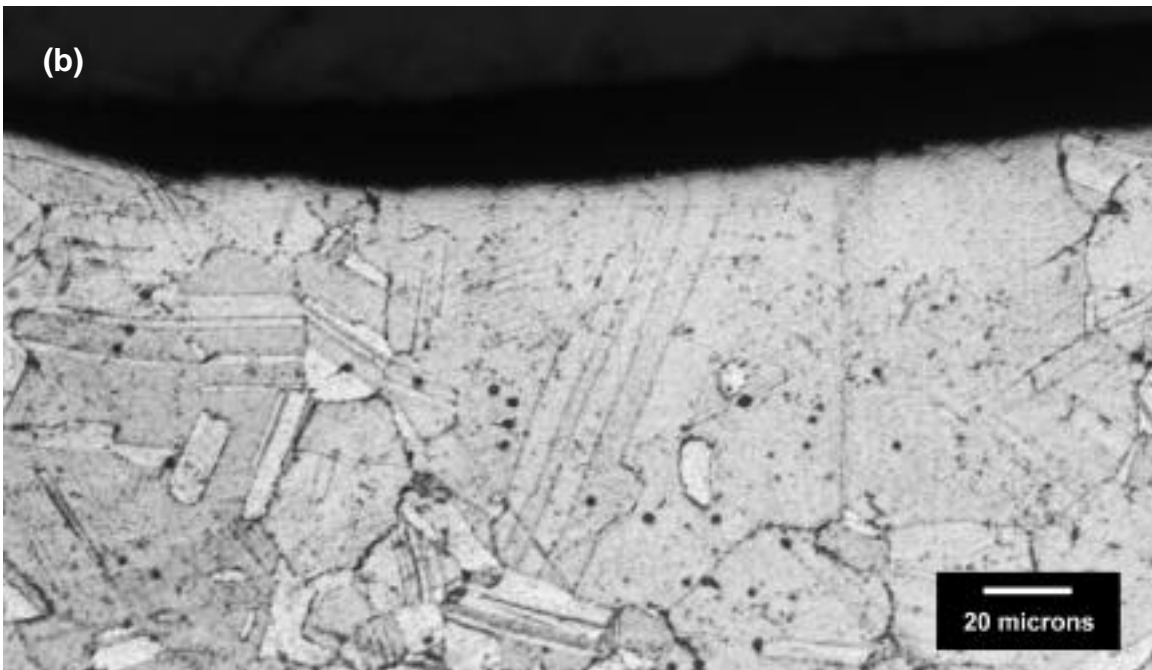
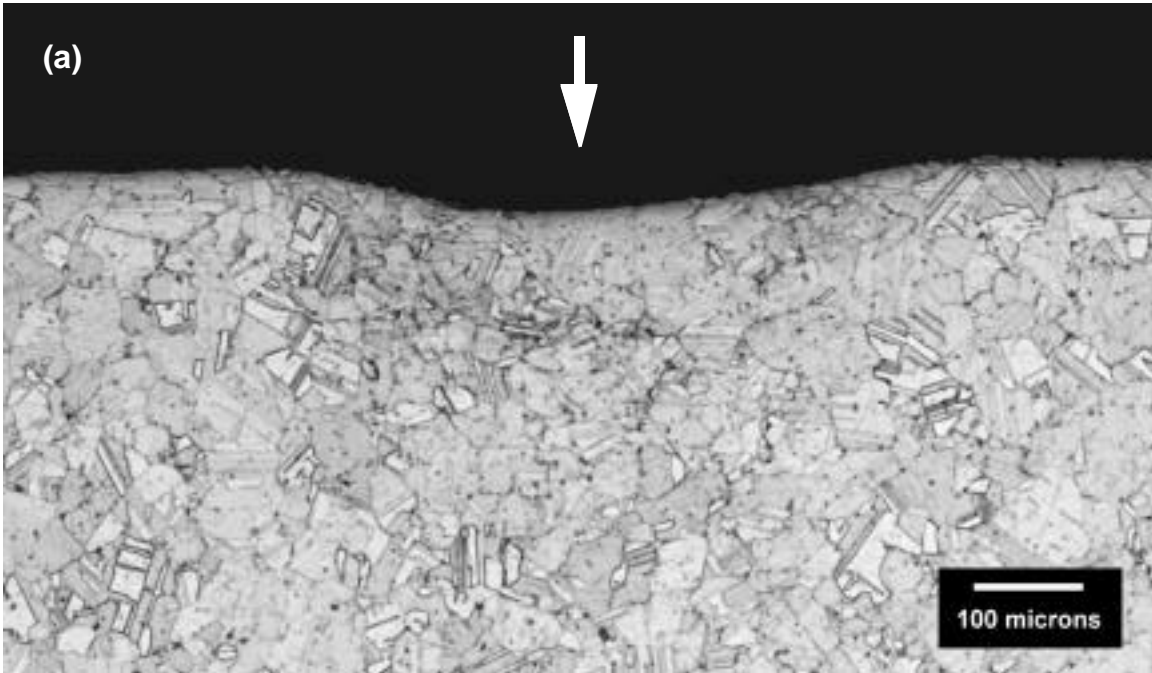
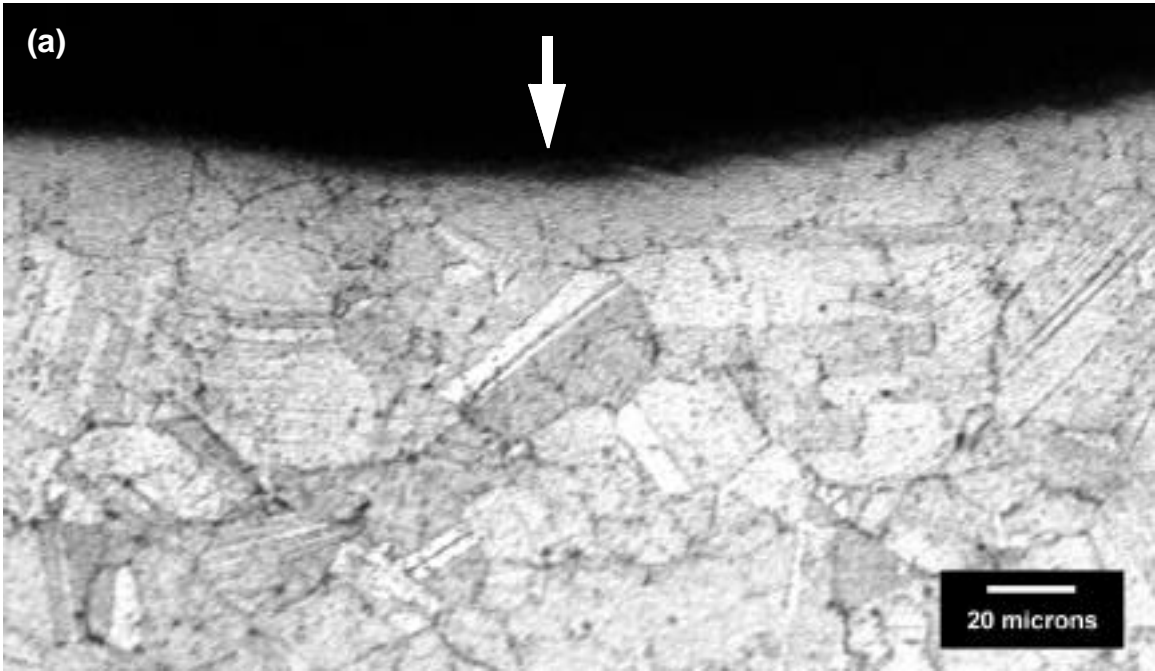
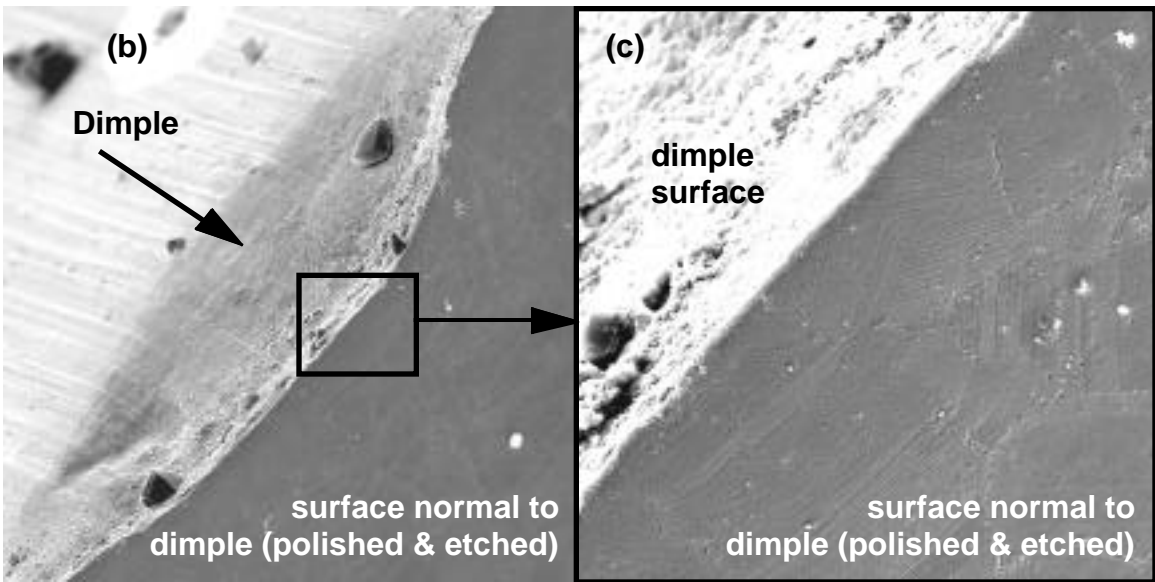


Figure B.14 Dimple #3-012, CCW52, $V_0 = 2,670$ in/s (68 m/s), 90°
(a) $100\ \mu\text{m} = 3.9$ mils; (b) $20\ \mu\text{m} = 0.8$ mils



(a) Optical micrograph. 100 μm = 3.9 mils



(b) SEM image of precision section

(c) SEM image - zoom in on rectangle.

Figure B.15 Dimple #3-001, CCW52, $V_0 = 3,690 \text{ in/s}$ (94 m/s), 90°

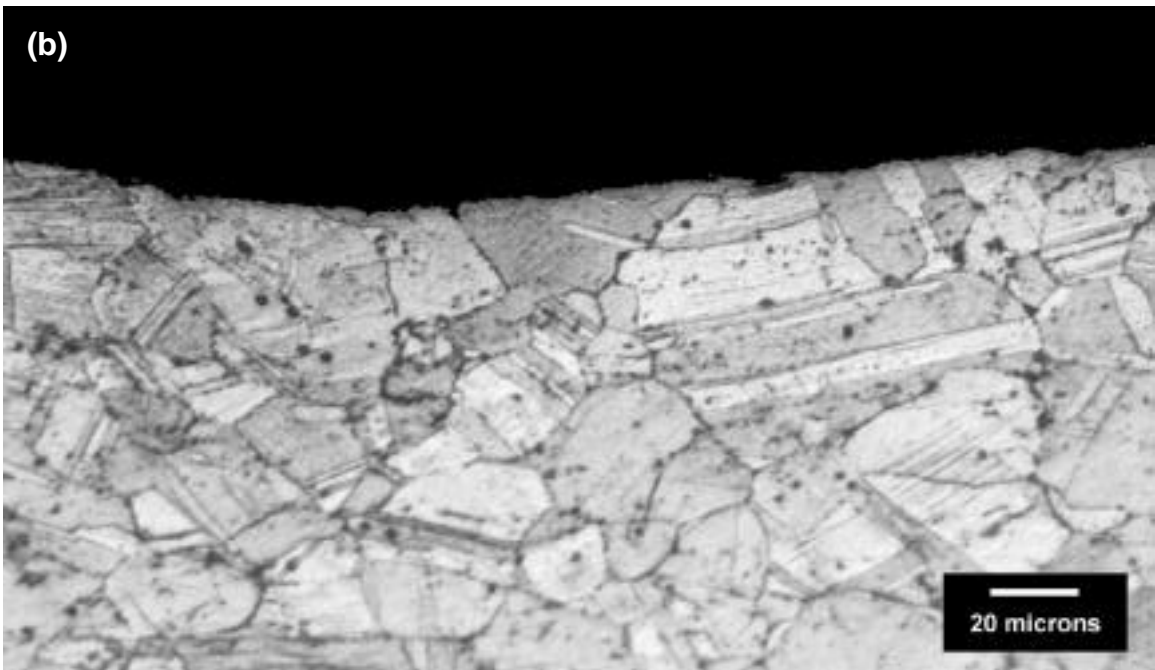
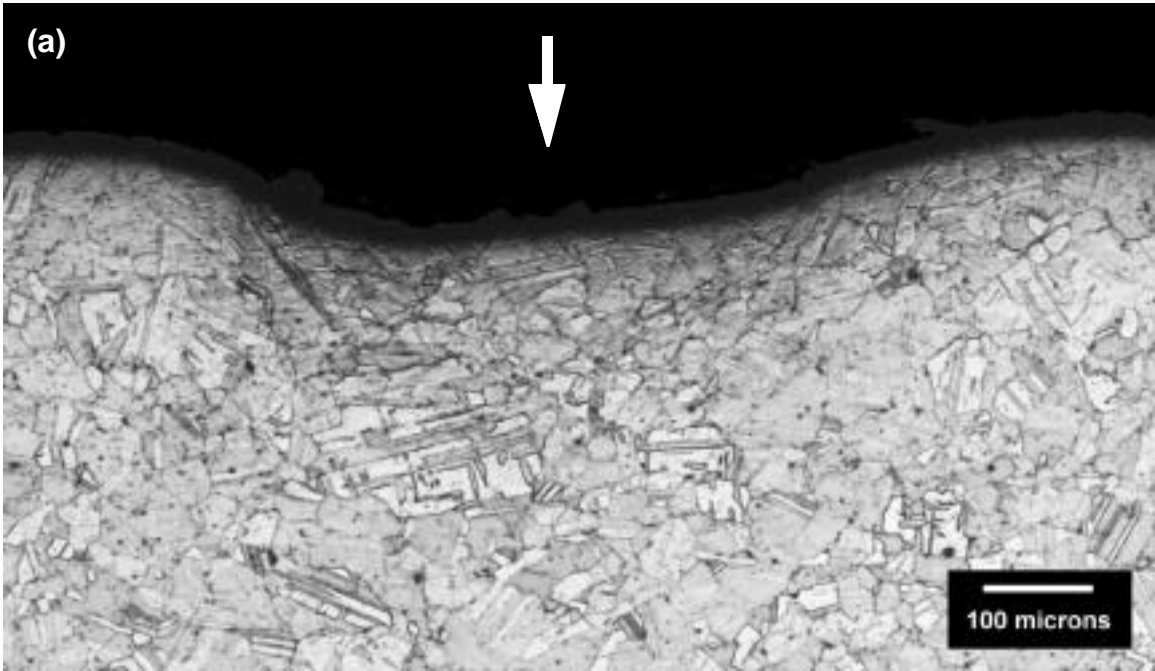


Figure B.16 Dimple #3-020, CCW52, $V_0 = 8,270$ in/s (210 m/s), 90°
(a) $100\ \mu\text{m} = 3.9$ mils; (b) $20\ \mu\text{m} = 0.8$ mils

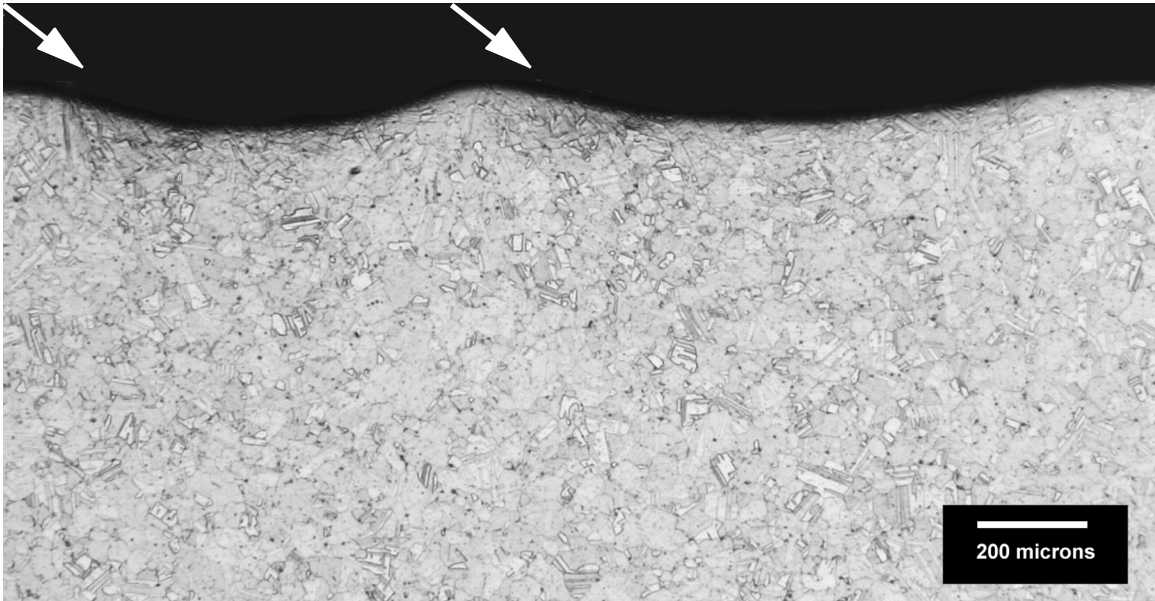


Figure B.17 Dimple #3-065 (right), CCW52, $V_0 = 8,580$ in/s (218 m/s), 45° , and Dimple #3-066, CCW52, $V_0 = 8,980$ in/s (228 m/s), 45° (left)

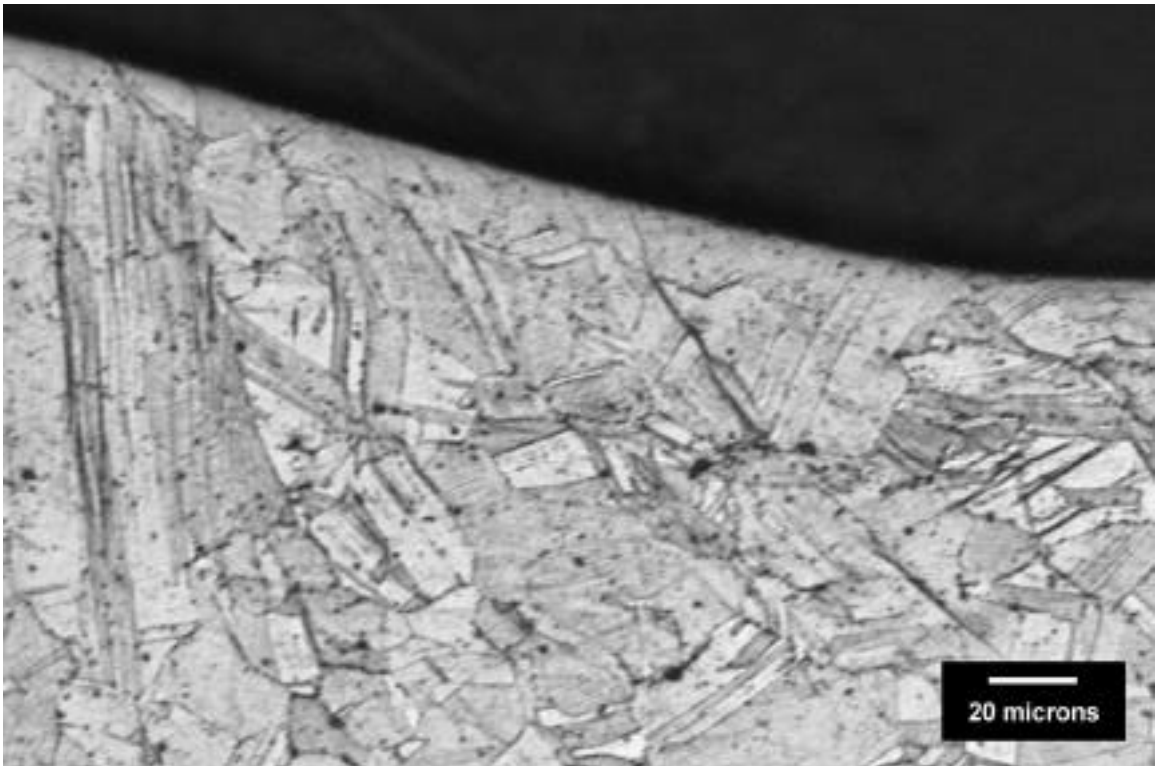


Figure B.18 Dimple #3-066 (zoom), CCW52, $V_0 = 8,980$ in/s (228 m/s), 45°
Normal velocity, $V_n = 6,350$ in/s (161 m/s)

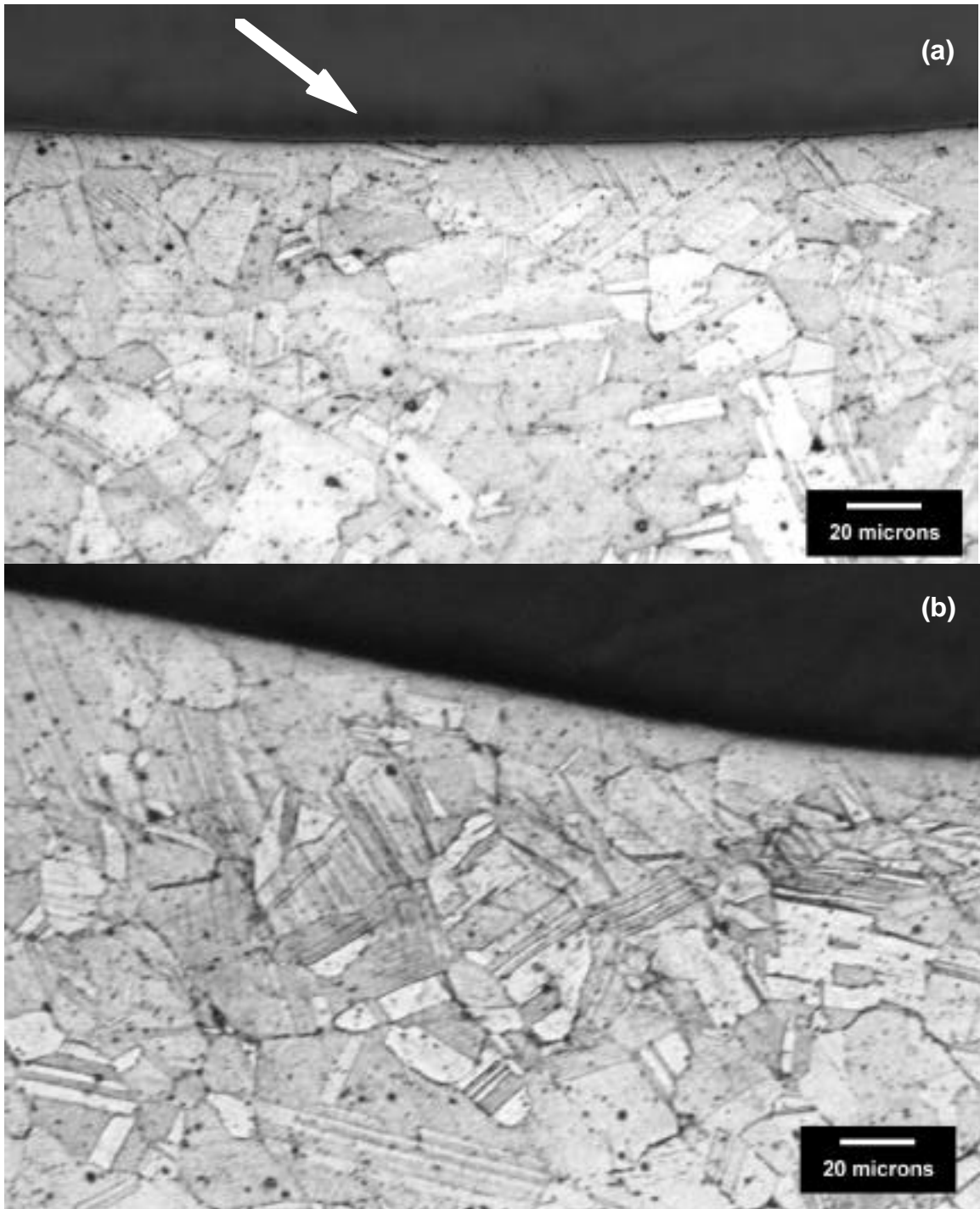


Figure B.19 Dimple #3-065, CCW52, $V_0 = 8,580$ in/s (218 m/s), 45°
Normal velocity, $V_n = 6,060$ in/s (154 m/s)
(a) zoom underneath dimple center; (b) zoom of dimple edge

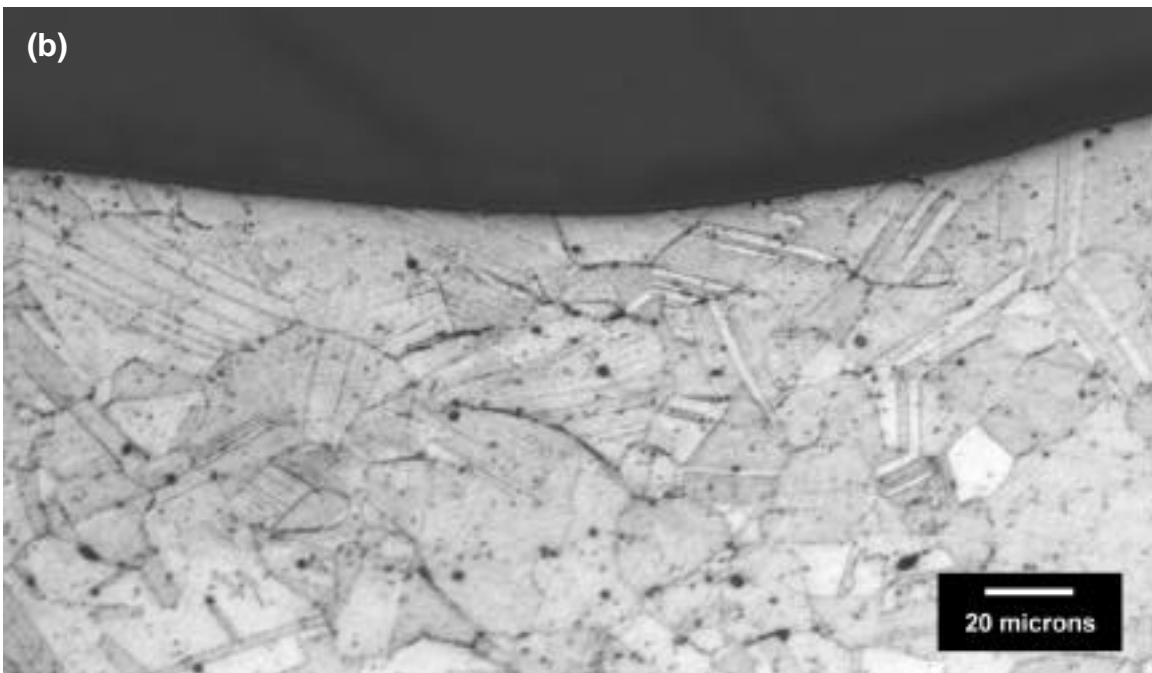
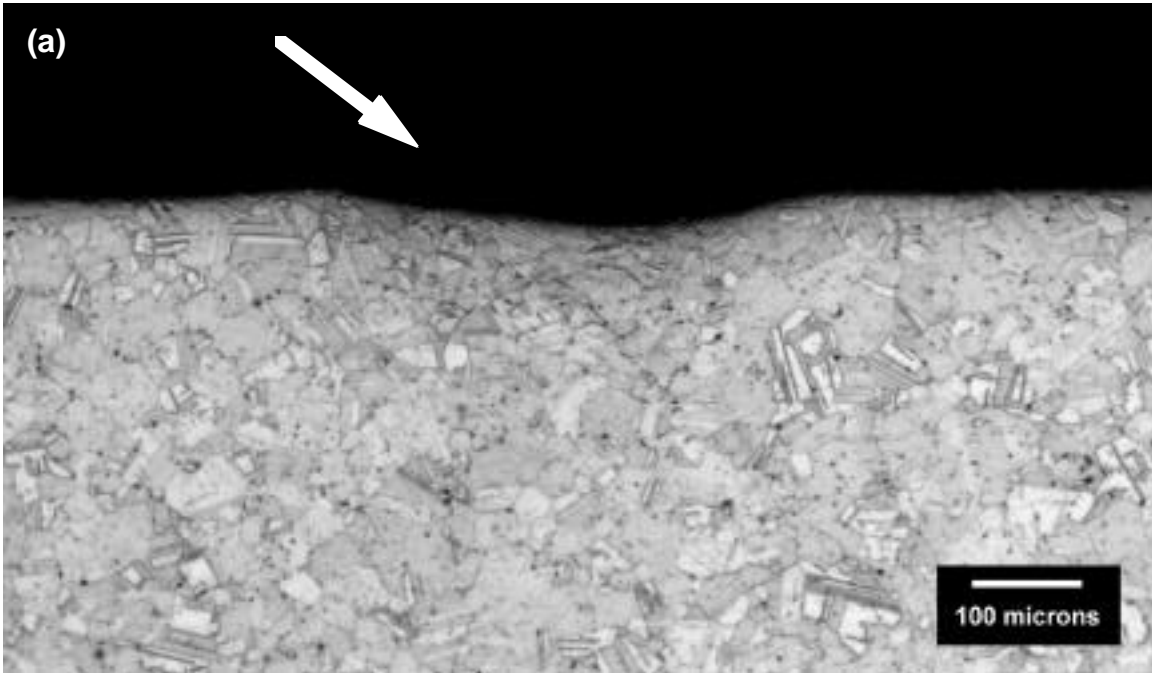


Figure B20 Dimple #3-068, CCW52, $V_0 = 3,770$ in/s (96 m/s), 45°
Normal velocity, $V_n = 2,670$ in/s (68 m/s)
(a) $100\ \mu\text{m} = 3.9$ mils; (b) zoom underneath dimple center

B.5.4 Estimation of Impact Stress Using Impact Dynamics

Since the strain rates involved in shot peening are fairly high, ranking in the dynamic high to hypervelocity impact range according to Table 1.1, it is useful to estimate the stress at impact using impact dynamics. Note that several references were used, and nomenclature varies slightly between references. It should be noted that the equations presented are generally used with macro projectiles, such as flyer plates, and not microparticles such as shot peen balls. An adjustment is added at the end to account for the additional stress concentration due to the spherical particle shape.

Using impulse and conservation of momentum, the pressure or stress, P , generated in a target at impact can be expressed as [42]:

$$P = \rho^* U_s u_p \quad (\text{B.2})$$

Where ρ^* is the force density of the target, U_s is the shock wave velocity in the target, and u_p is the velocity of particles in the target immediately after impact (not the projectile velocity, V_0). This equation assumes a body initially at rest, i.e. no previously generated shock waves acting. Typically, experimental data is obtained to evaluate U_s and u_p . But, it is possible to estimate these values using basic material properties.

U_s is normally defined as shown in equation (B.3) using experimentally determined coefficients, C_0 and S [42].

$$U_s = C_0 + S u_p \quad (\text{B.3})$$

C_0 is approximately the elastic longitudinal wave velocity in a semi-infinite medium. At low velocities, the data vary slightly from this linear form, resulting in higher shock velocities than predicted using the equation.

The wave velocity in a semi-infinite body can be estimated by [42]:

$$C_0 = \sqrt{\frac{E(1-\nu^*)}{\rho^*(1+\nu^*)(1-2\nu^*)}} \quad (\text{B.4})$$

This is often used to estimate the shock velocity in the target. Normally the projectile does not fit the description of a semi-infinite body. For a long bar or rod, the wave equation produces a reduced estimate of the wave velocity, denoted as C_{bar} [42]:

$$C_{bar} = \sqrt{\frac{E}{\rho}} \quad (B.5)$$

The wave velocities calculated have been for longitudinal waves. It is also possible to calculate velocities for shear waves and Rayleigh (surface), waves.

The particle velocity, u_p , is most accurately obtained using experimental data in the form of Pressure-Velocity relations for the projectile and target. For more details, see Meyers, *Dynamic Behavior of Materials* [42]. A schematic is given in Figure B.3. In the absence of data, the curves can be approximated using equation B.2. The shock wave velocity, U_s or C_0 , can be estimated depending on the geometry involved. For a longitudinal wave in a semi-infinite medium, C_0 is used as an estimate using equation (B.4). For the projectile, the bar wave velocity given by equation (B.5) can be used.

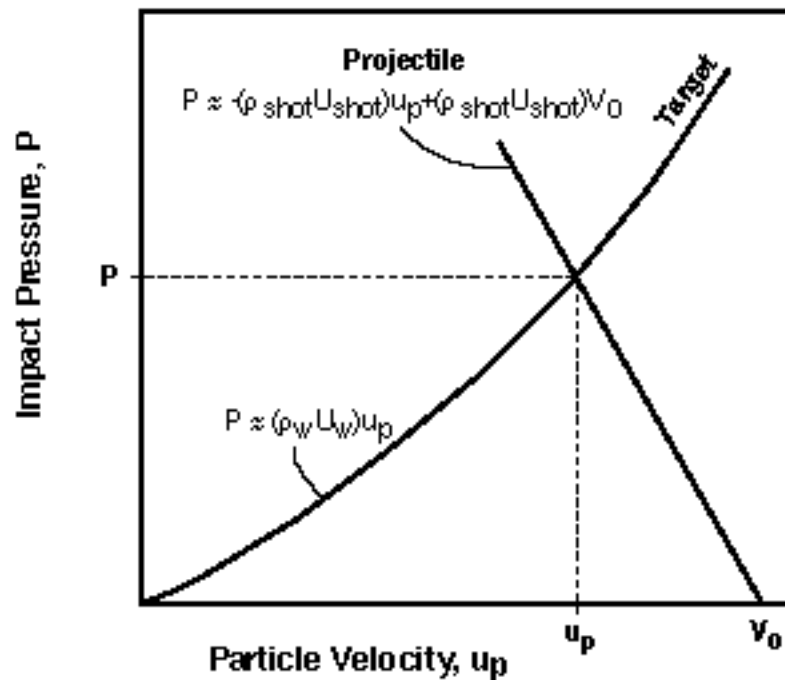


Figure B.21 – Schematic of Impact Pressure vs. Particle Velocity Diagram

The pressure-velocity diagram is constructed by placing the curve for the target at the origin. The slope of the projectile curve is made negative, and the curve is located on the x axis (velocity axis) at the initial projectile velocity, V_0 . The equations of the two curves can be expressed as:

$$\text{target:} \quad P = \left({}^*U_w \right) u_p \quad (\text{B.6})$$

$$\text{projectile:} \quad P = - \left({}^*U_{shot} \right) u_p + B \quad (\text{B.7})$$

$$\text{where} \quad B = \left({}^*U_{shot} \right) V_0 \quad (\text{B.8})$$

The point at which the curves cross gives the pressure, P, and particle velocity, u_p , at impact.

$$u_p = V_0 \frac{{}^*U_{shot}}{{}^*U_{shot} + {}^*U_w} \quad (\text{B.9})$$

$$P = {}^*U_w u_p = {}^*U_w V_0 \frac{{}^*U_{shot}}{{}^*U_{shot} + {}^*U_w} \quad (\text{B.10})$$

where

$$U_w = C_{0,w} = \sqrt{\frac{E_w(1-w)}{{}^*w(1+w)(1-2w)}} \quad (\text{B.11})$$

$$U_{shot} = C_{bar,shot} = \sqrt{\frac{E_{shot}}{{}^*shot}} \quad (\text{B.12})$$

For comparison of impact response between alloys, it is useful to normalize the impact stress by a material property characterizing onset of plastic deformation. For quasi-static events, the 0.2% yield strength is an appropriate property. For high strain-rate events, the Hugoniot Elastic Limit (HEL) represents the stress above which plasticity occurs. It is normally obtained through experimental data. In the absence of test data for the HEL, the yield strength will be used. By normalizing the impact stress, P, by the yield strength, a normalized parameter, P^* , is obtained which represents the severity of impact event relative to the material capability.

$$P / y = \frac{{}^* U_w V_0 \frac{{}^* U_{shot} U_{shot}}{{}^* U_{shot} + {}^* U_w}}{y} \quad (B.13)$$

This does not account for the additional stress concentration generated by the small, spherical shape of the projectile. These effects are estimated by defining a stress concentration factor calculated from dimple geometry using Equation (2.20) as modified below:

$$K_t = 1 + 4.0 \left(h / (2b) \right)^{1.3} \quad (B.14)$$

The resulting expression for a normalized, adjusted impact stress is given by:

$$P^* = K_t P / y = \frac{K_t {}^* U_w V_0 \frac{{}^* U_{shot} U_{shot}}{{}^* U_{shot} + {}^* U_w}}{y} \quad (B.15)$$

Note that this equation predicts impact stress to increase linearly with impact velocity and K_t , and to decrease linearly with increasing yield strength.

Of the terms represented in equation B.15, the **impact velocity**, V_0 , appears to have the greatest potential effect. From Figure 4.10 and the corresponding regression curve fits of production velocity data, a minimum velocity of 630 in/s is estimated for ccw14 shot at 6N (2A) intensity, 90° impact, whereas a maximum velocity of 4,400 in/s is estimated for ccw14 shot at 10A intensity, 45° impact. Thus, velocity changes can account for a 7X change in impact stress over this range (4,400/630).

Changes of yield strength from 150 ksi to 200 ksi would result in a 0.75X change (or 1.33X for a 200 ksi to 150 ksi change). Since yield strength generally increases with decreasing grain size, it can be inferred that alloys with larger grain sizes (lower yield strengths) will exhibit more sensitivity to peening conditions than finer grain alloys.

K_t 's measured to date ranged from 1.15 to 1.5 for conditioned cut wire shot, a relatively small effect compared with velocity.

For different alloys systems, such as Titanium, the relative magnitude of shot density to target density, and differences in elastic material properties may become significant to predicted impact stress trends.

The normalized impact stress was plotted in Figure 4.5 against the measured / calculated dimple depth, using equation B.16 for the calculated dimple depth.

$$h_{calc} = \frac{1}{2} \left(D - \sqrt{D^2 - d^2} \right) \quad (B.16)$$

This assumes a spherical dimple, of diameter D corresponding to the shot diameter. The minimum shot diameter, W, is used for D. Thompson's relation is used to calculate the dimple diameter, d, from shot velocity, shot diameter and material properties.

B.5.5 Transient Temperature Measurements

In order to obtain measurements of the transient temperature rise at impact, an array of 16 high speed infrared detectors were used for a subset of the experiments. The setup used is essentially the same as that used by Zehnder, Ramamurthy, Bless and Brar [78] for measurement rise in automotive paint finishes due to impact of stones. Figure B.21 shows the experimental setup. First, a calibration curve was obtained for the target material, relating detector voltage to temperature rise. From this information, voltage measurements could be converted into temperature readings.

An array of sixteen detectors, each 0.0032 by 0.0032 inches arranged in a single line at 0.00394 inch spacing was used. This resulted in a target area of only 0.0032 inches high by 0.063 inches wide. Successful tests required that detectors be focused on the area of impact. The extremely small projectile sizes and variations in projectile flight path made it difficult to get a direct hit on the target area on which the sensors were focused. Successful measurements were obtained for three tests: two using large ccw52 shot, one with medium ccw31 shot. It was not possible to obtain temperature rise measurements during the impact of the smallest shot size, ccw14.

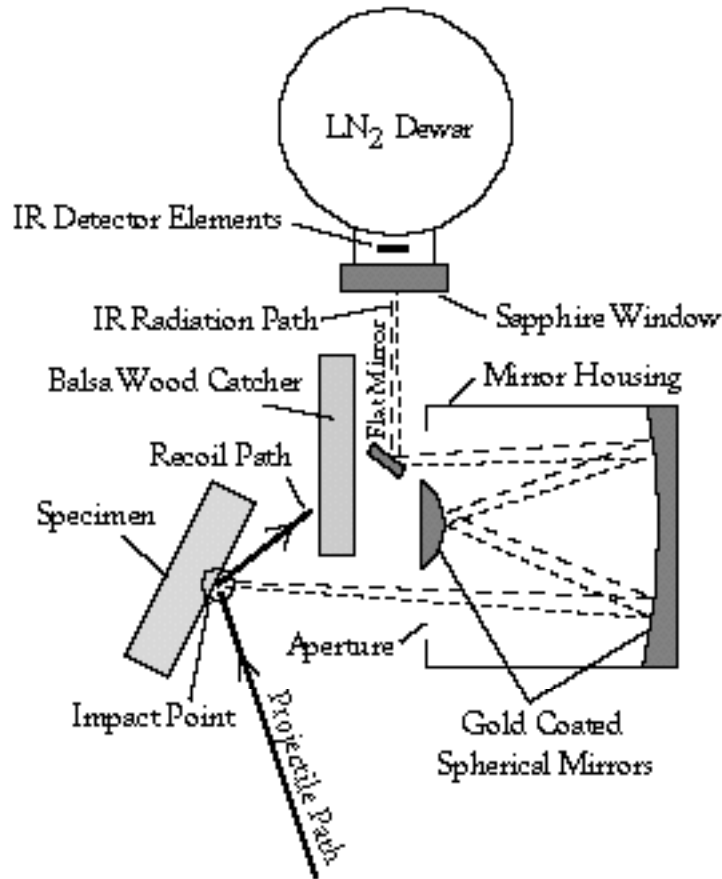
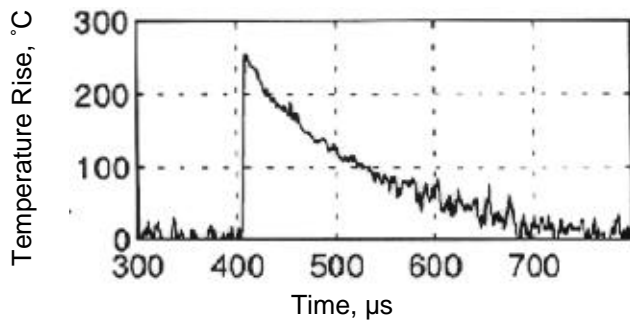


Figure B.22 – Schematic of Experimental Setup for Measuring Impact Temperature

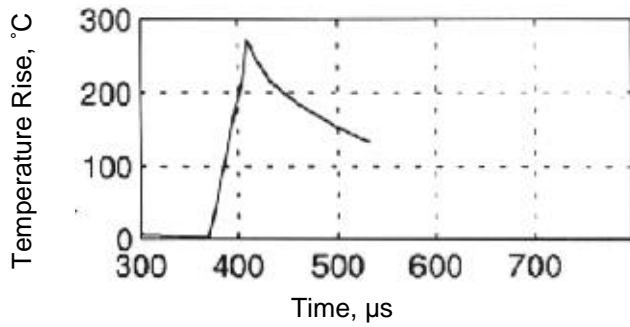
Table B.6 lists the test conditions for which successful temperature measurements were obtained. Figures B.22 - B.24 give the temperature profiles for the three successful tests. Temperatures exceeding 600°F were recorded, even though the very high strain rates corresponding to the small shot impacts at 10A intensity were not reached. This indicates that significant temperature rise and strain localization can be achieved by a single impact.

Table B.6 – Test Conditions for Successful Transient Temperature Measurements

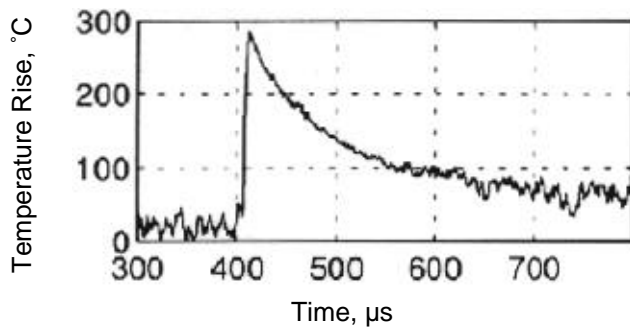
Test Number	Shot Size	Incident Velocity	Max. T (°C)	Estimated depth of heating
3-037	CCW52	7,350 in/s (191 m/s)	300°C (572°F)	0.0009 inches
3-038	CCW52	9,500 in/s (242 m/s)	330°C (626°F)	0.0011 inches
3-056	CCW31	9,800 in/s (249 m/s)	290°C (554°F)	0.0003 inches



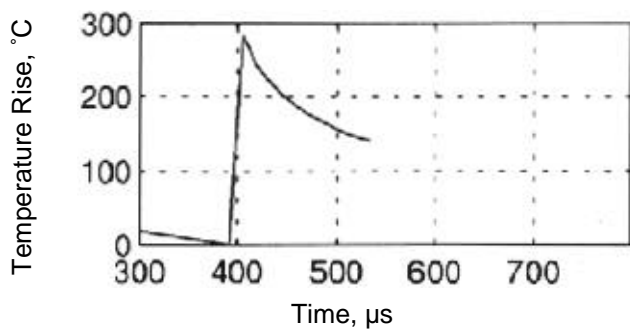
a) Channel 10



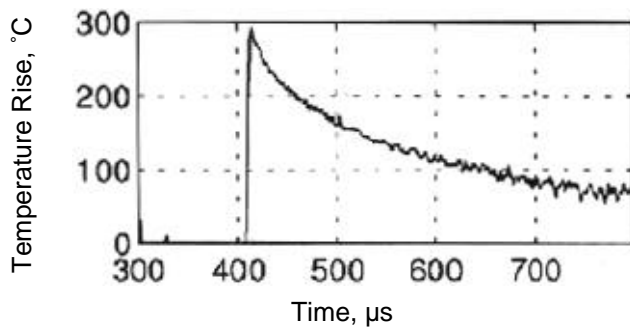
b) Channel 11



c) Channel 12

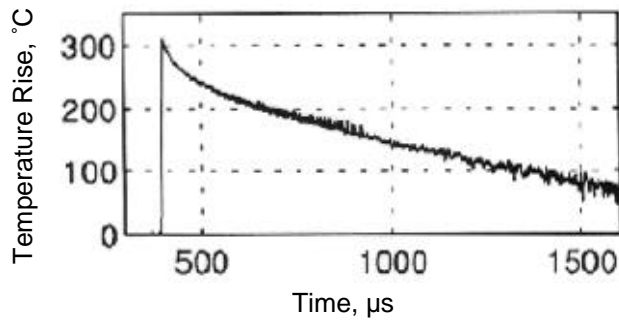


d) Channel 13

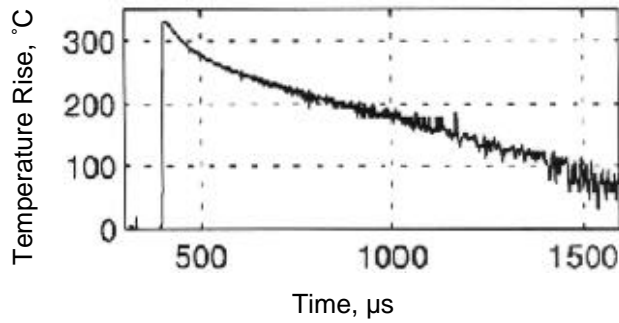


e) Channel 14

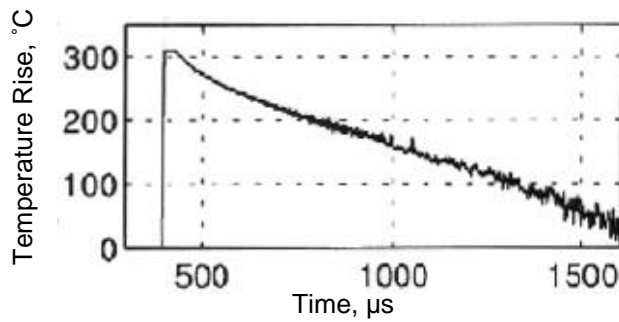
Figure B.23 Test #3-037, ccw52, V0=7,530 in/s (191 m/s), 45°



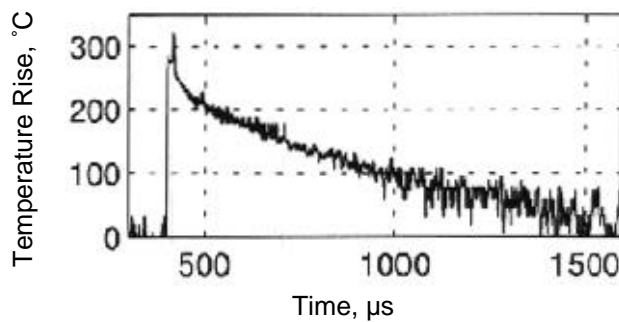
a) Channel 2



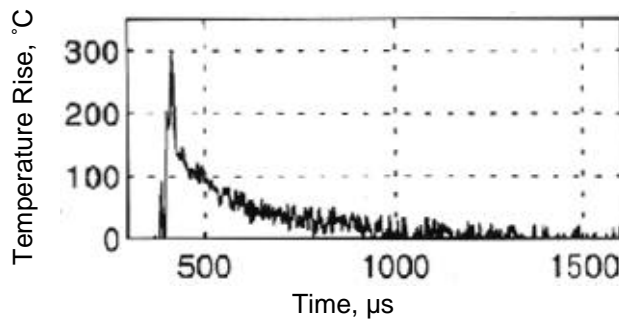
b) Channel 3



c) Channel 4

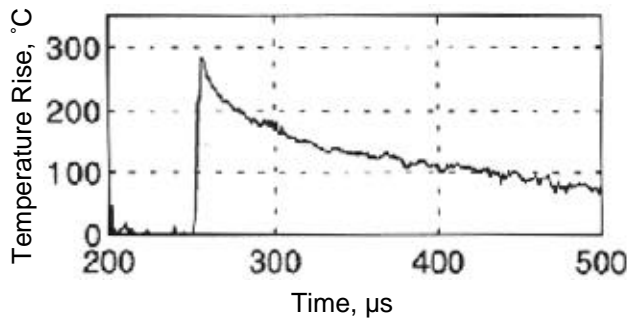


d) Channel 5

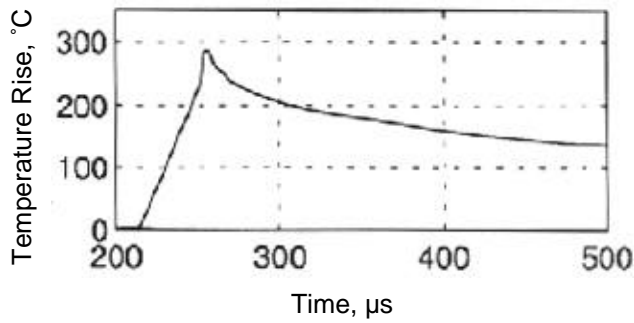


e) Channel 6

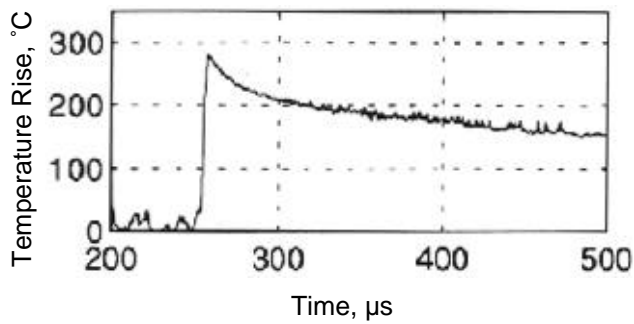
Figure B.24 Test #3-038, ccw52, V0=9,500 in/s (241 m/s), 45°



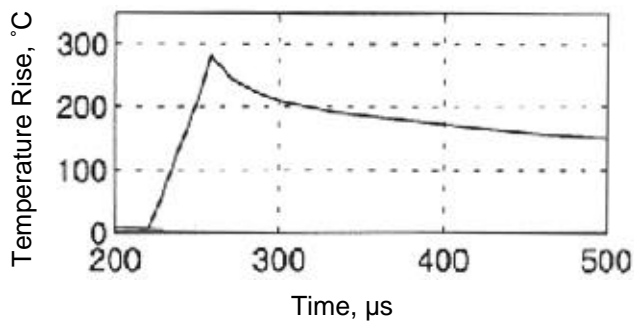
a) Channel 10



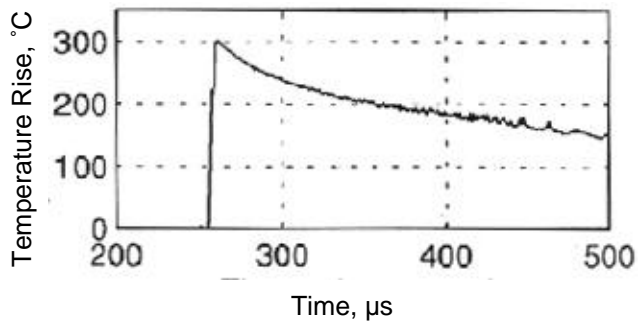
b) Channel 11



c) Channel 12



d) Channel 13



e) Channel 14

Figure B.25 Test #3-056, ccw31, V0=9,800 in/s (249 m/s), 45°

B.5.6 Derivation of Plastic Strain Estimate and Sample Dimple Profiles

Note: the **nomenclature** for this section is self-contained; terms introduced to describe spherical sectors, surface areas, dimple radii, etc., are not referenced outside this section. To simplify documentation, terms are defined in Figures B.26 and B.27, and in the text.

Popp and Thompson [79] developed a damage parameter based on estimated plastic strain derived from geometric considerations of dimple deformation. A similar approach was used by Timothy and Hutchings to characterize dimple volume due to impact [22]. The resulting parameter, $p = d^2 / (8D^2)$, provides a non-dimensional parameter which has equivalent elements to Timothy and Hutchings' correlation parameter, d/D , for onset of adiabatic shear [22]. The derivation of the plastic strain estimate follows for reference, followed by a discussion on observed dimple profiles and limitations of the parameter. Sample dimple profiles are included at the end.

If a shot of diameter D (radius R , where $D=2R$) makes a dimple of diameter d (radius a , where $d=2a$) on a surface, then the surface is deformed as shown in Figure B.25: the original surface area defined by a circle with dimple diameter, d , is deformed into a spherical section of height, h , and diameter, d :

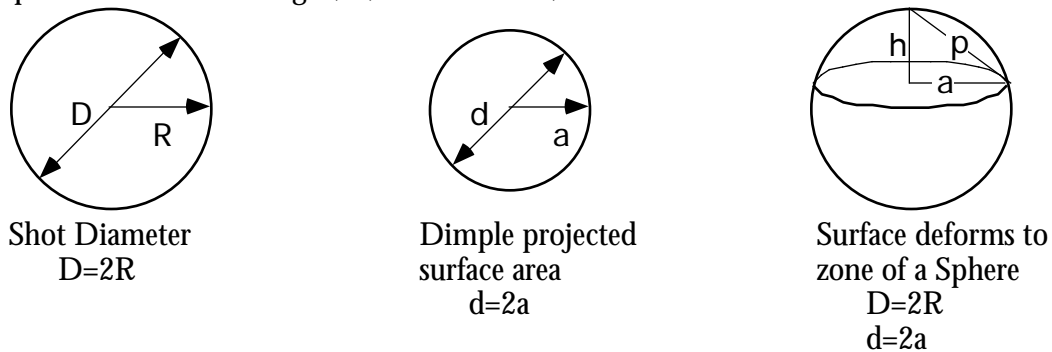


Figure B.26 – Geometric Dimple Formation Process

The initial, undeformed surface area defined by the projection of a dimple of radius a is:

$$A_o = \frac{d^2}{4} = a^2 \quad (B-17)$$

This area will deform to approximate the surface of a zone of a sphere. The surface area of a zone of a sphere is given by [80]:

$$S = 2 Rh = Dh = p^2 \quad (\text{B-18})$$

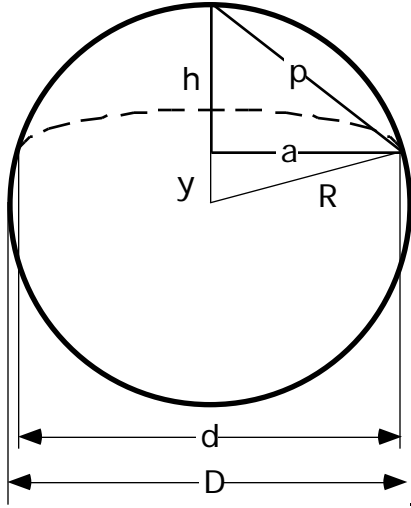


**Figure B.27 -
Schematic of a Spherical Sector**

Rearranging (B-18) in terms of d and D:

$$\begin{aligned} R &= h + y \\ y &= \sqrt{R^2 - a^2} \\ h &= R - \sqrt{R^2 - a^2} \\ A_f &= S = 2 R \left(R - \sqrt{R^2 - a^2} \right) \\ A_f &= \frac{D}{2} \left(D - \sqrt{D^2 - d^2} \right) \\ A_f &= \frac{D^2}{2} \left(1 - \sqrt{1 - \frac{d^2}{D^2}} \right) \end{aligned} \quad (\text{B-19})$$

The change in area can be defined by:

$$A = A_f - A_o \quad (\text{B-20})$$

$$A = \frac{D^2}{2} \left(1 - \sqrt{1 - \frac{d^2}{D^2}} \right) - \frac{d^2}{4} \quad (\text{B-21})$$

Dividing by A_o gives:

$$\frac{A}{A} = \frac{2D^2}{d^2} \left(1 - \sqrt{1 - \frac{d^2}{D^2}} \right) - 1 \quad (\text{B-22})$$

Let $\frac{d^2}{D^2} = x$

Then

$$\frac{A}{A} = \frac{2}{x} \left(1 - \sqrt{1 - x} \right) - 1 \quad (\text{B-23})$$

Using the Binomial Series

$$\sqrt{1+x} = 1 + \frac{1}{2}x - \frac{1}{(2)(4)}x^2 + \frac{(1)(3)}{(2)(4)(6)}x^3 - \frac{(1)(3)(5)}{(2)(4)(6)(8)}x^4 + \dots \quad (\text{B-24})$$

$$\sqrt{1-x} = 1 - \frac{1}{2}x - \frac{1}{(2)(4)}x^2 - \frac{(1)(3)}{(2)(4)(6)}x^3 - \frac{(1)(3)(5)}{(2)(4)(6)(8)}x^4 + \dots \quad (\text{B-25})$$

$$\frac{A}{A} = \frac{2}{x} \left(1 - \left(1 - \frac{1}{2}x - \frac{1}{(2)(4)}x^2 - \frac{(1)(3)}{(2)(4)(6)}x^3 - \frac{(1)(3)(5)}{(2)(4)(6)(8)}x^4 + \dots \right) \right) - 1 \quad (\text{B-26})$$

Rearranging, yields:

$$\begin{aligned}\frac{A}{A} &= \frac{2}{x} \frac{1}{2}x + \frac{1}{8}x^2 + \frac{1}{16}x^3 + \frac{5}{128}x^5 + \dots - 1 \\ \frac{A}{A} &= 1 + \frac{1}{4}x + \frac{1}{8}x^2 + \frac{5}{64}x^3 + \dots - 1 \\ \frac{A}{A} &= \frac{1}{4}x + \frac{1}{8}x^2 + \frac{5}{64}x^3 + \dots\end{aligned}\tag{B-27}$$

Substituting back $\frac{d^2}{D} = x$ into equation (B-27) gives:

$$\frac{A}{A} = \frac{d^2}{4D^2} + \frac{d^4}{8D^4} + \frac{5d^6}{64D^6} + \dots\tag{B-28}$$

Since plastic deformation is a constant volume process, the plastic tensile strain, $\epsilon_p =$

$A/2A$ becomes:

$$p \frac{d^2}{8D^2} + \frac{d^4}{16D^4} + \frac{5d^6}{128D^6} + \dots\tag{B-29}$$

If the higher order terms are small, this can be approximated by the first term, or:

$$p \frac{d^2}{8D^2}\tag{B-30}$$

Up until this point, nothing is material dependent. The following assumptions have been used:

- Shot is perfect sphere.
- Dimple is spherical segment of sphere having radius R.
- Impingement angle is not considered.

In practice, d is estimated from shot peening intensity, and D is taken as the shot diameter. It was found that elastic recoil occurs, reducing the dimple depth such that the dimple profile does not form a spherical sector having a diameter corresponding to the shot diameter.

From observations of impact dimples from the single particle impact test effort, the dimple shape was found to be closer to a hyperbolic paraboloid. A similar approach to a plastic strain estimate can be used, but numerical integration is required to solve for the

surface area of the dimple. In reality, the dimple surfaces observed were not uniform, symmetrical or smooth. Estimation of plastic strain from idealized representations of dimple diameter and height may be of limited value, particularly across a wide range of deformation behavior. However, the ratio of d/D , or $(d/D)^2$ did provide a useful benchmark for dimple deformation behavior, as observed in Figure 4.1.

For reference, a selection of dimple profiles follows. Table B.7 provides a summary of figure number, test number, and type of shot.

Table B.7 – Summary of Dimple Profile Plots Attached

Figure	Test Number	Shot Size	Velocity	Type Plot
B.28	3-015	CCW14	3,490 in/s	Contour
B.29	3-015	CCW14	3,490 in/s	Multiple Region
B.30	3-057	CCW31	7,580 in/s	Multiple Region (lip)
B.31	3-057	CCW31	7,580 in/s	Multiple Region (well)
B.32	3-015	CCW14	3,490 in/s	2D Analysis Profile
B.33	3-057	CCW31	7,580 in/s	2D Analysis Profile
B.34	3-057	CCW31	7,580 in/s	Contour Plot
B.35	3-018	CCW31	3,440 in/s	2D Analysis Profile
B.36	3-019	CCW31	460 in/s	Contour & 2D Analysis Profile
B.37	3-018	CCW31	3,440 in/s	3D View & 2D Analysis Profile
B.38	3-028	CCW31	low velocity	Contour & 2D Analysis Profile
B.39	3-028	CCW31	low velocity	3D View & 2D Analysis Profile

This is a limited selection of plots obtained from the WYKO profiler due to limited options for data capture and transfer from the WYKO system.

Figure B.28 – Test #3-015, CCW14, $V_0=3,490$ in/s, 90° – Contour Plot

Title: 3-015, r88-4 impact
 Note: 10X lens

Contour

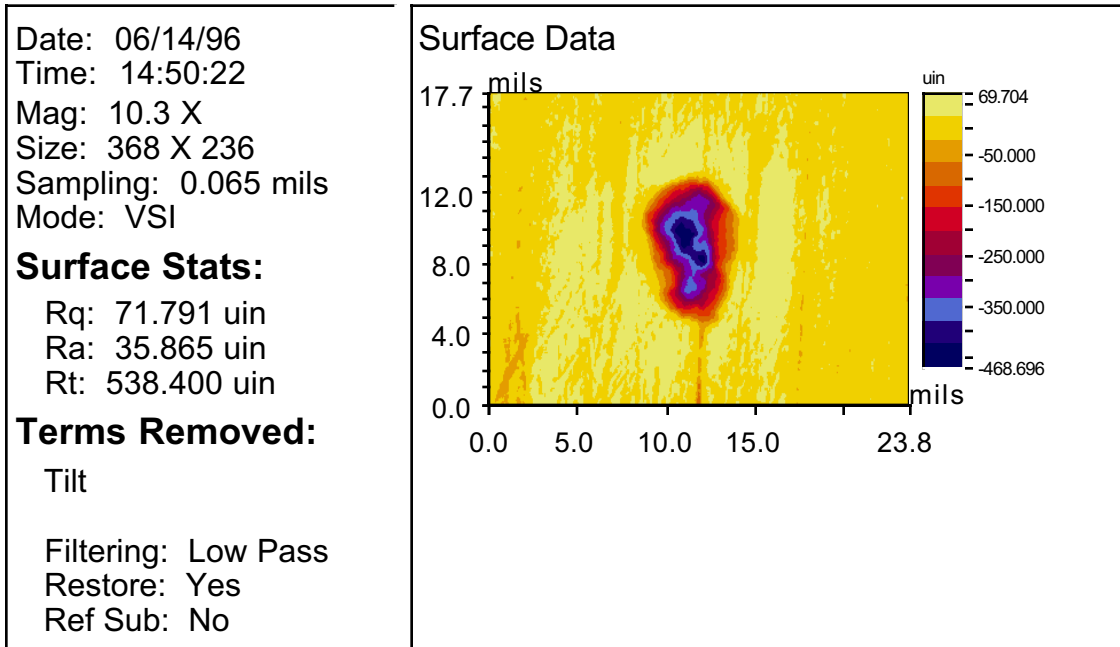


Figure B.29 – Test #3-015, CCW14, $V_0=3,490$ in/s, 90° – Multiple Region Plot

Title: 3-015, r88-4 impact
 Note: 10X lens

Multiple Region

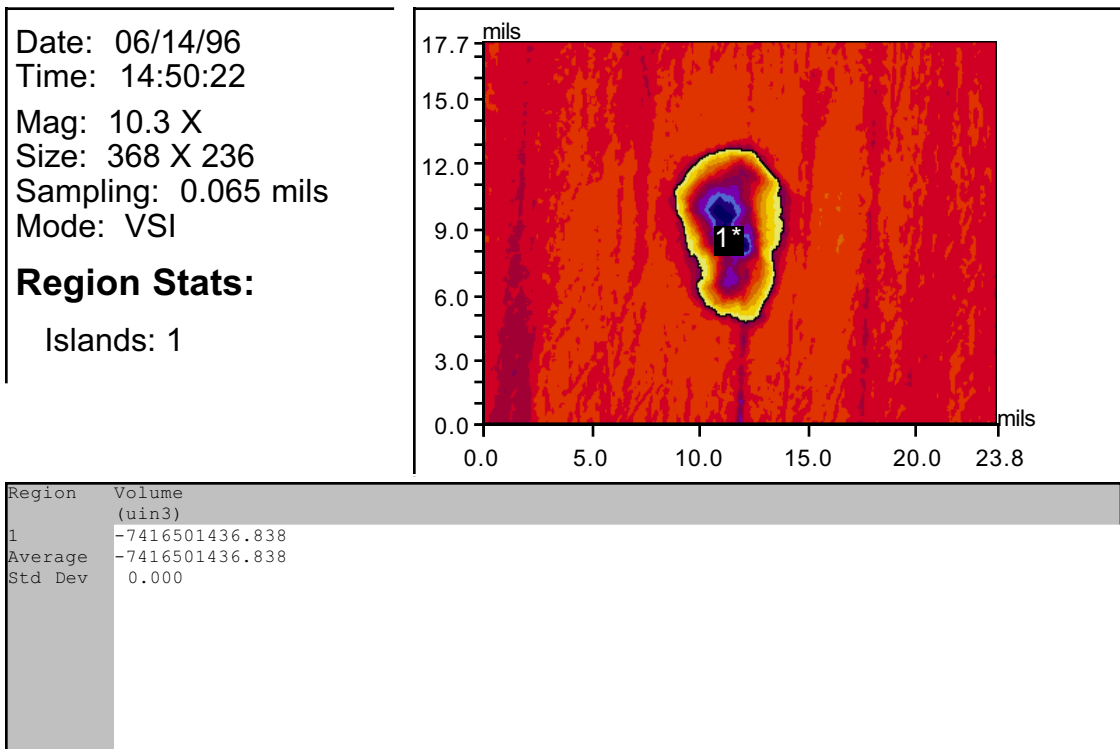


Figure B.30 – Test #3-057, CCW31, $V_0=7,580$ in/s, 45° – Multiple Region Plot

Title: 3-057, r88-16 impact

Note: 2.5X lens (cw31)

Multiple Region

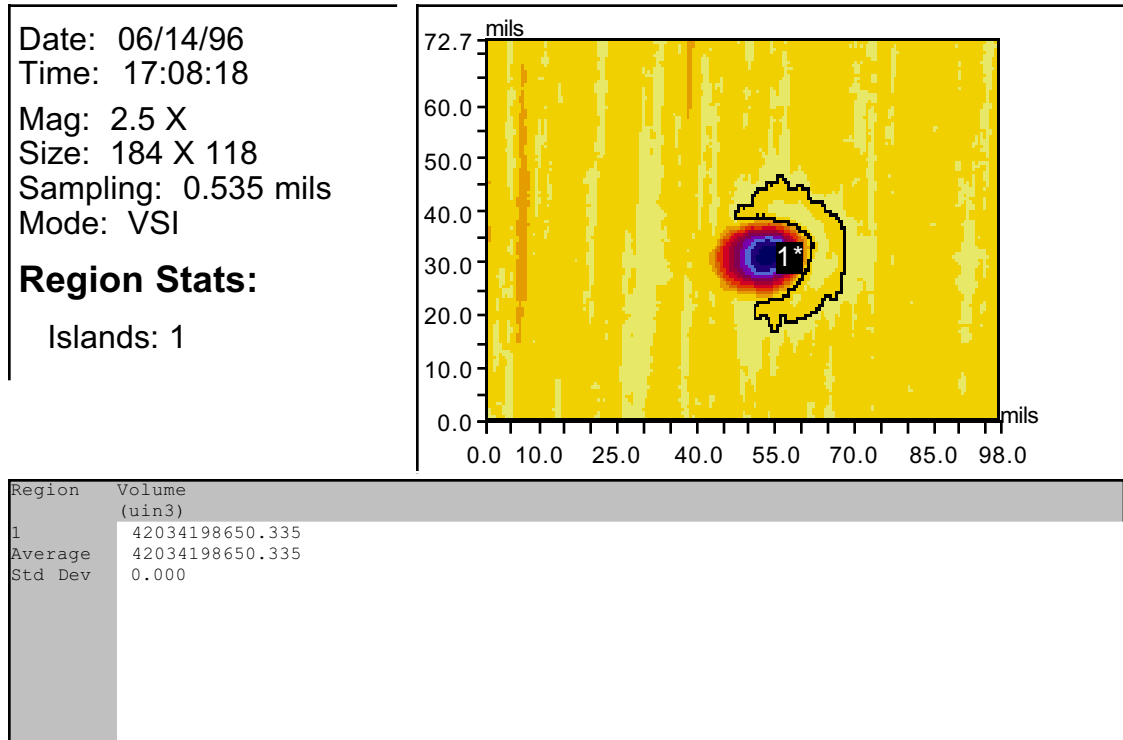


Figure B.31 – Test #3-057, CCW31, $V_0=7,580$ in/s, 45° – Multiple Region Plot

Title: 3-057, r88-16 impact

Note: 2.5X lens (cw31)

Multiple Region

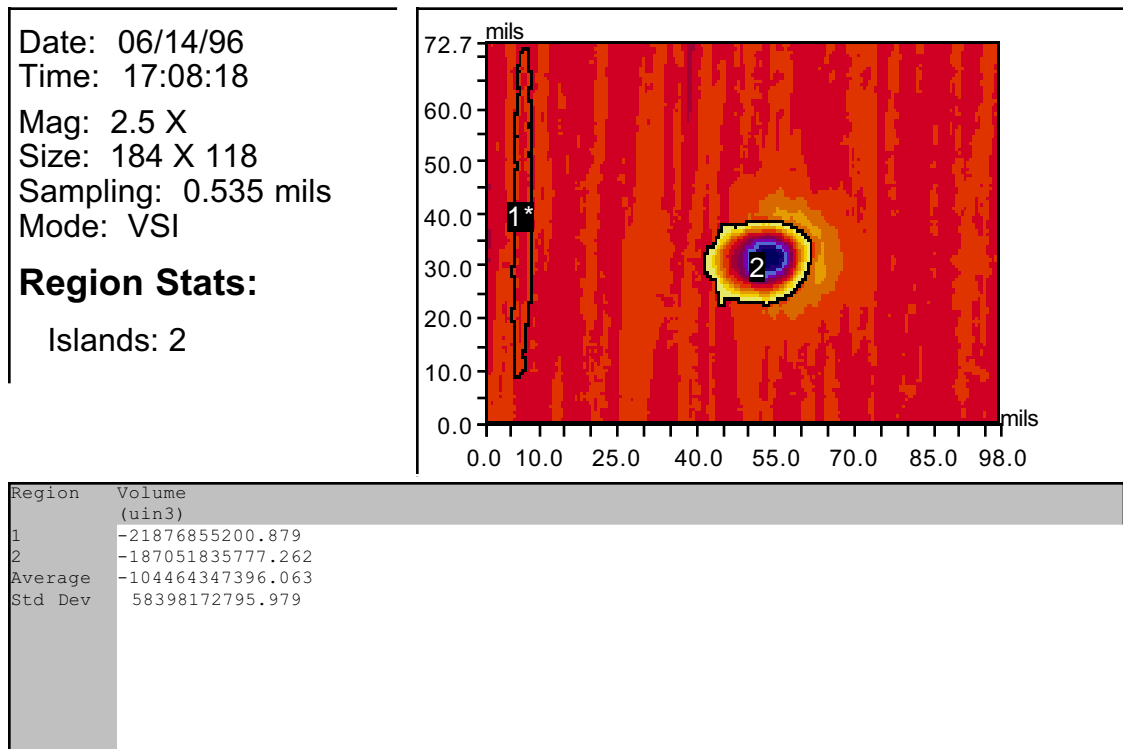
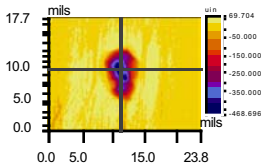


Figure B.32 – Test #3-015, CCW14, $V_0=3,490$ in/s, 90° – 2D Analysis Profile

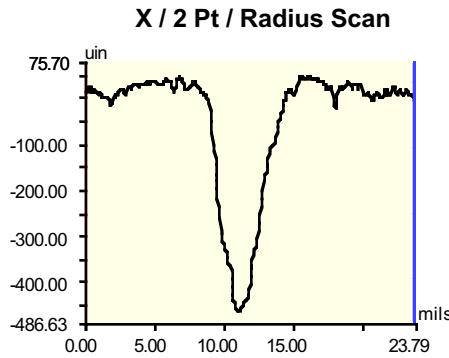
Title: 3-015, r88-4 impact
 Note: 10X lens

2D Analysis

Date: 06/14/96
 Time: 14:50:22
 Mag: 10.3 X
 Mode: VSI
 Rq: 71.791 uin
 Ra: 35.865 uin
 Rt: 538.400 uin

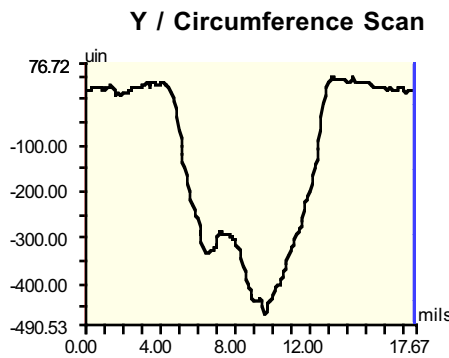


1: 172,129



Rq: 135.90 uin
 Ra: 98.44 uin
 Rt: 511.21 uin
 Rp: 50.14 uin
 Rv: -461.07 uin

L: 0.00 mils ---
 R: 23.79 mils ---
 D: 23.79 mils ---
 Angle: ---
 Curve: 329.42 mils
 Terms: None



Rq: 178.80 uin
 Ra: 165.73 uin
 Rt: 515.68 uin
 Rp: 50.93 uin
 Rv: -464.74 uin

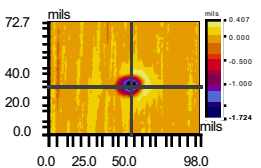
L: 0.00 mils ---
 R: 17.67 mils ---
 D: 17.67 mils ---
 Angle: ---
 Curve: 82.36 mils
 Terms: None

Figure B.33 – Test #3-057, CCW31, $V_0=7,580$ in/s, 45° – 2D Analysis Profile

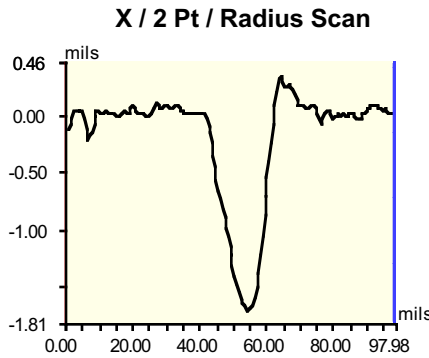
Note: 2.5X lens (cw31)

2D Analysis

Date: 06/14/96
 Time: 17:08:18
 Mag: 2.5 X
 Mode: VSI
 Rq: 177.422 uin
 Ra: 70.136 uin
 Rt: 2.131 mils

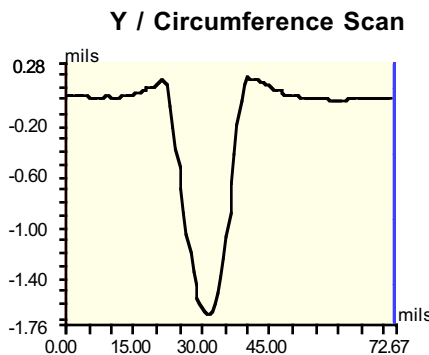


1: 99,50



Rq: 0.50 mils
 Ra: 0.35 mils
 Rt: 2.06 mils
 Rp: 0.36 mils
 Rv: -1.70 mils

L: 0.00 mils ---
 R: 97.98 mils ---
 D: 97.98 mils ---
 Angle: ---
 Curve: 1.69 in
 Terms: None



Rq: 0.52 mils
 Ra: 0.38 mils
 Rt: 1.85 mils
 Rp: 0.19 mils
 Rv: -1.66 mils

L: 0.00 mils ---
 R: 72.67 mils ---
 D: 72.67 mils ---
 Angle: ---
 Curve: 869.33 mils
 Terms: None

Figure B.34 – Test #3-057, CCW31, $V_0=7,580$ in/s, 45° – Contour Plot

Title: 3-057, r88-16 impact
 Note: 2.5X lens (cw31)

Contour

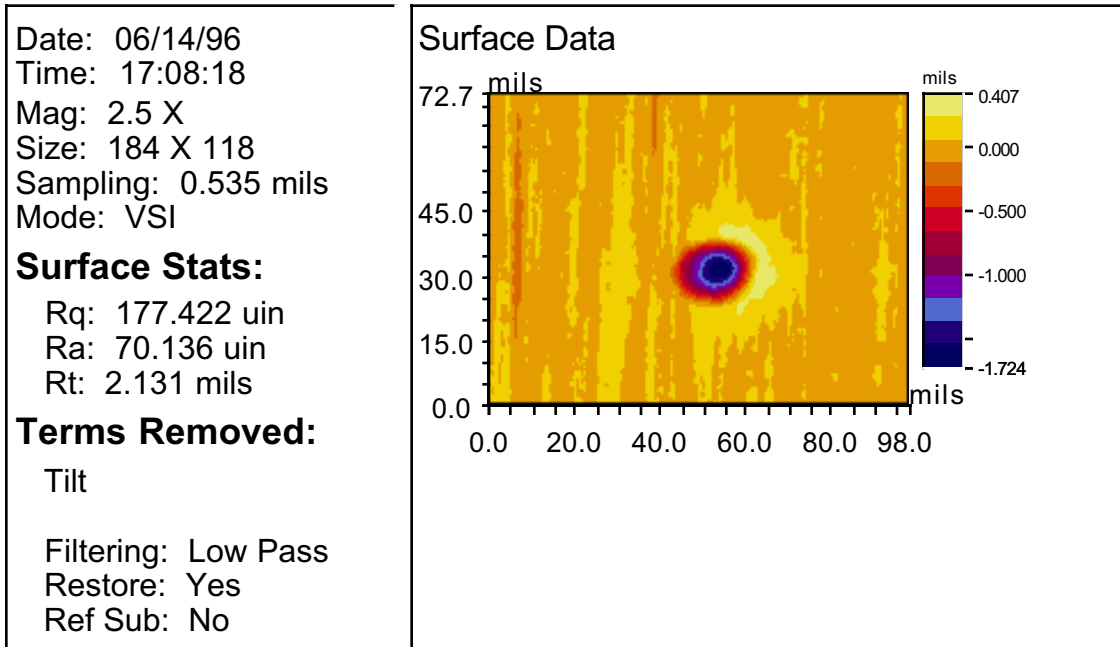


Figure B.35 – Test #3-018, CCW31, $V_0=3,440$ in/s, 90° – 2D Analysis Profile

Title: R88-10 Dimple 18
 Note: d10-18-3; Largest Diameter

Date: 05/08/96
 Time: 14:11:48
 Mag: 10.3 X

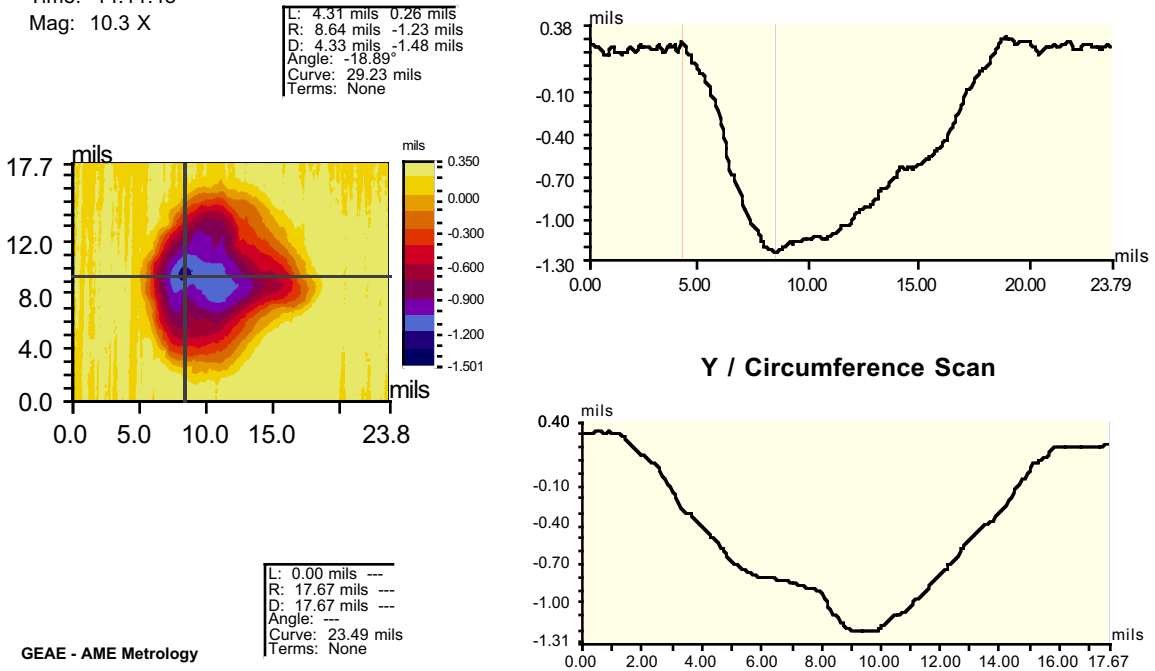


Figure B.36 – Test #3-019, CCW14, $V_0=460$ in/s, 90° – Contour & 2D Profile Plot

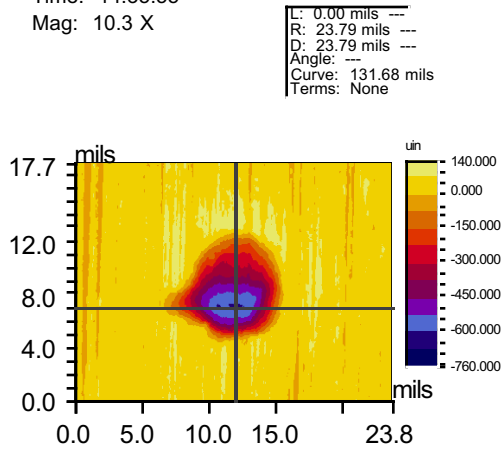
Title: R88-10 Dimple 19

Note: d10-19-2

Date: 05/08/96

Time: 14:35:55

Mag: 10.3 X



GEAE - AME Metrology

L: 0.00 mils
R: 17.67 mils
D: 17.67 mils
Angle: ---
Curve: 64.02 mils
Terms: None

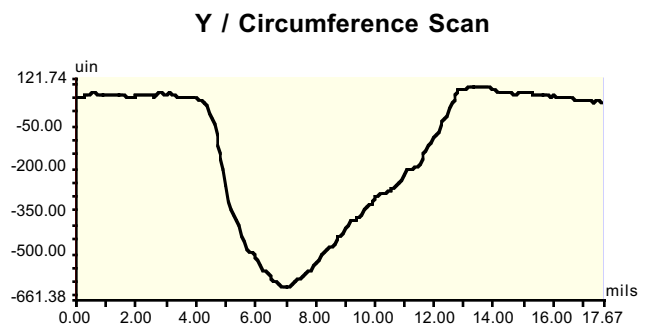
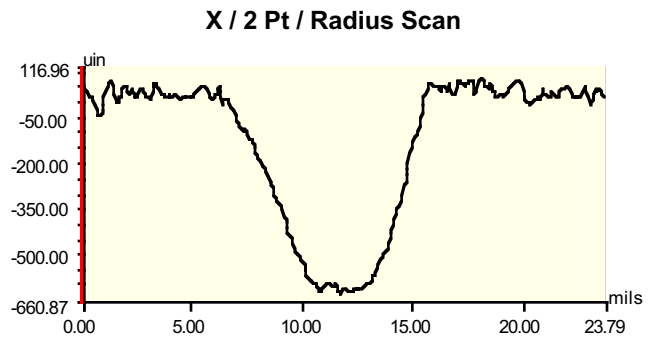
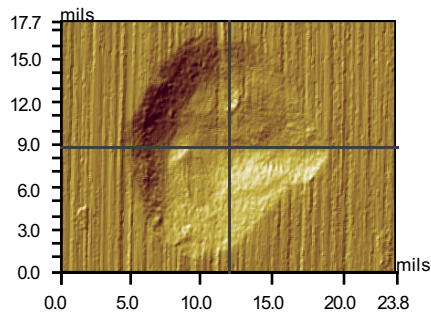
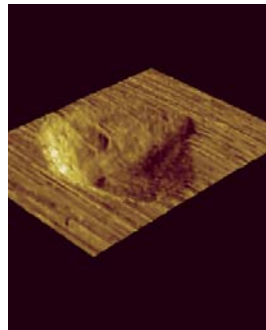


Figure B.37 – Test #3-018, CCW31, $V_0=3,440$ in/s, 90° – 3D view & 2D Analysis Profile

Mag: 10.3 X



GEAE - AME Metrology

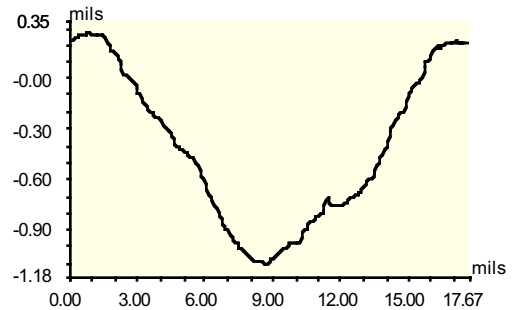
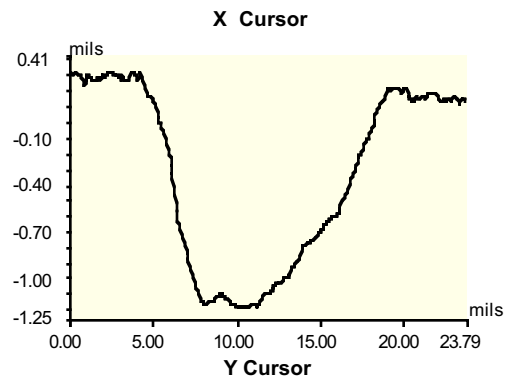


Figure B.38 – Test #3-028, CCW14, low velocity, 90° – Contour & 2D Profile Plot

Title: R88-10 Dimple 28

Note: d10-28-2

Date: 05/10/96

Time: 09:22:27

Mag: 20.1 X

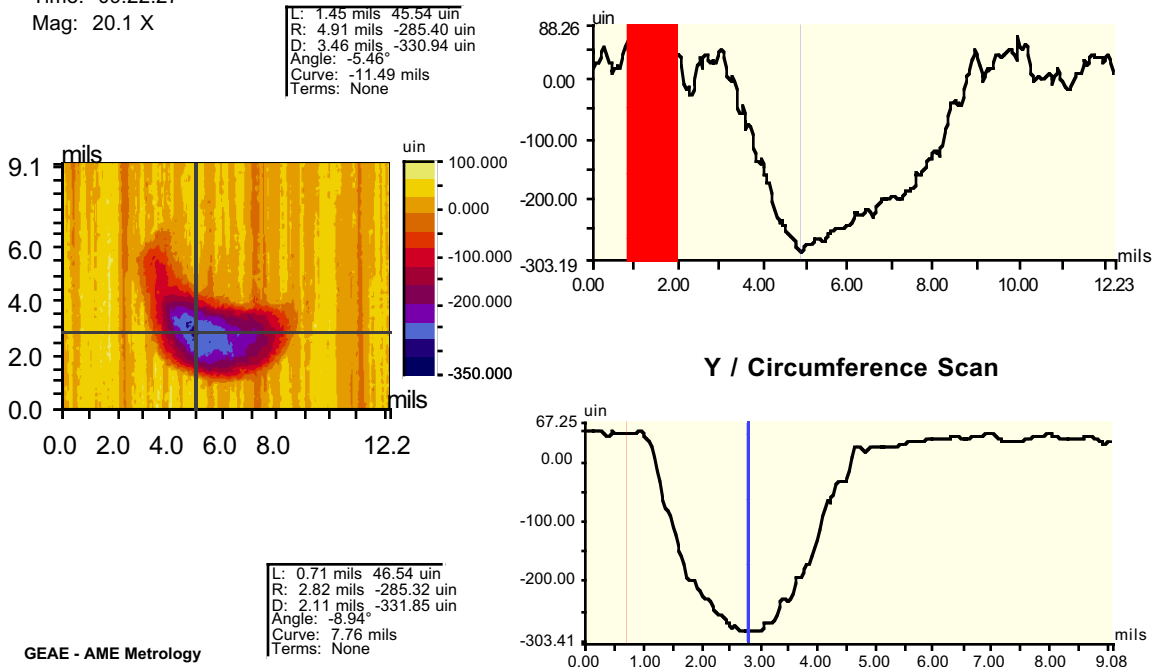
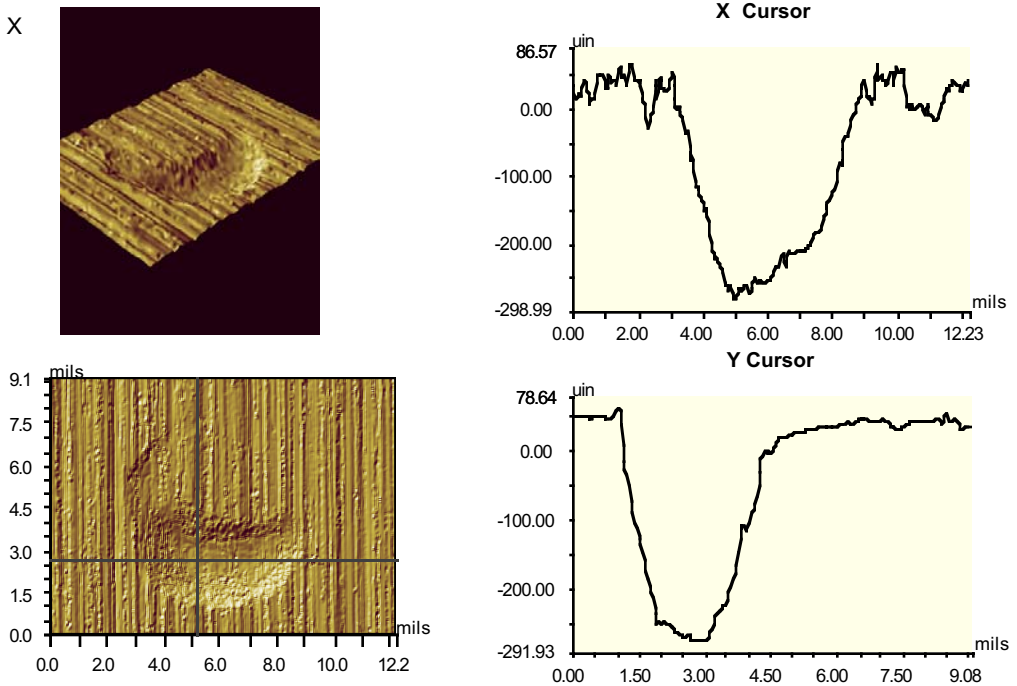


Figure B.39 – Test #3-028, CCW14, low velocity, 90° – 3D view & 2D Analysis Profile

Mag: 20.1 X



GEAE - AME Metrology

APPENDIX C

PRODUCTION PEENED COUPONS

C.1 Contents

A subset of these results are presented in Chapter 4. This section is provided to complement that material, providing:

- 1) sample microstructures,
- 2) residual stress profiles (from x-ray diffraction data)
- 3) plastic strain distributions (from x-ray diffraction data), and
- 4) saturation curve profiles

for the sixteen DOE conditions, as designated in Table C.1. In general, the data will be formatted with four plots to a page. Conditions 1, 2, 9, and 10 will be grouped together (ccw14 and ccw31 – 6A, 45°, 100% & 800% coverage) and so on. This arrangement permits a direct comparison of ccw31 shot results with ccw14 shot results at the same intensity and incidence angle conditions.

Table C.1 – DOE Conditions in Standard Order

#	shot	intensity	angle	coverage	#	shot	intensity	angle	coverage
1	ccw14	6A	45	100%	9	ccw31	6A	45	100%
2	ccw14	6A	45	800%	10	ccw31	6A	45	800%
3	ccw14	6A	85	100%	11	ccw31	6A	85	100%
4	ccw14	6A	85	800%	12	ccw31	6A	85	800%
5	ccw14	10A	45	100%	13	ccw31	10A	45	100%
6	ccw14	10A	45	800%	14	ccw31	10A	45	800%
7	ccw14	10A	85	100%	15	ccw31	10A	85	100%
8	ccw14	10A	85	800%	16	ccw31	10A	85	800%

C.2 Sample Microstructures – Production Peening DOE Conditions

After polishing and etching, microstructures were taken at three locations along the surface: 1/4 distance, 2/4 distance and 3/4 distance from left edge. This ensured that different locations were sampled, but that edge effects (from peening at corners) were avoided in the microstructures used for slip depth measurements. Microstructures were also taken at the left and right corners, for future reference.

Microstructures were taken using a Cambridge Stereoscan 260 Scanning Electron Microscope (SEM) with Polaroid film. Slip depth measurements were made using vernier calipers with the original Polaroid photos. For documentation purposes, sample photo from each specimen were scanned using a Hewlett Packard ScanJet Plus, and edited in Adobe Photoshop software on a Macintosh (Power Macintosh 7500 and Macintosh Quadra 840 AV computers were used during the process). Image processing included adjustments to brightness and contrast, to optimize printing contrast on a Hewlett Packard LaserJet 5si. Unfortunately, some detail and resolution is lost in the scanning and printing process. Variability in original photo contrast, surface preparation and etching also contribute to variation in clarity of slip features between images.

For the slip depth measurements used for initial crack size in the Fracture Mechanics calculations, minimum slip depth measurements from each of the three surface locations were averaged. Maximum slip depth measurements were also taken for comparison purposes.

Figure C.1 (on the following four pages) shows a sample microstructure corresponding to each DOE condition. Careful examination of the images is needed to see the slip for some of the peening conditions; slip bands from DOE conditions #6 and #14 are most readily observable.

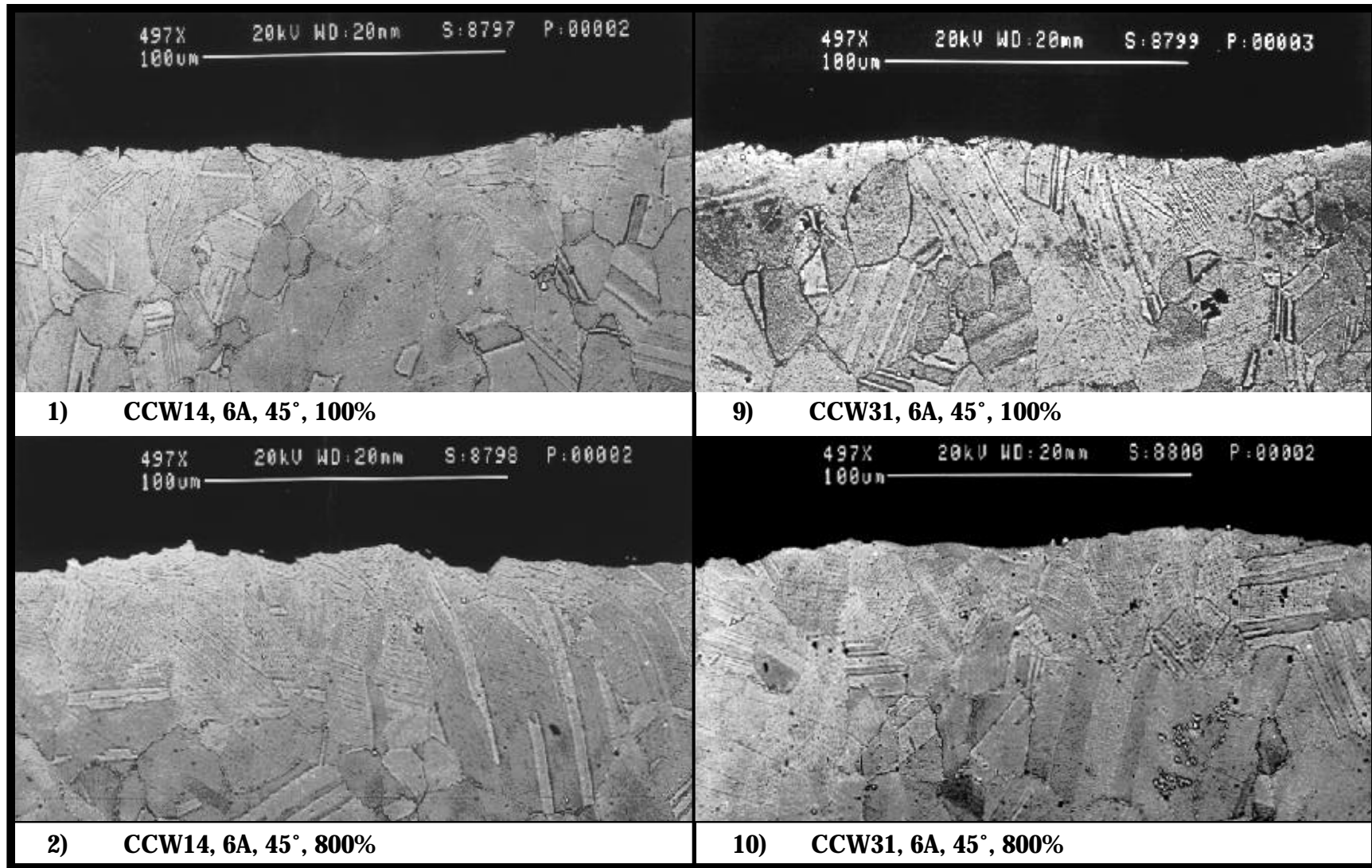


Figure C.1 – Sample Microstructures

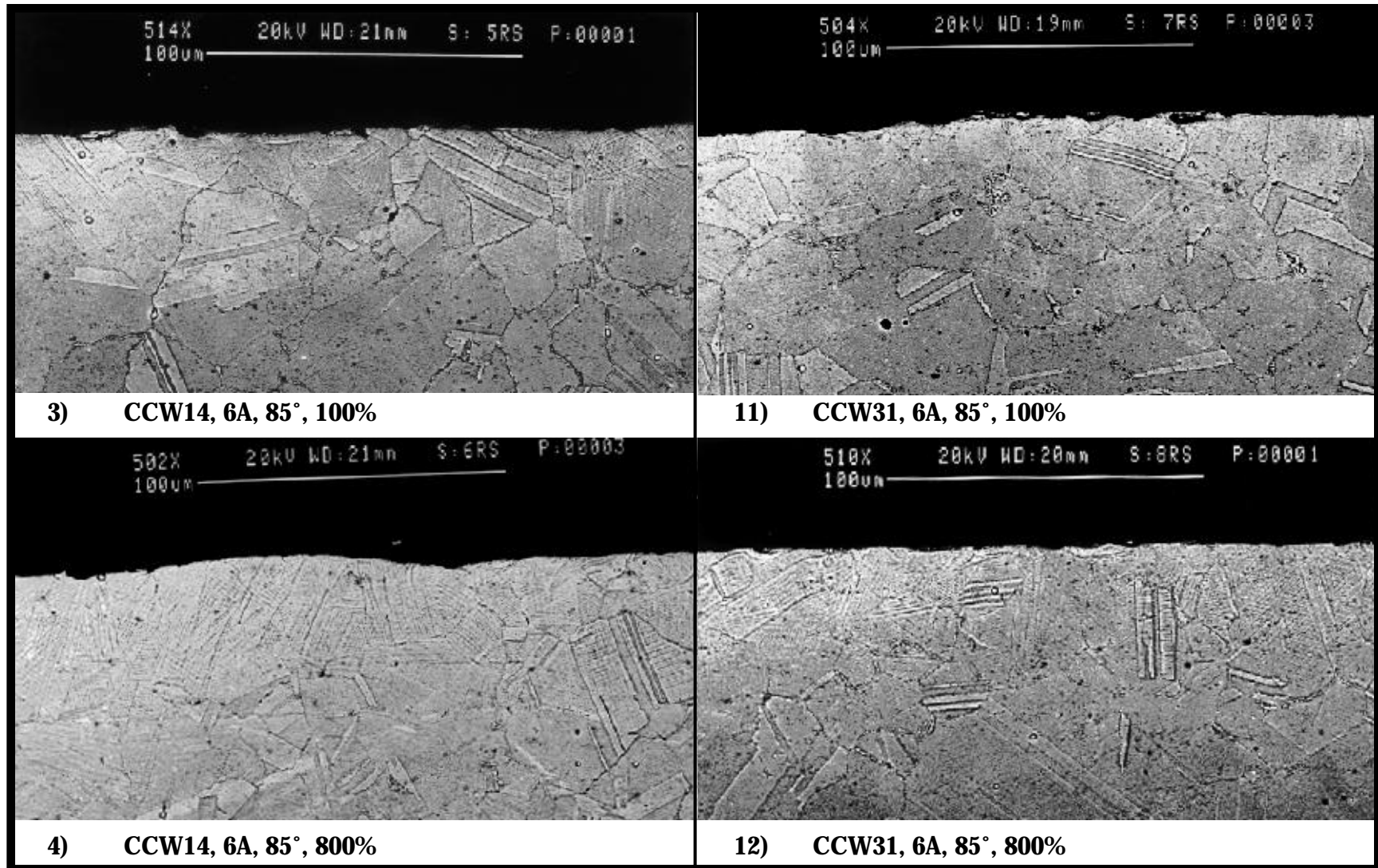


Figure C.1 – Sample Microstructures, continued

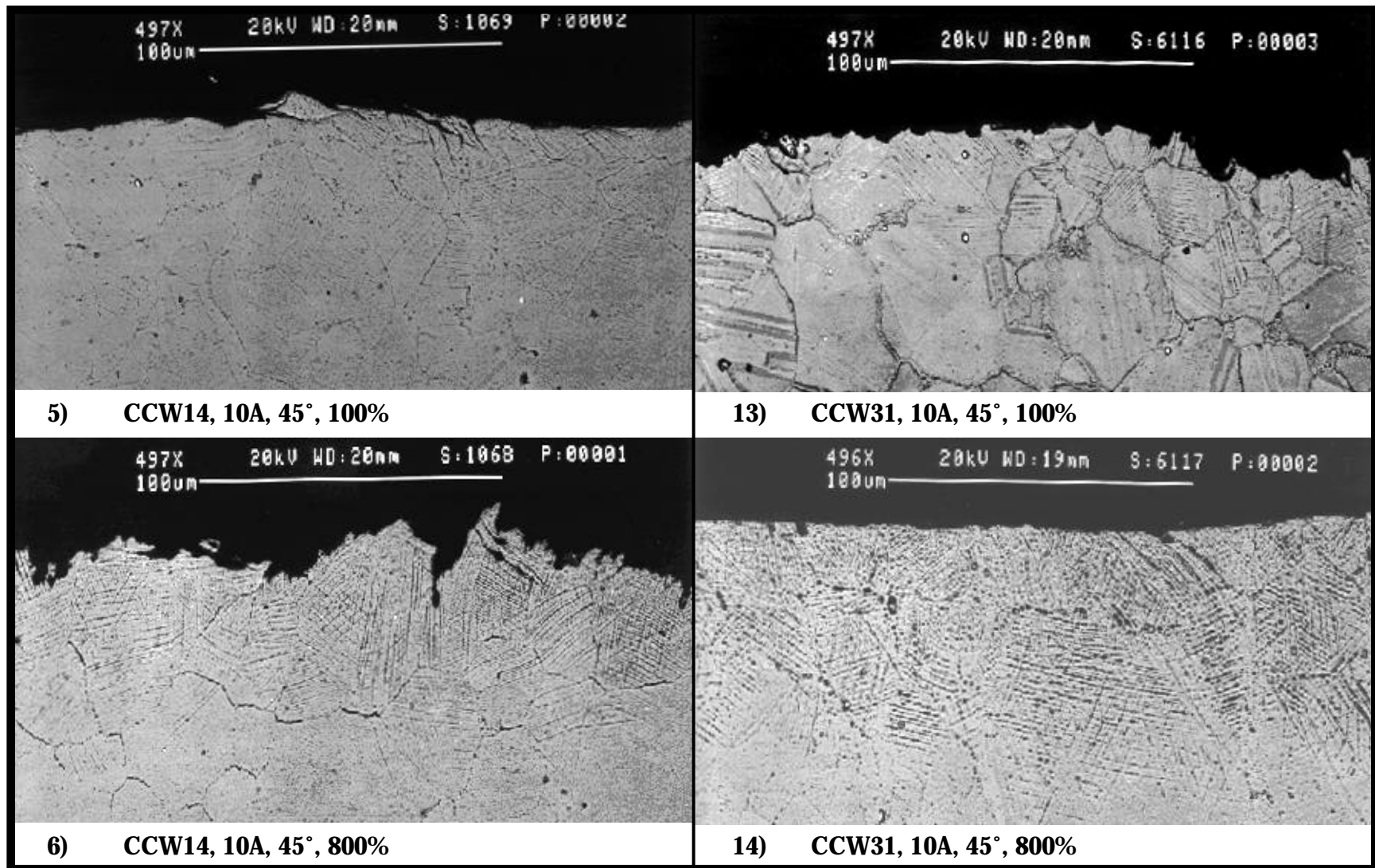


Figure C.1 – Sample Microstructures, continued

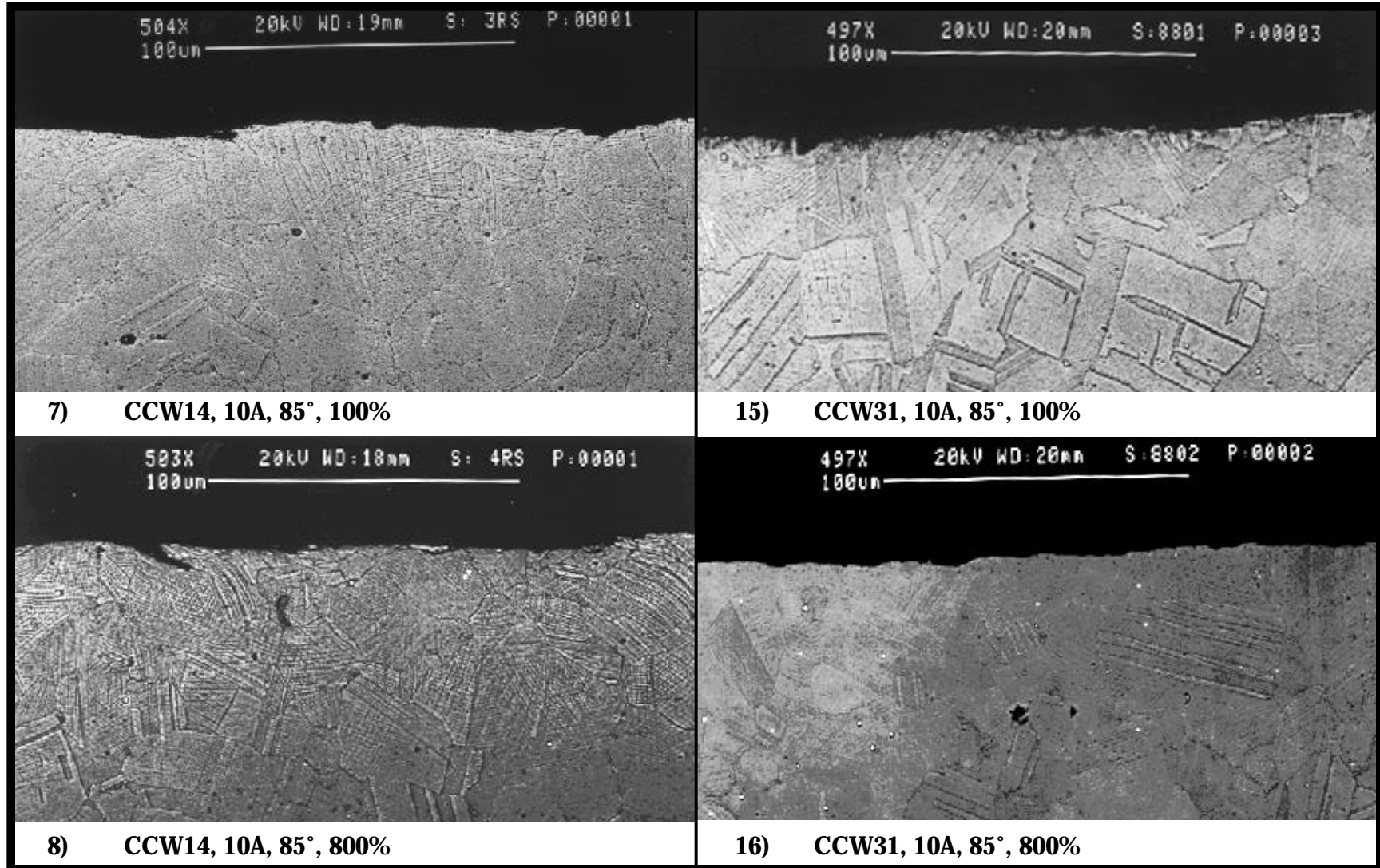


Figure C.1 – Sample Microstructures, continued

C.3 Residual Stress Profiles

Residual stress profiles were obtained using x-ray diffraction for each of the 16 DOE conditions. Work was conducted by Lambda Research, Inc., Cincinnati, Ohio. Profiles were taken in the direction of peening, as this appeared to generate the smallest amount of compressive residual stress (thus most conservative profile). Machining (and peening) processes have a directional effect, which is reflected in the residual stress state.

The low stress ground target specimens used for the single particle impact tests showed a distinct grind texture from the manufacturing process. As a result, x-ray diffraction measurements were taken both parallel to the grind and perpendicular to the grind direction to determine whether there were any significant differences in the residual stress state. Table C.2 shows the measurements obtained at three different locations. A distinct directional effect was observed.

Figure C.2 shows the residual stress profiles for each of the DOE conditions, along with the curve fit obtained using equation 2.19. Each plot includes both the 100% and 800% coverage conditions. In addition, four additional points are plotted at arbitrary stress locations near the bottom of the plot, corresponding to the minimum and maximum slip depths (“a”) measured for the 100% (1) and 800% (8) peening conditions. **Note that the depth of slip observed corresponds to the approximate location of the maximum compressive stress.**

Table C.2 – Residual Stress Measurements Taken from a Low Stress Ground Coupon

Location	Direction relative to grind	Residual Stress (ksi)	Peak Width (deg.)	Direction relative to grind	Residual Stress (ksi)	Peak Width (deg.)
1	parallel	+48.5	4.42	perpendicular	-78.0	3.95
2	parallel	+6.7	4.21	perpendicular	-84.5	3.76
3	parallel	-16.6	3.16	perpendicular	-102.0	3.13

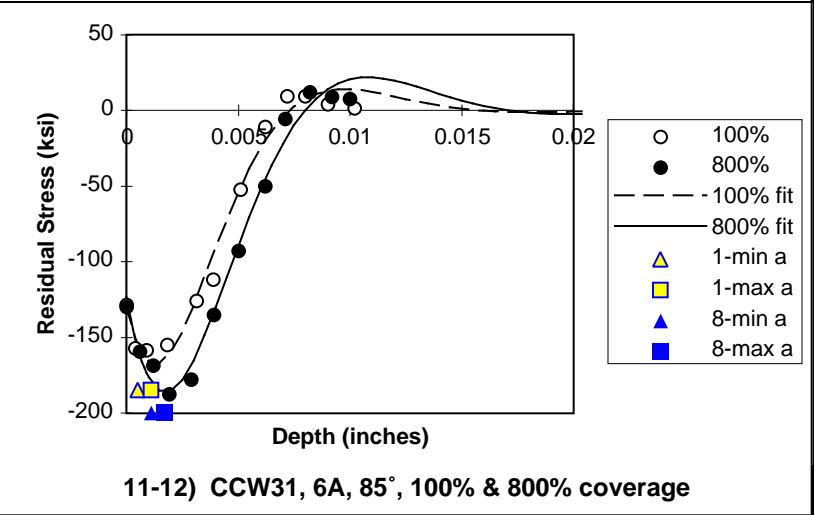
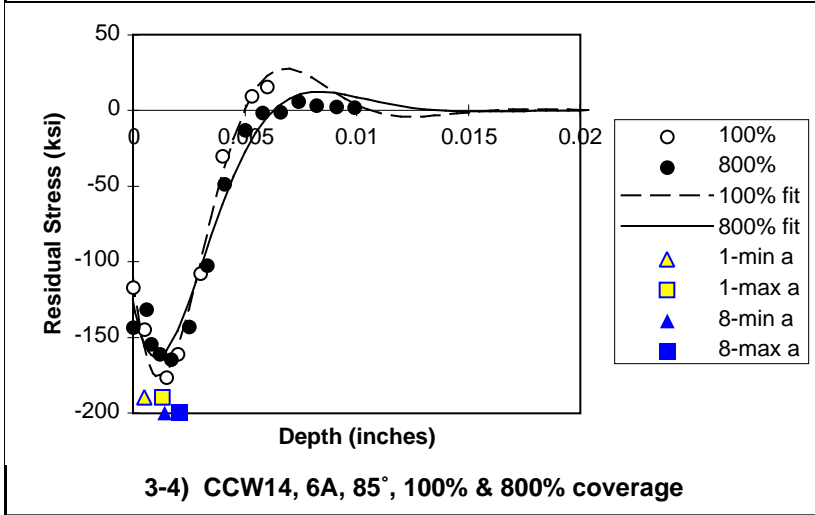
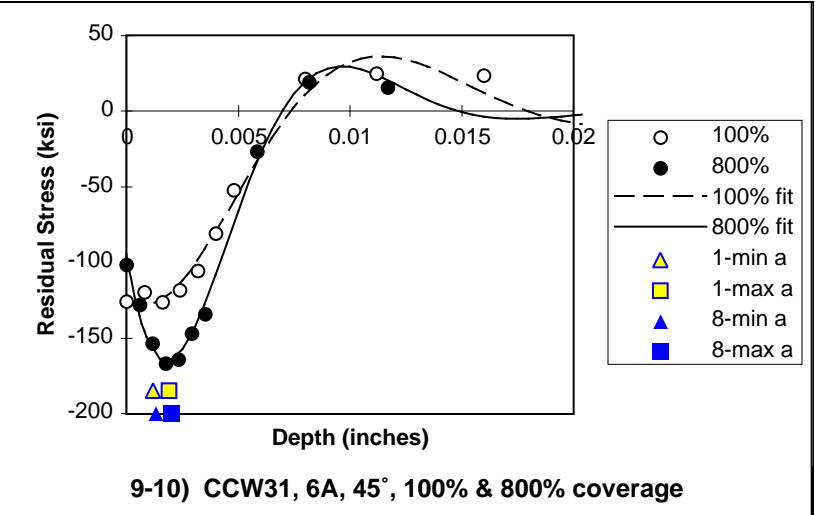
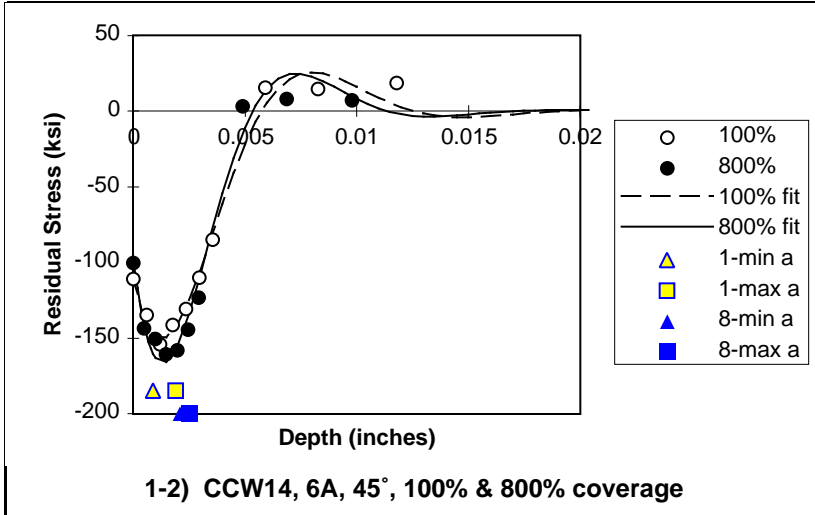


Figure C-2: Residual Stress Profiles

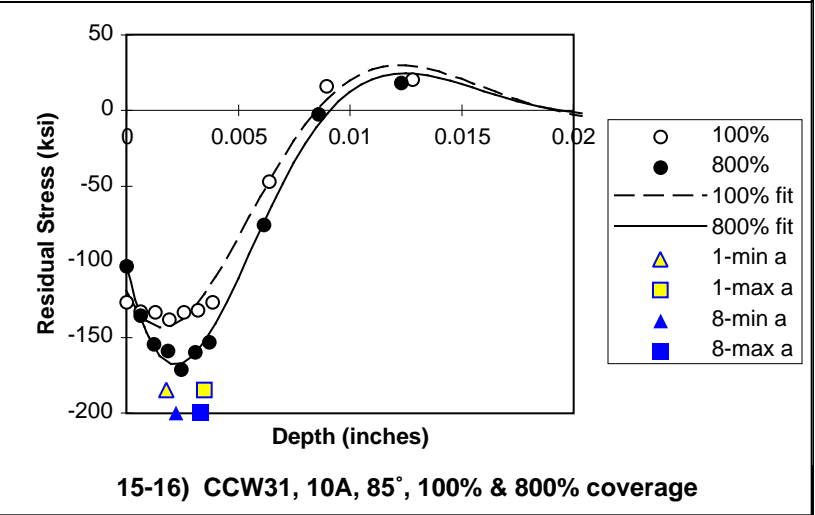
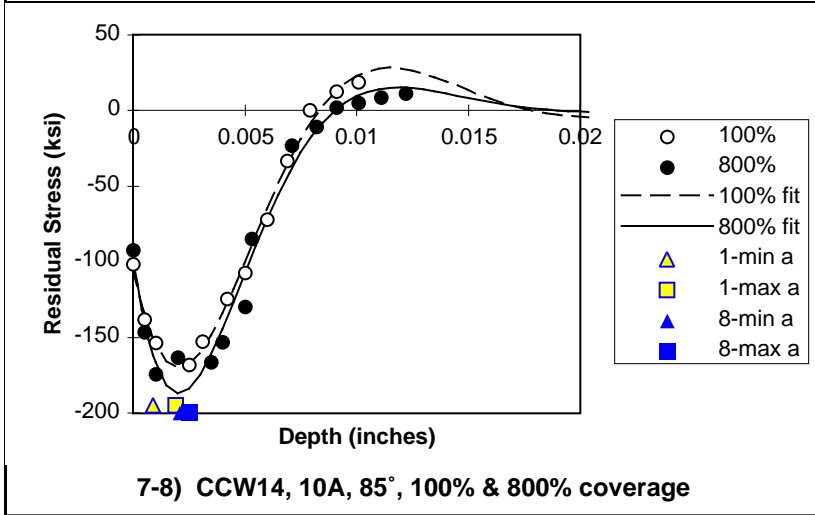
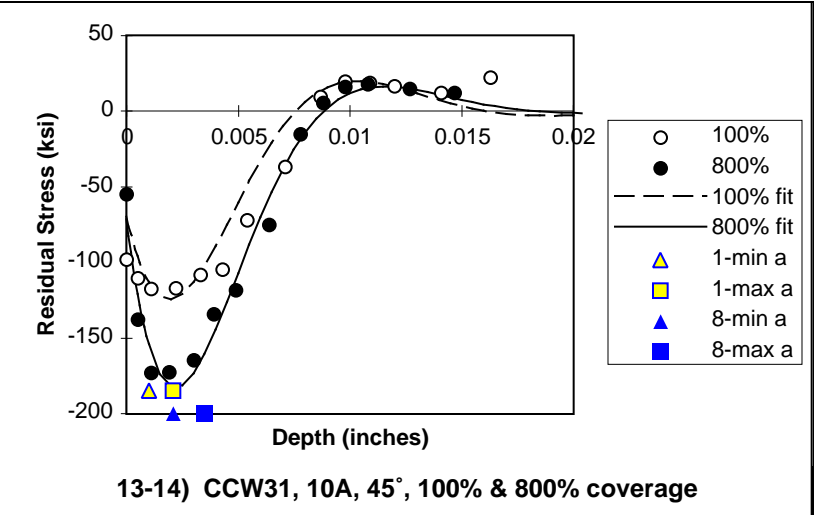
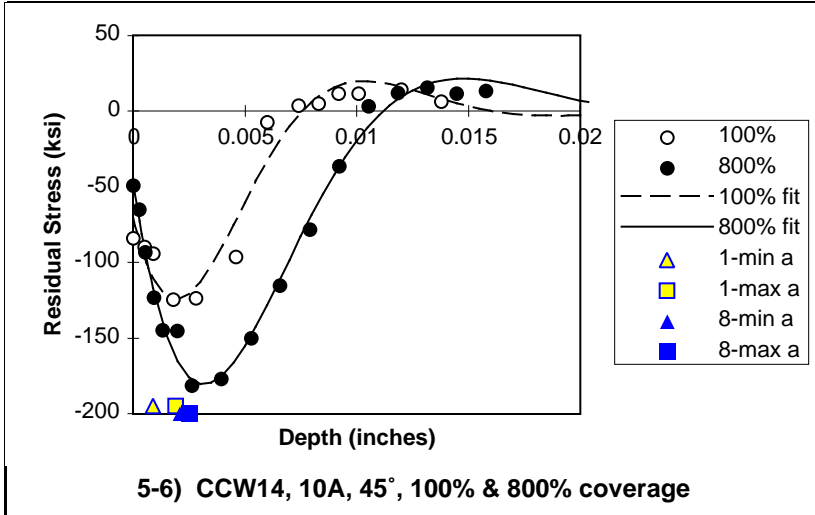


Figure C-2: Residual Stress Profiles, continued

C.4 Plastic Strain Profiles

Plastic strain distributions were calculated from x-ray diffraction peak broadening measurements conducted by Lambda Research, Inc., Cincinnati, Ohio. This required a separate calibration effort on René 88DT to correlate observed peak broadening effects to known states of plastic strain.

Comparisons of surface plastic strain as well as depth of specific levels of plastic strain were made across all DOE conditions during development of the fracture mechanics model. Estimates of plastic strain from x-ray diffraction peak broadening measurements did not permit correlation or clarification of the damage state associated with shot peening. It did not provide a useful characterization of the depth of damage layer, or of strain localization.

The strength of the x-ray diffraction technique is that it provides an average reading over a surface. Larger spot sizes provide more stable readings. However, life behavior is controlled by the extremes - the weakest link. Thus, an averaging technique may not provide the qualitative information needed. However, the plastic strain measurements are a good indicator of the significant amounts of plastic deformation accumulated in the surface layers. The material in the surface layer is significantly different from that in the substrate. It has been significantly altered by shot peening.

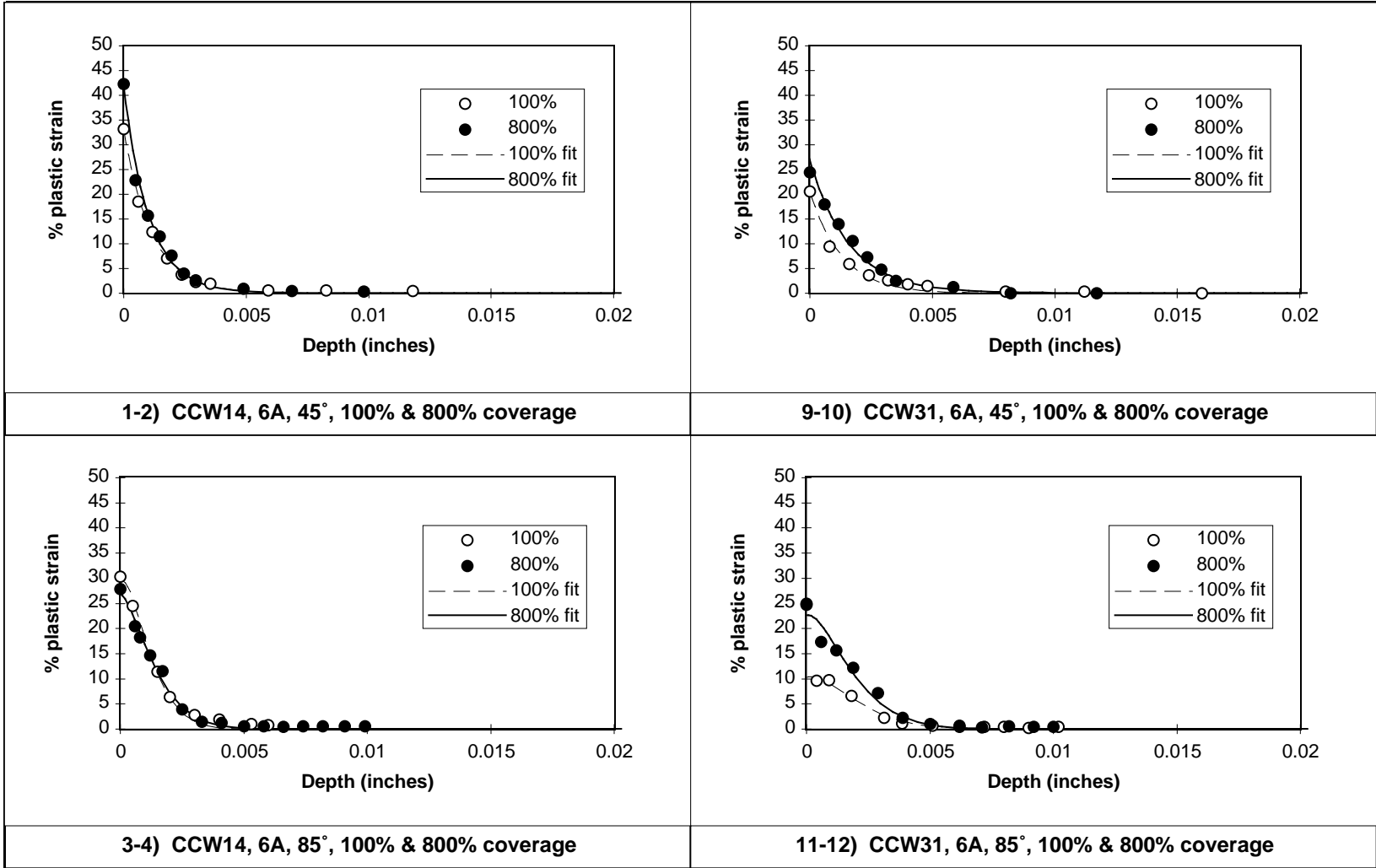
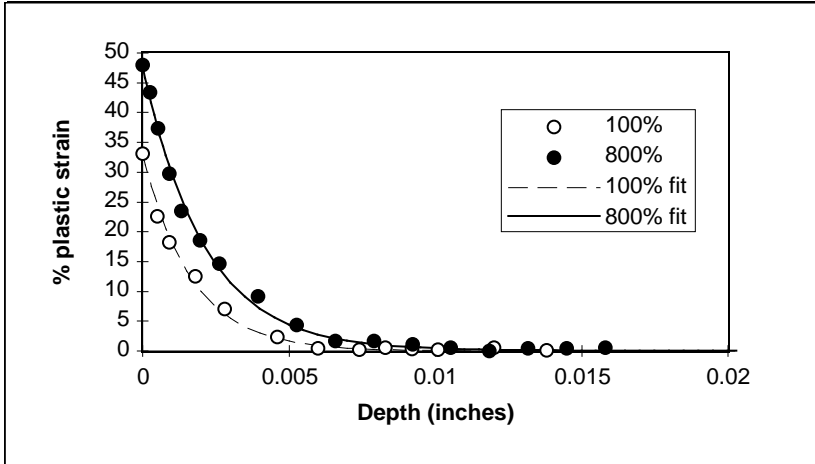
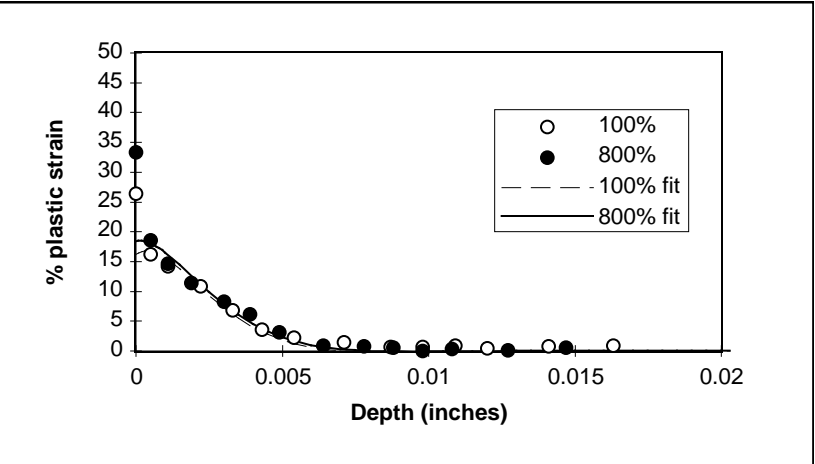


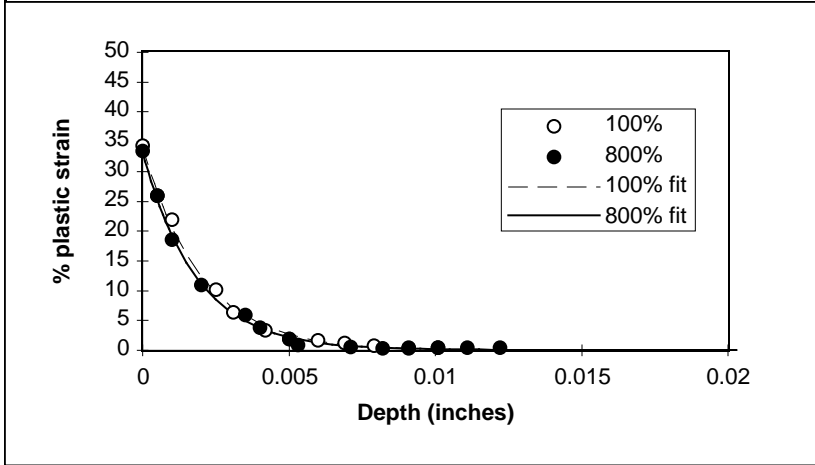
Figure C-3: Plastic Strain Profiles (estimated from x-ray diffraction data)



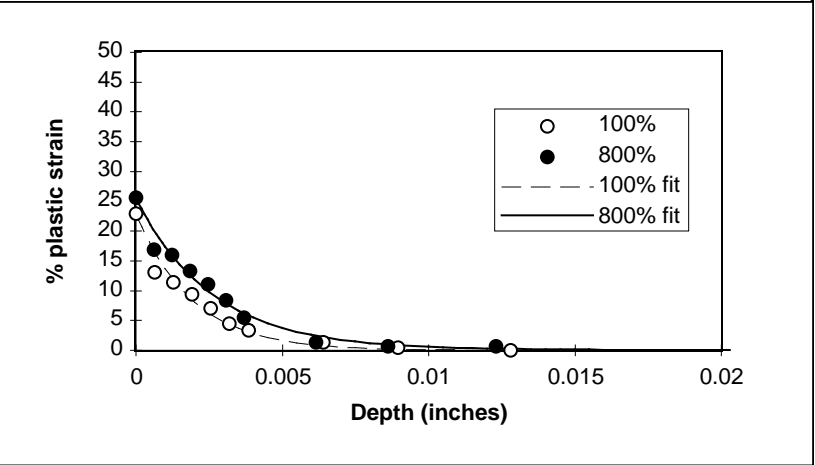
5-6) CCW14, 10A, 45°, 100% & 800% coverage



13-14) CCW31, 10A, 45°, 100% & 800% coverage



7-8) CCW14, 10A, 85°, 100% & 800% coverage



15-16) CCW31, 10A, 85°, 100% & 800% coverage

Figure C-3: Plastic Strain Profiles (estimated from x-ray diffraction data), continued

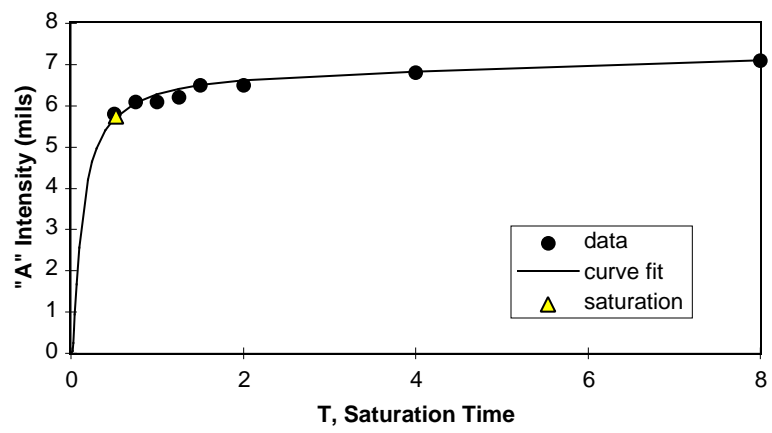
C.5 Saturation Curves

Due to the nature of the intensity definition, saturation curve data were requested and retained for each peening condition. Initially, four point curves were requested for the first group of specimens. Later, eight point curves were requested. Figure C.4 provides the saturation curves obtained for each condition, along with a curve fit and calculated saturation point using the curve fit, and solving for the point at which doubling saturation time results in a 10% increase in arc height. Due to the nature of the saturation curve, there is only one curve per shot-intensity-incidence angle combination (100% and 800% coverage conditions are simply two different points on the same curve).

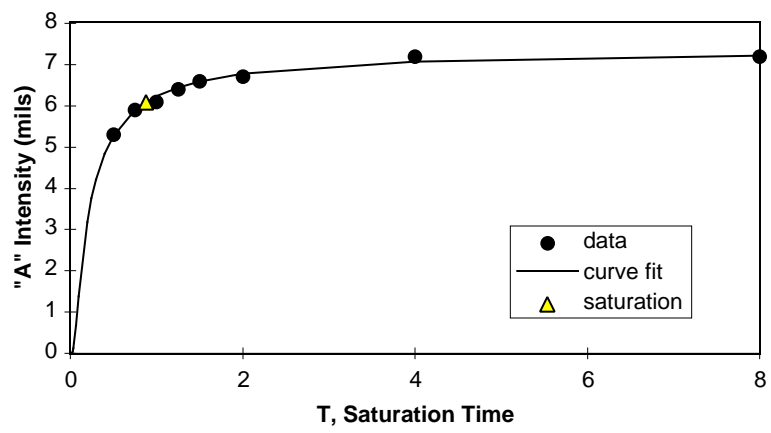
A curve fit of the form given in equation C.1 was used, where H is the arc height deflection in mils, T is the saturation time (inverse of the feed rate used here), A and B are regression constants. This equation is not the only equation that could be used; other forms provide better fits in the knee area. However, this form is simple enough that it can be linearized and solved using linear regression techniques. It does not require a non-linear solution.

$$H = A \exp(-B/T) \quad (C.1)$$

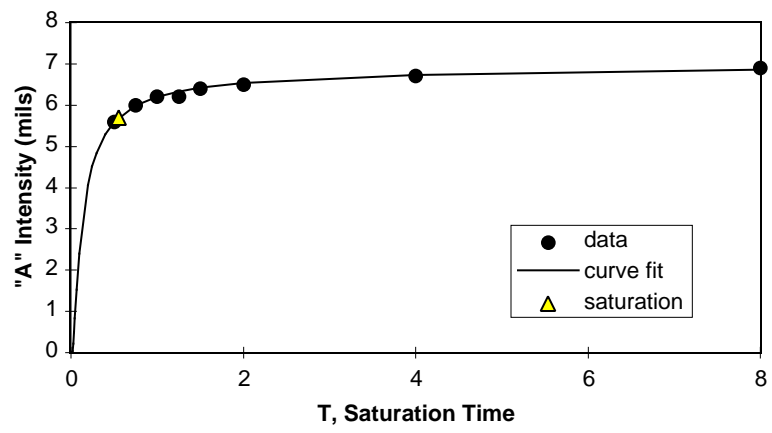
Standardization on a curve fitting technique could improve the robustness and usefulness of the intensity definition across vendors. This would require buy-in across the peening industry.



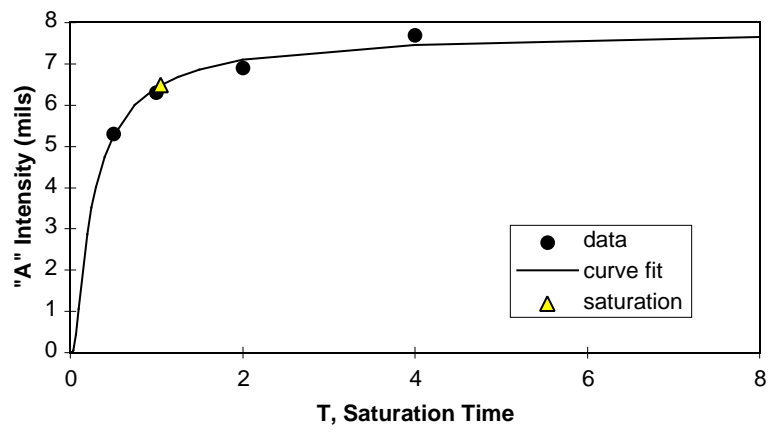
1-2) CCW14, 6A, 45°, 100% & 800% coverage



9-10) CCW31, 6A, 45°, 100% & 800% coverage



3-4) CCW14, 6A, 85°, 100% & 800% coverage



11-12) CCW31, 6A, 85°, 100% & 800% coverage

Figure C-4: Saturation Curves

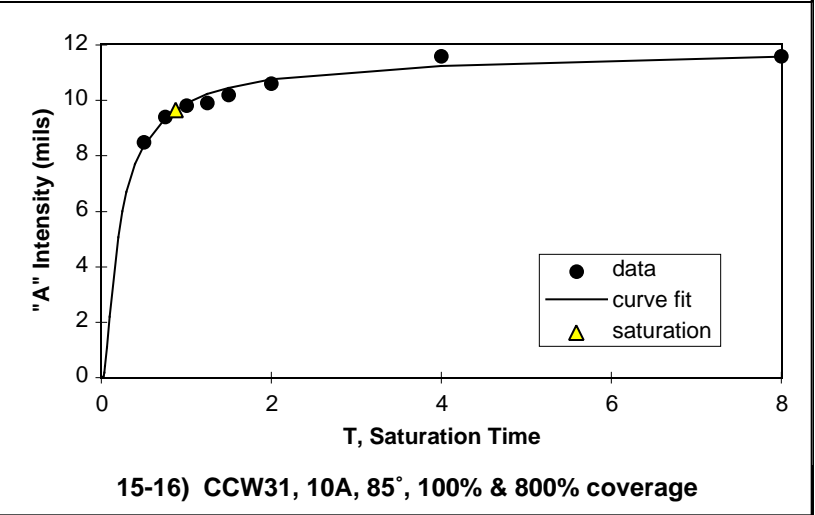
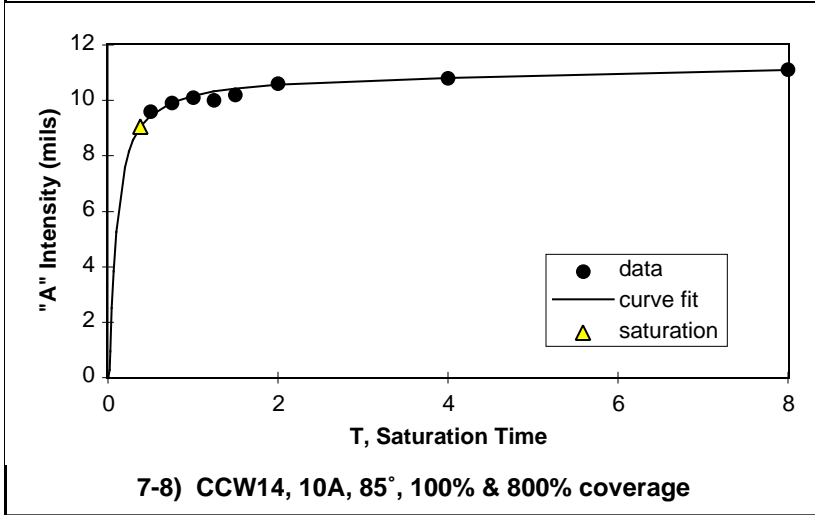
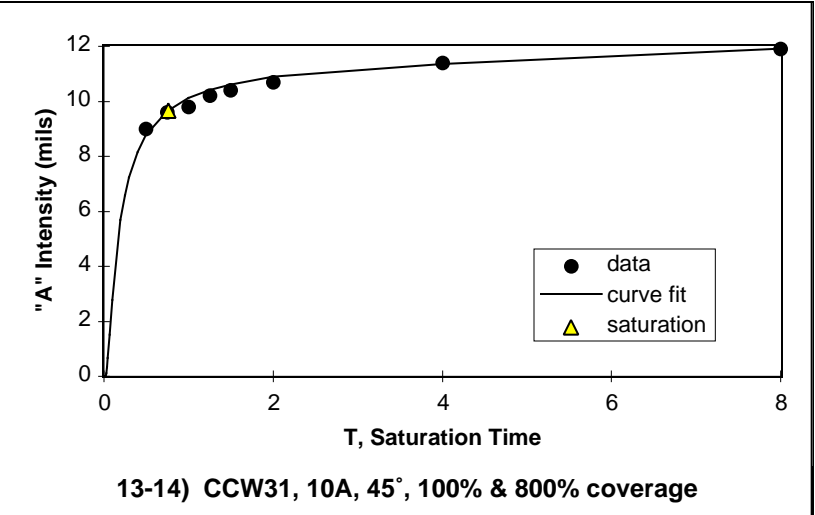
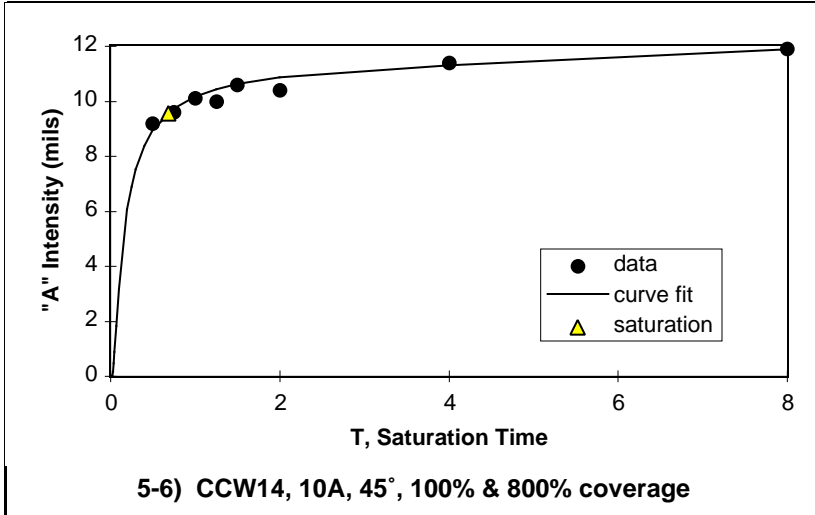


Figure C-4: Saturation Curves, continued

REFERENCES

- 1 Verpoort, C.M., C. Gerdes. 1989. "Influence of shot peening on material properties and the controlled shot peening of turbine blades." *Shot Peening: Theory and Application*, John Eckersley & Jack Champaigne, editors. IITT International, pp. 11-70.
- 2 Niku-Lari, A. 1981. "Shot-Peening." *First Int'l. Conf. on Shot Peening, Sept. 1981*, Pergamon Press, pp. 395-403.
- 3 Dörr, T. and L. Wagner. 1996. "Effect of shot peening on residual life of fatigue pre-damaged 2024 Al." *Sixth International Conference on Shot Peening*, Oct. 1996, pp. 174-183.
- 4 Wagner, L., G. Luetjering. 1981. "Influence of shot-peening on the fatigue behavior of titanium alloys" *First Int'l. Conf. on Shot Peening, Sept. 1981*, Pergamon Press, pp. 453-460.
- 5 Tufft, M.K. 1996. "Development of a fracture mechanics methodology to assess the competing mechanisms of beneficial residual stress and detrimental plastic strain due to shot peening." Paper presented at the *Sixth International Conference on Shot Peening*, held in San Francisco, CA, USA, September 3-6, 1996, pp. 2-3.
- 6 MIL-S-13165C, "Military specification shot peening of metal parts." 7 June 1989, p. 11, ¶ 6.12.
- 7 Sollich, A., H. Wohlfahrt. 1996. "Optimization of the fatigue strength of heat treated steels as a consequence of an optimum state of the surface and of subsurface layers after shot peening." *Sixth International Conference on Shot Peening*, Oct. 1996, pp. 251-262.
- 8 Bailey, P.G., D.R. Lombardo, H.G. Popp, R.A. Thompson. 1996. "Full assurance shot peening of aircraft gas turbine engine components." *Sixth International Conference on Shot Peening*, Oct. 1996, pp. 320-327.
- 9 Gillespie, Bob. 1996. "Image analysis of shot peening media." *Sixth International Conference on Shot Peening*, Oct. 1996, pp. 213-222.
- 10 Fuchs, H.O. 1981. "The Strength of Shot Peened Parts." *First International Conference on Shot Peening, Sept. 1981*, Pergamon Press: New York. pp. 323-332.
- 11 Happ, M.B., D.L. Rumpf. 1996. "Almen strip variability – a statistical treatment." *Sixth International Conference on Shot Peening*, Oct. 1996, pp. 302-311.
- 12 Kirk, D. 1996. "Developments in interactive control of shot peening intensity." *Sixth International Conference on Shot Peening*, Oct. 1996, pp. 95-106.
- 13 Lombardo, D.L., P.G. Bailey. 1996. "The reality of shot peen coverage." *Sixth International Conference on Shot Peening*, Oct. 1996, pp. 493-504.
- 14 Abyaneh, M.Y. 1996. "Fundamental aspects of shot peening coverage control part one: formulation of single and multiple impacting." *Sixth International Conference on Shot Peening*, Oct. 1996, pp. 438-447.

-
- 15 Lukáš, Petr. 1996. "Fatigue crack nucleation and microstructure." *ASM Handbook Volume 19: Fatigue and Fracture*. ASM International, Materials Park, Ohio. pp. 96-109.
 - 16 Christ, H.-J., H. Mughrabi. 1992. "Microstructure and Fatigue." *Low Cycle Fatigue and Elasto-Plastic Behavior of Materials - 3*. K.T. Rie, editor. Elsevier Applied Science: New York, pp. 56-69.
 - 17 Pangborn, R.N., S. Weissmann, I.R. Kramer. 1979. "Prediction of Fatigue Life by X-Ray Diffraction Methods." *Fatigue Fract. Engng. Mater. Struct.* Vol. 1, No. 3, pp. 363-369.
 - 18 Komotori, Jun and Masao Shimizu. 1992. "Microstructural Effect Controlling Exhaustion of Ductility in Extremely Low Cycle Fatigue." *Low Cycle Fatigue and Elasto-Plastic Behavior of Materials - 3*. K.T. Rie, editor. Elsevier Applied Science: New York, pp. 136-141.
 - 19 Burck, L.H., C.P. Sullivan, C.H. Wells. 1970. "Fatigue of a glass bead blasted Nickel-base superalloy." *Met. Transactions*, v 1, June 1970, pp. 1595-1600.
 - 20 Al-Hassani, S.T.S. 1982. "The shot peening of metals—mechanics and structures," *Shot Peening for Advanced Aerospace Design , SP-528*, Society of Automotive Engineers: Warrendale, PA. p. 2.
 - 21 Burck, L.H., C.P. Sullivan, C.H. Wells. 1970. "Fatigue of a glass bead blasted Nickel-base superalloy." *Met. Transactions*, v 1, June 1970, pp. 1595-1600.
 - 22 Timothy, S.P., I.M. Hutchings. 1981. "Microstructural features associated with ballistic impact in Ti6Al4V." *7th International Conference on High Energy Rate Fabrication*, pp. 19-28.
 - 23 Ru, Jilai, Renzhi Wang, Xiangbin Li. 1996. "Investigation on shot peening strengthening of René 95 powder alloy." 1996 Conference Proceedings of the Sixth International Conference on Shot Peening. pp. 338-347.
 - 24 Al-Obaid, Y.F. 1991. "The automated simulation of dynamic non-linearity to shot-peening mechanics." *Computers & Structures*, Vol. 40, No. 6, pp. 1451-1460.
 - 25 Al-Obaid, Y.F. 1990. "Three-dimensional dynamic finite element analysis for shot-peening mechanics." *Computers & Structures*, Vol. 36, No. 4, pp. 681-689.
 - 26 Fathallah, R., G. Inglebert, L. Castex. 1996. "Modeling of shot peening residual stresses and plastic deformation induced in metallic parts." *Sixth International Conference on Shot Peening*, Oct. 1996, pp. 464-473.
 - 27 Chang, Hong, F.C. Schoening, Jr., J.A. Soules. 1996. "Non-destructive residual stress measurement using eddy current." *Sixth International Conference on Shot Peening*, Oct. 1996, pp. 356-384.
 - 28 Starker, P. H. Wohlfahrt and E. Macherauch. 1979. "Subsurface crack initiation during fatigue as a result of residual stresses," *Fatigue Engng. Mater. Struct.* 1, pp. 319-327.
 - 29 Schutz, W. 1981. "Fatigue life improvement of high-strength materials by shot-peening." *First Int'l. Conf. on Shot Peening, Sept. 1981*, Pergamon Press, pp. 423-433
 - 30 Li, J.K., Yao Mei, Wang Duo, Wang Renzhi. 1992. "An analysis of stress concentrations caused by shot peening and its application in predicting fatigue

- strength," *Fatigue and Fracture of Engineering Materials & Structures*, Vol. 15, No. 12, Dec. 1992, pp. 1271-1279.
- 31 Hertzberg, R.W. 1989. *Deformation and Fracture Mechanics of Engineering Materials*. John Wiley & Sons: NY.
 - 32 Zeng, K., K. Breder, D.J. Rowcliffe. 1992. "The Hertzian stress field and formation of cone cracks–I. theoretical approach." *Acta metall. mater.* v 40, n 10, pp. 2295-2600.
 - 33 Zeng, K., K. Breder, D.J. Rowcliffe. 1992. "The Hertzian stress field and formation of cone cracks–II. determination of fracture toughness." *Acta metall. mater.* v 40, n 10, pp. 2601-2605.
 - 34 Lu, Jyh-Woei, G.A. Sargent, Hans Conrad. 1995. "A study of the mechanisms of erosion in silicon single crystals using Hertzian fracture tests." *Proc. of 8th Int'l Conf. on Erosion by Liquid and Solid Impact.* pp. 105-116. *SSDI* 0043-1648(95) 07128-8.
 - 35 Finnie, Iain, Jan Wolak, Yehia Kabil. 1966. "Erosion of Metals by Solid Particles." *Journal of Materials*. Presented at the 69th Annual Meeting of ASTM. pp. 682-700.
 - 36 Finnie, Iain, G.R. Stevick, J.R. Ridgely. 1992. "The influence of impingement angle on the erosion of ductile metals by angular abrasive particles." *Wear*, 152. pp. 91-98.
 - 37 Misra, Ambrish and Iain Finnie. 1981. "On the size effect in abrasive and erosive wear." *Wear*, 65. pp. 359-373.
 - 38 Tilly, G.P. 1973. "A two stage mechanism of ductile erosion." *Wear*, 23 (1973), pp. 87-96.
 - 39 Hutchings, IM. 1977. "Strain rate effects in microparticle impact." *J. Physics D: Appl. Phys.*, Vol 10. pp. L179-L184.
 - 40 Frost, H.J., M.F. Ashby. 1982. *Deformation–Mechanism Maps: The Plasticity and Creep of Metals and Ceramics*. Pergamon Press: NY, Oxford. ISBN 0 08 029338 7.
 - 41 de Rosset, W., A.V. Granato. 1970. "Strain rates in dislocation dynamics." *Fundamental Aspects of Dislocation Theory, Volume II*. National Bureau of Standards Special Publication 317, Washington, D.C., pp. 1099-1113.
 - 42 Meyers, Marc. 1994. *Dynamic Behavior of Materials*. John Wiley & Sons: New York. ISBN 0-471-58262-X. pp. 296-299.
 - 43 Field, J.E. and I.M. Hutchings. 1987. "Surface Response to Impact." *Materials at High Strain Rates*, edited by T.Z. Blazynski. Elsevier Applied Science, Essex, England.
 - 44 Hammond, D.W. and S.A. Meguid. 1990. "Crack propagation in the presence of shot-peening residual stresses," *Engineering Fracture Mechanics*, Vol. 37, No. 2, 1990, pp. 373-387.
 - 45 Koster, W.P., L.R. Gatto, J.T. Cammett. 1981. "Influence of shot peening on surface integrity of some machined aerospace materials." *First International Conference on Shot Peening, Sept. 1981*, Pergamon Press: New York. pp. 287-293.
 - 46 Nevarez, I.M., D.V. Nelson, Marcos Esterman, Kosuke Ishii. 1996. "Shot peening and robust design for fatigue performance." 1996 Conference Proceedings of the Sixth International Conference on Shot Peening. pp. 517-529.
 - 47 VanStone, R.H. 1988. "Residual Life Prediction Methods for Gas Turbine Components." *Materials Science and Engineering, A103*, pp. 49-61.

-
- 48 Raju, I.S. and J.C. Newman. 1986. "Stress-intensity factors for circumferential surface cracks in pipes and rods under tension and bending loads," *Fracture Mechanics: Seventeenth Volume, ASTM STP 905*, ASTM, Philadelphia, pp. 789-805.
- 49 Yau, J.F. 1986. "An empirical surface crack solution for fatigue propagation analysis of notched components." *Fracture Mechanics: Seventeenth Volume, ASTM STP 905*. pp. 601-624.
- 50 Gallagher, J.P., F.J. Giessler, A.P. Berens, R.M. Engle, Jr. 1982. "USAF damage tolerant design handbook: guidelines for the analysis and design of damage tolerant aircraft structures." USAF document AFWAL-TR-82-3073.
- 51 Irwin, G.R. 1960. "Plastic Zone Near a Crack and Fracture Toughness." *Proceedings of Seventh Sagamore Conference*, pp. iv-63.
- 52 Graman, R.D., E.E. Bryan. 1986. "Update to F101-GE-102 B-1B engine structural durability and damage tolerance analysis final report (ENSIP)", GEAE Report R83AEB650, Revision 2, GE Aircraft Engines, Cincinnati, Ohio 45215, January 31, 1986.
- 53 Van Stone, R.H., M.S. Gilbert, O.C. Gooden, J.H. Laflen. 1988. "Constraint-loss model for the growth of surface fatigue cracks." *Fracture Mechanics: Nineteenth Symposium, ASTM STP 969*, ASTM. pp. 637-656.
- 54 Paris, P.C. 1964. "Fatigue - an interdisciplinary approach." *Proceedings 10th Sagamore Conference*, Syracuse University Press, Syracuse, NY, p. 107.
- 55 Coles, A., W. Johnson, H.G. Popp. 1976. *J. Eng. Mat. Tech.*, 98, p. 305.
- 56 VanStone, R. contribution to R83AEB650, "F101-GE-102 B-1B Update to Engine Structural Durability and Damage Tolerance Analysis Final Report (ENSIP) Volume 2." General Electric. p. 5-2-2.
- 57 Krueger, D.D., R.D. Kissinger, and R.G. Menzies. 1992. "Development and introduction of a damage tolerant high temperature nickel-base disk alloy, René 88DT," *Superalloys, 1992*, pp. 277-286.
- 58 General Electric Aircraft Engines MPM database.
- 59 SAE J441. Rev. JUN93. "(R) CUT WIRE SHOT" Surface vehicle recommended practice. SAE specification. 6 pages.
- 60 Eylon, D., J.M. Hyzak. 1978. "An investigation of fatigue origins in superalloy powder compacts." *Metallurgical Transactions A*, Vol. 9A, Jan. 1978, pp. 127-130.
- 61 Prevey, P.S. 1986. *Adv. in X-Ray Anal.*, Vol. 29, pp. 103-111.
- 62 Prevey, P.S. 1977. *Adv. in X-Ray Anal.*, Vol. 20, pp. 345-354.
- 63 Koistinen, D.P., R.E. Marburger. 1959. *Trans. ASM.*, Vol. 51, pp. 537-550.
- 64 Moore, M.G., W.P. Evans. 1958. *Trans. SAE.*, Vol. 66, pp. 340-345.
- 65 Bailey, P.G., D.M. Comassar, J.M. Whalen, and R.A. Thompson. 1993. "New challenges for shot peening of aircraft gas turbine engine components," *Metal Finishing, Vol. 91 No. 3 March 1993*, pp. 21-25.
- 66 Bailey, P.G. 1994. in a "Letter to the Editor" in *The Shot Peener*, Spring 1994, Volume 8, Issue 1, p.17.
- 67 *Structural Alloys Handbook*, Volume 1, 1990 Edition. Batelle, Columbus, OH.
- 68 Callister, Jr., William D. 1991. *Materials Science and Engineering: An Introduction. Second Edition*. John Wiley & Sons: New York.

-
- 69 Le Guernic, Y., J. Eckersley. 1996. "Peenstress software selects shot peening parameters." *Sixth International Conference on Shot Peening*, Oct. 1996, pp. 481-492.
- 70 Miller, K.J. 1993. "The two thresholds of fatigue behavior." *Fatigue Fract. Engng. Mater. Struct.* Vol. 16, No. 9, pp. 931-939.
- 71 Rabinowicz, E. 1965. *Friction and Wear of Materials*. John Wiley and Sons, Inc. NY.
- 72 Zukas, J.A., Theodore Nicholas, H.F. Swift, L.B. Greszczuk, D.R. Curran. 1992. *Impact Dynamics*. Krieger Publishing Company, Malabar, FL, pp. 342.
- 73 Domas, P.A. 1995. "Elevated temperature component fatigue robustness – an holistic approach." *AGARD Conference Proceedings 569: Thermal Mechanical Fatigue of Aircraft Engine Materials*, October 1995, pp. 21-1 to 21-15.
- 74 Lubliner, J. 1990. *Plasticity Theory*. Macmillan Publishing Co., NY.
- 75 Box, G.E.P., W.G. Hunter, J.S. Hunter. 1978. *Statistics for Experimenters*. John Wiley & Sons, Inc.: NY.
- 76 Abernethy, R. B. 1993. *The New Weibull Handbook*. Published by Robert Abernethy, 536 Oyster Road, North Palm Beach, FL 33408-4328.
- 77 Tufft, M. K. 1996. "Instrumented single particle impact tests using production shot: the role of velocity, incidence angle and shot size on impact response, induced plastic strain and life behavior." Paper presented at the *Sixth International Conference on Shot Peening*, held in San Francisco, CA, USA, September 3-6, 1996.
- 78 Zehnder, A.T., A.C. Ramamurthy, S.J. Bless, N.S. Brar. 1993. "Stone impact damage to automotive paint finishes: measurement of temperature rise due to impact." *Int. J. Impact Engng.* Vol. 13, No. 1, pp. 133-143.
- 79 Popp, H. 4/27/93. Unpublished notes: "Original Development of Damage Limit Concept."
- 80 Beher, W.H., editor. 1991. *CRC Standard Mathematical Tables and Formulae, 29th Edition*. CRC Press, Boston, p. 111.